

Three Dimensional Discrete Element Modelling of Open-Ended Tubular Pile Penetration in Weak Rocks

by Xiangyu Zhang

Thesis submitted in fulfilment of the requirements for
the degree of

Doctor of Philosophy

under the supervision of Behzad Fatahi and Hadi Khabbaz

University of Technology Sydney
Faculty of Engineering and Information Technology

February 2020

CERTIFICATE OF ORIGINAL AUTHORSHIP

I, Xiangyu Zhang declare that this thesis, is submitted in fulfilment of the requirements for the award of Ph.D. degree, in the School of Civil and Environmental Engineering at the University of Technology Sydney.

This thesis is wholly my own work unless otherwise reference or acknowledged. In addition, I certify that all information sources and literature used are indicated in the thesis.

This document has not been submitted for qualifications at any other academic institution.

This research is supported by the Australian Government Research Training Program.

Signature:

Production Note:
Signature removed prior to publication.

(Xiangyu Zhang)

29 Feb 2020

To My Parents

Acknowledgement

Pursuing doctoral studies is challenging and exciting. This four-year journey would not have been possible without the guidance and support from my supervisors, and those who helped me, encouraged me, and accompanied me.

Firstly, I would like to express my most cordial gratitude to my principal supervisor A/Prof Behzad Fatahi and my co-supervisor A/Prof Hadi Khabbaz for their structured guidance, continuous support, understanding, and patience not only limited to the specific field of study but beyond. My Ph.D. thesis could not have been achieved without their constructive feedback and worthy recommendations.

I would like to express my very great appreciation to the Faculty of Engineering and Information Technology (FEIT) at UTS and the Centre of Built Infrastructure Research (CBIR) for providing me the platform to pursue my Ph.D.

I would also like to thank my friends, colleagues, and staffs in the School of Civil and Environmental Engineering for their kind assistance.

Finally, I wish to acknowledge my parents for their love, care, encouragement, understanding, and all the sacrifices they have made to support me throughout my study, without whom I would never have enjoyed so many opportunities.

List of Publications

- Published Journal Articles

Zhang, X., Fatahi, B., Khabbaz, H. & Poon, B. 2019, Assessment of the Internal Shaft Friction of Tubular Piles in Jointed Weak Rock Using the Discrete-Element Method, *Journal of Performance of Constructed Facilities*, vol. 33, no. 6, p. 04019067.

- Published Conference Papers

Zhang, X., Fatahi, B., and Khabbaz, H., 2018, ‘Investigating Effects of Individual Fracture Length on Behaviour of Weak Rock Using Discrete Element Method’, 5th GeoChina International Conference (GeoChina 2018), Hangzhou, China.

Zhang, X., Fatahi, B., and Khabbaz, H., 2018, ‘Investigating Effects of Fracture Aperture and Orientation on the Behaviour of Weak Rock Using Discrete Element Method’, GeoShanghai International Conference 2018 (GeoShanghai 2018), Shanghai, China.

Zhang, X., Fatahi, B., Khabbaz, H. and Zhang, H., 2017, ‘Investigating Effects of Fracture Density on Stress-Strain Behaviour of Jointed Rocks Using Discrete Element Method’, The 15th International Conference of the International Association for Computer Methods and Advances in Geomechanics (15IACMAG), Wuhan, China.

Table of Contents

CERTIFICATE OF ORIGINAL AUTHORSHIP	ii
Acknowledgement.....	iv
List of Publications	v
List of Figures	x
List of Tables.....	xviii
List of Abbreviations	xx
Nomenclature	xxii
Abstract	xxviii
Chapter 1 - Introduction.....	1
1.1 General.....	1
1.2 Statement of the Problem.....	4
1.3 Research Objectives.....	5
1.4 Significance of Research.....	7
1.5 Organisation of the Thesis	9
Chapter 2 - Literature Review	10
2.1 General.....	10
2.2 Ultimate Axial Capacity	12
2.2.1 Bearing Capacity of Tubular Piles in Sands and Clays	12
2.2.2 Bearing Capacity in Weak Rocks	22
2.3 Open-ended Tubular Piles	25

2.3.1 Soil Plug.....	25
2.3.2 Factors Affecting the Degree of Plugging	29
2.3.3 Effect of Pile Shoes.....	34
2.4 Characteristics of Weak Rocks.....	38
2.4.1 Formation and Classification	39
2.4.2 Discontinuities	43
2.4.3 Weak Rock Mass Strength.....	44
2.5 Numerical Analysis	46
2.5.1 Finite Element Method	48
2.5.2 Discrete Element Method	51
2.5.3 Coupled Analysis	57
2.6 Case History of Driven Tubular Piles on the Macleay River (NSW, Australia).58	
2.7 Summary and Gap Identification.....	60
Chapter 3 - Investigating the Mechanical Behaviour of Weak Rocks.....	62
3.1 General.....	62
3.1.1 Fundamentals of Flat-joint Model	64
3.1.2 Fundamentals of Smooth-joint Contact Model.....	68
3.2 Effects of Joint Density.....	70
3.2.1 Numerical Modelling.....	71
3.2.3 Results and Discussions.....	74
3.3 Effects of Rock Joints	79
3.3.1 Discrete Element Simulation	79

3.3.2 Effects of Joint Dip on the Mechanical Properties of Jointed Rock.....	84
3.3.3 Effects of Joint Aperture on the Mechanical Properties of Jointed Rock.....	85
3.4 Effects of Joint Length	87
3.4.1 Numerical Modeling	88
3.4.2 Results and discussions.....	95
3.5 Summary	99
Chapter 4 - Assessment of the Internal Shaft Friction	102
4.1 General.....	102
4.2 Background	102
4.3 Discrete Element Simulations	109
4.3.1 Calibration of Discrete Element Model	109
4.3.2 Push-up Load Tests in Tubular Pile on Jointed Mudstone	113
4.4 Effect of Loading Rate.....	116
4.5 Effect of Joint Density	118
4.6 Effects of Joint Dip	124
4.6.1 Effect of Joint Dip on the Triaxial Shear Test Results	124
4.6.2 Effect of Joint Dip on Push-up Load Test	125
4.7 Summary	131
Chapter 5 - Investigation of the Axial Load Transfer Mechanism.....	134
5.1 General.....	134
5.2 Background	135

5.3	Numerical Modelling	141
5.3.1	Fundamentals of the Contact Model	141
5.3.2	Calibration of the Adopted Contact Model for Weak Rock	144
5.3.3	Numerical Modelling of Pile Penetration	147
5.4	Results and Discussions	152
5.4.1	Predicted Resistances	152
5.4.2	Unit Shaft Frictions	155
5.4.3	Particle Displacement Patterns	157
5.4.4	Porosity and Stress Distributions	158
5.5	Impacts of Pile Shoe.....	163
5.5.1	Predicted Resistances for Pile with Driving Shoe	163
5.5.2	Effect of Pile Shoe on Unit Shaft Frictions	165
5.5.3	Porosity and Stress Distributions for Pile with Driving Shoe	166
5.6	Degree of Plugging	172
5.7	Summary	176
Chapter 6 - Conclusion		179
6.1	Summary	179
6.2	Key Concluding Remarks	180
6.3	Recommendations for Future Studies	185
Bibliography.....		187

List of Figures

Figure 1.1. Representative of the DEM modelling of simulating the open-ended tubular pile penetrating in rock masses.....	3
Figure 2.1. Soil disturbance beneath (a) a single solid pile; and (b) an open-ended tubular pile (after Tomlinson and Woodward 2008)	11
Figure 2.2. Load bearing components of open-ended tubular piles for (a) fully coring pile; and (b) plugged pile.....	15
Figure 2.3. Possible failure mechanism for open-ended piles (a) fully coring, (b) partially plugged, and (c) fully plugged (after White et al. 2005; Igoe et al. 2009; Ko and Jeong 2014)	27
Figure 2.4. Prediction of potential plugging in sand based on field evidence (after Jardine et al. 2005).....	31
Figure 2.5. Schematic diagram of (a) the shear zone adjacent to the pile shaft; (b) variation in the shear zone during driving (after Yu and Yang 2011).....	32
Figure 2.6. Different types of pile shoes: (a) outer shoe; (b) inner shoe; and (c) thick plate shoe (after Tomlinson and Woodward 2008).....	35
Figure 2.7. Hypothesised stress changes due to driving shoe in sandy soil: (a) the soil flow for open-ended tubular pile with inner pile shoe; (b) the soil flow for open-ended tubular pile with outer pile shoe; and (c) stress change at zone I, II, and III for open-ended tubular pile with inner shoe (after De Nicola and Randolph 1997; White et al. 2000).....	36
Figure 2.8. Formation of weak rocks and their position in the soil and rock mechanics (after Dobereiner and Freitas 1986; Zhai et al. 2017).....	41

Figure 2.9. Normalised rock mass strength against GSI illustrating marked differences between conventional Hoek-Brown behaviour (after Carter et al. 2008).....	46
Figure 2.10. Finite element model and boundaries conditions for analysis of plug mechanism (Liyanapathirana et al. 1998).....	50
Figure 2.11. “Zipper-type” technique for simulating pile penetration process in FEA (Henke and Grabe 2008)	51
Figure 2.12. An example of the Geometry of the CPT test in DEM (Ciantia et al. 2016)..	53
Figure 2.13. Arch development during penetration (after Li et al. 2019)	57
Figure 2.14. Finite element mesh and geometry for the soil domain in the CEL analysis of driving open-ended piles (Ko et al. 2016)	58
Figure 3.1. Behaviour of flat-joint contact (a) schematic diagram of flat-joint contact with the notional surfaces; (b) rheological components and behaviour of the unbonded element; and (c) rheological components and behaviour of the bonded element	66
Figure 3.2. The schematic illustration of smooth-joint contact model of (a) before installation; and (b) after installation.....	69
Figure 3.3. (a) Numerical model for intact rock specimen; (b) Failure mode for intact rock (yellow: shear crack and grey: tension crack); and (c) Smooth-joint contact model for simulating joints	72
Figure 3.4. Stress-strain curve of the intact rock specimen under unconfined compression test.....	73
Figure 3.5. Discrete fracture network for specimen with joint density values of (a) $10 \text{ m}^2/\text{m}^3$, (b) $50 \text{ m}^2/\text{m}^3$, (c) $100 \text{ m}^2/\text{m}^3$, and (d) $200 \text{ m}^2/\text{m}^3$	74

Figure 3.6. Effect of joint density on rock mass unconfined compressive strength of jointed rock specimens	75
Figure 3.7. Failure mechanism for specimens with joint density values of (a) 10 m ² /m ³ , (b) 50 m ² /m ³ , (c) 100 m ² /m ³ , and (d) 200 m ² /m ³ (green: joint; yellow: shear crack and grey: tension crack).....	76
Figure 3.8. Effect of joint density on Young’s modulus of jointed rock specimens	77
Figure 3.9. (a) Numerical model of the intact rock specimen, and (b) numerical representation of the rock grains with the flat-joint contact and the joint with the smooth-joint contact	80
Figure 3.10. The stress-strain curve of experimental measurements and model predictions of the intact rock specimen for confining pressure of 392 kPa	82
Figure 3.11. Representative of jointed rock specimen with the joint dip (α) to the direction of cell pressure.....	83
Figure 3.12. Normalised deviatoric strength at 15% axial strain of jointed specimen for different joint dips and apertures	84
Figure 3.13. Volumetric strain at 15% axial strain of jointed specimens with different joint dips and apertures	85
Figure 3.14. Comparisons of the intact specimen and jointed specimens with different joint apertures for the given joint dip of 30°	86
Figure 3.15. Volumetric strain of different joint apertures for jointed rock specimens	87
Figure 3.16. (a) Numerical model of intact rock specimen under triaxial test with six rigid walls; (b) Contact force chain for intact rock specimen (line thickness and dip represent force	

magnitude and direction, respectively), and (c) The smooth-joint contact model for simulating joints	90
Figure 3.17. Stress-strain curve of the intact rock specimen calibration exercise.....	92
Figure 3.18. Volumetric strain variations of the intact rock specimen during shearing - calibration exercise	92
Figure 3.19. Discrete fracture network for the rock specimen with individual joint length of (a) 140 mm, (b) 84 mm, (c) 11.2 mm, and (d) 5.6 mm, (Note: the joint density remains constant $\xi = 7 \text{ m}^2/\text{m}^3$)	95
Figure 3.20. Predicted stress-strain curves of jointed specimens with different individual joint length.....	96
Figure 3.21. Volumetric strain of jointed specimens with different individual joint length	97
Figure 3.22. Applied axial stress to cell pressure ratio (σ_1/σ_3) versus the ratio of individual joint length to the specimen width (η/L) at 15% axial strain	97
Figure 3.23. Volumetric strain versus normalised joint length for jointed rock specimens	98
Figure 3.24. Particle displacement representation for jointed specimens at the axial strain of 15 % with normalised joint length (η/L) of (a) 1.4, (b) 0.84, (c) 0.28, (d) 0.112, (e) 0.056, and (f) 0.028 (grey: particle displacement and black: smooth-joint model contacts for joints)	99
Figure 4.1. (a) Application of steel tubular piles for bridge foundation; and (b) installation technique for the tubular piles, for Pacific Highway Upgrade project in east coast of Australia	103

Figure 4.2. Components of bearing-capacity of an open-ended tubular pile	105
Figure 4.3. UCS test results for (a) high strength Phyllite before testing; (b) high strength Phyllite after testing; (c) low strength Phyllite before testing; and (d) low strength Phyllite after testing	106
Figure 4.4. Back-calculated pile shaft resistances obtained from CAPWAP analysis for rocks with different point load strength indexes	107
Figure 4.5. (a) Numerical model for intact mudstone under triaxial loading; and (b) displacement of individual grains of the specimen at an axial strain of 0.8%	110
Figure 4.6. Stress-strain curves of triaxial tests from experimental and calibration exercises, (a) deviatoric stress against axial strain, and (b) deviatoric stress against lateral strain ...	112
Figure 4.7. Analysis models of the push-up load test of model components and model dimensions	114
Figure 4.8. Representation of the jointed rock plugs with joint dip of 0° and joint density of (a) 1.1 m ² /m ³ , (b) 4.4 m ² /m ³ , and (c) 8.9 m ² /m ³	116
Figure 4.9. Comparison of loading rates on the push-up load tests.....	118
Figure 4.10. Behaviour of intact rock plug of (a) relationship between push-up displacement and force, and (b) vertical stress along the rock plug.....	120
Figure 4.11. Relationship of the push-up displacement and force of jointed rock plugs with joint density of (a) 1.1 m ² /m ³ , (b) 4.4 m ² /m ³ , and (c) 8.9 m ² /m ³	123
Figure 4.12. Stress-strain curves of triaxial test for intact and jointed specimens, (a) deviatoric stress against axial strain, and (b) deviatoric stress against lateral strain.....	125

Figure 4.13. Yield axial stress of (a) rock plug in push-up load test, and (b) rock mass in triaxial test	127
Figure 4.14. Displacement of individual grains of push-up load test for (a) intact rock plug, (b) joint dip of 0°, (c) joint dip of 30°, (d) joint dip of 45°, (e) joint dip of 60°, and (f) joint dip of 90°	128
Figure 4.15. Distribution of unit shaft friction along the rock plugs with joint density of 4.4 m ² /m ³ and joint dip of (a) 0°, (b) 30°, (c) 45°, (d) 60°, and (e) 90°	131
Figure 5.1. (a) flat-jointed particles with the contact interface; and (b) representatives of the elements discretised from the interface	141
Figure 5.2. Rheological components of the flat-joint model for (a) bonded element, and (b) unbonded element.....	142
Figure 5.3. (a) Numerical triaxial test sample dimension; (b) particle displacement at the end of the triaxial test for confining pressure of 100 kPa; and (c) particle displacement at the end of the triaxial test for confining pressure of 350 kPa.	145
Figure 5.4. Calibration exercises comparing with the experimental results for the weak rock	146
Figure 5.5. Geometry and dimension of the (a) the testing chamber; (b) the tested open-ended tubular pile; and (c) schematic diagram of the open-ended tubular pile with and without a shoe.....	148
Figure 5.6. (a) Schematic illustration of the top view of the testing chamber with particle refinement upscale factors and radial distances; and (b) the side view of the measurements from top to bottom of the model.....	150

Figure 5.7. The initial condition of the large-scale model of (a) distribution of the porosity, and (b) vertical stress and radial stress	152
Figure 5.8. Pile resistance of open-ended tubular pile with depth	153
Figure 5.9. Contact network for the open-ended tubular pile without driving shoe at a penetration depth of (a) 0.4 m, and (b) 1.0 m.....	155
Figure 5.10. (a) Unit internal shaft friction of open-ended tubular pile at different penetration depths; and (b) Unit external shaft friction of open-ended tubular pile at different penetration depths.....	156
Figure 5.11. Individual particle displacement of the open-ended tubular pile without pile shoe at a pile penetration depth of (a) 0.1 m, (b) 0.5 m, and (c) 1.0 m	158
Figure 5.12. The porosity distribution pile before and after driving for the open-ended tubular pile (a) at the location inside the pile; and (b) at the location outside and adjacent to the pile	159
Figure 5.13. Stresses at different depth for open-ended pile: (a) radial stress at 0.2 m, (b) vertical stress at 0.2 m, (c) radial stress at 1 m, (d) radial stress at 1 m, and (e) peak stresses at 0.2 m and 1 m	162
Figure 5.14. Pile resistance of open-ended tubular pile with an inner pile shoe.....	163
Figure 5.15. Contact network for the open-ended tubular pile with driving shoe at a penetration depth of (a) 0.1 m, and (b) 1.0 m.....	165
Figure 5.16. Comparison of the unit external and internal shaft friction for open-ended tubular piles with and without shoe.....	166
Figure 5.17. Individual particle displacement of the open-ended tubular pile with inner pile shoe at a penetration depth of (a) 0.1 m, (b) 0.5 m, and (c) 1.0 m	167

Figure 5.18. The porosity distribution pile before and after driving for the open-ended tubular pile with the inner shoe (a) at the location inside the pile; and (b) at the location outside and adjacent to the pile..... 168

Figure 5.19. Stresses at different depth for open-ended pile with the inner shoe: (a) radial stress at 0.2 m, (b) vertical stress at 0.2 m, (c) radial stress at 1 m, (d) radial stress at 1 m, and (e) peak stresses at 0.2 m and 1 m 171

Figure 5.20. IFR and PLR values of open-ended tubular piles with and without driving shoe 173

Figure 5.21. Inclination angle of the top surface of the rock plug in relation to (a) PLR, and (b) IFR 174

Figure 5.22. Relationship between the PLR and IFR and compared with other studies ... 175

List of Tables

Table 2.1. Some of the recommended design parameters for cohesionless siliceous soils (after American Petroleum Institute 2002).....	16
Table 2.2. Bearing resistance factor Nk proposed by different researchers (after Irvine et al. 2015).....	23
Table 2.3. Ks for different tectonic stress levels (after González de Vallejo and Hijazo 2008; Terente et al. 2017).....	24
Table 2.4. Summary of factors affecting the degree of plugging	30
Table 2.5. Usual type of weak rocks (after Kanji 2014).....	40
Table 2.6. Summary of classification systems of weak rocks	42
Table 2.7. Uniaxial compressive strength and description of shales and sandstones as related to porosity (after Klein 2001)	43
Table 2.8. Comparison of FEM and DEM methods for pile penetration problems	47
Table 2.9. Examples of 2D DEM simulations on the pile installation process or CPT test	54
Table 2.10. Examples of 3D DEM simulations on the pile installation process or CPT test	56
Table 2.11. Interpreted design values for shaft friction and base resistance of tubular piles in different subsurface conditions (Zhang et al. 2013)	59
Table 3.1. Summary of microparameters for the intact rock specimen.....	73
Table 3.2. Details of tested specimens, rock mass unconfined compressive strength ratio and Young's modulus ratio of jointed rock to intact rock.....	78

Table 3.3. The joint apertures and dips investigated in the study	83
Table 3.4. Summary of calibrated flat-joint parameters for the intact weak rock specimen	93
Table 3.5. Summary of smooth-joint parameters for joints.....	93
Table 3.6. Different joint configurations used in the simulation of jointed rock sample....	94
Table 4.1. Calibrated parameters used in the discrete element modelling of weak mudstone in the triaxial test	113
Table 4.2. Micro-parameters of smooth-joint contact for the joints adopted in this study	115
Table 4.3. Predicted push-up forces at the yielding point for jointed rock plugs.....	122
Table 5.1. The calibrated micro-parameters adopted in the numerical model to simulate pyroclastic weak rock	147

List of Abbreviations

API:	American Petroleum Institute
BPM:	Bonded Particle Model
CAPWAP:	Case Pile Wave Analysis Program
CEL:	Coupled Eulerian-Lagrangian
CPT:	Cone Penetration Test
DEM:	Discrete Element Method
DFN:	Discrete Fracture Network
FEA:	Finite Element Analysis
FEM:	Finite Element Method
FinnRA:	Finnish National Road Administration
FJM:	Flat-joint Model
GSI:	Geological strength index
HKU:	Hong Kong University
ICP:	Imperial College Pile
IFR:	Incremental Filling Ratio
LCPC:	Laboratoire Central des Ponts et Chaussées

NGI:	Norwegian Geotechnical Institute
PFC3D:	Particle Flow Code in Three Dimension
PLR:	Plug Length Ratio
RMR:	Rocking mass rating
SJM:	Smooth-joint Contact Model
USC:	Unconfined Compressive Strength
UWA:	University of Western Australia

Nomenclature

The following notations are used in this research:

A :	Constant;
A^e :	area of the element (m ²);
A_p :	gross end area of the pile (m ²);
A_r :	effective area ratio (non-dimensional);
A_s :	shaft area of the pile (m ²);
A_{shoe} :	area of the driving shoe (m ²);
A^{sj} :	area of the smooth-joint cross-section (m ²);
B :	Constant;
C :	Constant;
c :	undrained shear strength of soil (kPa);
c_c :	contact cohesion (Pa);
D :	pile diameter (m);
D_{CPT} :	cone diameter (m);
D_{inner} :	inner diameter of the pile (m);
D_{outer} :	outer diameter of the pile (m);
D_r :	relative density (non-dimensional);
d_{50} :	median particle diameter (mm);
d_{max} :	maximum diameter of the particles (mm);
d_{min} :	minimum diameter of the particles (mm);
E_c :	Young's modulus at each particle contact (Pa);
E_f :	Young's modulus values for jointed specimens (MPa);

E_i :	Young's modulus values for intact specimens (MPa);
e :	void ratio (non-dimensional);
F_n^{sj} :	normal force carried by the smooth-joint contact (N);
$F_n^{sj-\psi}$:	shear force due to dilation (N);
F_s^{sj} :	shear force of smooth-joint contact (N);
F_s^{sj-c} :	shear force determined by the imposed Coulomb limit (N);
F_s^{sj-s} :	shear force determined by the force-displacement law (N);
$(F_n^{sj})_0$:	initial normal force carried by the smooth-joint contact (N);
\bar{F}_n^e :	normal force acting at the element (N);
\bar{F}_s^e :	shear force acting at the element (N);
$f_T(\sigma_{ci})$:	correction factor for transition material (non-dimensional);
f :	unit skin friction (kPa);
f_{s-i} :	unit internal shaft friction (kN/m);
f_{s-o} :	unit external shaft friction (kN/m);
G :	operational shear modulus (GPa);
g :	interface gap (m);
H_z :	embedded shaft length (m);
H_i :	penetration depth (m);
H_{plug} :	height of the rock plug (m);
ΔH :	change in pile penetration depth (m);
h :	height of soil layer above the pile toe (m);
$I_{s(50)}$:	point load strength index (MPa);
I_{v0} :	relative void index (non-dimensional);

I_{vy} :	relative void index at yield (non-dimensional);
K :	coefficient of lateral earth pressure (non-dimensional);
K_C :	a factor depend on yield stress ratio (non-dimensional);
K_f :	coefficient of radial effective stress at failure (non-dimensional);
K_S :	coefficient of horizontal stress of rock mass (non-dimensional);
k^* :	normal-to-shear stiffness ratio (non-dimensional);
k_n :	contact normal stiffness (Pa/m);
k_{ns} :	contact normal stiffness for smooth-joint contact (Pa/m);
k_s :	contact shear stiffness (Pa/m);
k_{ss} :	contact shear stiffness for smooth-joint contact (Pa/m);
L :	smallest characteristic model length (m);
l_i :	soil plug length (m);
Δl :	incremental change of plug length (m);
$m_b, m_i, s, \text{ and } a$:	original Hoek-Brown parameters;
$m_b^*, s^*, \text{ and } a^*$:	corrected Hoek-Brown parameters;
N_c :	bearing capacity factor (non-dimensional);
N_q :	bearing capacity factor (non-dimensional);
N_γ :	bearing capacity factor (non-dimensional);
P_a :	atmospheric pressure (kPa);
p'_0 :	effective overburden pressure (kPa);
$Q_{annular}$:	resistance of the annular area (kN);
Q_b :	ultimate resistance of the base (kN);
Q_{base} :	resistance of the equivalent base (kN);
Q_{bottom} :	bearing capacity of the soil beneath the plug base (kN);

Q_{inner} :	bearing capacity of inner shaft (kN);
Q_{outer} :	resistance of outer shaft (kN);
Q_p :	ultimate resistance of the pile (kN);
Q_{plug} :	bearing capacity of soil plug (kN);
Q_s :	ultimate resistance of the shaft (kN);
q :	unit end bearing capacity (kPa);
q_c :	local CPT tip resistance (kPa);
q_{uc} :	uniaxial compressive strength of the intact rock (MPa);
R :	radius of the pile (m);
R^* :	equivalent radius of the pile (m);
R^A :	radii of the contacting particle A (m);
R^B :	radii of the contacting particle B (m);
R^{fj} :	radius of the flat-joint contact (m);
R_{inner} :	inner radius of the pile (m);
R_{outer} :	outer radius of the pile (m);
r :	radial distance (m);
Δr :	radial displacement (m);
S_t :	clay sensitivity (non-dimensional);
T :	tensile strength of the rock mass (MPa);
t_{pile} :	thickness of the pile (mm);
t_{pile} :	pile wall thickness (mm);
UCS :	unconfined compressive strength (MPa);
UCS_{RM} :	uniaxial compressive strength of rock mass (MPa);

UCS_f :	unconfined compressive strength for jointed rock (MPa);
UCS_i :	uniaxial compressive strength of intact rock material (MPa);
W :	width of the base (m);
W_p :	weight of the pile (m);
Z :	depth (m);
α :	joint dip (degree);
β :	adhesion factor (non-dimensional);
χ :	a multiplier (non-dimensional);
γ :	effective density of the rock mass (kg/m^2);
δ :	friction angle between the soil and pile wall (degree);
δ :	friction angle between pile and soil (degree);
δ_{cv} :	interface angle of friction at failure (degree);
δ_f :	operational interface angle of frictional failure (degree);
$\Delta\delta_n^{sj}$:	elastic portions of the normal displacement increment (m);
$\Delta\delta_s^{sj}$:	shear displacement increment (m);
ϕ :	internal friction angle (degree);
ϕ_c :	contact friction angle (degree);
ϕ_{rc} :	contact residual friction angle (degree);
η :	plugging coefficient (non-dimensional);
η :	individual joint length (mm);
Ψ :	dilation angle (degree);
λ :	radius multiplier (non-dimensional);
μ_c :	contact friction coefficient;

μ_{cs} :	contact friction coefficient for smooth-joint contact;
σ_1 :	major principle stress (kPa);
σ_3 :	minor principle stress (kPa);
σ_b :	normal stress on the notional surface (Pa);
σ_c :	contact tensile strength (Pa);
σ_{ci} :	uniaxial compressive strength (MPa);
σ^e :	normal stress in the element (Pa);
σ'_{rc} :	equalized radial effective stress (kPa);
σ'_{rc} :	local radial effective stress (kPa);
σ_{ten} :	tensile strength limit (Pa);
σ'_{vo} :	in-situ initial vertical effective stress (kPa);
σ'_{vy} :	vertical yield stress (kPa);
$\Delta\sigma'_{rd}$:	increase in radial effective stress during pile loading (kPa);
τ_b :	shear strength of the contact (Pa);
τ^e :	shear stress in the element (Pa);
τ_f :	local shear stress (kPa);
τ_{lim} :	shear strength limit (Pa);
τ_{sp} :	shear strength of the element from slipping (Pa);
ξ :	joint density (m^2/m^3);
ω :	joint aperture (mm);

Abstract

Open-ended tubular piles, usually made of steel, are commonly used in offshore structures and bridge projects due to the high capacity and less required installation effort. Predicting the load – displacement response of the open-ended piles is of interest to many practicing engineers and researchers. Although the behaviour of the piles embedded in sands and clays has been studied extensively, clear and adequate recommendation is not currently available for predicting the load – displacement response of open-ended piles embedded in weak rocks. However, the increasing number of projects in Australia requires adopting the open-ended piles embedded in weak rock layers to sustain the axial and lateral structural loads. Current recommendations for the design of tubular piles in weak rocks are mainly based on the methods originally proposed for gravels, sands and clays, which cannot predict the shaft and base resistances of tubular piles in weak rocks accurately. Furthermore, the behaviour of weak rock masses is complex due to their characteristics, and the plugging mechanism of tubular piles influenced by the characteristics of the weak rock is not well understood. Therefore, there is a need to enhance the understanding of the load bearing mechanism of open-ended tubular piles embedded in weak rocks to optimise the construction cost and improve safety.

In this thesis, initially the effects of joint properties on the behaviour of weak rock masses are discussed. The discrete element method (DEM) is adopted which can simulate interacting rock grains. The interaction between grains is controlled by the adopted contact models. The flat-joint model that follows the elasto-plastic force-displacement constitutive law is employed in the analysis. Meanwhile, the discrete fracture network (DFN) along with the smooth-joint model are adopted to replicate the sliding of the joints. Initially, the effects of joint dip, joint density, joint aperture, and joint length on the mechanical behaviour of the

rock mass are investigated through simulating unconfined compressive strength and triaxial tests.

Moreover, this research provides an insight into the impacts of joint dip and joint density on the internal shaft friction of open-ended tubular piles through DEM analysis. The flat-joint and smooth-joint contact models are adopted to replicate the rock mass and the sliding of the joints, respectively. The push-up load tests are performed on the intact rock plug and jointed rock plug to analyse the effects of joints on the internal shaft frictions of tubular piles. It is noticed that the joints could reduce the capacity of the rock plug, and the joints parallel to the loading direction have the largest impact compared to other joint dips, where the joints parallel to the axial loading direction in the triaxial test do not result in the lowest strength. This indicates that the internal shaft friction of open-ended tubular piles is not solely a function of the rock strength, and the effects of joint properties need to be taken into consideration.

Furthermore, the axial load bearing mechanism of open-ended tubular piles penetrating into weak rock is discussed. The numerical modelling using the discrete element method is adopted since tubular pile driving involves extremely large displacements that DEM can accommodate. Effects of an inner driving shoe attached to the open-ended tubular pile on the load bearing mechanism is also investigated. The incremental filling ratio (IFR) and plug length ratio (PLR) are used to assess the plugging of the piles. As expected, the base resistance can mobilise at the early stage of the pile penetration, while the internal and external shaft frictions increase continuously as the pile penetrates deeper. The unit internal shaft friction is mainly mobilised at the bottom portion of the rock plug due to the arching effect. Moreover, partial plugging is observed for both piles with and without driving shoe, and the correlations between IFR and PLR are proposed.

Chapter 1 - Introduction

1.1 General

Weak rocks are widely spread all over the world, which are normally found as the transition layer of the hard soils to rocks. Sometimes, the subsurface conditions of the superstructure can be very undesirable which have the alluvial soils up to 50 m deep overlying weathered rocks (Zhang et al. 2013). To design the foundation for superstructures, open-ended tubular piles are often employed, with refusal driving effort to the weak rock layers instead of sitting on the medium strength rocks. Potentially, embedding the tubular piles in weak rocks can result in economic and time efficient construction with sufficient bearing capacity, while assessing the axial capacity of the pile in weak rock required for design is quite challenging.

The weak rock characteristics can be quite complex due to the undesired behaviours, such as low strength, high deformability, and the presence of discontinuities. Many researchers (e.g., Dobereiner and Freitas 1986; Kanji 2014) have conducted extensive research to investigate the formation and the classification of weak rocks. Most of these classification systems are based on intact rock strength. However, joints and discontinuities are commonly encountered in natural rock masses, which contribute to the complexity of their analysis due to the textural anisotropy. Certain studies (e.g., Singh et al. 2002; Tommasi et al. 2014) considered the pattern, orientation, spacing, size and distribution of joints, and concluded that discontinuities contribute significantly to the strength and deformability of rock mass. Therefore, predicting the load-displacement relationship and bearing capacity of open-ended piles, especially for those embedded in weak rocks, can be quite challenging.

The open-ended piles have gained significant popularity due to the advantages such as less installation effort, less disturbance to the surrounding ground, and large axial and lateral resistances against applied structural loads. The design methods of tubular piles are rather well

developed for sands and clays and widely used around the world. The well-known design methods for open-ended piles are the API method (American Petroleum Institute 2002) and the ICP method (Jardine et al. 2005). However, there are no practical and reliable recommendations for the design of tubular piles in weak rock conditions, and usually, formulations originally developed for soils (e.g., hard clay or stiff granular materials) are used which may not result in reliable and accurate axial bearing capacity predictions.

To properly predict the axial load – displacement capacity of tubular piles, a deep understanding of the plugging mechanism is required. Some of the design methods for open-ended tubular piles in sands and clays take the considerations of the plugging. For example, the ICP method recommends using different relationships to predict the resistance of a plugged and unplugged pile. Meanwhile, the incremental filling ratio (IFR), which indicates the degree of plugging, is adopted in the UWA method (Lehane et al. 2005) to the prediction of shaft resistance of open-ended tubular piles. At the same time, many researchers (e.g., Thongmuneet al. 2011; Henke and Grabe 2013) have studied the plugging effect considering the pile diameter, the friction between pile and soil, and the installation methods. However, most of the studies were conducted in sands. The presence of the joints in the weak rock masses contributes to the complexity of investigating the plugging mechanism, which has rarely been studied and is one of the focuses of this study.

Considering the rather recent advancements in sensor technology, the internal and external shaft frictions can be investigated separately in the field or laboratory conditions by using the twin-walled system, which is composed of two concentric tube with one pile being larger in diameter than the other pile and they are connected at the top or bottom (Paik et al. 2003; Han et al. 2019a). Measuring gauges are attached on both of the piles to obtain the internal and external shaft friction individually. However, the base area is significantly larger than the common open-ended tubular pile used in the field. The discrete element method is an

alternative numerical method for such analysis to investigate the bearing mechanism of open-ended tubular piles. Meanwhile, DEM has some advantages such as providing the micro-mechanics and macro-behaviour of the ground and the interaction between pile and the ground. DEM analysis can allow assessing the internal and external shaft frictional forces and base resistance separately, while it can also provide an insight into understanding the variations of ground porosity, stress distribution, and particle movements. An example of the DEM modelling to simulate the open-ended tubular piles penetrating into the ground is shown in Figure 1.1.

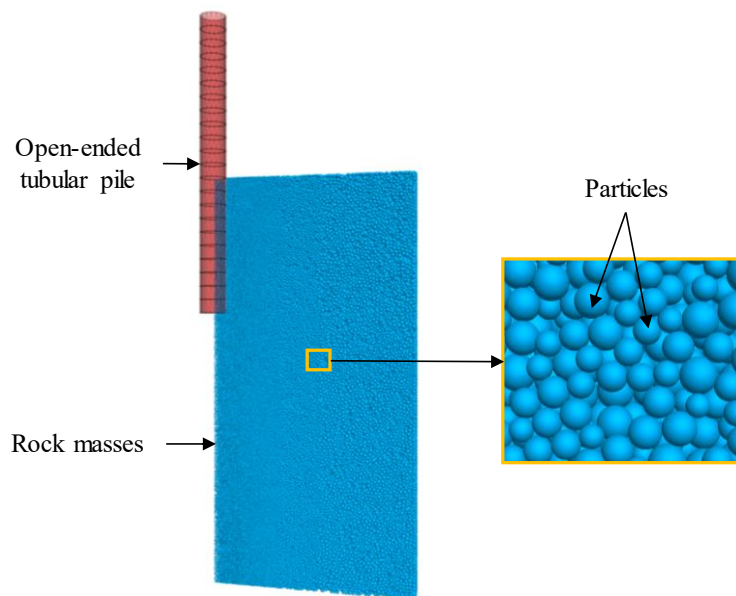


Figure 1.1. Representative of the DEM modelling of simulating the open-ended tubular pile penetrating in rock masses

In the present study, the effects of joint properties on the characteristics of weak rock are studied numerically, mainly focusing on the joint density, joint dip, joint aperture, and joint length. The effects of joint dip and joint density on the internal shaft friction of tubular piles are also assessed. The internal and external shaft resistances as well as the toe resistance of tubular piles in weak rocks are investigated through simulating the pile penetration processes using the discrete element method. In particular, the plugging mechanism of open-ended

tubular piles incorporating the characteristics of the pile and weak rock are investigated and discussed.

1.2 Statement of the Problem

Establishing reliable load-displacement relationship as well as capacity of the open-ended tubular piles embedded in weak rocks is essential to ensure cost effective and safe designs of major infrastructure and structures such as bridges and tall buildings. Although the response of open-ended tubular piles in sands and clays have been studied extensively, the axial load – displacement relationship of these piles embedded in weak rocks cannot yet be adequately assessed due to absence of suitable design tools. Indeed, difficulties and uncertainties in weak rock characteristics and the interaction between pile and rock added to the complexity of the design. Limited recommendations exist for predicting the axial bearing capacity of open-ended tubular piles embedded in weak rocks, and they are either over conservative or not adequate (Zhang et al. 2013). Indeed, most of existing recommendations were developed for pile design in sands and clays and are used for design and assessment of tubular piles in weak rock due to unavailability of alternative methods. However, it is noted that the behaviour of weak rocks differs from soils, which may be significantly influenced by the heavily weathered nature of the rock and the presence of joints.

Furthermore, the driving process of the open-ended tubular piles in the weak rocks, required to assess the plugging mechanism, has not been well studied. Indeed, understanding the degree of plugging and the plug capacity is important for the accurate prediction of the bearing capacity and driving resistance of the pile. It is noted that the uncertainties generated by the degree of plugging may result in hard driving, not allowing the pile to reach the desired design depth, as reported by Zhang et al. (2013) and Randolph (2018). Meanwhile, the plug capacity contributes to the bearing capacity of the open-ended tubular pile. It is known that the bearing

components of the open-ended tubular piles are the internal shaft resistance or the plug capacity, the external shaft resistance, and the base resistance. For a plugged pile, the internal shaft resistance or the plug capacity is larger than the corresponding value for an unplugged pile. When the pile is driven under the fully plugged mode, the pile even can be regarded as a closed-ended or solid pile, referring to the API method (American Petroleum Institute 2002). Although many studies have been done on the plugging effect of open-ended tubular piles, most of them are for sandy soils and not weak rocks. Therefore, the degree of plugging considering the characteristics of the pile and weak rock need to be studied further, resulting in more reliable predictions of the axial load – displacement relationship for the tubular piles. Furthermore, different from soils, weak rocks may contain joints, which can alter the strength of the rock mass, and the effect of joint properties on the degree of plugging is not clear and needs further studies.

Thus, a deeper understanding of the behaviour of weak rocks, plugging mechanism of open-ended tubular piles in the intact rock mass and jointed rock mass, and the load bearing mechanism of tubular pile in weak rock can improve the reliability of the foundation design.

1.3 Research Objectives

The ultimate aim of this study is assessing the axial bearing mechanism of the open-ended tubular piles in weak rocks using the discrete element simulation, which can accommodate large deformations while providing micro and macroscopic assessment of the response of the rock subjected to the transferred loads. In order to gain a more in depth understanding of the jointed rock response to loading, the effects of joint properties on the mechanical behaviour of weak rocks are studied. In addition, the degree of plugging is analysed for open-ended tubular piles in weak rocks for both the intact rock and jointed rock masses. In addition, feasibility of simulating the penetration of open-ended tubular piles in weak rock using DEM is evaluated,

while analysing the results in term of internal and external shaft frictional forces, base resistance and plugging mechanism.

The specific objectives of the numerical simulations in this research are as follows:

- Examining the effects of joint density on the strength of rock samples using the discrete element method;
- Investigating the effects of joint properties on the mechanical behaviour of weak rocks through simulation of triaxial tests;
- Estimating the plugging mechanism of open-ended piles in intact rock mass and jointed rock mass by performing push-up load tests on the rock plug;
- Assessing the feasibility of using discrete element method to simulate penetration process of open-ended tubular piles into weak rocks;
- Investigating the axial bearing mechanisms including the internal and external shaft frictions and base resistance of the tubular piles in weak rock pile; and
- Assessing the impact of introducing the inner pile shoe on the axial load bearing mechanism and degree of plugging of open-ended tubular piles in weak rocks.

For the numerical simulations, the DEM based software particle flow code in three dimensions (PFC3D) is adopted. One of the rigorous bonded particle models, named the flat-joint model, is employed to replicate the mechanical behaviour of the intact rock mass. With the imposed Coulomb limit, the shear strength predicted by the flat-joint model is controlled by the cohesion and friction angle at each contact. Moreover, the flat-joint model provides a more accurate prediction of the tensile strength. For the rock joints, the discrete fracture network (DFN) works together with the smooth-joint contact model to simulate the sliding of the joints. Existing laboratory tests are selected for the calibration process and to replicate the behaviour of natural weak rocks. To control the number of particles generated in the model and the efficiency of the

numerical modelling of the pile penetration, the particle refinement method is adopted, such that the particles near and around the pile have finer particle sizes similar to what was adopted in the calibration exercise using triaxial tests, and the particle sizes increased with radial distance from the pile.

In addition, it is necessary to address the limitations of this research, which are:

- Only the drained condition excluding water effects for weak rock is considered;
- The effect of particle crushing is not captured, while bond breakages between existing particles are considered;
- The pile is simulated as a rigid wall, where the steel pile deformability and damage or pile failure are not considered.

1.4 Significance of Research

Australian Government announced in 2016 a record \$50 billion investment in land transport infrastructure for fixing and modernising the nation's transport infrastructure (Australian Government 2016). Overall, the government has committed funding for planning of several major infrastructure projects such as the Baxter and Waurin Ponds rail upgrades in Victoria, Cross River Rail in Brisbane and Western Sydney Airport. Thus, there is an urgent need to find cost effective and reliable design methods for foundations of infrastructure such as road and railway bridges, such as steel tubular piles embedded driven to weak rock to carry heavy structural loads.

Recently, there are many projects in Australia employing tubular piles as the most suitable foundation option to structures. For example, many bridges on the Pacific Highway upgrade projects in NSW adopted tubular piles. These projects include an overflow bridge near Iluka, a twin bridge near Woodburn, and a multi-span bridge near Harwood, which employed the tubular pile with a diameter of 1,050 mm, 900 mm, and 2,400 mm, respectively (Zhang 2017).

Some of the bridge and offshore projects in Western Australia also utilised the tubular piles, such as the Swan River Pedestrian Bridge, and Barrow Island Load-Out Jetty, which employed 74 tubular piles with a diameter of 730 mm, and 654 tons of 1,219 mm diameter steel tubular piles, respectively (Engineering Heritage Western Australia 2014). In addition, many projects in Victoria also adopt tubular piles, such as Victoria Harbour, which is still under construction.

Weak rock conditions are encountered world-wide as the transition zone between the subsoil and strong bedrock. The presence of a weak rock layer and its depth can contribute to the difficulties for the pile design, especially, the design of the tubular pile. In Australia, many projects need to deal with weak rock, which is not limited to pile foundations. For instance, the weak fine-grained rocks caused the major problem for the stability of slopes along a coastal escarpment in the northern Illawarra region (Ghobadi 1994). For the Macleay river and floodplain bridge project, the weak rock layer was relatively deep and ranged from 12 m to 50 m (Zhang et al. 2013). According to Bertuzzi and Pells (2002), the sandstone and shale in the Sydney region can be classified into different classes and most of these classes correspond to rock with rather low strength, which is similar to weak rock. For example, for class VI-V sandstone, the uniaxial compressive strength of the rock mass is around 1 to 4 MPa; and for shale class I to V, the UCS of the rock mass ranges from less than 1 MPa to 20 MPa, respectively.

The above mentioned points clearly indicate the significance of this research addressing the wide spread problem of predicting the axial capacity of tubular piles in weak rocks. Indeed, outcomes of this research can help designers to achieve more reliable and safer designs for tubular piles in weak rock and in some cases, the enhanced design and construction reliabilities can result in reduced construction and maintenance costs.

1.5 Organisation of the Thesis

This thesis contains six chapters, which can be summarised as below:

- Chapter 1 introduces the current problems related to the prediction of the bearing capacity of open-ended tubular piles in weak rocks, and highlights the scope and significance of this research.
- Chapter 2 provides a comprehensive literature review on the current design methods, the soil plug mechanism in tubular piles, and the characteristics of weak rocks. In addition, the existing numerical methods for the simulation of piles are critically reviewed.
- Chapter 3 assesses the effects of joint properties on the mechanical behaviour of the rock masses via 3D discrete element modelling. The investigated joint properties include joint density, joint dip, joint aperture, and joint length.
- Chapter 4 investigates the influence of joint density and joint dip on the internal shaft resistance of the rock plug. Moreover, the behaviour of the intact rock plug and the jointed rock plug with different joint properties are compared.
- Chapter 5 introduces the real scale numerical model for simulating the penetration of open-ended tubular piles in weak rocks. The axial load bearing mechanism is presented with the analysis of the internal shaft friction, external shaft friction, base resistance, changes in weak rock porosity, stress distribution in the surrounding material, and degree of plugging. Moreover, the effects of inner pile shoe on the load- displacement relationship for the open-ended tubular pile are presented and discussed.
- Chapter 6 summarises the main conclusions of this research and presents the recommendations for future studies.

Chapter 2 - Literature Review

2.1 General

The function of piles is transferring load from buildings, bridges, or marine structures through water or weak geomaterials onto stiffer and less compressible soils or rocks (Tomlinson and Woodward 2008). They are also required to sustain the uplift loads and lateral loads, particularly for the piles used in supporting tall structures subjected to wind loads or marine structures that experience high lateral loads from the waves. Piles supporting retaining walls, bridge piers, and abutments, need to carry both horizontal and vertical loads (FinnRA 2000; Xu 2007; Tomlinson and Woodward 2008; Yu and Yang 2012). Open-ended tubular piles, in comparison with other types of piles, have some features worth of mentioning regarding performance, costs, and installation effort.

Firstly, open-ended tubular piles require less installation effort. Some researchers (e.g., FinnRA 2000; Tomlinson and Woodward 2008) pointed out that the driving of open-ended tubular piles is relatively easy. In addition, it is necessary to employ open-ended piles to achieve the required penetration depth. Paik et al. (2003) depicted that open-ended piles require less number of hammer blow count than closed-ended piles. Moreover, for the same ground conditions, the open-ended piles required less installation effort and time (Paik et al. 2003; Zhang 2017).

Secondly, the disturbance of ground during the driving of open-ended piles is less. The disturbance of soil masses during pile installation is one of the factors that causing a reduction in soil strength, which is illustrated in Figure 2.1. According to Tomlinson and Woodward (2008), the soil mass displaced by open-ended piles, particularly unplugged open-ended piles, is small so that resulting in less disturbance of soil compared to other means of driving piles. Therefore, this type of piles is favourable when applying to the areas adjacent to sensitive structures (FinnRA 2000). Another factor that contributes to the reduction in the shear strength

is the development of the excess pore water pressure during the pile penetration, which can be limited by using open-ended piles (Tomlinson and Woodward 2008).

Thirdly, open-ended piles can sustain high axial and lateral loads. Particularly, large diameter open-ended steel tubular piles, which have a pile diameter greater than 900 mm, are suitable for the applications with water structures, difficult soil conditions, large pile loads and bending loads (FinnRA 2000; Zhang 2017). Even for an equivalent group of small diameter driven piles, it is observed that large diameter open-ended steel tubular piles provide higher axial and lateral resistance. However, Paik et al. (2003) revealed that the settlement of the open-ended piles is larger than that of closed-ended piles under the same load and soil conditions.

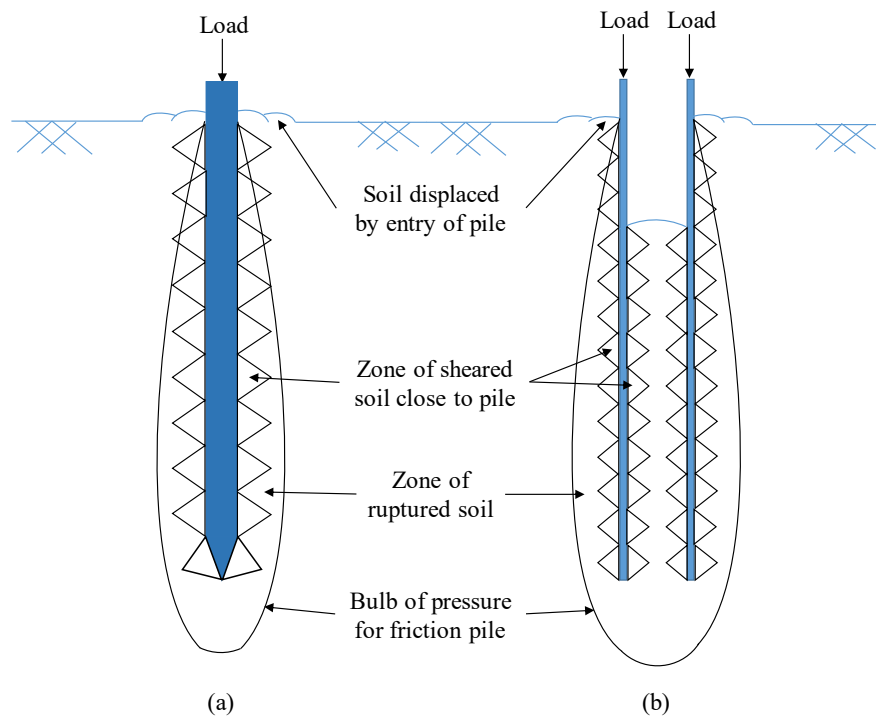


Figure 2.1. Soil disturbance beneath (a) a single solid pile; and (b) an open-ended tubular pile
(after Tomlinson and Woodward 2008)

Many researchers (e.g., Gavin 1999; American Petroleum Institute 2002; Jardine et al. 2005) studied the behaviour of open-ended piles in sands and clays. Then, they developed the guidelines for the design of tubular piles in these ground conditions with the consideration of

the plugging effect. However, weak rock conditions are often encountered in construction projects. The studies on the piles in weak rocks can be traced back to 1977 (The Institution of Civil Engineers 1977). From collections of studies and data on bored, driven and cast-in-place piles in chalk, mudstone, marl and shale, they concluded that for piles in weak rocks, the ultimate resistance is more sensitive to the effects of installation than these piles in soils. In addition, other geotechnical and structural designs in weak rocks, especially for tunnelling projects, have been studied deeply to form the well established guidelines by some researchers (Fell et al. 2000; Klein 2001; Hoek et al. 2005; Carter et al. 2008). Whereas, the studies on the behaviour and design of open-ended piles in weak rocks are certainly insufficient.

The problems associated with open-ended tubular piles in weak rocks are:

- a) The guidelines for the design of the axial bearing capacity of tubular piles in weak rocks are not clear.
- b) For ground conditions with a very deep weak rock layer, the tubular piles are hard to reach the medium strength rock layer considering the installation economic and drivability.
- c) Some of the effects are not clearly understood, such as the plugging effect, the impact of pile shoes, and the effect of discontinuities on the bearing capacity.

2.2 Ultimate Axial Capacity

2.2.1 Bearing Capacity of Tubular Piles in Sands and Clays

For the design of tubular piles in sands and clays, there are several recommendations including the Laboratoire Central des Ponts et Chaussées (LCPC) method (Bustamante and Gianeselli 1982), the Finnish National Road Administration (FinnRA) method (FinnRA 2000), the recommendations of the American Petroleum Institute (API) (American Petroleum Institute 2002), the Norwegian Geotechnical Institute (NGI) method (Clausen et al. 2005), the

University of Western Australia (UWA) method (Lehane et al. 2005), the Hong Kong University (HKU) method (Yu and Yang 2012), and Imperial College Pile (ICP) design method (Jardine et al. 2005). Most of these methods were developed based on in situ pile tests or correlated to Cone Penetration Test (CPT) data (Guo and Yu 2016). Among these methods, the API and the ICP methods are widely adopted in practice.

The API method is easy to apply due to a small number of parameters required for the design. However, as Tomlinson and Woodward (2008) reported, this method is over-conservative for short piles design with the pile embedded length over diameter ratios (Z/D) up to 30 with a relative density of more than 60%. In contrast, the ICP method can provide more accurate design, reduce cost, and improve foundation performance, which was developed from numerous field tests, laboratory tests, analysis and verifications (Zhang et al. 2013). However, adopting the ICP methods in design requires a comprehensive site investigation identifying a vast number of parameters. Some researchers (e.g., Jardine et al. 2005; Tomlinson and Woodward 2008; Zhang et al. 2013) noted that the ICP method is more reliable than traditional methods. As comparing the calculated shaft capacity and measured shaft capacity, the shaft capacity predicted by the ICP method is very close to the measured value with a variation of less than 30%, while in the API method, the variation can be as high as 60%.

To predict the ultimate resistance of a pile (Q_p), the most basic relationship is:

$$Q_p = Q_b + Q_s - W_p \quad (2-1)$$

where, Q_b is the ultimate base resistance, Q_s is the ultimate shaft resistance, and W_p is the weight of the pile.

The design of open-ended piles for the offshore piling was first addressed in the API method. For cohesive soils, the ultimate shaft resistance (Q_s) can be calculated by the unit skin friction (f) and the shaft area of the pile (A_s), as depicted in Equation (2-2).

$$Q_s = fA_s \quad (2-2)$$

An adhesion factor (β) is proposed to compute the unit skin friction based on the undrained shear strength of the soil (c). In the API method, it is assumed that the shaft frictions act on both inside and outside of the piles are equal. The adhesion factor can be calculated as shown in Equations (2-4) and (2-5) with the constraint that α should not exceed 1, where p'_0 is the effective overburden pressure.

$$f = \beta c \quad (2-3)$$

$$\begin{cases} \beta = 0.5\Psi^{-0.5} & \Psi \leq 1.0 \\ \beta = 0.5\Psi^{-0.25} & \Psi > 1.0 \end{cases} \quad (2-4)$$

$$\Psi = c/p'_0 \quad (2-5)$$

In the API method, it is suggested that the base resistance (Q_b) is the minimum value of the resistance of the equivalent base (Q_{base}) or the resistance of the annular area ($Q_{annular}$) plus the resistance of the inner shaft (Q_{in}), as presented in Figure 2.2 and Equation (2-6). It is noted that the soil column forms inside the pile when the driving the open-ended tubular piles. Due to the size of the pile, the mechanical properties of the soil, the soil column may increase in height at the same rate as driving rate, which is known as fully coring. While the soil column may move down as driving further with no further increase in height, which is known as plugged (Ko and Jeong 2014).

$$Q_b = \min(Q_{base}, Q_{annular} + Q_{inn}) \quad (2-6)$$

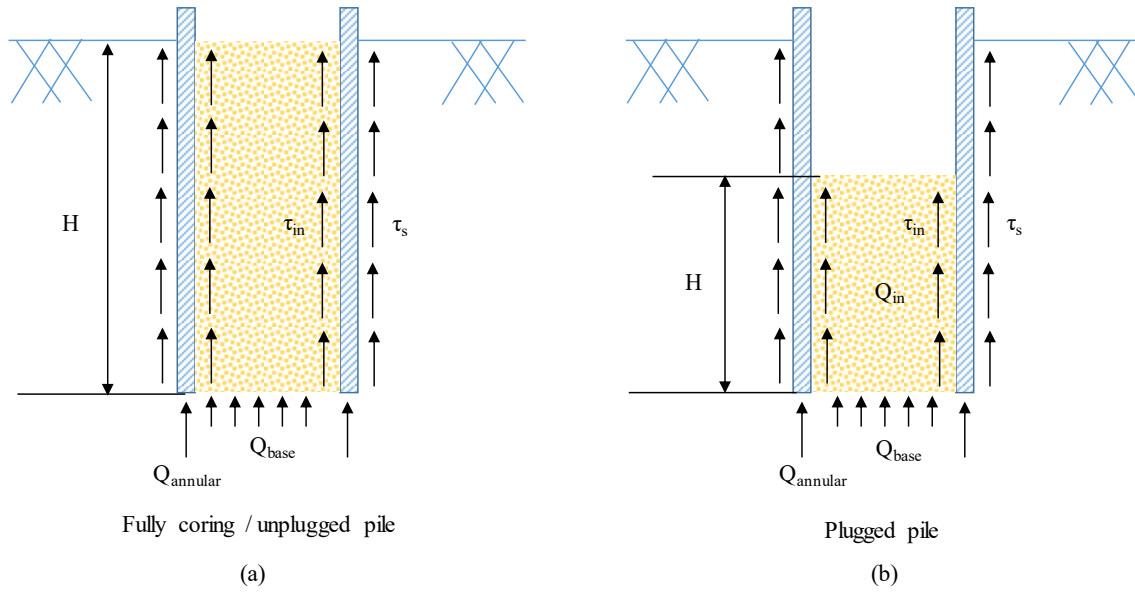


Figure 2.2. Load bearing components of open-ended tubular piles for (a) fully coring pile; and (b) plugged pile

The resistance of the equivalent base (Q_{base}) can be predicted from the unit end bearing capacity (q) and gross end area of the pile (A_p), as presented in Equation (2-7), in which the unit end bearing capacity can be computed from the undrained shear strength of the soil (c).

$$Q_{base} = qA_p \quad (2-7)$$

$$q = 9c \quad (2-8)$$

As proposed in the API method, the unit shaft friction (f) for cohesionless soils may be calculated by the coefficient of lateral earth pressure (K), effective overburden pressure (p'_0) and friction angle between the soil and pile wall (δ), as presented in Equation (2-9). The value of K is based on the base condition and plugging mode of the driven pile, as shown in Equation (2-10).

$$f = Kp'_0 \tan \delta \quad (2-9)$$

$$\begin{cases} K = 0.8, & \text{for open - ended piles driven unplugged} \\ K = 1.0, & \text{for plugged or closed end piles} \end{cases} \quad (2-10)$$

The unit end bearing capacity can be predicted by the effective overburden pressure (p'_0) and a bearing capacity factor (N_q). The recommended values for δ and N_q can be found in Table 2.1.

$$q = p'_0 N_q \quad (2-11)$$

Table 2.1. Some of the recommended design parameters for cohesionless siliceous soils (after American Petroleum Institute 2002)

Soil type	Density	Friction angle between the soil and pile wall, δ (degrees)	Bearing capacity factor, N_q
Sand	Very loose	15	8
	Loose	20	12
	Medium	25	20
	Dense	30	40
	Very dense	35	50
Sand – Silt	Loose	15	8
	Medium	20	12
	Dense	25	20
	Very dense	30	40
Silt	Medium	15	8
	Dense	20	12
Gravel	Dense	35	50

It should be noted that for applying the API method in the design of open-ended piles in either cohesive or cohesionless soils, a limited number of parameters are required, while in the case of plugged or unplugged, the calculation recommendations are not clearly defined (Xu et al. 2008; Zhang et al. 2013). To predict the plug resistance, it is assumed the inside and outside unit shaft resistances are equal. According to (Xu 2007), other limitations of the API method includes over predicting the capacity of long piles in loose sand, and over estimating the ratio of the tension to compression shaft capacity.

For the FinnRA method, the approach for predicting the unit end bearing capacity and the unit shaft friction in cohesionless soil is similar to the API method. While the FinnRA method provided recommendations on selecting bearing capacity factor (N_q) based on the internal friction angle of the soil (ϕ), and they suggested that the friction angle between the soil and pile wall (δ) is smaller than the internal friction angle of the soil (ϕ) with a reduction factor of 0.7, as depicted in Equation (2-12). Meanwhile, the FinnRA method suggested a limiting value of the shaft resistance, which should not exceed 0.15 MPa.

$$\tan \delta = 0.7 \tan \phi \quad (2-12)$$

For cohesive soils, the FinnRA method recommended an adhesion factor ranging from 0.4 to 0.8. It is assumed that the internal shaft resistance is half of the external shaft resistance for unplugged piles. There are some conditions for the formation of a plug that addressed in the FinnRA method, the cohesionless soil layer should be medium dense or denser, and the pile driving should be performed using a slow driving hammer. In this case, the base resistance is calculated with a plugging coefficient (η), which is determined by the ratio of installation depth (Z) to the pile diameter (D), as depicted in Equations (2-13) and (2-14). It is recommended that the plugging coefficient reduces linearly when the penetration ratio ($\frac{Z}{D}$) decreases.

$$Q_{base} = \eta q A_p \quad (2-13)$$

$$\begin{cases} \eta = 0.8, & \text{if } \frac{Z}{D} = 10 \text{ in moraine condition} \\ \eta = 0.8, & \text{if } \frac{Z}{D} = 10 \text{ in sand or gravel} \end{cases} \quad (2-14)$$

The ICP method provides detailed considerations of the cases for the piles in compression and tension separately. In addition, it provides the method for predicting the potential of full plugging or partial plugging of the piles. The detailed design procedures, which are specific to open-ended piles, are explained below.

According to Jardine et al. (2005), for open-ended piles driven in clays, the total shaft resistance can be predicted from integrating local shear strength along the embedded shaft length (H_Z), as presented in Equation (2-15).

$$Q_s = \pi H_Z \int \tau_f dz \quad (2-15)$$

In which, the local shear strength (τ_f) can be calculated from the coefficient of radial effective stress for shaft at failure (K_f), the coefficient of earth pressure at rest (K), the equalized radial effective stress (σ'_{rc}), and the operational interface angle of frictional failure (δ_f).

$$\tau_f = (K_f/K)\sigma'_{rc} \tan \delta_f \quad (2-16)$$

$$\sigma'_{rc} = K_c \sigma'_{v0} \quad (2-17)$$

where, K_f/K_0 is the loading factor that is equal to 0.8, K_c depends on Yield Stress Ratio (YSR) or apparent over-consolidation ratio, and σ'_{v0} is the in-situ vertical effective stress. The YSR is the ratio of the vertical yield stresses (σ'_{vy}) over the initial vertical effective stresses (σ'_{v0}). To define K_c for open-ended tubular piles, Equations (2-18) and (2-19) can be utilised, which involves the height of the soil layer above the pile toe (h), the equivalent radius of the pile (R^*), the relative void index (I_{v0}) or the relative void index at yield (I_{vy}), and the clay sensitivity (S_t).

$$K_c = [2.2 + 0.016YSR - 0.870\Delta I_{vy}]YSR^{0.42}(h/R^*)^{-0.20} \quad (2-18)$$

$$K_c = [2 - 0.625\Delta I_{v0}]YSR^{0.42}(h/R^*)^{-0.20} \quad (2-19)$$

The relative void index at yield (I_{vy}) and the equivalent radius of the pile (R^*) can be computed from Equations (2-20) and (2-21), respectively.

$$\Delta I_{vy} = \log_{10} S_t \quad (2-20)$$

$$R^* = (R_{outer}^2 - R_{inner}^2)^{0.5} \quad (2-21)$$

where R_{inner} is the inner radius of the pile and R_{outer} is the outer radius of the pile.

For the base resistance of the open-ended piles, two cases need to be considered, namely fully plugged piles or unplugged piles. As addressed in the ICP method, the open-ended piles would be considered as plugged during static load when the condition in Equation (2-22) is satisfied.

$$[D_{inner}/D_{CPT} + 0.45q_c/P_a] < 36 \quad (2-22)$$

where, D_{inner} is the inner diameter of the pile, D_{CPT} is the cone diameter which is equal to 0.036 m, and P_a is the atmospheric pressure with a value of 100 kPa.

For fully plugged piles, the ultimate resistance of the base (Q_b) is calculated from the gross area of the pile tip. The base capacity (q) can be predicted from the cone resistance (q_c), which is obtained from CPT average results over a distance of 1.5 times the pile diameter (D) above and below the toe. The base capacity (q) is recommended to be determined using Equation (2-24).

$$Q_b = q\pi D^2/4 \quad (2-23)$$

$$\begin{cases} q = 0.4q_c, & \text{Undrained loading} \\ q = 0.65q_c, & \text{Drained loading} \end{cases} \quad (2-24)$$

For the unplugged conditions, the ultimate resistance of the base (Q_b) is fully supported by the annular area only, which can be calculated using Equations (2-25) and (2-26).

$$Q_b = q\pi(R_{outer}^2 - R_{inner}^2) \quad (2-25)$$

$$\begin{cases} q = q_c, & \text{Undrained loading} \\ q = 1.6q_c, & \text{Drained loading} \end{cases} \quad (2-26)$$

Compared to the API method for the design of open-ended piles in clays, the ICP method requires more laboratory tests or site investigation to obtain the values for the parameters YSR , ΔI_{vy} and ΔI_{v0} (Jardine et al. 2005). These properties can be obtained from three tests, i) odometer tests on good quality undisturbed samples, ii) consolidated undrained triaxial compression tests, or iii) CPT or field vane tests. In contrast, for the application of the ICP method in sands for the open-ended piles, only the testing data of the static cone penetration test would be required. The ultimate resistance of the shaft (Q_s) can be calculated from Equation (2-15), in which the local shear stress (τ_f) in sands is predicted by the interface angle of friction at failure (δ_{cv}):

$$\tau_f = (\sigma'_{rc} + \Delta\sigma'_{rd}) \tan \delta_{cv} \quad (2-27)$$

where, the local radial effective stress (σ'_{rc}) and the increase in radial effective stress during pile loading ($\Delta\sigma'_{rd}$) are recommended to be calculated using Equations (2-28) and (2-29), respectively.

$$\sigma'_{rc} = 0.029q_c(\sigma'_{v0}/P_a)^{0.13}(h/R^*)^{-0.38} \quad (2-28)$$

$$\Delta\sigma'_{rd} = 2G\Delta r/R \quad (2-29)$$

where q_c is the local CPT tip resistance, σ'_{v0} is the local vertical effective stress, h is the relative pile tip depth, R is the radius of the pile, and R^* is the equivalent radius of the pile. Equation (2-29) is adopted from the cavity expansion equation, in which Δr is the radial

displacement when slipping occurs and G is the operational shear modulus that can be calculated using Equation (2-30).

$$G = q_c [A + B q_c (P_a \sigma'_{vo})^{-0.5} - C [q_c (P_a \sigma'_{vo})^{-0.5}]^2]^{-0.5} \quad (2-30)$$

where, A , B , and C are constants with the corresponding values as 0.0203, 0.00125, and 1.216e-6, respectively. When the piles are under tension loading, the local shear stress (τ_f) can be calculated using Equation (2-31). While this equation is for close-ended pile, the shear stresses in tension should reduce further by 10% for the open-ended piles.

$$\tau_f = (0.8\sigma'_{rc} + \Delta\sigma'_{rd}) \tan\delta_{cv} \quad (2-31)$$

The ICP method recommends that the plugging of the open-ended tubular piles in sands should satisfy both conditions as shown in Equations (2-32) and (2-33), in which D_r is the relative density of the sand.

$$D_{inner} < 0.02(D_r - 30) \quad (2-32)$$

$$D_{inner}/D_{CPT} < 0.083q_c/P_a \quad (2-33)$$

In the case of the fully plugged piles, the base resistance (q) is calculated the CPT tip resistance (q_c), the diameter of the pile (D), and the diameter of the cone (D_{SPT}).

$$q = q_c [0.5 - 0.25 \log\left(\frac{D}{D_{SPT}}\right)] \quad (2-34)$$

For the unplugged piles, the base resistance (q) is assumed to be equal to the CPT tip resistance (q_c).

$$q = q_c \quad (2-35)$$

Although ICP methods are widely used for driven piles in sands and clays, there is limited information of its use for rocks, particularly referring to uncertainty over whether a rock plug

can be formed and how much penetration is needed to form a rock plug (Tomlinson and Woodward 2008).

2.2.2 Bearing Capacity in Weak Rocks

For the open-ended piles penetrated into weak rock, the pile load may highly concentrate at the toes of piles. Compared to the end bearing capacity, the shaft capacity may not be significant (Tomlinson and Woodward 2008). However, issues, such as brittle rocks may be split by the toe of the slender-section pile. The design method, addressed in the work of Tomlinson and Woodward (2008), assumes that the ultimate bearing capacity is calculated from the shaft resistance, base resistance, and the self-weight of the pile, as indicated in Equation (2-1). The shaft and base resistances values are formed based on the correlations between pile loading tests and the results of field tests in rock formations or laboratory tests on cored specimens. The rock joint characteristics are major concerns in the design of piles embedded in rocks. For widely spaced joints (i.e., the spacing is more than 600 mm) or tightly closed joints, the base capacity (q) may be predicted from Equation (2-36), which involves a bearing capacity factor (N_k) that depends on the friction angle of the rock (ϕ), and the uniaxial compressive strength of the intact rock (q_{uc}).

$$q = N_k q_{uc} \quad (2-36)$$

$$N_k = 2 \tan^2\left(45^\circ + \frac{\phi}{2}\right) \quad (2-37)$$

Different researchers (Williams et al. 1980; Rowe and Armitage 1987; Fleming et al. 2008) proposed various values for the bearing capacity factor (N_k), as listed in Table 2.2.

Table 2.2. Bearing resistance factor N_k proposed by different researchers (after Irvine et al. 2015)

Method proposed by	Bearing resistance factor	Rock or pile types
Williams et al. (1980)	5	Rock socket pile in mudstone
Rowe and Armitage (1987)	2.5	Specific to rock sockets
	3	For weak rock
Fleming et al. (2008)	0.3	Rock with open joints or limited penetration into rock

Meanwhile, limiting end bearing resistance values that range from $2.5 q_{uc}$ to $5 q_{uc}$ are recommended by Irvine et al. (2015). Kulhawy and Goodman (1980) stated that the bearing capacity (q) of the jointed rock can be computed from the undrained shear strength (c), the base width (W), the base depth (Z) in the rock layer, the effective density of the rock mass (γ), the bearing capacity factors related to friction angle (N_c , N_q and N_γ), as indicated in Equation (2-38).

$$q = cN_c + \gamma ZN_q + \gamma \frac{WN_\gamma}{2} \quad (2-38)$$

Due to the degradation of rocks and the reduction in friction resulted from shattering of the rock when driving adjacent piles, the shaft friction cannot always be calculated from the results of laboratory tests on rock cores (Tomlinson and Woodward 2008). The equation for calculating the ultimate shaft resistance in coarse-grained soil may be adopted as follows:

$$Q_s = \frac{1}{2} K_s \sigma'_{v0} A_s \tan \delta \quad (2-39)$$

where K_s is a coefficient of horizontal stress of rock mass, σ'_{v0} is the initial vertical effective stress, δ is the friction angle between pile and soil, A_s is the area of the shaft. Terente et al. (2017) suggested that the peak friction angle between pile and soil is generally correlated to the friction angle of the rock (ϕ), which ranging between 0.6ϕ and 0.8ϕ . The coefficient of horizontal stress of rock mass can be obtained from pressuremeter tests. According to González de Vallejo and Hijazo (2008), based on the tectonic stress level of the rock mass, the coefficient of horizontal stress of rock masses (K_s) can be summarised as Table 2.3.

Table 2.3. K_s for different tectonic stress levels (after González de Vallejo and Hijazo 2008; Terente et al. 2017)

Tectonic stress level	The coefficient of horizontal stress of rock masses, K_s
Low	Less than 1
Medium	1 to 1.5
High	1.5 to 2
Very high	2 to greater than 5

It should be noted that the pile toe may settle in the order of 20% of the pile diameter when the base resistance determined by Equation (2-38) is fully mobilised (Tomlinson and Woodward 2008). Thus, an ample safety factor that is greater than 2.5 is required to ensure the settlement of the proposed pile is within the allowable limits under the working load.

As addressed in the work of Irvine et al. (2015), the shaft resistance (Q_s) of piles in weak rock can also be calculated from the adhesion factor (β), the uniaxial compressive strength of the

intact rock (q_{uc}), and the shaft area of the pile (A_s). Depending on the socket roughness, the adhesion factor ranges from 0.1 to 0.4, where 0.1 represents a smooth socket (CIRIA 1999).

$$Q_s = \beta q_{uc} A_s \quad (2-40)$$

There are some other recommendations about the adhesion factor, which are mainly based on test data correlations. Terente et al. (2017) proposed a correlation between the adhesion factor (β) and the rock strength (q_{uc}) based on some available data for driven piles in rock materials, the relationship is indicated in Equation (2-41). The relationship proposed by CIRIA (1999) is presented in Equation (2-42), which involves a multiplier (χ) and the atmospheric pressure (P_a). The values of χ usually range from 1 to 3 for rocks.

$$\beta = 0.11 q_{uc}^{-0.5} \quad (2-41)$$

$$\beta = \chi \left(\frac{q_{uc}}{2P_a} \right)^{-0.5} \quad (2-42)$$

Terente et al. (2017) pointed out that many effects were not studied in detail, such as the level of fracturing of the rock mass, rock block displacements, the crushability of the rock material, the use of pile driving shoes and cyclic degradation effects. These effects could influence the prediction of the bearing capacity of tubular piles in the rock to a different extent.

2.3 Open-ended Tubular Piles

2.3.1 Soil Plug

During the initial driving of the open-ended tubular piles, the soils enter the pile. As the pile penetrates deeper, the soil may fill the tubular pile. Otherwise, the interior soil column moves down as the pile is driven further due to the inner shaft friction. The former known as the unplugged piles, while the latter is called the plugged piles, which may be partially or fully plugged (Ko and Jeong 2014), as shown in Figures 2.2 and 2.3. The indication of forming a fully plugged pile is when the height of the plug stops increasing while the pile is driving further.

The inner shaft friction has some impacts on determining the ultimate base resistance of open-ended tubular pile, as indicated in Equation (2-6). As addressed by many researchers (e.g., FinnRA 2000; Gavin and Lehane 2003a; Henke and Grabe 2008; Tomlinson and Woodward 2008; Guo and Yu 2016), the degree of plugging has a significant influence on the capacity of open-ended piles, which can result in higher axial capacity, but increases the driving resistance at the same time. According to the API method (2002), for fully plugged piles, the bearing resistance may act over the entire base area of the pile, while for unplugged piles the bearing resistance acts on the annulus area only, refer to Figure 2.2.

The effect of soil plug on the ultimate bearing capacity of a single open-ended pile has been reported in many studies. For instance, Randolph et al. (1992) reported that the capacity of the soil plug increased exponentially with its length due to the arching effect produced by the soil confined inside the tubular pile. Later on, Matsumoto et al. (1995) carried out field tests on tubular piles driven into weak mudstone and then reported that the internal shaft resistance resulted in larger ultimate bearing capacity, while Fattah and Al-Soudani (2016) carried out a laboratory investigation into the bearing capacity of tubular piles in sand. They found removing the soil plug reduced the load capacity, and that trend was more evident in dense sand compared to loose sand.

There are different recommendations on considering or predicting the inner shaft resistance. In the API design method (American Petroleum Institute 2002), it is assumed the inner unit shaft friction is equal to the outer unit shaft friction. If the soil resistance generated around the inner shaft is larger than the base resistance of the equivalent area, then the pile is regarded as a fully plugged pile. While in the Finnish National Road Administration method (FinnRA 2000), the plugging coefficient is introduced, refer to Equation (2-14).

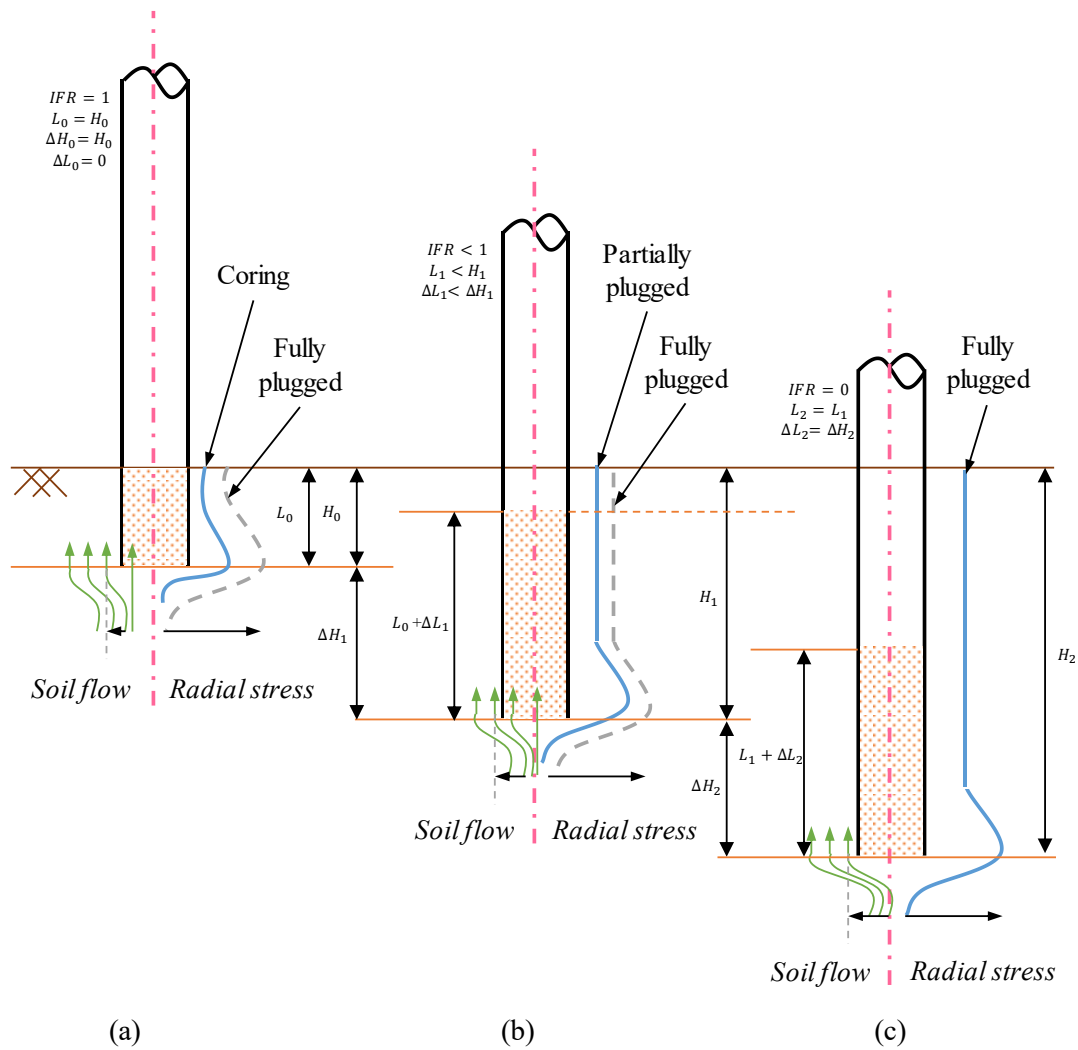


Figure 2.3. Possible failure mechanism for open-ended piles (a) fully coring, (b) partially plugged, and (c) fully plugged (after White et al. 2005; Igoe et al. 2009; Ko and Jeong 2014)

Meanwhile, as Randolph et al. (1992) stated, under the dynamic conditions of installation and the static conditions of loading during service, the response of the plug of the open-ended tubular piles is very different. To understand the degree of plugging, many researchers (e.g., Gavin and Lehane 2003b; White et al. 2005; Igoe et al. 2009) suggested using the incremental filling ratio (IFR) that was introduced after Bruzy et al. (1991). Another parameter that is widely used to quantify the plugging effect is the plug length ratio (PLR) (Paik and Lee 1993). The IFR and PLR are calculated from Equations (2-43) and (2-44), respectively.

$$IFR = \frac{\Delta l}{\Delta H} \times 100 \quad (2-43)$$

$$PLR = \frac{l_i}{H_i} \quad (2-44)$$

where Δl is the incremental change of plug length, ΔH is the change in pile penetration depth, l_i is the soil plug length, and H_i is the penetration depth, as illustrated in Figure 2.3.

When the open-ended pile is penetrating in a full coring mode with no plugging effect, IFR would be equal to 1, which means that the incremental change of plug length increases in the same rate as the increase in pile penetration depth, as illustrated in Figure 2.3 (a). IFR would be equal to zero when the pile is fully plugged; in this case, as the pile is driven further, the soil has to be displaced sideways, as shown in Figure 2.3 (c). For a fully-plugged pile, the base capacity is regarded as equivalent to the closed-ended pile (American Petroleum Institute 2002; Guo and Yu 2016). When IFR has a value between 0 and 1, the pile is considered as partially plugged, as shown in Figure 2.3 (b). When IFR = 0, the surrounding soils experience the highest radial displacement and radial stresses (White et al. 2005; Lüking and Kempfert 2013). The illustration of the radial displacement and radial stress of soil element at the pile wall for the different degrees of plugging is plotted in Figure 2.3.

White et al. (2005) defined the effective area ratio (A_r) as the ratio of the added volume to the gross pile volume, in which the added volume is the gross pile volume minus any soil entering the plug. Hence, when the pile is fully plugged and acts as a closed-ended pile, the value of A_r is 1, as shown in Figure 2.3 (c). For unplugged or partially plugged pile, the effective area ratio (A_r) can be estimated by the pile outer diameter (D_{outer}), the pile inner diameter (D_{inner}), and the incremental filling ratio (IFR), as shown in Equation (2-45). For full coring mode, the effective area ratio would have a value of around 0.1 for typical offshore piles, as indicated in Figure 2.3 (a) (White et al. 2005).

$$A_r = 1 - IFR \frac{D_{inner}^2}{D_{outer}^2} \quad (2-45)$$

In the UWA method (Lehane et al. 2005), the incremental filling ratio (IFR) and the effective area ratio (A_r) are employed to estimate the shaft friction of open-ended tubular piles in sand. The shaft resistance is calculated from the local shear strength along the embedded shaft length (τ_f), as presented in Equation (2-15). The local shear strength along the embedded shaft length (τ_f) can be computed from the radial effective stress after installation (σ'_{rc}) and the change in radial effective stress during pile loading ($\Delta\sigma'_{rd}$), and interface friction angle at failure (δ_{cv}), as shown in Equation (2-46).

$$\tau_f = Y(\sigma'_{rc} + \Delta\sigma'_{rd})\tan\delta_{cv} \quad (2-46)$$

where, Y is a dimensionless factor, 1 for compression and 0.75 for tension. The radial effective stress after installation (σ'_{rc}) is calculated based on the effective area ratio (A_r), the local CPT tip resistance (q_c), the pile embedment depth (H_z), and the outer diameter of the pile (D_{outer}), as presented in Equation (2-47). The effective area ratio (A_r) can be predicted by Equation (2-45), in which IFR can be estimated by Equation (2-48).

$$\sigma'_{rc} = 0.03q_c(A_r)^{0.3}[\max(\frac{H_z}{D_{outer}}, 2)]^{-0.5} \quad (2-47)$$

$$IFR \approx \min[1, (\frac{D_{inner}}{1.5})^{0.2}] \quad (2-48)$$

where D_{inner} is the inner diameter of the pile in meters.

2.3.2 Factors Affecting the Degree of Plugging

There are many factors that can affect the degree of plugging, including the relative density of the sand, the internal diameter of the pile, the pile embedment depth, and the installation method, all of which are directly related to the capacity of the plug, as reported by many researchers (e.g., De Nicola and Randolph 1997; Xu 2007; Henke and Grabe 2008; Igoe et al.

2009; Yu and Yang 2011). A summary of these factors can be found in Table 2.4 with the corresponding effects.

Table 2.4. Summary of factors affecting the degree of plugging

Factors	Influence on the degree of plugging	Ref.
Relative density	Increase with dense material	Jardine et al. (2005)
		Thongmunee et al. (2011)
		De Nicola and Randolph (1997)
		Paik and Salgado (2003)
		Paik et al. (2003)
Internal pile diameter	Reduce with increasing internal pile diameter	Liyanapathirana et al. (1998)
		Jardine et al. (2005)
		Jeong et al. (2015)
		Ko and Jeong (2014)
		Henke and Bienen (2013)
Pile embedment depth	Increase with increasing the ratio of plug height to plug diameter	Gudavalli et al. (2013)
		Thongmunee et al. (2011)
Installation method	Driven piles resulted in larger plug length than jacked piles. Jacked piles tend to plug more easily than driven piles.	Yu and Yang (2012)
		De Nicola and Randolph (1997)
		White et al. (2000)
		Henke and Grabe (2008)
		Henke and Grabe (2013)

Pile shoe

Increase with increasing the height of internal pile shoe

Kumara et al. (2016)

Henke and Grabe (2008) mentioned that soil density and pile diameter are the primary factors that affect the formation of the plug inside the pile. Referring to the ICP method (Jardine et al. 2005), the plugging of the open-ended tubular piles in sands needs to satisfy both Equations (2-32) and (2-33), which depends on the internal diameter of the pile (D_{inner}) and the relative density (D_r). Based on the field evidence of plugged and unplugged piles reported by Jardine et al. (2005), the relationship between the pile diameter and soil density is shown in Figure 2.4. However, this was obtained from jacked piles, as a result, these relationships are only valid for jacked piles.

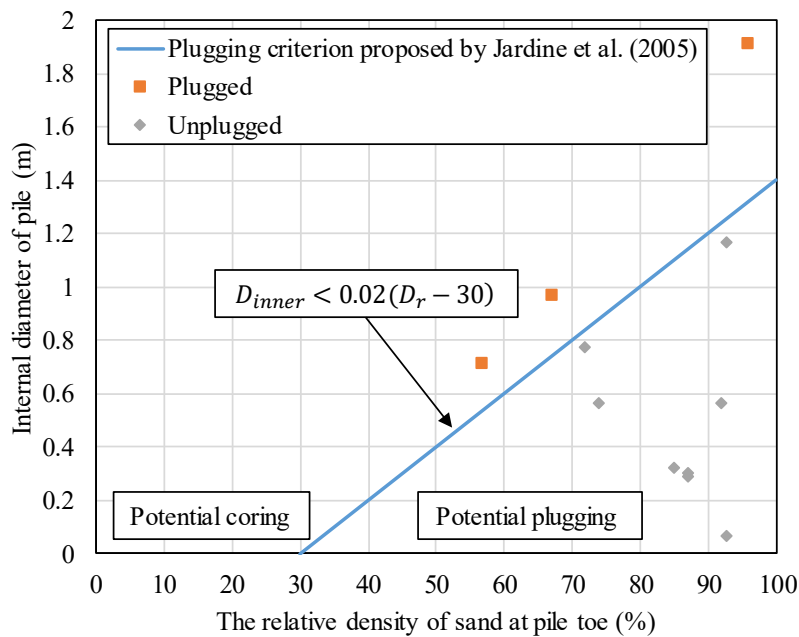


Figure 2.4. Prediction of potential plugging in sand based on field evidence (after Jardine et al. 2005)

The factors that affect the inner shaft resistance or the capacity of the soil plug have been investigated through field tests or laboratory experiments. For example, Paik et al. (2003) carried out field tests to analyse the behaviour of open-ended and closed-ended piles in the

sand; the inner and outer shaft resistances were obtained separately using the twin-wall system. The results showed that the unit inner shaft resistance was higher than the unit outer shaft resistance, and soil plug resistance was generated because enough friction had been developed between the soil plug and the internal surface of the pile. Yu and Yang (2011) studied the effect of the radial effective stress on the pile shaft in the sand. They focused on the shear zone adjacent to the pile shaft that is responsible for the reduction in lateral effective stress and friction fatigue, the schematic illustration for the shear zone is shown in Figure 2.5. The findings revealed that the degree of plugging was largely affected by the radial effective stress and the radial displacement of soil during penetration. The increased value of the plug length ratio (PLR) resulted in an increase in radial effective stress. In order to understand the effects of the pile sleeve on the internal shaft resistance and lateral stresses at the pile sleeve, Kumara et al. (2016) conducted an experimental study using several small-scale tubular piles driven into sandy soil. The differences in the coefficient of lateral earth pressure indicated that the internal frictional resistance increased with the height of the sleeve.

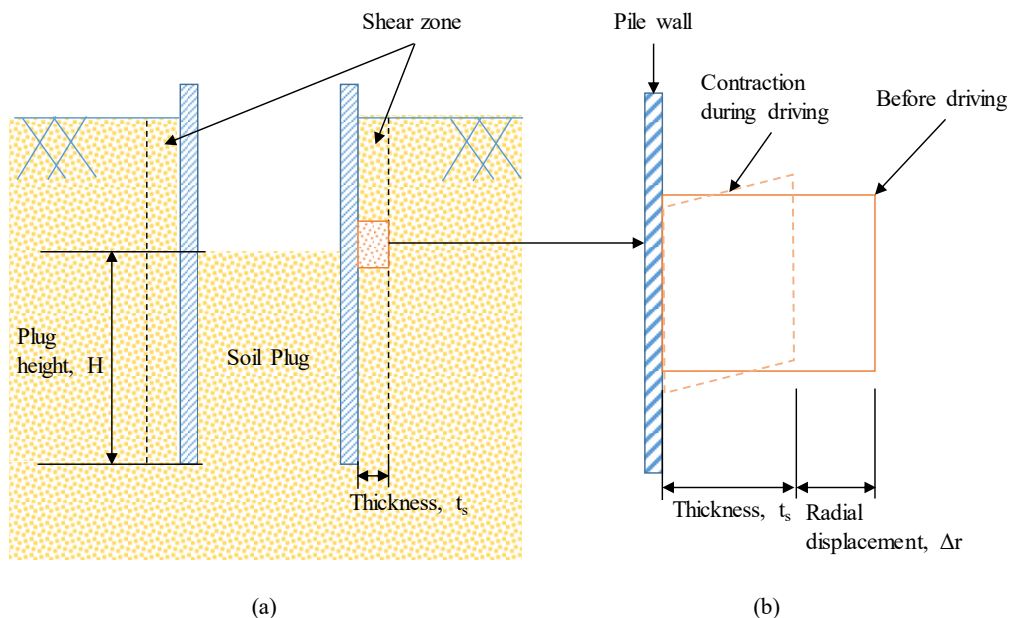


Figure 2.5. Schematic diagram of (a) the shear zone adjacent to the pile shaft; (b) variation in the shear zone during driving (after Yu and Yang 2011)

According to Yu and Yang (2012), the capacity of a plug is mainly due to friction along the inner shaft of the pile, particularly along the lower part of the soil plug where soil arching is significant and there is a large lateral coefficient of earth pressure. Similar trends were observed by other researchers (e.g., Thongmuneet al. 2011; Fatahi et al. 2014; Jeong et al. 2015; Zhang et al. 2019). The field tests to examine the internal skin friction and the degree of soil plugging were carried out by Jeong et al. (2015). They tested three instrumented piles with different diameters in sandy soil and found that the plugging effect of open-ended piles decreased as the diameter of the pile increased. Furthermore, shaft friction between the soil plug and the internal wall of the piles varied due to the degree of soil plugging; and the soil plug in the lower portion had a great influence over the internal skin friction. These phenomena were also observed in field tests carried out by Gudavalli et al. (2013).

Along with field tests, numerical simulations have also been used to investigate the plugging mechanisms of tubular piles. Thongmuneet al. (2011) used push-up load tests to examine how the height and the packing state can affect sand plugs. Laboratory tests and numerical modelling based on the discrete element method (DEM) were carried out, and the results revealed that the push-up force increased significantly as the ratio of plug height to plug diameter increased. In addition, Thongmuneet al. (2011) mentioned that the tendency of forming a sand plug in open-ended piles was increased as the relative density increased. Guo and Yu (2016) insight into the plugging mechanism of large open-ended pipe piles in sandy soils using the discrete element method. They also found that changes in porosity and increase in plug resistance were due to the arching effect, which greatly enhanced the internal unit shear resistance along with the pipe piles, and higher horizontal stresses were mobilised at the bottom of the soil plug. By adopting the finite element method (FEM) to simulate the driving of open-ended piles into sandy soil, Ko et al. (2016) pointed out that the distribution and magnitude of radial stresses inside and outside the pile tip decreased as the diameter of the pile increased.

For different installation methods, De Nicola and Randolph (1997) pointed out that the formation of plug exhibits different behaviour during driving and jacking the piles. They noticed that higher relative density resulted in larger plug length during driving, while resulted in shorter plug length during jacking. Furthermore, they revealed that the jacked piles are more likely to be plugged than the driven piles. In addition, Henke and Grabe (2008) compared the effect of three installation methods on the tendency of plugging for medium dense sand through numerical modelling. Later on, Henke and Grabe (2013) conducted field tests to investigate these effects further. The studied installation methods include pile jacking, vibratory pile driving, and impact driving. They concluded that the plug was more likely to be formed in jacked piles rather than the piles installed by impact driving or vibratory driving methods, which was also observed by White et al. (2000). The phenomenon can be explained by the relative motion between the soil and pile during driving. The vibratory pile driving process resulted in high compaction of the soil around the pile, which led to a decrease in horizontal stress inside and outside the pile, which is claimed as the major cause of forming a plug. While the pile jacking process initiated the arching in the soil, which contributes to the formation of soil plug.

2.3.3 Effect of Pile Shoes

According to Tomlinson and Woodward (2008), a steel ring that is welded on the toe of the pile enhances the strength of the toe, which is known as pile shoes, as illustrated in Figure 2.6. The pile shoe is often used to improve driveability and protect the pile tip especially driving into hard ground materials. The pile shoes are often applied on open-ended piles to be able to obtain deeper penetrations and penetrate into moderately strong layers. As De Nicola and Randolph (1997) mentioned, to develop the full outer shaft resistance, the internal ring may be used. In contrast, the external ring is applied for reducing the external shaft friction, so that the piles can be driven to deep penetration depth.

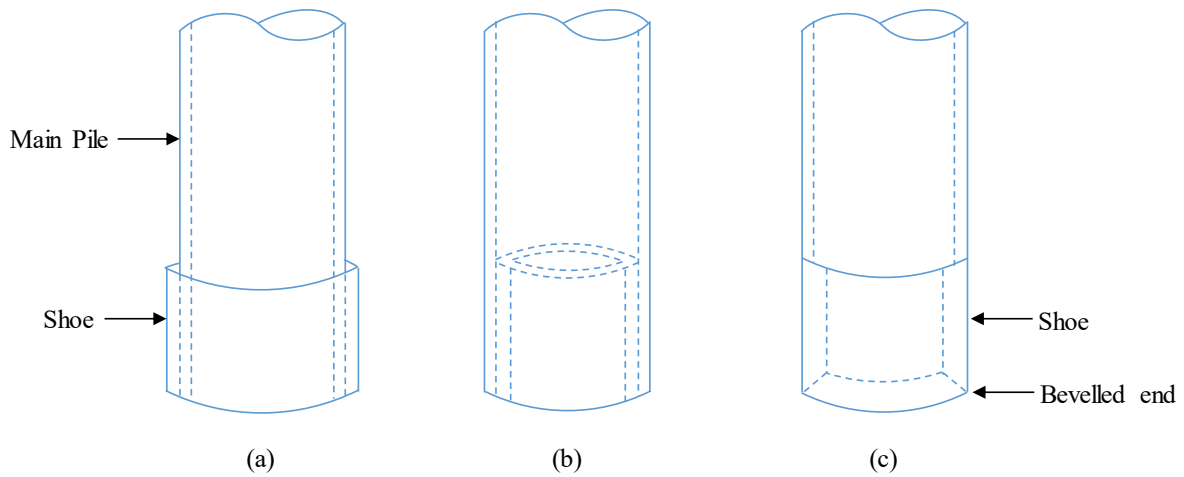
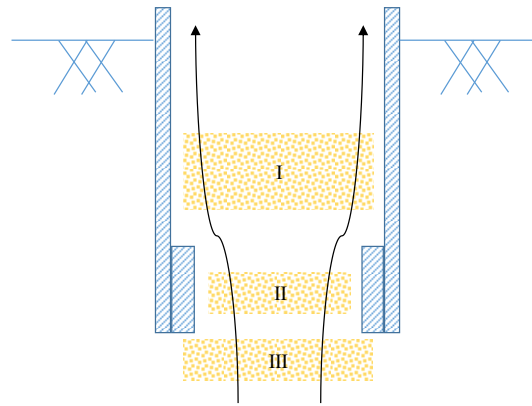
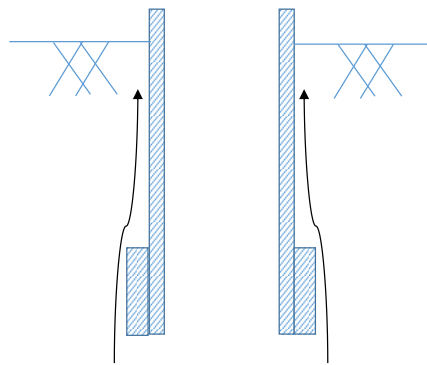


Figure 2.6. Different types of pile shoes: (a) outer shoe; (b) inner shoe; and (c) thick plate shoe (after Tomlinson and Woodward 2008)

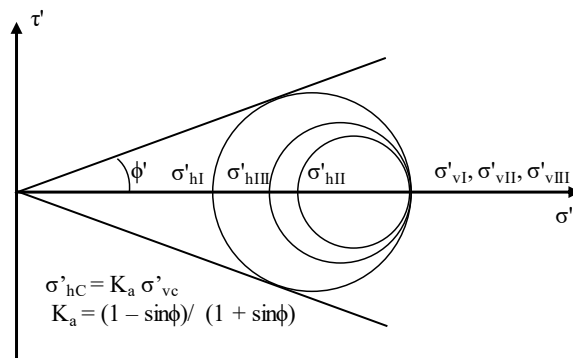
One of the applications of driving shoe is to provide a reduction in jacking load to relief hard driving, in which the performance of the foundation would not be compromised with the increasing of base area (Finlay et al. 2001; Karlowskis 2014). Other methods are available for relief hard driving, while adopting driving shoe is the most preferable method, due to less intrusive and no additional equipment is required. As illustrated in Figures 2.7 (a) and (c), the horizontal effective stress acting on the inner shaft reduced due to the alteration in the flow of soil when applying the inner shoe, hence, leading to a reduction in shaft friction (De Nicola and Randolph 1997; Finlay et al. 2001). Similarly, external pile shoe tends to change the soil flow adjacent to the outer shaft, as presented in Figure 2.7 (b).



(a)



(b)



(c)

Figure 2.7. Hypothesised stress changes due to driving shoe in sandy soil: (a) the soil flow for open-ended tubular pile with inner pile shoe; (b) the soil flow for open-ended tubular pile with outer pile shoe; and (c) stress change at zone I, II, and III for open-ended tubular pile with inner shoe (after De Nicola and Randolph 1997; White et al. 2000)

Internal or external pile shoes are often adopted to protect the pile toe from damage. In the Macleay river and floodplain bridge project, a 25 mm external pile shoe was adopted to strengthen the pile with a diameter of 750 to 825 mm (Zhang et al. 2013). Han et al. (2019a) adopted a twin-wall pile system attached with cutting shoe to the inner pile to investigate the axial resistance of open-ended tubular pile in gravelly sand. Pile shoe is also applied for the purpose of increase the end area, hence, to increase the capacity of the pile. For the project of Los Angeles Export Terminal wharf, the open-ended tubular piles were adopted to support the free-standing wharf, however, the capacity of the first three piles only reached 50% of the design capacity. In order to achieve the design capacity, thick pile shoes were used to increase the base area. The pile capacity has been doubled with the attachment of the thick pile shoe (Bhushan 2004).

Some researchers (e.g., Byrne 1995; De Nicola and Randolph 1997; Finlay et al. 2001; Kumara et al. 2016) studied the effects of pile shoe in sandy soil. Field tests were conducted by Byrne (1995) on different end conditions of the pile, including closed-ended, flush pile (i.e., open-ended without shoe), open-ended pile with straight internal pile shoe, and open-ended pile with tapered internal pile shoe. They found that the piles with internal pile shoe generated a larger length of the plug, and the longer the internal pile shoe, the higher of the plug. It is noticed that the internal pile shoe provides a stress release of the soil entered the pile. Meanwhile, the internal pile shoes with tapered sleeve intended to result in more plug penetration compared to the straight sleeve. Finlay et al. (2001) conducted filed tests and studied the effect of the internal and external pile shoes in sandy ground, and both types of shoes had a thickness of 15 mm and welded to a 319 mm diameter tubular pile. A significant reduction in effective horizontal stress and external shaft friction, by a factor of 4, was found for the pile with an external driving shoe. While no evident influence on external shaft friction was observed for the pile with an internal driving shoe. In contrast, internal pile shoe not only influences the effective horizontal stress,

but also the plug height. Finlay et al. (2001) reported that a reduction in internal shaft friction by a factor of 3 was found when applying the internal pile shoe. However, in terms of the jacking force, the changes were minimal due to the reduction in shaft friction was partially balanced by the increase in base resistance created by the additional area of the driving shoes. Meanwhile, large-scale model tests were conducted on open-ended piles with or without pile shoes. Kumara et al. (2016) studied the effect of internal pile shoe on the capacity of tubular piles in sandy soil. The model piles with a diameter (D) of 50 mm and different heights of internal pile shoe ranging from $0.2D$ to $2D$ were adopted in the experiments. By measuring the penetration resistance, they found that the penetration resistance increases with increasing the height of internal pile shoe, hence, increase the bearing capacity of the pile. Through the model tests of open-ended tubular piles with and without pile shoe, De Nicola and Randolph (1997) found that internal driving shoe provided significant stress relief within the soil plug during jacking, as indicated in Figures 2.7 (a) and (c). As De Nicola and Randolph (1997) mentioned that the penetration depth of the experiment was relatively shallow, the relief of stress at the lower part of the soil plug was not significant. In addition, the increased base area generated higher base resistance, which was not compensated by plug stress relief. Hence, the driving resistance of the open-ended tubular pile with the shoe in this experiment was higher than the pile without the shoe.

2.4 Characteristics of Weak Rocks

Weak rock characteristics are of significant importance in geotechnical design and construction, e.g., deep construction pits, tunnel excavations, open cast mines, and open-end pile driving, which are mostly influenced by the complex nature and inadequate definitions of their behaviour (Klein 2001; Nickmann et al. 2006; Zhai et al. 2017). Several types of problems are associated with weak rocks, which can be summarized as follows:

- a) The undesirable behaviours such as low strength, high deformability, high plasticity, a high degree of weathering, and many others that build up the difficulties for geotechnical design;
- b) The strength of weak rocks falls in between the strength of soils and hard rocks, hence, neither the rock mechanics equipment nor the soil mechanics equipment would be fully suitable for testing;
- c) The sampling and specimen preparation for testing is usually problematic due to the rock core destruction; and
- d) The classification of weak rocks experiences great difficulty since the conventional geotechnical classification systems are developed mainly for discontinuous media such as hard rocks (Bell 2000; Klein 2001; Nickmann et al. 2006; Santi 2006; Sun et al. 2006; Kanji 2014).

2.4.1 Formation and Classification

Weak rocks can fall in any of the major rock categories, i.e., igneous rock, sedimentary rock, or metamorphic rock as summarised in Table 2.5. Referring to Dobereiner and Freitas (1986) and Nickmann et al. (2006), the origin of weak rocks is from the process of sedimentation or weathering. According to Zhai et al. (2017), weak rocks can be classified as young sedimentary rock, weathered competent rock and tectonically disturbed competent rock based on the origin and formation processes. Figure 2.8 illustrates the formation of weak rocks and the position in the subjects of soil and rock mechanics. Dobereiner and Freitas (1986) mentioned that weak rocks could rarely be ignored by either discipline (i.e., rock mechanics and soil mechanics) as they often occur interbedded or intermixed with materials that are unquestionably either rocks or soils.

Table 2.5. Usual type of weak rocks (after Kanji 2014)

Primary category	Sub-category
Sedimentary rocks	Mudstones, shales, siltstones, sandstones, limestone, dolomite, gypsum
Igneous rocks	Volcanic conglomerates, pyroclastic deposits, volcanic ash, basaltic breccia, tuff, ignimbrite
Metamorphic rocks	Slate, schists, metavolcanic deposits, phyllite

Due to the mechanical behaviour of weak rocks (e.g., low strength and high deformability), various classification systems are developed to define the boundaries between soils and weak rocks, and weak rocks and hard rocks, which are known as the lower and upper boundaries, respectively. According to Bell (2000), Klein (2001), and Santi (2006), most of the classification systems are based on the unconfined compressive strength (UCS) of the intact rock.

Terzaghi and Peck (1967) reported that weak rocks behave more like rocks than soils and usually have an SPT above 50 and UCS greater than 0.4 MPa. According to Bell (2000), UCS of intact weak rocks is 1.25 to 5 MPa, while based on IAEG (1979), the material can be defined as weak rocks provided that the strength of the material is less than 15 MPa. The International Society for Rock Mechanics (ISRM) describes rocks with values of UCS in the range of 0.25 to 25 MPa as “extremely weak” to “weak” (Kanji 2014; Zhai et al. 2017). Moreover, Klein (2001) suggested that a more appropriate upper bound strength limit of weak rocks might be 20 MPa. It should be noted that the rock weaker than this limit (i.e., $UCS = 20 \text{ MPa}$) behaves

differently when sheared, particularly for sandstones, as sandstones with such a low value of UCS generally contract whereas stronger rocks tend to dilate (Klein 2001). Furthermore, Santi (2006) claimed that weak rocks have unconfined compressive strength between 1 and 20 MPa, slake durability less than 90%, clay content greater than 15%, poor induration, a significant amount (e.g., 50% to 70%) of matrix between hard blocks, or high moisture content. Table 2.6 summarises the classification of weak rocks based on the above mentioned approaches.

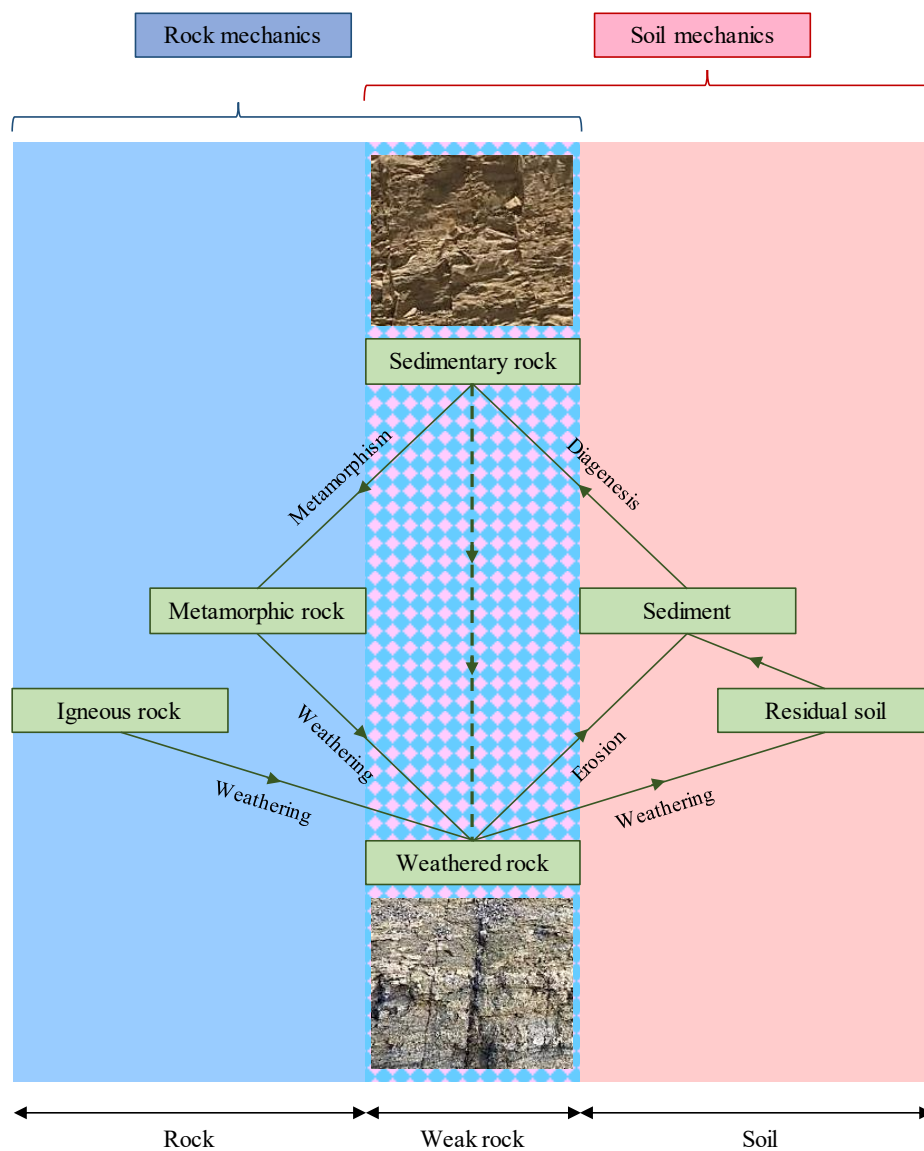


Figure 2.8. Formation of weak rocks and their position in the soil and rock mechanics (after Dobereiner and Freitas 1986; Zhai et al. 2017)

The porosity of weak rocks influences the strength significantly (Klein 2001; Tommasi et al. 2014). In general, low porosity and high strength are due to the dense arrangement of grains, whereas high porosity correlates with low strength. Typically, weak rocks exhibit high porosity. For example, the weak pyroclastic rocks in Italy had a porosity of more than 40%, and the porphyrite which sampled from Japan has a porosity as high as 50%, as reported by Tommasi et al. (2014) and Sun et al. (2006), respectively. In addition, the uniaxial compressive strength of shales and sandstones is highly related to porosity, as shown in Table 2.7.

Table 2.6. Summary of classification systems of weak rocks

Properties	Description	Classification systems
$UCS_{intact} > 0.4 \text{ MPa}$ and $SPT > 50$	Soils and weak rocks boundary	Terzaghi and Peck (1967)
$1 \text{ MPa} < UCS_{intact} < 25 \text{ MPa}$	Very low strength rocks	Bieniawski (1973)
$1.25 \text{ MPa} < UCS_{intact} < 5 \text{ MPa}$	Weak rocks	Bell (2000)
$UCS_{intact} < 15 \text{ MPa}$	Weak rocks and hard rocks boundary	IAEG (1979)
$0.25 \text{ MPa} < UCS_{intact} < 25 \text{ MPa}$	Extremely weak to Weak	ISRM (Kanji 2014; Zhai et al. 2017)
$UCS_{intact} < 20 \text{ MPa}$	Weak sandstones	Klein (2001)
$1 \text{ MPa} < UCS_{intact} < 20 \text{ MPa}$; slake durability less than 90%	Weak rocks	Santi (2006)
$0.5 \text{ MPa} < UCS_{intact} < 10 \text{ to } 15 \text{ MPa}$	Weak rocks	Carvalho et al. (2007)

(Note: UCS_{intact} is the unconfined compressive strength of the intact rock mass)

Table 2.7. Uniaxial compressive strength and description of shales and sandstones as related to porosity (after Klein 2001)

Rock Type	Porosity, n (%)	Uniaxial compressive strength (MPa)	Description (after Hoek et al. 1998)
Shales (Mudstones) (after Hoshino, 1981)	10	7 to 15	Weak
	20	4 to 10	Very weak to weak
	30	1 to 5	Very weak
Sandstones (after Dobereiner and Freitas 1986)	10	50 to 120	Strong to very strong
	20	10 to 30	Weak to Medium strong
	30	1.5 to 5	Very weak

2.4.2 Discontinuities

Discontinuities (e.g., bedding planes, joints, foliation, and faults) are commonly observed in weak rocks due to the destruction of the original structure during folding and shearing, which would affect the behaviour of weak rock masses under overstressed conditions (Klein 2001; Zhai et al. 2017). The well-known rock mass classification systems, including RMR system (Bieniawski 1989), Q system (Barton et al. 1974), and GSI system (Hoek et al. 2000), are highly based on the characteristics of the jointing structure of the rock masses and the joint surface conditions. Several researchers (Marinos 2010; Mohammadi and Hossaini 2017) have worked on modifying these traditional systems so that the systems could better depict the behaviour of weak rock masses; this is particularly important when geotechnical designs (e.g., tunnels) are associated with weak rock masses. Most of these systems take the characteristics of discontinuities consisting of the joint pattern (i.e., joint dip, spacing, continuity), a number

of the joint sets, and joint roughness as important considerations for characterizing rock masses (Bieniawski 1973; Marinos 2010).

The effects of the characteristics on the weak rock masses have been studied experimental, empirically, and numerically by various researchers (Gokceoglu and Aksoy 2000; Mughieda and Alzo'ubi 2004; Prudencio and Jan 2007; Paluszny et al. 2012; Bahaaddini et al. 2013). Gokceoglu and Aksoy (2000) have studied the joint characteristics and behaviour of clay-bearing, densely jointed and weak rock masses extensively, which mainly were marl, mudstone, sandstone, and schist. They recorded that for these jointed weak rock masses, the width of the aperture varied from 0 to 20 mm with or without infill materials, and the joint set was found to be at least three sets for each rock mass. Moreover, the behaviour of non-persistent cracks was analysed through numbers of synthetic weak rock masses by Mughieda and Alzo'ubi (2004), and it was concluded that wind cracks initiated at the joint tips were due to high tensile stress concentration. Furthermore, Prudencio and Jan (2007) investigated the effects of several joint properties on the mechanical behaviour of an artificial weak rock mass. They discovered that the joint dip and spacing influenced the failure envelopes and mechanism, in addition, they discussed the potential of the existing joint propagating and connecting with the neighbouring joint associated with these joint characteristics, which was also investigated by many researchers (e.g., Zhang et al. 2015; Yang et al. 2016). Later, Bahaaddini et al. (2013) extended this work (i.e., Prudencio and Jan 2007) numerically and studied the impacts of joint length and aperture, and proved that the wider the joint opened, the lower the strength of weak rock masses due to the joint dip and direction of the loading.

2.4.3 Weak Rock Mass Strength

To estimate the rock mass strength of weak rock, the empirical methods based on the Hoek-Brown failure criterion (Hoek et al. 2002) have been developed and assessed by some

researchers (e.g., Carvalho et al. 2007; Dinc et al. 2011; Zhai et al. 2017). As Carvalho et al. (2007) and Carter et al. (2008) pointed out, the more soil-like the material, the more it tended to behave linearly, whereas non-linear behaviour was observed in the rock-like material. Furthermore, Carter et al. (2008) illustrated this phenomenon as shown in Figure 2.9, which was the normalised rock mass strength (i.e., UCS_{RM} / UCS_i , the uniaxial compressive strength of rock mass over the uniaxial compressive strength of intact rock material) against Geological Strength Index (GSI), especially considering the high m_i rock masses (i.e. for $m_i \approx \sigma_{ci} / \sigma_t = UCS_i / T > 15$). It should be noted that the normalised rock mass strength becomes closer to 1 when UCS_i decreases to 0.5 MPa. Moreover, the weak rock transition curves (refer to Figure 2.9) spread uniformly from the Hoek-Brown conventional GSI curve to the Mohr-Coulomb line. Note that the transition in behaviour is fairly smooth and the traditional Hoek-Brown criterion may not be adequate for weak rock masses (Carvalho et al. 2007; Carter et al. 2008; Dinc et al. 2011). Hence, Carvalho et al. (2007) and Carter et al. (2008) have modified Hoek-Brown failure criterion to develop a transition function which was more suitable for the behaviour of the weak rock masses (i.e. $UCS_i < 10$ to 15 MPa), as shown in the following equations:

$$f_T(\sigma_{ci}) = \begin{cases} 1, & UCS_i \leq 0.5 \text{ MPa} \\ e^{\frac{-(UCS_i - 0.5)^2}{25}}, & UCS_i > 0.5 \text{ MPa} \end{cases} \quad (2-49)$$

$$s^* = s + (1 - s)f_T(\sigma_{ci}) \quad (2-50)$$

$$a^* = a + (1 - a)f_T(\sigma_{ci}) \quad (2-51)$$

$$m_b^* = [m_b + (m_i - m_b)f_T(\sigma_{ci})] / (4a^* - 1) \quad (2-52)$$

where $f_{(T)}(\sigma_{ci})$ is the correction factor for transition material, UCS_i or σ_{ci} is the uniaxial compressive strength, m_b , m_i , s and a are original Hoek-Brown parameters (referring to Hoek et al. 2002) and m_b^* , s^* , and a^* are corrected Hoek-Brown parameters.

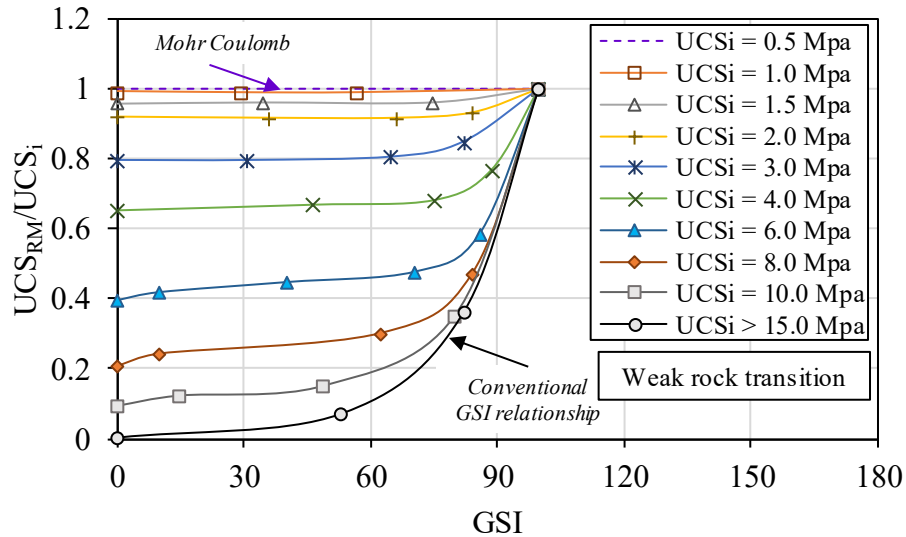


Figure 2.9. Normalised rock mass strength against GSI illustrating marked differences between conventional Hoek-Brown behaviour (after Carter et al. 2008)

2.5 Numerical Analysis

With the advancement of numerical methods, different techniques such as Coupled Eulerian-Lagrangian (CEL), Finite Element Method (FEM), and Discrete Element Method (DEM) are adopted in the studies related to pile foundations and rock mechanics. The development of FEM can be traced back to the 1940s. In the finite element method, the continua are discretised into meshes and connected by points, which are known as elements and nodes, respectively. The interactions between elements and nodes are usually solved with elasticity and plasticity with constitutive models such as the Mohr-Coulomb model, Hoek-Brown model, and Cam-clay model. In the coupled Eulerian-Lagrangian method, the Eulerian analysis allows simulation of large deformation without element distortions, and the Lagrangian analysis is used to model interactions between deformable materials and stiff bodies (Qiu et al. 2011). The

discrete element method was first introduced by Cundall (1971) and then developed rapidly as one of the popular computational mechanics for granular materials. In the DEM, the domain of interest is treated as an assemblage of particles and the interaction between particles is controlled by contact models. The contact force is updating through Newton’s second law and a force-displacement law. The contact patterns are changing continuously in the discrete element method, while the patterns are fixed in the finite element analysis (Jing 2003). The advantages and disadvantages of using FEM and DEM in pile penetration or large deformation problems are summarised in Table 2.8.

Table 2.8. Comparison of FEM and DEM methods for pile penetration problems

Method	Advantages	Disadvantages	Some Applications
FEM	<ul style="list-style-type: none"> • Cost effective compared to field tests and model tests • Capable of simulating large scale problems 	<ul style="list-style-type: none"> • Difficult to simulate the entire penetration process • Special techniques are required to allow the penetration of an object into the soil continuum • A hole on the axis of penetration needs to be modelled before pile penetration • Dimensional restriction (2D) 	<p>Open-ended piles installation method (Henke and Grabe 2008)</p> <p>The pile installation process (Mabsout and Tassoulas 1994)</p> <p>Impact driving of open-ended piles (Liyanapathirana et al. 1998)</p>

<p>• Capable of simulating large deformation problems</p>		
<p>• Provides holistic simulations of inter-particle and particle structure interactions</p>	<p>• A large number of particles</p> <p>• Time-consuming</p> <p>• Idealized particle shapes</p>	<p>Soil plug mechanism (Guo and Yu 2016)</p> <p>The installation process of the open-ended pile (Li et al. 2019)</p>
<p>DEM</p> <p>• Provides soil response macroscopically and macroscopically</p>	<p>• High computational cost</p> <p>• Dimensional restriction (2D)</p>	<p>CPT test (Ciantia et al. 2016)</p>
<p>• provides the distribution of porosity and particle movement</p>		

2.5.1 Finite Element Method

Considering the cost of field tests and model tests, many researchers (e.g., Leong and Randolph 1991; Liyanapathirana et al. 1998; Joseph et al. 2017; Dong et al. 2018) adopted Finite Element Analysis (FEA) to simulate the problems associated with piles. However, most of the simulations were limited to some parts of the penetration processes due to the continuum soil element of FEA which creates a constraint on simulating large deformation problems.

The behaviour of the soil plug has been studied by using the FEA method (e.g., Leong and Randolph 1991; Liyanapathirana et al. 1998). Leong and Randolph (1991) investigated the end-

bearing capacity of the soil plug in an open-ended tubular pile under short-term loading by using 2D Finite Element Analysis (FEA). They compared the responses of different constituted models when simulating the soil plug and soil-pile interface, which were elastic, elastic-perfectly-plastic (Mohr-Coulomb) and elastoplastic (modified Cam clay). Comparing the numerical prediction with experimental data, they claimed that the response was modelled well using a modified Cam clay model for the soil plug and Mohr-Coulomb model for the soil-pile interface. In addition, the plugging mechanism of open-ended tubular piles was studied by Liyanapathirana et al. (1998) using an axisymmetric 2D finite element model. They assume the piles were infinitely-long, and the adopted boundary conditions are shown in Figure 2.10. The force of a falling hammer was simulated on top of the pile, and then different pile radius and interface friction were studied. Liyanapathirana et al. (1998) found that the plugging of the pile was influenced by the friction at the pile-soil interface and the shear wave velocity of the soil. Later on, Joseph et al. (2017) adopted 1D finite element analysis to investigate the plug behaviour and comparing the design capacities that computed from API, ICP and UWA methods with the numerical predictions. The model was able to model each component of the plug-pile-soil interaction that contained predictions on end bearing of the pile, end bearing of the plug, shaft friction and total capacity. Joseph et al. (2017) adopted 2-noded elements for the soil, pile and plug, and 4-noded elements for the interfaces. They found that the CPT based design methods (i.e., ICP and UWA method) have reliable predictions of the overall base capacity of open-ended tubular piles.

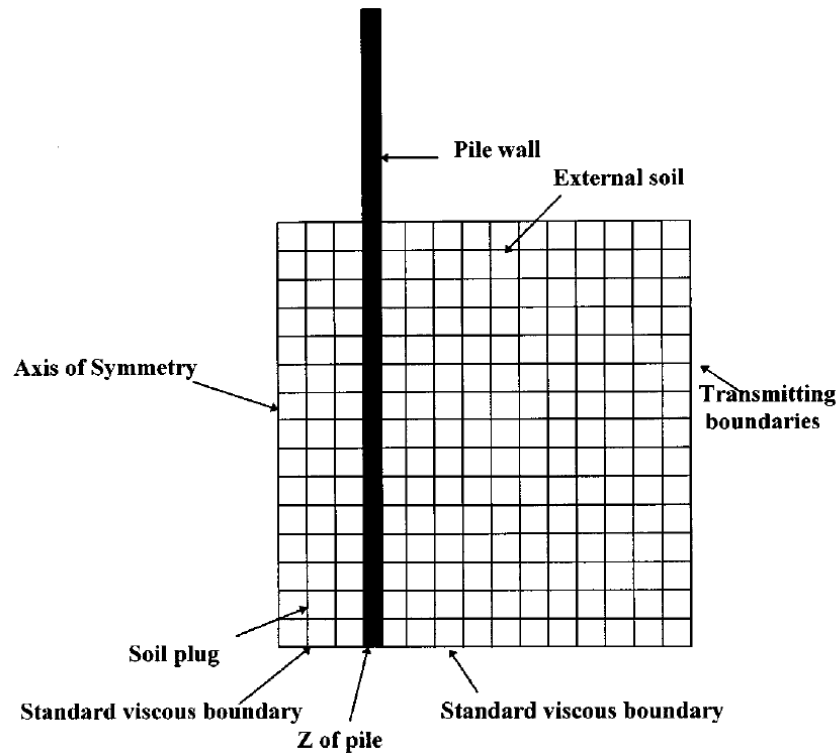


Figure 2.10. Finite element model and boundaries conditions for analysis of plug mechanism

(Liyanapathirana et al. 1998)

Meanwhile, the pile penetration processes were simulated in FEM by applying special techniques. Different pile installation methods were compared by Henke and Grabe (2008) with adopting a finite element model. In order to simulate the pile penetration process in a continuum media, the technique “zipper-type” was adopted to allow penetration of a tubular pile, which modelled a pre-existing frictionless tube along the axis of pile penetration with a width of 0.001 m, as illustrated in Figure 2.11. During the penetration process, the tested pile slipped along the tube, then the soil was separated from the tube. The soil around the pile was simulated with axisymmetric continuum elements with a very fine mesh, while for far filed soil, infinite elements were applied. Henke and Grabe (2008) modelled pile jacking as a displacement-controlled quasistatic process, and vibratory and impact driving as dynamic problems. They found that no obvious high stress peaks were observed for the horizontal stresses outside the pile, while that observed inside the pile for the jacking pile. This revealed

that a soil plug forms inside the tubular pile due to jacking, which can be claimed to the dilatation and arching inside the pile. In comparison, no notable increase in horizontal stresses can be observed for impact driving, which indicates that soil plugs did not form. Due to the continuous cyclic shearing while vibratory driving, Henke and Grabe (2008) mentioned that a reduction in horizontal stresses was observed and no soil plug was formed with the tested pile diameter.

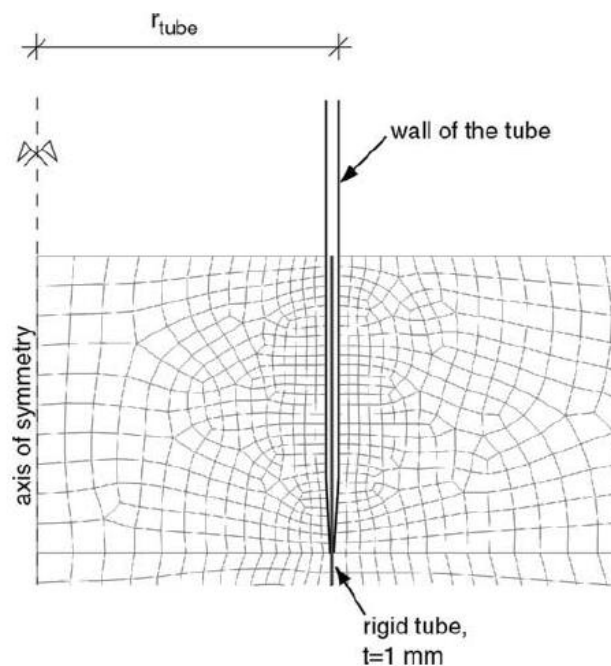


Figure 2.11. “Zipper-type” technique for simulating pile penetration process in FEA (Henke and Grabe 2008)

2.5.2 Discrete Element Method

The discrete element method was originated for the analysis of rock mechanics problem (Cundall 1971; Cundall and Strack 1979; Jing 2003). DEM is capable of simulating the fracturing processes and jointed properties, and provides explicit consideration of the discrete nature of the rock masses. The applications of DEM in studying rock mechanics are numerous, including investigating the effect of non-persistent jointed rock mass under uniaxial

compression (Bahaaddini et al. 2013), the effect of joint dip (e.g., Chiu et al. 2013; Huang et al. 2015), the stability of heavily jointed rock slopes (e.g., Wang et al. 2003; Scholtès and Donzé 2015). Due to the advantages of simulating discrete nature of geomaterials and large deformation problems, DEM method has been adopted widely in studies such as pile penetration (e.g., Kinloch and O'Sullivan 2007; Li et al. 2019) and CPT test (e.g., Jiang et al. 2006; McDowell et al. 2012).

The discrete element method (DEM) is more suitable for analysis that involves large deformation and investigates both the macroscopic and microscopic behaviour (Li et al. 2019). Since DEM can provide holistic simulations of inter-particle interactions and nonlinear stress-dilatancy behaviour of granular soils, many researchers (e.g., Guo and Yu 2016; Li et al. 2019) adopted DEM to analyse the problems associated with pile penetration and CPT test. For example, the three-dimensional discrete element analysis was conducted by Ciantia et al. (2016) to investigate the effect of grain crushing on the tip resistances of CPT tests, the model that was adopted in their study is presented in Figure 2.12. A simplified Hertz-Mindlin elasto-frictional model was adopted to simulate the behaviour of granular soils. They observed that most particle crushing occurs at some distance below the cone tip during cone penetration. The sensitivity analysis was conducted by Esposito et al. (2018) using DEM in two-dimensional for different penetration velocity, pile-soil friction, method of installation, lateral boundary distance, and particle rotation. They found that the tip resistance increased with the increase in penetration velocity. The results for different boundary distances were found to be similar in values and behaviour of the tip resistance and skin friction. There are many applications of using DEM in large deformation simulation, the summaries of some examples of two-dimensional and three-dimensional analysis of pile penetration or CPT test using DEM are presented in Table 2.9 and Table 2.10, respectively. More examples can be found in the work of Esposito et al. (2018).

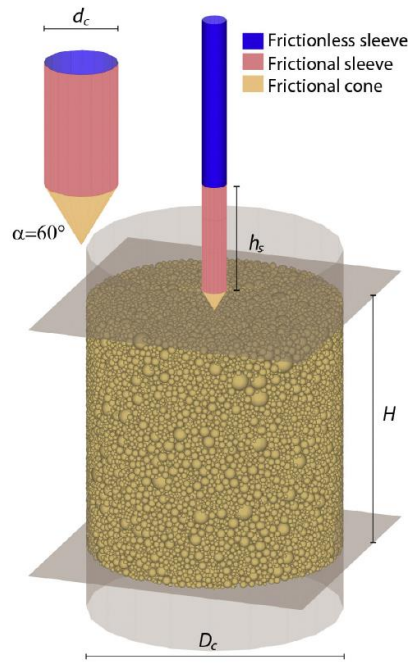


Figure 2.12. An example of the Geometry of the CPT test in DEM (Ciantia et al. 2016)

The plugging mechanism has also been analysed through DEM (e.g., Thongmuneet et al. 2011; Guo and Yu 2016; Li et al. 2019). Guo and Yu (2016) investigated the plugging mechanism through simulating the soil plugging inside an open-ended tubular pile and the plugging process was simulated by moving the pile down with a constant velocity. The soil column had a height of 4 m and a diameter of 0.6 m, which consisted of 20,250 particles. The results indicated that the internal unit shear resistance along the pile increased due to the arching effect, and the porosity was lower and stresses were concentrated at the bottom of the soil plug, which is line with the findings from Li et al. (2019). Meanwhile, they found that the particles at the bottom part are squeezed together that leading to higher horizontal stress.

Table 2.9. Examples of 2D DEM simulations on the pile installation process or CPT test

Ref.	Pile or cone diameter	Particle diameter	Boundary to pile diameter¹	The final pile toe height to base / the pile diameter	No. of particles	Test
Jiang et al. (2006)	36 mm	2.25 mm to 3.525 mm	8.75 <i>D</i>	1.5 <i>D</i>	10,000	CPT test
Kinloch and O'Sullivan (2007)	120 mm	5 mm 7.5 mm 10 mm	7 <i>D</i> 14 <i>D</i>	8.75 <i>D</i> 27 <i>D</i>	29,457 117,828	Penetration of CPT test, closed-ended pile, and open-ended pile
Lobo-Guerrero and Vallejo (2007)	30 mm	6 mm	6.7 <i>D</i>	11.7 <i>D</i>	26,000	Pile installation in crushable sand
Wang and Zhao (2014)	8 mm	0.6 mm to 1.2 mm (0.069 to 0.278 mm)	15 <i>D</i>	5 <i>D</i>	140,000	Close-ended pile in crushable sands

¹Boundary to pile diameter is calculated based on the distance from the centre of the pile or cone to the boundary of the testing chamber over the diameter of the pile or cone.

Li et al. (2019) adopted PFC2D to simulate the installation process of the open-ended pile and investigated the plugging mechanisms macroscopically and microscopically. The tested open-ended pile had an outer diameter of 120 mm and a wall thickness of 10 mm and jacked to a depth of 300 mm. The numerical predictions indicated that the soil plug behaviour was different with increasing penetration depth. Although the behaviour observed in the analysis remained qualitative rather than quantitative, Li et al. (2019) found that the inner shaft resistance increased rapidly at the lower part, while no evident change was observed at the upper part, which demonstrated that the lower part of the soil plug carried most of the load while the upper part acted as surcharge, and this phenomenon was claimed by many researchers (e.g., Randolph et al. 1991; Henke and Grabe 2008). The stress in DEM analysis can be measured in the measurement circle in the 2D modelling or measurement sphere in 3D modelling. By measuring the stress inside the measurement circle, they observed that the horizontal stresses decrease with increasing distance from the pile shaft for both inside and outside the pile, and the maximum horizontal stress was found at the pile tip. A dense zone was found to form at the pile tip, meanwhile, the porosity of the soil mass inside the pile decreased with increasing penetration depth. By observing the contact force chains that scaled by the magnitude of the carried load, Li et al. (2019) pointed out there are passive concave arch (i.e., Arch A in Figure 2.13) and active convex arch (i.e., Arch B in Figure 2.13) in the soil plug, which shed a light that DEM analysis may provide a new perspective to determine the critical plug height or active length.

Table 2.10. Examples of 3D DEM simulations on the pile installation process or CPT test

Ref.	Pile or cone diameter	Particle diameter	Boundary to pile diameter ¹	The final pile toe height to base / the pile diameter	No. of particles	Test
Butlanska et al. (2009)	71.2 mm	18 mm to 40 mm	8.4 <i>D</i>	2.1 <i>D</i>	60,000	CPT test
					30,000	
					15,000	
Lin and Wu (2012)	0.5 mm	0.048 mm to 2.295 mm	20 <i>D</i>	Less than 1 <i>D</i>	422,191	Penetro- meter
	1 mm		10 <i>D</i>			
	2 mm		5 <i>D</i>			
(Butlanska et al. 2013)	71.2 mm	4.5 mm to 26.5 mm (<i>d</i> ₅₀)	8.4 <i>D</i>	2.1 <i>D</i>	59,986	CPT test
Falagush et al. (2015)	18 mm	1 mm (<i>d</i> ₅₀)	8.3 <i>D</i>	2.7 <i>D</i>	33,600	CPT test
					34,700	
					37,050	

¹Boundary to pile diameter is calculated based on the distance from the centre of the pile or cone to the boundary of the testing chamber over the diameter of the pile or cone.

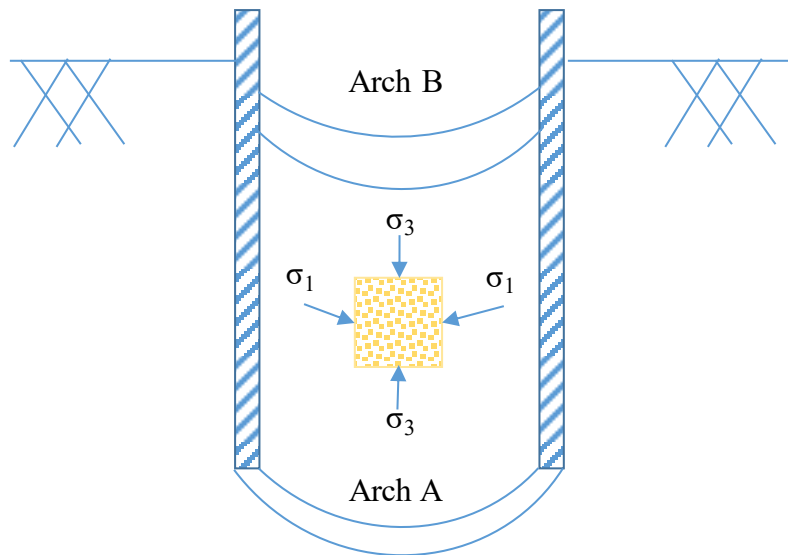


Figure 2.13. Arch development during penetration (after Li et al. 2019)

2.5.3 Coupled Analysis

To overcome the limitation of FEM in simulating large deformation problems, some researchers (e.g., Wang and Zhao 2014; Ko et al. 2016; Zhou et al. 2016; Grabe and Heins 2017; Sun et al. 2019) adopted coupled analysis. Wang and Zhao (2014) conducted a 2-dimensional discrete-continuum analysis to investigate the behaviour of close-ended pile installation in crushable sands. The area adjacent to the pile penetration was simulated by the discrete element method, and the full-field stress distributions were calculated using a grid-based method. They observed a strong dilation at the near field for the case that the void ratio was high and particle crushability was low, while no obvious dilation for the case that the particle crushability was high. Then, Zhou et al. (2016) adopted one of the CEL methods, which allows automatic remeshing of the entire domain, to analyse the effect of tip geometry on soil flow mechanisms inside and outside the double-walled steel casing with a tapered tip. The six-noded triangular elements and elastoplastic nodal joint elements were adopted for the simulation of the soil and the casing-soil interface, respectively. They found that the tip geometry had a significant influence on the soil movements inside and outside the casing that

was about 20% differences in bevelled caisson and flat-tipped caisson, while the minimal effect was observed on the penetration resistance. Meanwhile, Ko et al. (2016) adopted the coupled Eulerian-Lagrangian numerical technique and simulated the driving of open-ended piles in sandy soil. They treated the pile as a Lagrangian domain and the soil as Eulerian domain that contained a void layer and a soil layer, as presented in Figure 2.14. Due to the large deformation in this study, the contact tracking algorithm was employed to track nodes. They found that the degree of plugging highly relied on driving energy.

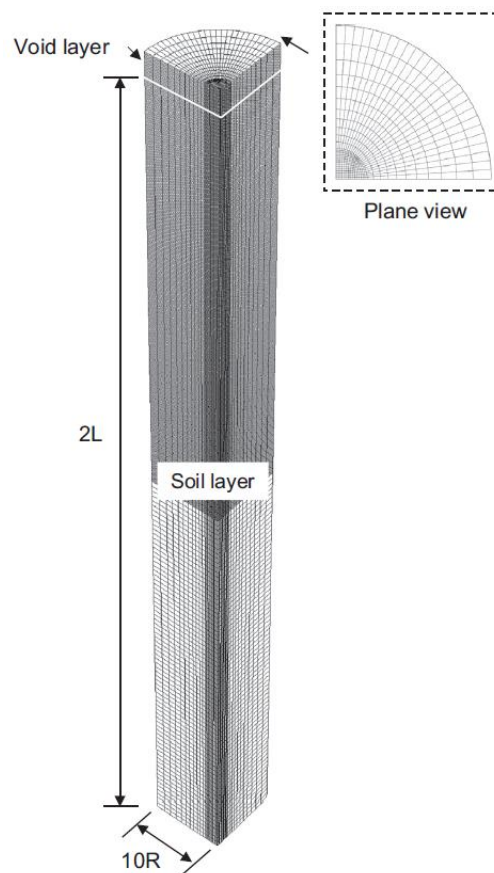


Figure 2.14. Finite element mesh and geometry for the soil domain in the CEL analysis of driving open-ended piles (Ko et al. 2016)

2.6 Case History of Driven Tubular Piles on the Macleay River (NSW, Australia)

For the bridge over the Macleay River and floodplain in NSW in Australia, the subsurface conditions are mainly siltstones often with interbedded or interlaminated sandstones, from

extremely low to very high strength (Zhang et al. 2013). In this project, a combination of steel tubular piles of 750 mm and 825 mm in diameter has been adopted as the foundation to the depth of 20 m to 47 m. The design of the tubular piles was based on the Imperial College Pile (ICP) method (Jardine et al. 2005). However, due to the limited information on applying this method in weak rocks and the uncertainty over whether a rock plug could be formed, limitations existed for pile design (Zhang et al. 2013).

It is noted that the major part of the shaft resistance is from the weak rock layer in this project. As Zhang et al. (2013) stated, unit shaft resistance in weak rocks was fully mobilised and ranged from 100 to 800 kPa, depending on weathering degree, rock strength and penetration. In addition, based on the measured results of the pile head forces which were recorded from the pile driving analyser (PDA), the mobilised shaft and base resistance values have been proposed as shown in Table 2.11.

Table 2.11. Interpreted design values for shaft friction and base resistance of tubular piles in different subsurface conditions (Zhang et al. 2013)

Soil and rock description	Shaft friction (kPa)	Base resistance (MPa)
Soft to firm clay / Very loose to loose sand	20	-
Stiff to hard clay / Medium-dense to dense sand	30-60 (40)	-
Extremely low strength rock	100-200	3-6
Very low strength rock	200-400	5-10
Low strength rock	400-600	8-15

Although the results from the Macleay River project can help designers, uncertainty over the plug capacity and how much penetration is needed to form a rock plug is still unclear. Practicing engineers generally assume that plugging is formed in the weak rock if the minimum penetration is about two times the pile diameter. Meanwhile, driving further into the medium strength rock would increase the risk of pile toe buckling and deduct the resistance significantly (Zhang et al. 2013). Therefore, the plugging mechanism of tubular piles in weak rocks, the influence of rock joints on the ultimate axial strength of tubular piles need to be studied further.

2.7 Summary and Gap Identification

Nowadays, the open-ended tubular piles are widely used in offshore structures, bridge foundations, and buildings. The bearing capacity and degree of plugging of open-ended tubular piles in sands and clays are investigated comprehensively and design recommendations are well-established. Different design methods were proposed based on the field data and CPT-test, such as the ICP method, the API method, and the UWA method. The degree of plugging is addressed and applied for the pile design in some of the recommendations for the open-ended tubular piles in sands and clays, for example, the ICP method and the FinnRA method. However, as the advancement of the technology and increase in population, more and more piles are required to reach the rock layers to sustain the load. The existing studies and current understanding of the open-ended tubular piles in weak rocks are limited. In general, weak rock is the transition materials between hard soils and medium strength rocks. Different from the behaviour of sands or clays, weak rocks may contain discontinuities and the shattering of the rock fabric during the pile penetration may reduce the strength of the rock masses. Many effects are still unclear and problems related to the open-ended tubular piles including the prediction of the driving force, the degree of plugging, the discontinuities of the weak rock, pile toe damage during hard driving, and the effect of pile shoe.

Various techniques and methods are adopted by researchers to investigate the bearing mechanism of open-ended tubular piles in sands and clays. These methods include field tests, experimental model tests, analytical methods, and numerical methods. Among these numerical methods, the discrete element method stands out due to the ability to simulate large deformation problems and replicate the discrete nature of the granular materials. Accordingly, the effects of discontinuities on the rock strength, the influence of the joint properties on the plug resistance, the bearing mechanism of open-ended tubular pile driven into the weak rock, as well as the effect of inner pile shoe were studied in this research by adopting the discrete element method. However, there are some effects were not considered in this study, such as the crushing of the rock masses and the joint propagation during pile penetration, which requires further studies.

Chapter 3 - Investigating the Mechanical Behaviour of Weak

Rocks

3.1 General

To understand the mechanical behaviour of weak rock masses during open-ended pile penetration, the behaviours of weak rock were first investigated through discrete element modelling. Different from soils, rock contains discontinuities. Hence, the understanding on the behaviour of weak rocks should be studied in regard of joint properties, including joint density, joint length, joint spacing, joint dip, and joint aperture.

Adopting discrete element method (DEM) to simulate the behaviour of jointed rocks is becoming more common due to discrete nature of the medium. The discontinuum based software, particle flow code in three-dimension software (PFC3D), was employed to analyse the effects of joint density on the rock mass unconfined compressive strength of jointed rocks. The flat-joint model allowing partial damages at the contact surfaces was utilised to simulate the mechanical behaviour of the rock, while the smooth-joint contact model was employed to simulate the sliding effect of joints. Indeed, 18 jointed rock specimens with different joint density values, which were presented as the joint area over the volume of the specimen, ranging from $5 \text{ m}^2/\text{m}^3$ to $240 \text{ m}^2/\text{m}^3$ were simulated. Via comparing the stress-strain behaviour and failure mechanisms of the jointed rocks subjected to unconfined compression, the impact of joint density was investigated. It can be concluded that the rock mass unconfined compressive strength decreased significantly when the joint density increased to $60 \text{ m}^2/\text{m}^3$ for the simulated medium strength marble, and then reduced gradually and eventually the rock mass unconfined compressive strength of the jointed rock dropped below 5 MPa. The modulus of elasticity also reduced with increasing joint density.

The effects of the joint aperture and dip on the behaviour of weak rock were numerically investigated using discrete element method (DEM). The mechanical behaviour of the intact and jointed rock specimens was simulated by adopting the discontinuum based software PFC3D. The rock specimens with various joint apertures and dips were replicated, and the effects of these two joint characteristics were studied through triaxial tests. The flat-joint model was employed for simulating the stress-strain behaviour of intact rock and had the ability to reproduce the cementation effect. The smooth-joint contact model was utilised to simulate the sliding effect of the joints. The effects of five different joint dips were investigated in the combination of three different joint aperture categories, namely very tight, open, and moderately wide. It can be concluded that the strength of the jointed weak rock specimens reduces as the joint aperture width increases. The amount of alternation in strength and deformability that were contributed by joint apertures differed with the dips of the joint. With the joint dip that was parallel to the deviatoric loading, the effect of joint aperture on the strength and deformability of the specimens was less evident.

Weak rock specimens with different individual joint lengths are numerically simulated using the discrete element method (DEM). Effects of micro or macro-mechanical responses of intact and jointed specimens subjected to triaxial test have been studied. Various individual joint lengths with a given joint density within the weak rock specimens were reproduced using the particle flow code in three-dimension software (PFC3D). Different lengths of joints were simulated by altering the size of each joint to give insight over the influence of continual joints and non-persistent joints within bonded assemblies. As expected, for a given joint density the individual joint length affected the strength and deformability of rock mass. For an individual joint length to specimen width ratio (the normalised joint length) less than a limiting value, the effects of the individual joint length on the stress-strain behaviour of rock specimens were more evident. Indeed, the strength decreased with decreasing the normalised joint length. However,

with a ratio above the limiting value, the effects of the individual joint length were minimal. It can be concluded that for a given joint density, presence of shorter mini-joints could be potentially more detrimental to stiffness and strength of the rock mass in comparison to longer major joints.

3.1.1 Fundamentals of Flat-joint Model

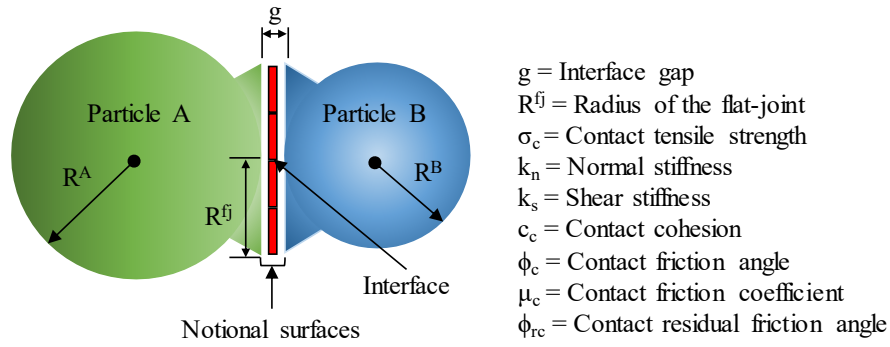
How the contacts behave is the most important aspect in discrete element simulations. Various bonded-particle models (BPM) are available, each of which focuses on particular aspects of the contact models, are capable of replicating the mechanical behaviour of rock, as well as the cementation degradation of cemented soils due to volumetric or shear strains (Nguyen and Fatahi 2016; Nguyen et al. 2017). The flat-joint model (FJM) was used in this study to replicate the behaviour of an intact rock mass because it has some features that surpass the other contact models (Wu and Xu 2016; Xu et al. 2016). Compared to traditional contact models such as the linear parallel bond model and the linear contact bond model, FJM has some significant improvements. Referring to Figure 3.1 (a), a flat-joint contact simulates an interface between two notional surfaces, which in turn allows partial breakage of the particle bonds because the interface can further discretise into several elements (Potyondy 2015). This model can predict the tensile strength of rock mass more accurately due to the additional parameter for tension cut-off, and instead of having constant shear strength, the shear strength in a flat-joint model is controlled by cohesion, the friction angle, and the normal stress.

A flat-joint contact can be bonded, unbonded, or frictional depending on the contact gap, while the force can be sustained by the bond, as shown in Figures 3.1 (b) and (c) (Itasca 2015). The shear strength of the bonded element is pressure dependent and follows the Coulomb criterion with a tension cut-off (σ_c), and also considers the cohesion and the friction angle of contact (c_c and ϕ_c). The unbonded element has two forms. When the contact gap is equal to 0, the

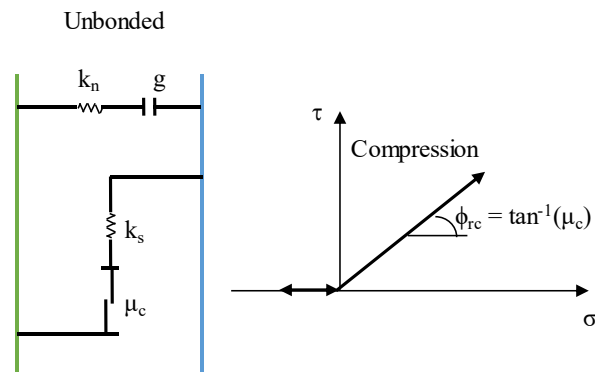
unbonded element is frictional with slip accommodated by imposing a Coulomb limit on the shear force. While the element is unbonded with the contact gap greater than 0, no force or moment is carried by the element (Itasca 2015; Potyondy 2015). The force and moment carried by the bonded and unbonded element obey the force-displacement law, which is an emergent behaviour controlled by the normal stiffness (k_n) at each particle contact and the normal-to-shear stiffness ratio (k_n/k_s). The stiffness of the element is determined by the particle to particle contact Young's modulus (E_c), which is given by the relationship, as shown in Equation (3-1) as reported in (Itasca 2015).

$$E_c = \frac{k_n(R^A+R^B)}{\pi[\min(R^A,R^B)]} \quad (3-1)$$

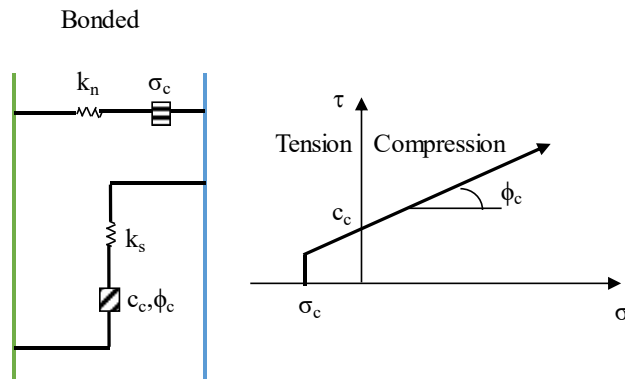
where R^A and R^B are the radii of the contacting particles A and B, respectively, as shown in Figure 3.1 (a).



(a)



(b)



(c)

Figure 3.1. Behaviour of flat-joint contact (a) schematic diagram of flat-joint contact with the notional surfaces; (b) rheological components and behaviour of the unbonded element; and (c) rheological components and behaviour of the bonded element

Due to the notional surface of the flat-joint model, it is discretised into several elements such that the moment at contact makes a limited contribution to the stresses, hence it can be omitted

(Ding and Zhang 2014; Wu and Xu 2016). The normal and shear stresses in the element (i.e., σ^e and τ^e) are calculated from the normal and shear forces acting at the element (\bar{F}_n^e and \bar{F}_s^e), and the area of element (A^e), as shown in Equations (3-2) and (3-3) (Itasca 2015). The radius of the flat-joint (R^{fj}) is adopted from the smaller radius of the two contacting particles with the user-defined parameter radius multiplier (λ), as given in Equation (3-4) (Itasca 2015).

$$\sigma^e = \frac{\bar{F}_n^e}{A^e} \quad (3-2)$$

$$\tau^e = \frac{\bar{F}_s^e}{A^e} \quad (3-3)$$

$$R^{fj} = \lambda[\min(R^A, R^B)] \quad (3-4)$$

The normal stress in the element can be either in tension or compression, and the normal stress on the notional surface (σ_b) is calculated by the interface gap (g) and the contact normal stiffness (k_n), as presented in Equation (3-5) (Potyondy 2012, 2013; Itasca 2015). When the element is bonded with a positive gap (i.e., $g > 0$), the element carries a tensile load, but while the gap is negative, the element sustains a compressive load.

$$\sigma_b = k_n g \quad (3-5)$$

When the normal stress under tension exceeds the limit of the tension cut-off at the element (i.e., $\sigma_b > \sigma_c$), then the element breaks with a tension crack. The shear strength (τ_b) is determined through the Coulomb criteria, as shown in Equation (3-6) (Itasca 2015). When the shear stress exceeds the shear strength limit (i.e., $\tau^e > \tau_b$), then shear rupture occurs and the bond between the ruptured elements becomes frictional. In this case, the shear strength of the element comes from the notional surface (τ_{sp}) slipping, which is determined by the contact residual friction angle (ϕ_{rc}), as given in Equation (3-7) (Itasca 2015).

$$\tau_b = \sigma_b \tan \phi_c + c_c \quad (3-6)$$

$$\tau_{sp} = \sigma_b \tan \phi_{rc} \quad (3-7)$$

3.1.2 Fundamentals of Smooth-joint Contact Model

The smooth-joint (SJM) contact model can replicate the behaviour of pre-existing joints (Bahrani et al. 2014; Park and Min 2015). This model simulates the behaviour of a planar interface, which is created by the discrete fracture network (DFN). The DFN technique allows for a random distribution of joints in the specimen with controlled joint areas, length, location, and dip angle to replicate natural jointed rocks. The bonds between particles that contact the plane disregard the dips of local particles, therefore the bonds then follow the dip of the DFNs, as shown in Figures 3.2 (a) and (b) (Itasca 2015). A smooth-joint contact is formed at the dip of the joint (α). The normal force carried by the contact (F_n^{sj}) is determined by the initial normal force ($(F_n^{sj})_0$), the elastic portions of the normal displacement increment ($\Delta\delta_n^{sj}$), the area of the smooth-joint cross-section (A^{sj}), and the normal stiffness (k_{ns}), as indicated in Equation (3-8) (Potyondy 2007; Itasca 2015). The radius of the cross-section is calculated from the smaller radius of the contacting particles.

$$F_n^{sj} = (F_n^{sj})_0 + k_{ns}A^{sj}\Delta\delta_n^{sj} \quad (3-8)$$

The shear force (F_s^{sj}) is determined by the value from the force-displacement law (F_s^{sj-s}) or the imposed Coulomb limit (F_s^{sj-c}), whichever is smaller, as expressed in Equations (3-9) and (3-10), respectively (Potyondy 2007; Itasca 2015). The former involves the elastic portions of the shear displacement increment ($\Delta\delta_s^{sj}$), the area of the smooth-joint cross-section (A^{sj}), and the shear stiffness (k_{ss}), while the latter involves the contact coefficient of friction (μ_{cs}).

$$F_s^{sj-s} = (F_s^{sj})_0 - k_{ss}A^{sj}\Delta\delta_s^{sj} \quad (3-9)$$

$$F_s^{sj-c} = -\mu_{cs}F_n^{sj} \quad (3-10)$$

When there is slipping on the plane, the normal force may increase due to an increase in shear displacement induced by dilation, and the increased shear force due to dilation ($F_n^{sj-\Psi}$) can be determined by the dilation angle (Ψ), as presented in Equation (3-11) (Itasca 2015).

$$F_n^{sj-\Psi} = \left(\frac{F_s^{sj-s} - F_s^{sj-c}}{k_{ss}} \right) k_{ns} \tan \Psi \quad (3-11)$$

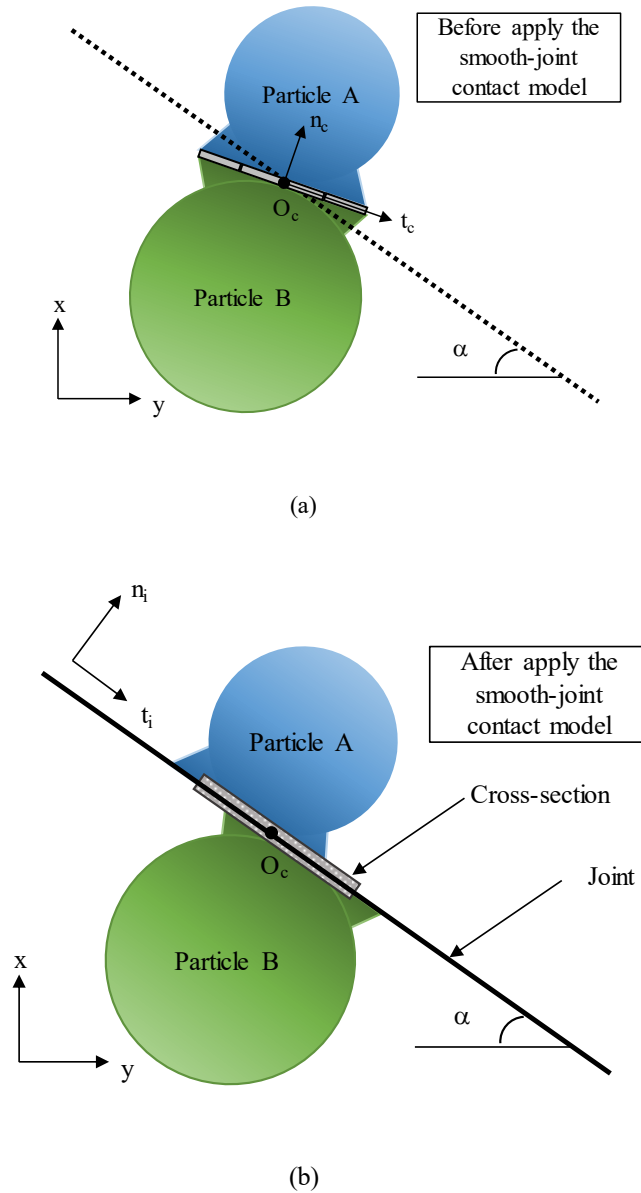


Figure 3.2. The schematic illustration of smooth-joint contact model of (a) before installation; and (b) after installation

3.2 Effects of Joint Density

Joints and discontinuities are commonly encountered in natural rock masses, which contribute to the complexity of their analysis due to the textural anisotropy (Hoek 1983; Bell 2000). Many experimental and numerical investigations considered the pattern, dip, spacing, size and distribution of joints, and concluded that the strength and deformability of rocks were dramatically altered due to the existence of joints (Tsoutrelis and Exadaktylos 1993; Singh et al. 2002). Most of these experiments and analyses only contained one or two sets of joint patterns. However, in the natural rock masses, the distribution of joints can be complex and random (Tsoutrelis and Exadaktylos 1993; Bell 2000). The impact of joint density on the strength of rocks has been rarely studied, due to the difficulties of obtaining natural rocks with countable joint content, or enormous effort on reproducing synthetic jointed rocks with randomly distributed joints. Discrete element method (DEM) has advantages to reproduce the rock mass with various randomly distributed joint contents (Jing 2003). In fact, the failure joint developed in the joint face can be simulated in DEM, while the joint faces can be randomly distributed with user defined joint area to provide a reasonable failure mode (Potyondy and Cundall 2004; Chiu et al. 2013). In this paper, the particle flow code in three dimension (PFC3D) is used to simulate the influence of joint content on the rock mass unconfined compressive strength. The bonded particle model (BPM) (Potyondy and Cundall 2004) and the discrete fracture network (DFN) (Dershowitz and Einstein 1988; Jing 2003) available in PFC3D, are adopted in this study. The former is used for reproducing the rock by introducing contacts between particles, while the latter is employed to form the joints and alter the properties of the contacts around the joints.

3.2.1 Numerical Modelling

The numerical simulation was initially calibrated and compared with the experimental data reported for intact Pendeli marble blocks by Tsoutrelis and Exadaktylos (1993). The test blocks were formed by the white marble of Pendeli, which was $60 \times 60 \times 80$ mm in size, and composed of 99% calcite and 1% quartz with the grain size of less than 1 mm.

In the numerical simulation, the particle contact model for the intact rock specimen was flat-joint model, which simulated the contact between two particles using rigidly connected surfaces. This interface was subdivided into 4 elements, and each element allowed sole breakage. Compared to the traditional BPM, the flat-joint model can simulate the tensile strength of rock mass more accurately (Potyondy 2013; Ding and Zhang 2014; Vallejos et al. 2016). The discrete fracture network (DFN) with the smooth-joint contact model then was introduced into the system to replicate the assemblage of joints, which has the ability to capture the interdependence of joint characteristics by simulating the joints as circular shaped plates (Dershowitz and Einstein 1988; Jing 2003; Chiu et al. 2013).

3.2.1.1 Calibration of microparameters for the intact rock

The simulated rock specimen had the same dimensions as the experimental test (i.e. $60 \times 60 \times 80$ mm), which contained 44,000 particles with a particle size of 1 mm. Particles were randomly distributed to achieve a porosity of 0.37. Calibration of microparameters for the flat-joint model was carried out by simulating the unconfined compression test in which the sample was loaded by moving the top and bottom walls toward each other at a low velocity to keep the specimen under quasi-static equilibrium. The adopted numerical model for the intact rock specimen is presented in Figure 3.3 (a).

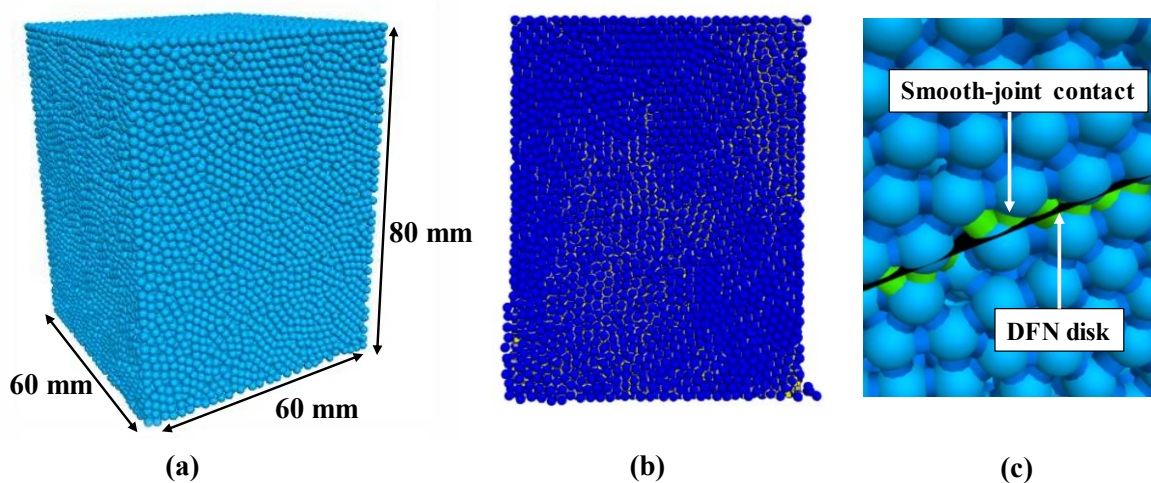


Figure 3.3. (a) Numerical model for intact rock specimen; (b) Failure mode for intact rock (yellow: shear crack and grey: tension crack); and (c) Smooth-joint contact model for simulating joints

The key microparameters that control the deformability of the specimen are Young's modulus at each particle contact (E_c) and normal-to-shear stiffness ratio (k_n/k_s) at the contacting surfaces. For the calibration, the first attempt was to set the microparameters equal to the macroparameters of the experimental specimens, as recommended by other researchers (Camusso and Barla 2009). Assuming a normal-to-shear stiffness ratio of 2.0 and a contact Young's modulus E_c of 8.5×10^9 Pa, the predicted intact rock Young's modulus and pre-peak stress-strain curve obtained were very close to the experimental results.

In order to achieve a good match for the unconfined compressive strength and axial strain at failure, the microscale tensile strength and cohesion values were calibrated through a trial and error process. The failure mechanism for the intact rock specimen is shown in Figure 3.3 (b). The microparameters used in the simulation are summarised in Table 3.1. The comparison of the stress-strain relationship for the numerical model and the experimental results are shown in Figure 3.4, revealing a good agreement.

Table 3.1. Summary of microparameters for the intact rock specimen

Microparameter	Description	Value
E_c	Young's modulus for particle to particle contact	8.5 GPa
k_n/k_s	Normal-to-shear stiffness ratio for contacts	2.0
σ_c	Contact tensile strength	10 MPa
c_c	Contact cohesion	33 MPa
ϕ_c	Contact friction angle	35 degrees

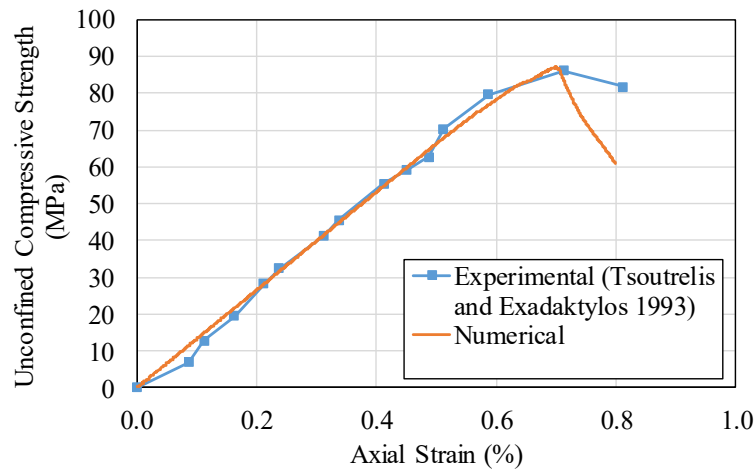


Figure 3.4. Stress-strain curve of the intact rock specimen under unconfined compression test

3.2.1.2 Simulation of jointed rock mass

The rock joints were simulated by introducing discrete fracture network (DFN) in the rock specimen, employing the smooth-joint contact model, as also applied by other researchers (Ivars et al. 2011; Bahaaddini et al. 2013; Chiu et al. 2013). The DFN technique allows random distribution of joints in the specimen with controlled joint areas to replicate the natural jointed rocks. The smooth-joint contact model was then assigned to the contacts between particles with their centres lying on the joint plane, as shown in Figure 3.3 (c). Similar to Bahaaddini et al.

(2013) a reduced contact Young's modulus E_c was adopted since the strength of the joints were weaker compared to the intact grains assembly.

The joint content can be reported using joint density (ξ), which is represented by the joint area over the volume of the specimen. According to Bell (2000), heavily jointed rocks have joints spaced 6 mm to 20 mm apart, hence, for a heavily jointed rock specimen in the simulation; with a narrow joint spacing of 6 mm in one plane, the joint density would be $150 \text{ m}^2/\text{m}^3$; while in two planes the corresponding joint density would be $300 \text{ m}^2/\text{m}^3$. In this study, 18 specimens of jointed rocks with the varying joint density values ranging from 0 (intact) to $240 \text{ m}^2/\text{m}^3$ were built and the unconfined compression tests were simulated (see Table 3.2). The diameter of individual joints was between 10 mm to 30 mm, and different number of joints were introduced into the test blocks to obtain the desired joint density (ξ). Some of the representative specimens with the joint density values of $10 \text{ m}^2/\text{m}^3$, $50 \text{ m}^2/\text{m}^3$, $100 \text{ m}^2/\text{m}^3$ and $200 \text{ m}^2/\text{m}^3$ are shown in Figure 3.5.

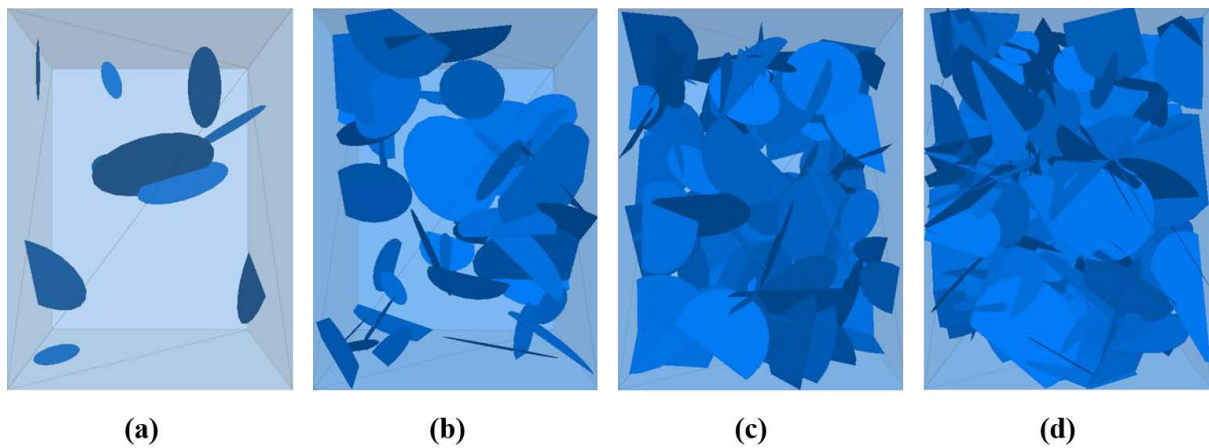


Figure 3.5. Discrete fracture network for specimen with joint density values of (a) $10 \text{ m}^2/\text{m}^3$, (b) $50 \text{ m}^2/\text{m}^3$, (c) $100 \text{ m}^2/\text{m}^3$, and (d) $200 \text{ m}^2/\text{m}^3$

3.2.3 Results and Discussions

The joint density versus variations of the rock mass unconfined compressive strength of the jointed rock masses are plotted in Figure 3.6. As expected, when more joints were introduced

into the specimen, the strength of the rock mass dropped. Referring to Figure 3.4, the most significant reduction in the rock mass unconfined compressive strength happens when $\xi < 60 \text{ m}^2/\text{m}^3$. As summarised in Table 3.2, the ratio of rock mass unconfined compressive strength of jointed rock specimens to intact rock reduced significantly up to sample No.6 (i.e. $\xi = 50 \text{ m}^2/\text{m}^3$). For example, sample No.6 experienced 78% reduction in the strength due to presence of $50 \text{ m}^2/\text{m}^3$ of joints. Beyond $60 \text{ m}^2/\text{m}^3$ joint density, the strength reduction was gradual. For example, as the joint density increased from $80 \text{ m}^2/\text{m}^3$ to $200 \text{ m}^2/\text{m}^3$, the strength reduction was about 58%. Indeed, the rock mass unconfined compressive strength of the specimen with $\xi = 200 \text{ m}^2/\text{m}^3$ was only 5.84 MPa. Referring to Figure 3.6, it can be observed that when the joint density increased beyond $210 \text{ m}^2/\text{m}^3$, the rock sample exhibited the rock mass unconfined compressive strength less than 5 MPa.

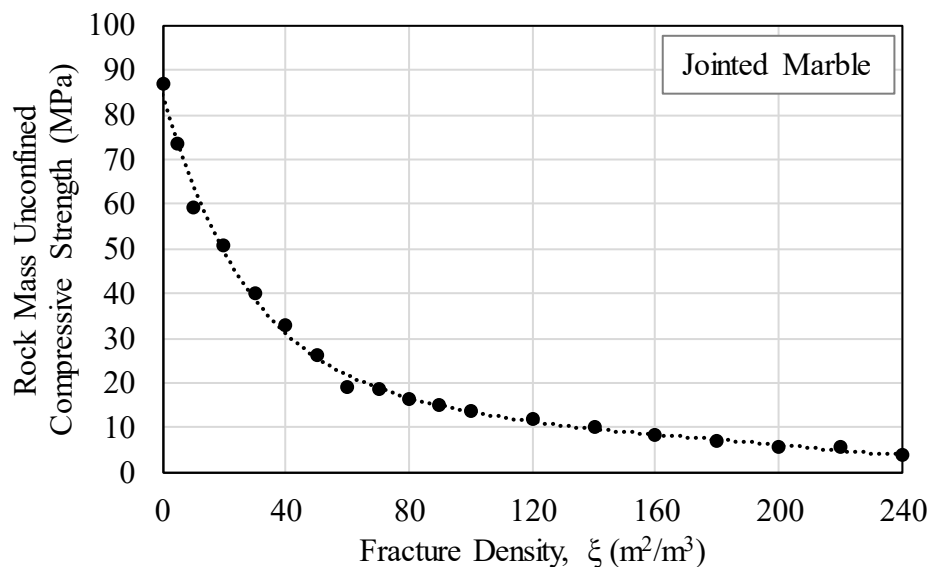


Figure 3.6. Effect of joint density on rock mass unconfined compressive strength of jointed rock specimens

Referring to Figure 3.7, the numerical results indicate that by introducing more joints, more tension cracks occur in the jointed rock specimens. In fact, the tension cracks were initially formed around the joints due to lower tensile strength of joint surfaces compared to rock grains. Hence, for low joint density values, the tension cracks mainly appeared in the intact parts of

the rock by breaking the bonds between the rock particles, while for the specimens with high joint density values, the tension cracks initiated around the joints. At the peak point, new cracks were linked to the existing joints of the rock specimens. Additionally, as could be seen in Figure 3.7 (d), when $\xi = 200 \text{ m}^2/\text{m}^3$, the joints caused some sliding failure. The failure mechanism with joint density values of $10 \text{ m}^2/\text{m}^3$, $50 \text{ m}^2/\text{m}^3$, $100 \text{ m}^2/\text{m}^3$ and $200 \text{ m}^2/\text{m}^3$ are illustrated in Figure 3.7.

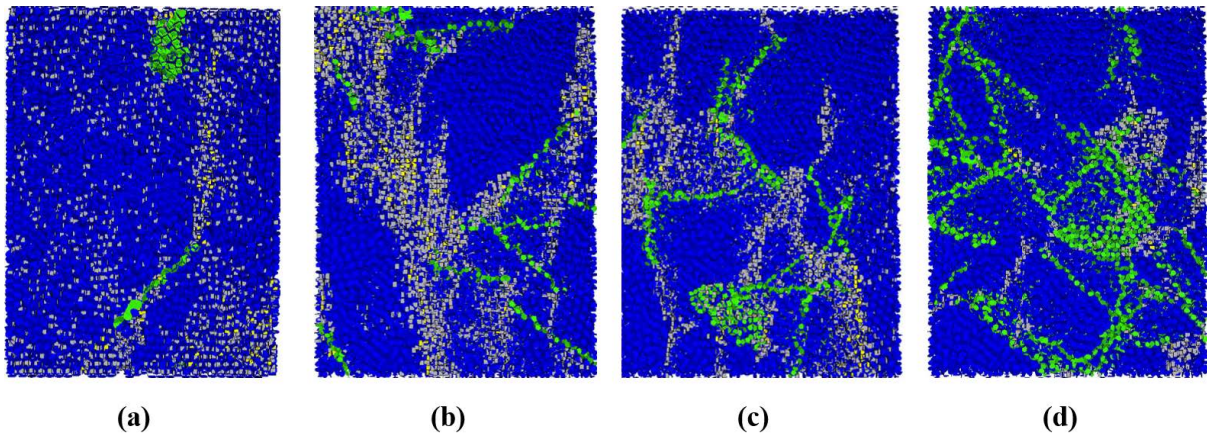


Figure 3.7. Failure mechanism for specimens with joint density values of (a) $10 \text{ m}^2/\text{m}^3$, (b) $50 \text{ m}^2/\text{m}^3$, (c) $100 \text{ m}^2/\text{m}^3$, and (d) $200 \text{ m}^2/\text{m}^3$ (green: joint; yellow: shear crack and grey: tension crack)

As plotted in Figure 3.8, Young's modulus values of the jointed specimens were considerably less than the corresponding value for the intact specimen. Comparing Figure 3.6 and Figure 3.8, the joint density had more influenced on the rock mass unconfined compressive strength than Young's modulus. For example, when $\xi = 240 \text{ m}^2/\text{m}^3$, Young's modulus reduced by 80%, while the rock mass unconfined compressive strength decreased by 96%.

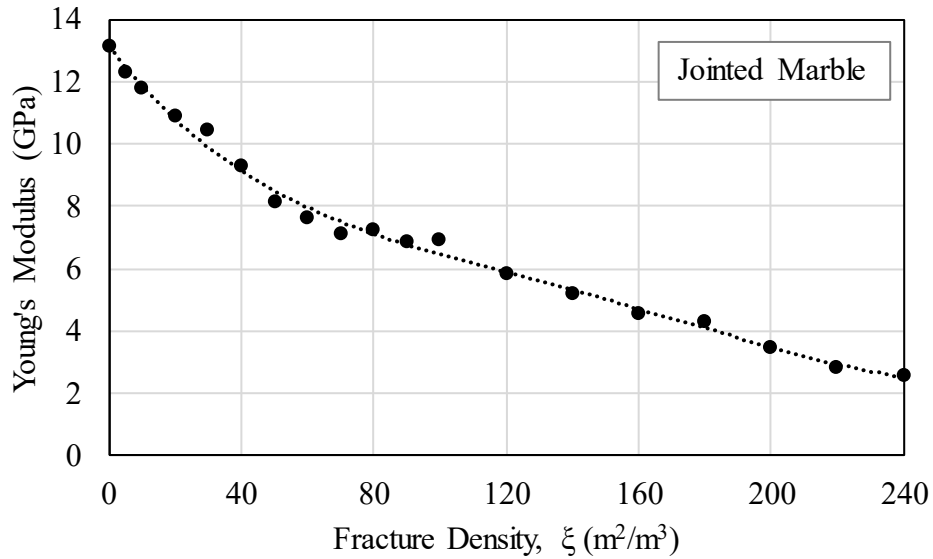


Figure 3.8. Effect of joint density on Young's modulus of jointed rock specimens

As the results shown, introducing randomly distributed joints into rock specimens using DEM would be a potential method for simulating weak rocks or cemented soils, where cementation degradation due to breaking the contact bonds can be observed from inducing the shear or tension cracks in the numerical model. Indeed a similar approach can be used to simulate behaviour of cemented soils incorporating cementation degradation due to compression, shear and tension since cementation degradation contributes to the reduction in the strength (Nguyen et al. 2014; Nguyen and Fatahi 2016; Nguyen et al. 2017). It was observed that by introducing more than $210 \text{ m}^2/\text{m}^3$ of joints in the adopted marble rock, the rock mass unconfined compressive strength dropped to less than 5 MPa (i.e. more than 94% reduction). Rock mass with unconfined compressive strength of 5 MPa could be classified as weak rock, hence, in this study, for a strong rock specimen with an unconfined compressive strength above 80 MPa, introducing randomly distributed joints could turn the rock mass unconfined compressive strength into a weak rock category.

Table 3.2. Details of tested specimens, rock mass unconfined compressive strength ratio and Young's modulus ratio of jointed rock to intact rock

Specimen No.	Joint density, ξ (m ² /m ³)	UCS_f/UCS_i	E_f/E_i
0	Intact	1	1
1	5	0.84	0.94
2	10	0.68	0.90
3	20	0.58	0.83
4	30	0.46	0.80
5	40	0.38	0.71
6	50	0.30	0.62
7	60	0.22	0.58
8	70	0.21	0.54
9	80	0.19	0.55
10	90	0.17	0.52
11	100	0.16	0.53
12	120	0.13	0.44
13	140	0.11	0.39
14	160	0.10	0.35
15	180	0.08	0.33
16	200	0.07	0.26
17	220	0.06	0.22
18	240	0.04	0.20

(Note: UCS_f and UCS_i are the rock mass unconfined compressive strength values for jointed specimens and intact specimen, respectively; E_f and E_i are the Young's modulus values for jointed specimens and intact specimen, respectively.)

3.3 Effects of Rock Joints

The existence of joints and discontinuities contributes to the complexity of investigating the mechanical behaviour of rock masses significantly (Bell 2000; Ivars et al. 2011; Bahaaddini et al. 2013; Huang et al. 2015; Wasantha et al. 2015). The joint characteristics such as the joint aperture and dip can influence the strength and deformability of rock mass to different extent (Bell 2000; Huang et al. 2015; Wasantha et al. 2015). The joint aperture largely affects the overall strength of rock mass, and can be classified into different categories based on the opening width (Bell 2000; Bahaaddini et al. 2013). The joint dip alters the failure mode and diminishes the strength of the rock mass (Bell 2000; Bahaaddini et al. 2013; Zhang and Wong 2013; Huang et al. 2015). Certain laboratory and numerical studies have investigated the effects of joint dip on the mechanical behaviour of rock mass subjected to unconfined compressive loading (Bahaaddini et al. 2013; Huang et al. 2015; Wasantha et al. 2015). In this study, the combined effects of the joint dip and aperture on the strength and deformability of weak rock specimens have been numerically investigated under triaxial confined conditions. The discrete element method based on particle mechanics has been adopted in this study, which allows explicit consideration of the discrete nature of the rock mass, replicating the natural joints, and reproducing the cementation degradation effect of cemented soils (Ivars et al. 2011; Bahaaddini et al. 2013; Chiu et al. 2013; Lambert and Coll 2014). For a controlled joint density, various joint dips and apertures have been simulated by employing the particle flow code in three-dimension (PFC3D).

3.3.1 Discrete Element Simulation

The numerical model of the intact specimen was initially calibrated with the experimental data reported for weak weathered porphyrite rock samples by Sun et al. (Sun et al. 2006). The numerical results were compared with the triaxial test measurements for a confining pressure

of 392 kPa of the weak rock specimen. In the numerical simulation, two types of contact models were adopted to replicate the mechanical behaviour of the rock mass, namely, the flat-joint model and the smooth joint contact model. The former was adopted for the simulation of the intact rock specimen, which could simulate the particle contacts using rigidly connected surfaces. These surfaces could be further discretised into 4 elements, and each element allowed sole breakage, which could result in the partial damage of the contact bonds. The later was applied to the discrete fracture network to replicate the natural joints. The discrete fracture network was introduced into the rock specimen as circular shaped plates, then the smooth joint contact model was assigned to the particles which had the contacts lied on both sides of the joints. The illustrations of the flat joint model between particles, the smooth joint contact model for joints, the joint dip (α), and the joint aperture (ω) are shown in Figure 3.9 (b).

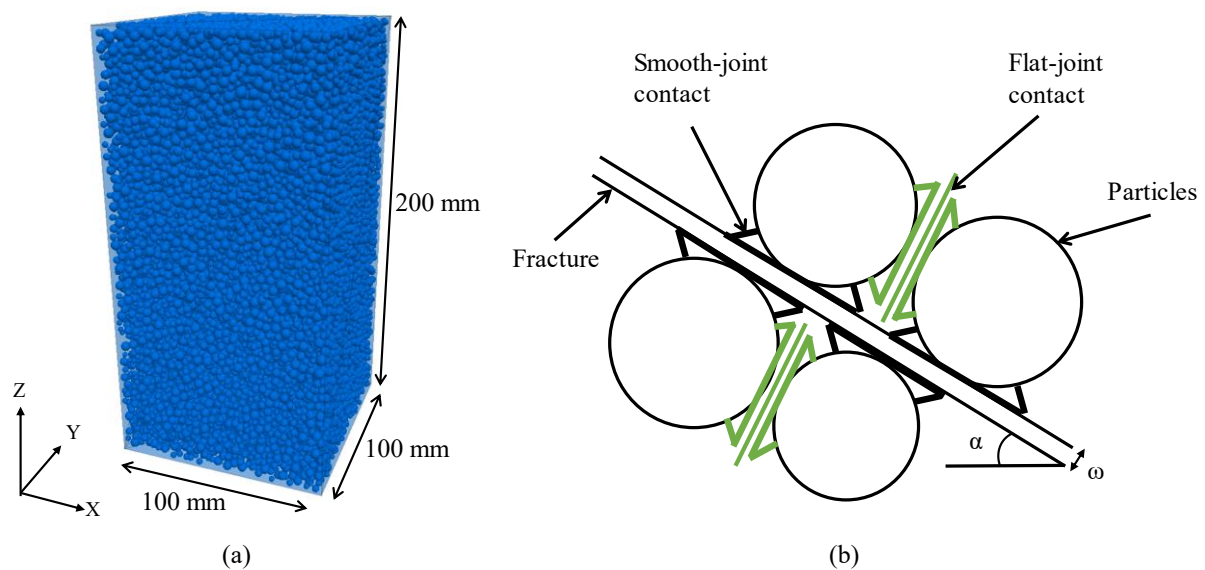


Figure 3.9. (a) Numerical model of the intact rock specimen, and (b) numerical representation of the rock grains with the flat-joint contact and the joint with the smooth-joint contact

3.3.1.1 Calibration of micro-parameters for the intact rock mass

The numerical model of the intact rock specimen is shown in Figure 3.9 (a), which has the dimensions of $100 \times 100 \times 200$ mm and contains 32,500 particles. Particles were randomly

distributed with a median diameter of 3.5 mm. Calibration of micro-parameters for the flat-joint model was carried out by simulating the triaxial test in which the specimen was loaded with the isotropic compression pressure of 392 kPa. To replicate the behaviour of the rock accurately, the void ratio of 1.25 was obtained after the confining pressure of 392 kPa was reached, which had the same value as the experimental measurements. Then the axial loading was applied on the top and bottom walls at a low speed to keep the specimen under quasi-static equilibrium. The side walls were controlled by a wall-servo mechanism to maintain the cell pressure throughout the test.

The strength and deformability of the specimen were mainly controlled by the normal and shear stiffness values of the interface at particle contacts. The shear strength was controlled by cohesion and friction angle at contacts. In order to replicate the macro-mechanical behaviour of the weathered porphyrite, numbers of trial-and-error processes were conducted until the stress-strain behaviour could be properly predicted in the numerical model. In this study, to replicate the mechanical behaviour of the weak rock, both the adopted normal stiffness and shear stiffness at contacts were 0.7 GPa/m, and the adopted cohesion, tensile strength and friction coefficient at contacts were 50 MPa, 10 MPa and 0.5, respectively. As shown in Figure 3.10, the numerical prediction of the strength and deformability of the intact rock specimen had a good agreement with the experimental results with the adopted micro-parameters.

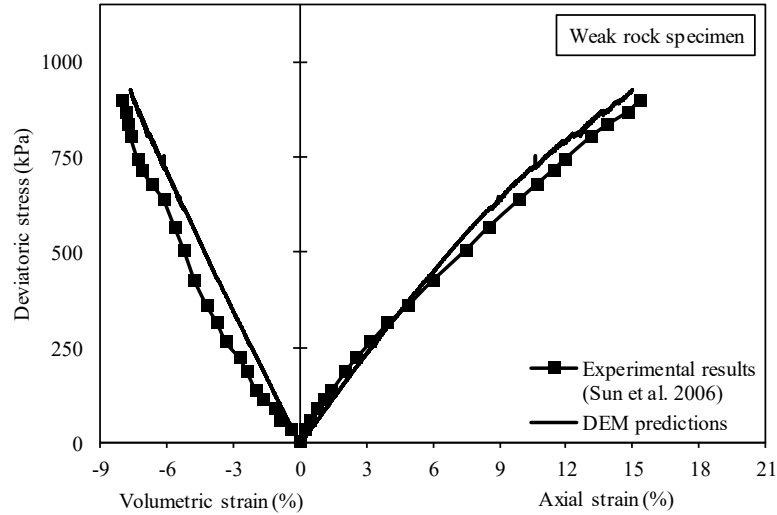


Figure 3.10. The stress-strain curve of experimental measurements and model predictions of the intact rock specimen for confining pressure of 392 kPa

3.3.1.2 Modelling of jointed rock mass

The discrete fracture network and smooth joint contact model were adopted for simulating the rock joints. Similar to previous research works (Bahaaddini et al. 2013; Huang et al. 2015), reduced contact normal stiffness and shear stiffness were adopted to simulate the joints since the strength of the joints should be weaker than the intact grain assembly. Joints were randomly distributed into the system with dips (α) of 0, 30, 45, 60, and 90 degrees to the loading direction of the cell pressure, as illustrated in Figure 3.11. A controlled joint density $\xi = 7 \text{ m}^2/\text{m}^3$ (known as the joint area over the volume of the specimen) was adopted to study the effects of joint apertures and dips on the mechanical behaviour of the weak rock specimens. The joint aperture was simulated by controlling the contact gap of the smooth joint contact model. Indeed, by introducing a particular joint aperture (ω), the two sides of joint would not contact and exchange forces unless the gap was closed during the analysis. The adopted joint aperture (ω) values in this paper were 0, 1, and 4 mm, which corresponded to very tight, open, and moderately wide joint opening, respectively (Bell 2000). The joint characteristics of the tested joint specimens are summarized in Table 3.3. In order to analyse the effects of these two joint

characteristics (i.e. dip and aperture), the jointed specimens were subjected to the same isotropic compression pressure as the intact specimen reported in the calibration exercise.

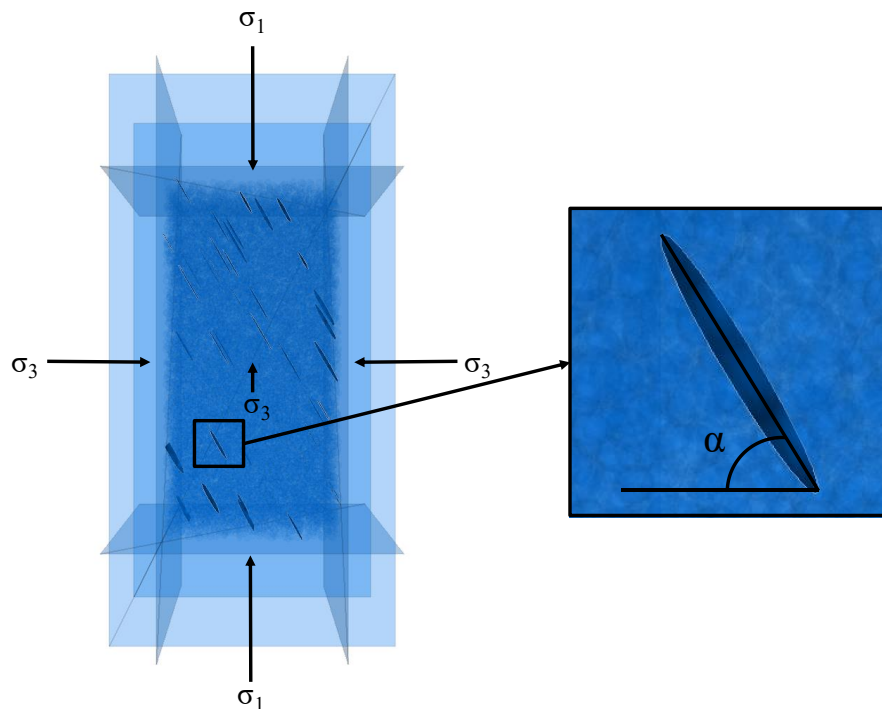


Figure 3.11. Representative of jointed rock specimen with the joint dip (α) to the direction of cell pressure

Table 3.3. The joint apertures and dips investigated in the study

Joint aperture description	Width of aperture, ω (mm)	Joint dip, α (degrees)
Very tight	0	0, 30, 45, 60, 90
Open	1	0, 30, 45, 60, 90
Moderately wide	4	0, 30, 45, 60, 90

3.3.2 Effects of Joint Dip on the Mechanical Properties of Jointed Rock

As expected, the joint dip influences the strength of the jointed specimen as shown in Figure 3.12. It is noted that the lowest value for the ratio of deviatoric stress at 15% axial strain of the jointed rock specimen to the corresponding value for the intact rock specimen, namely the normalised deviatoric strength, was encountered when joint dip $\alpha = 45^\circ$ was adopted. With the same joint aperture width, when $\alpha = 45^\circ$, the particle assembly was more likely to slide on the joint plane compared to other joint dips. Similar to Bahaaddini et al. (2013) and Huang et al. (2015), for these steeper joint planes (i.e. $\alpha = 45^\circ$ and 60°), the sliding on the joint plane was more obvious. The joint plane was weaker than the intact grain assembly, hence, with the failure in the intact material, the sliding effect would result in further reduction in the strength. However, when $\alpha = 90^\circ$, the existence of joints had the least effect on the reduction of strength. In this case, since the joint dip was parallel to the axial loading direction, the joints and the slip surfaces between grains were not aligned. Comparing to the intact specimen, the most reduction in normalised deviatoric strength at 15% axial strain was encountered in the specimen with 45° moderately open joint (i.e. $\alpha = 45^\circ$ and $\omega = 4$ mm).

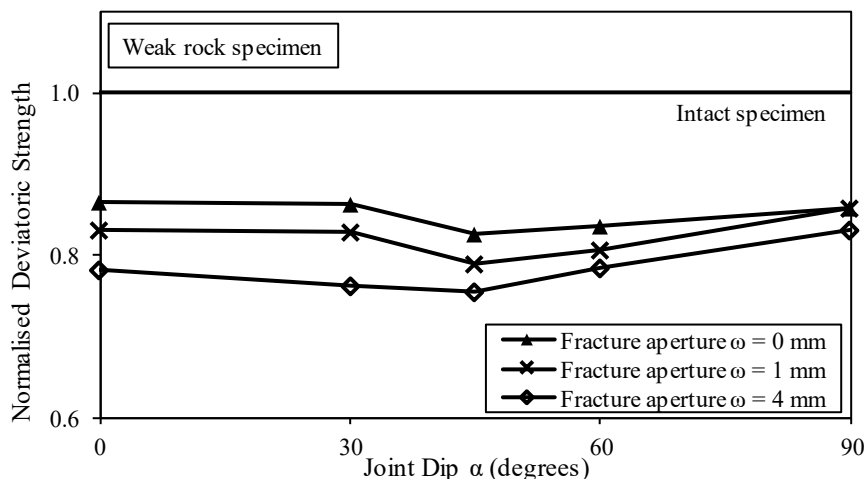


Figure 3.12. Normalised deviatoric strength at 15% axial strain of jointed specimen for different joint dips and apertures

The deformability of the jointed specimens was varied for different joint dips. Since the joints did not dilate in this study (i.e. dilation angle = 0), no volume change during shearing of joints were expected. Therefore, as shown in Figure 3.13, the jointed specimens had less volume change compared to the intact specimen. It is noted that for a given joint aperture, for the specimens with $\alpha = 45^\circ$ and 60° , the volumetric strains of specimens with $\alpha = 45^\circ$ and 60° were less than the corresponding values for the specimens with $\alpha = 0^\circ$ and 30° . Furthermore, as the joint has been distributed randomly, the effect of random distribution with different distribution methods on the stress-strain behaviour of jointed rock can be studied further in future.

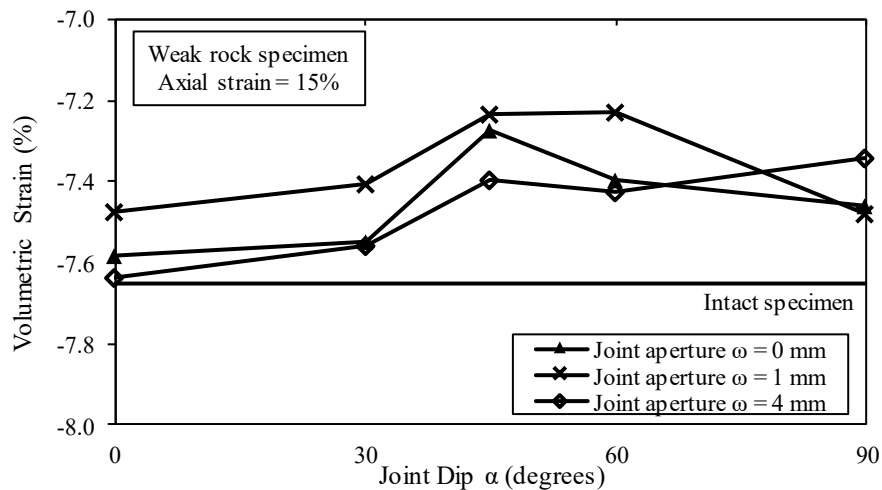


Figure 3.13. Volumetric strain at 15% axial strain of jointed specimens with different joint dips and apertures

3.3.3 Effects of Joint Aperture on the Mechanical Properties of Jointed Rock

As plotted in Figure 3.14, for the joint dip $\alpha = 30^\circ$, the strength of the jointed rock specimens decreased with increasing joint aperture. The specimen with moderately wide joint aperture (i.e. $\omega = 4$ mm) had a 12% further reduction in strength, comparing to the specimen with very tight joint aperture (i.e. $\omega = 0$). It is noticed that the specimens with larger joint apertures experienced more deformation under the same deviatoric stress.

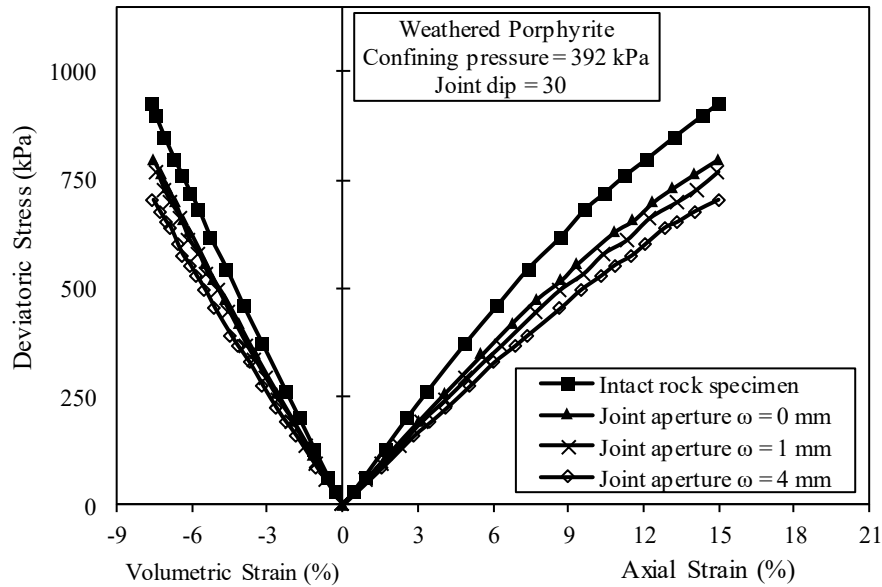


Figure 3.14. Comparisons of the intact specimen and jointed specimens with different joint apertures for the given joint dip of 30°

Referring to Figure 3.12, the extent in which joint aperture contribute the reduction in the strength of the rock specimens depends on the dips of the joints. With different joint apertures, the changes in strength were the least for the specimens with $\alpha = 90^\circ$. In contrast, the most alteration was encountered for the joint dip of 30°. When $\alpha = 90^\circ$, the joint aperture could close during the isotropic compression loading, while this phenomenon would readily evident for inclined joints. Therefore, the effects of the joint aperture were minimal for the specimens with joint dip of 90°. Referring to Figure 3.14, for a given deviatoric stress, samples with wider aperture experienced larger axial strains. This can be attributed to the fact that more shear forces would be mobilized in the intact parts of the specimen inducing more axial displacement.

As expected, at a given deviatoric stress (e.g. 600 kPa), the jointed specimens had higher volumetric strains (attributed to larger axial displacement of dilative material) comparing to the intact rock specimen, as illustrated in Figure 3.15. As the studied weak rock specimen had a high void ratio of 1.25, the specimens only experienced contraction during shearing. As

increases the joint aperture, more volume contraction was observed for joint dip of 0° , 30° , 45° and 60° , while for $\alpha = 90^\circ$, the effect of joint apertures on volume change was insignificant. Moreover, as the effect of apertures on permeability has not been considered in this paper, hence, further study inspired by the effects of excess pore water pressure can be studied in future (Le et al. 2016; Le et al. 2017).

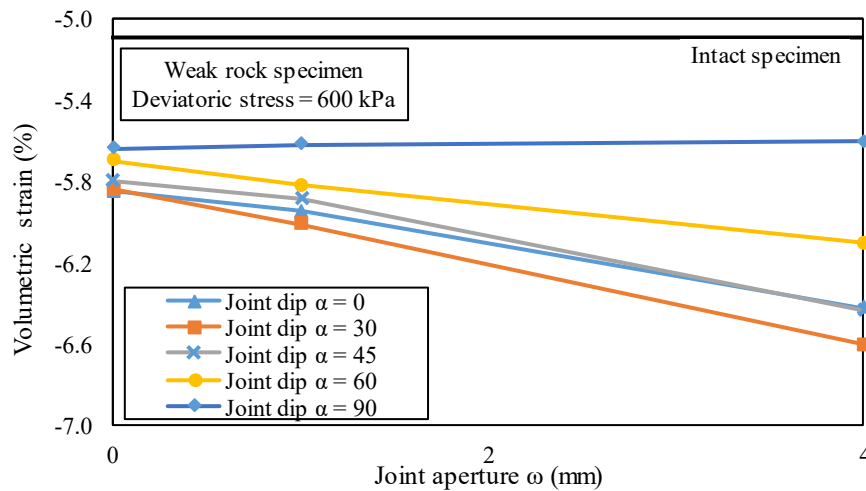


Figure 3.15. Volumetric strain of different joint apertures for jointed rock specimens

3.4 Effects of Joint Length

Weak rocks have complex characteristics including low shear strength, often being jointed and weathered with significant deterioration. These aspects contribute to the complexity of understanding the behaviour of weak rocks, especially for the tunnel and deep foundation designs in which difficult ground conditions are often encountered (Goodman and Ahlgren 2000; Klein 2001; Nickmann et al. 2006; Santi 2006). Many studies have been conducted on classifying and investigating the behaviour of weak rocks through the field, laboratory and numerical approaches (Goodman and Ahlgren 2000; Nickmann et al. 2006; Santi 2006; Sun et al. 2006). Certain laboratory tests have been conducted on artificial weak rocks, namely the mixture of cement and soils, and the mechanical behaviour of cemented soils has been investigated deeply (Fatahi et al. 2012; Fatahi et al. 2013; Nguyen and Fatahi 2016). The effect

of characteristics of joints in terms of the pattern, dip, spacing, size, distribution, roughness, and aperture on various rock types have also been studied by many researchers (Tsoutrelis and Exadaktylos 1993; Prudencio and Jan 2007; Bahaaddini et al. 2013; Chiu et al. 2013). According to Klein (2001) and Santi (2006), discontinuities tend to contribute significantly to the weakness and deformability of rock masses. However, for a given joint density, the effects of the individual joint length on the weak rock mass is not understood well.

The discrete element method (DEM) based on particle mechanics has several advantages to investigate the effects of individual joint length on the strength and deformability of weak rock. DEM allows for the explicit consideration of the heterogeneity and localized microscopic-mechanical properties of the rock mass and replicating the natural joints (Potyondy and Cundall 2004; Bahaaddini et al. 2013; Chiu et al. 2013). The bonded particle model, which is embedded in the discrete element method, can replicate the processes of breaking the contact bonds for rocks, and the cementation degradation of cemented soils (Fatahi et al. 2013; Nguyen et al. 2016; Potyondy and Cundall 2004). In this paper, the rock mass has been simulated by adopting discrete element method to investigate the alteration of stress-strain behaviour due to the variation in the individual joint length for a given joint density in the rock sample.

3.4.1 Numerical Modeling

The numerical model was initially calibrated using the triaxial test results on a weak rock sample reported by Sun et al. (2006) for a confining pressure of 392 kPa. The weak rock in the study was described as weathered porphyrite obtained from a dam site in Hyogo Prefecture in Japan. The void ratio and specific gravity of this specimen were reported as 1.25 and 2.74, respectively.

3.4.1.1 Numerical Model Components

As recommended by Potyondy and Cundall (2004), to pull particles together to create an initial sample, first, a loose assembly of particles was generated randomly with the specified diameter adopting frictionless walls. The system was adjusted by allowing the particles to move considering no friction. Then, a nominal low isotropic stress was applied on the assembly of particles to reduce the magnitude of locked-in stresses. Finally, floating particles which had less than three contacts were eliminated, and then bonded particle model (BPM) was assigned as the contact model between particles. The rock specimen had a size of $100 \times 100 \times 200$ mm. The median diameter of the particles adopted in the numerical model was 3.5 mm, while the ratio of maximum diameter to minimum diameter (d_{max}/d_{min}) was 2 with a uniform distribution, similar to those reported in the literature for investigating the behaviour of rock mass through discrete element method (e.g. Potyondy and Cundall 2004; Ding et al. 2014). A ratio of the smallest characteristic model length (i.e. the width of the specimen in this test) to median particle diameter (L/d_{50}) greater than 25 was suggested for the DEM simulation to obtain mechanical properties within a 2% variation level for rock modeling (Ding et al. 2014). In this study, L/d_{50} ratio of 27 was adopted to ensure the behaviour of rock mass is properly replicated. An illustration of the numerical model of intact rock specimen with the frictionless walls is shown in Figure 3.16 (a).

The flat-joint model (FJM) was adopted to simulate the particle contacts in the intact rock specimen. The FJM has several capabilities and advantages for simulating the behaviour of rock mass compared with the traditional linear parallel bond model. Figure 3.16 (b) displays the contact force chain between particles. The flat-joint model allows partial breakage of the particle bonds as the contact between grains are discretized into several elements, and each element can be bonded or unbounded with friction. Comparing to the linear parallel bond model

with a constant shear strength, the particle assembly bonded by the FJM follows the Coulomb criterion, which is controlled by cohesion, friction angle and normal stress.

The smooth-joint contact model originally proposed by Pierce et al. (2007), can be assigned to the discrete fracture network (DFN) to replicate the characteristics of joints in the rock mass. The discrete fracture network can be inserted with defined dip, size, and position, and then the SJM can be assigned to contacts between particles. At the joint contacts, the initial bonds are removed and smooth joints are defined in a direction parallel to the joint plane. The illustration of the SJM and DFN in the jointed rock model used in this study is shown in Figure 3.16 (c).

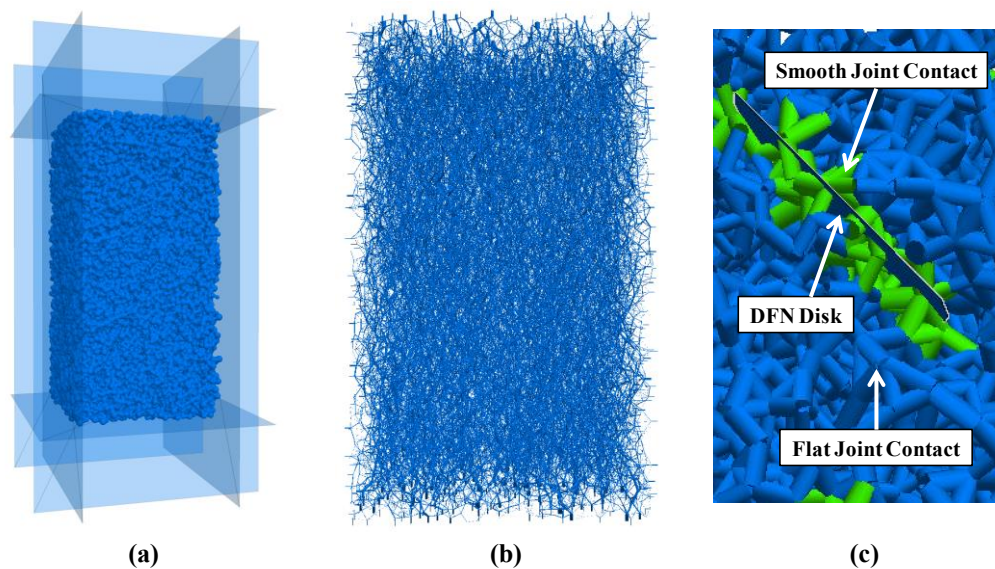


Figure 3.16. (a) Numerical model of intact rock specimen under triaxial test with six rigid walls; (b) Contact force chain for intact rock specimen (line thickness and dip represent force magnitude and direction, respectively), and (c) The smooth-joint contact model for simulating joints

3.4.1.2 Model Calibration for Intact Rock Specimen

The sample porosity has great influence on the behaviour of the rock mass in the DEM simulations (Zhang et al. 2014). The natural rock mass of the weak rock adopted in this study

had a uniform porosity of 0.56 subjected to a confining pressure of 392 kPa (Sun et al. 2006). Therefore, in order to replicate the behaviour of the rock specimen, it was ensured that the numerical specimen had a porosity within 1% variation of the natural rock mass porosity after the isotropic compression loading. Then, a strain controlled loading was assigned to the specimen in the vertical direction similar to the loading done in the laboratory. The side walls were controlled by a wall-servo mechanism to maintain the cell pressure of 392 kPa throughout the test.

As the particle contacts in the numerical model were simulated using the flat-joint model adopting springs to transfer forces between particles, the strength of the specimen was controlled by the normal stiffness at each particle contact and the normal-to-shear stiffness ratio (k_n/k_s). The shear strength of the rock specimen was controlled by the cohesion (c_c) and friction coefficient (μ_c) between contacting particles. It should be noted that the Poisson's ratio of the specimen is mainly affected by the value of k_n/k_s . Through the trial and error procedures following the recommendation by Ding et al. (2014) and Potyondy and Cundall (2004), a number of numerical simulations of the rock specimen were conducted until the macro-properties could be properly reproduced. The micro-mechanical model parameters were calibrated resulting in a good agreement between the DEM prediction and laboratory measurements as observed in Figures 3.17 and 3.18. The calibrated micro-mechanical parameters are summarised in Table 3.4.

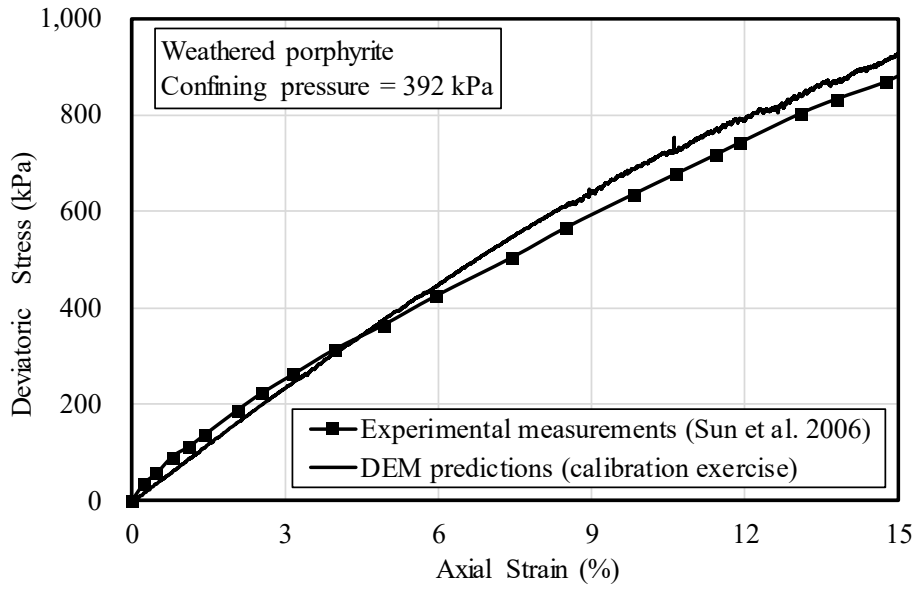


Figure 3.17. Stress-strain curve of the intact rock specimen calibration exercise

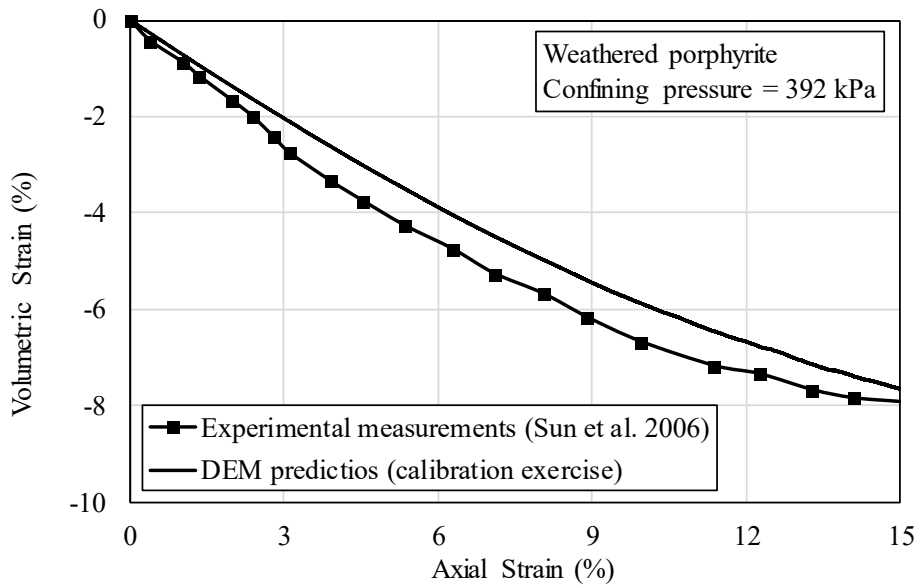


Figure 3.18. Volumetric strain variations of the intact rock specimen during shearing - calibration exercise

Table 3.4. Summary of calibrated flat-joint parameters for the intact weak rock specimen

Parameter	Description	Value
d_{50}	Median grain diameter	3.5 mm
d_{max}/d_{min}	Ratio of maximum to minimum grain diameter	2
k_n	Contact normal stiffness	700 MPa/m
k_n/k_s	Normal-to-shear stiffness ratio of contacts	1.0
σ_c	Contact tensile strength	10 MPa
c_c	Contact cohesion	50 MPa
μ_c	Contact friction coefficient	0.5

Table 3.5. Summary of smooth-joint parameters for joints

Parameter	Description	Value
k_{ns}	Contact normal stiffness	400 MPa/m
k_{ss}	Contact shear stiffness	100 MPa/m
μ_{cs}	Contact friction coefficient	0.7

3.4.1.3 Jointed Rock Simulation

For a controlled joint density (ξ), which is defined as the joint area over the volume of the specimen, various individual joint lengths (η) were adopted to analyze the effects of the individual joint length on the behaviour of the weak rock specimens. A controlled joint density of $\xi = 7 \text{ m}^2/\text{m}^3$ was selected in this study. A joint dip of 45 degrees was adopted since it could

have great influence on the rock strength and deformability referring to Prudencio and Jan (2007) and Yang et al. (2008). The individual joint lengths varying from 2.8 mm to 140 mm, adopted in this study are summarised in Table 3.6. It should be noted that the tested specimens with shorter individual joint length had plenty of small joints distributed randomly over the rock mass, while for the individual joint length of 140 mm, only one joint was present in the specimen as illustrated in Figure 3.19.

Table 3.6. Different joint configurations used in the simulation of jointed rock sample

Specimen No.	Individual joint length (η, mm)	Normalised joint length (η/L)	Joint density (ξ, m²/m³)	Confining pressure (kPa)
0	Intact	N/A	N/A	
1	2.8	0.028		
2	5.6	0.056		
3	11.2	0.112	7	392
4	28	0.28		
5	84	0.84		
6	140	1.4		

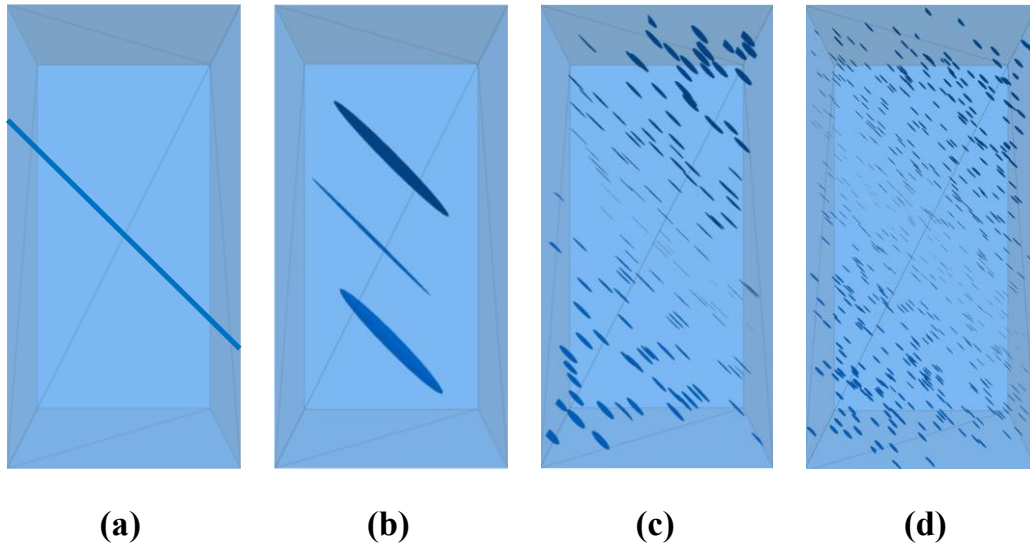


Figure 3.19. Discrete fracture network for the rock specimen with individual joint length of (a) 140 mm, (b) 84 mm, (c) 11.2 mm, and (d) 5.6 mm, (Note: the joint density remains constant $\xi = 7 \text{ m}^2/\text{m}^3$)

3.4.2 Results and discussions

The effects of the individual joint length on the stress-strain behaviour and volume change characteristics of the jointed rock specimen are plotted in Figures 3.20 and 3.21, respectively. Comparing Figures 3.17 and 3.19, the pre-existing joints contributed to a significant reduction in the strength and stiffness of the rock mass. As reported in Figure 3.20, for a given joint density (i.e. $\xi = 7 \text{ m}^2/\text{m}^3$), the reduction in strength varied with the individual joint length. It is noticed that plenty of non-persistent joints with a short length (i.e. η/L less than 0.28) distributed over the specimen resulted in lower strength compared with the continual longer joints. As expected, this observation is in a good agreement with Griffith's criterion (Bieniawski 1967), since new fissures are formed at the tip of the pre-existing non-persistent joints when subjected to loading, generating a further reduction in the strength of the rock mass. However, as shown in Figure 3.22, when the ratio of joint length to the specimen width (i.e. the normalised joint length, η/L) is greater than 0.28, the predicted strength remains unchanged.

Indeed, for a given joint density, the smaller the individual joint length, the lower the strength and stiffness of the rock mass.

As plotted in Figures 3.18 and 3.21, the volumetric strains were less for the jointed rock specimens in comparison to corresponding values for the intact specimen. In this study, it has been assumed that joints do not dilate (i.e. dilation angle = 0), hence, no volume change during shearing of joints was expected. Therefore, as more joints were introduced, the volume changes of the sample under applied shear loads decreased. Thus, as observed in Figure 3.21, for a given joint density (i.e. $\xi = 7 \text{ m}^2/\text{m}^3$), shorter but more abundant joints could lead to further joints during loading, resulting in less volume change of this contractive weak rock.

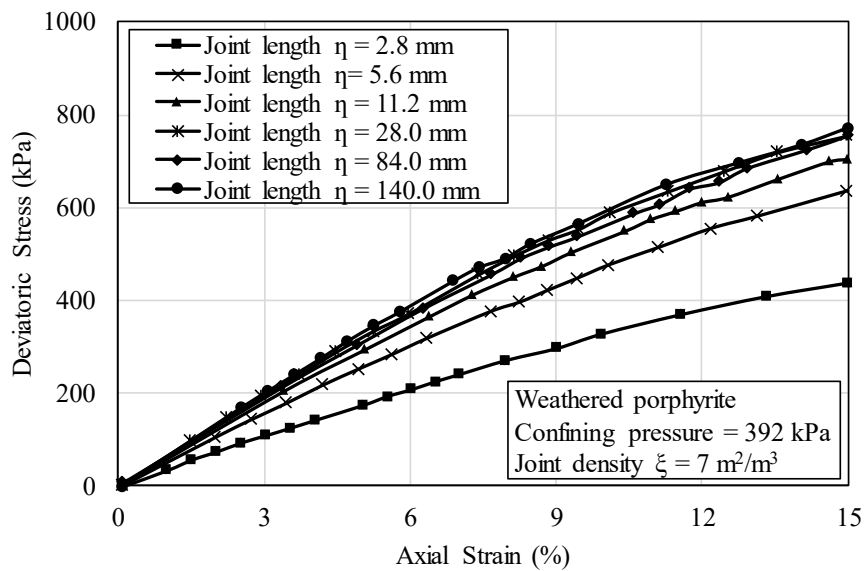


Figure 3.20. Predicted stress-strain curves of jointed specimens with different individual joint length

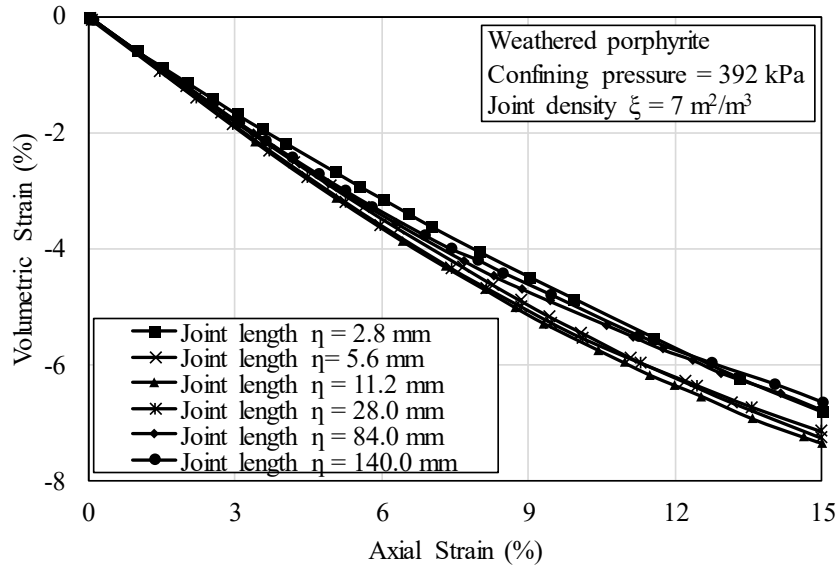


Figure 3.21. Volumetric strain of jointed specimens with different individual joint length

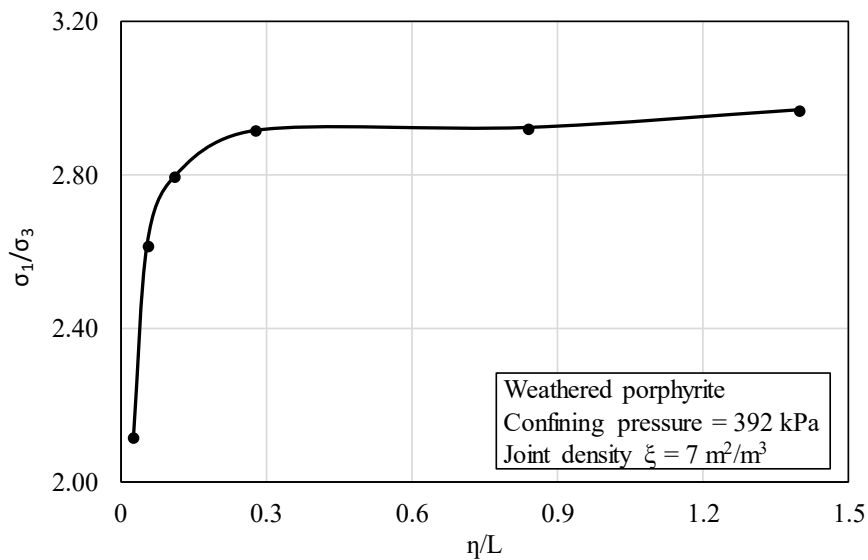


Figure 3.22. Applied axial stress to cell pressure ratio (σ_1/σ_3) versus the ratio of individual joint length to the specimen width (η/L) at 15% axial strain

Indeed, wing joints, which were connected to the tips of two neighboring joints, tended to form easier when more abundant and therefore more closely spaced joints (i.e. shorter joints) were present. In addition, the total number of joint tips were higher for the case of shorter but more abundant joints, leading to further growth of wing joints.

As shown in Figure 3.23, at the same shear stress level, it is noticed that the specimens with shorter individual joints (i.e. $\eta < 28$ mm) have experienced more significant volume contraction. As the weak intact rock adopted in this study had a high void ratio (i.e. $e = 1.25$), notable volume contraction had been observed during the shearing. Referring to Figures 3.20 and 3.23, for a given deviatoric stress level, samples with shorter but more abundant joints experienced larger shear strains, and therefore increased volume contraction. Referring to Figure 3.23, for a given deviatoric stress (e.g. 400 or 500 kPa), the sample volume contraction was very sensitive to the normalised joint length when $\eta/L < 0.112$, while for $\eta/L > 0.28$ the volume contraction prediction was almost insensitive to η/L ratio.

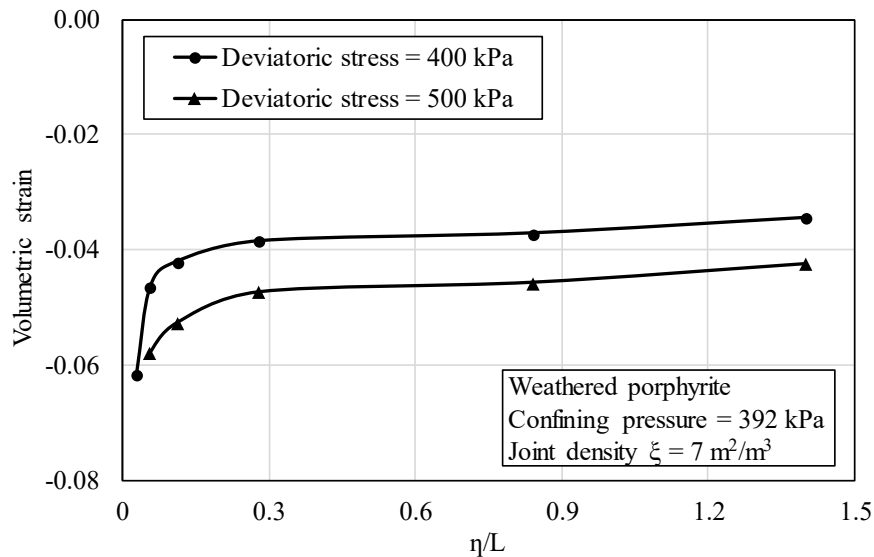


Figure 3.23. Volumetric strain versus normalised joint length for jointed rock specimens

Figure 3.24 illustrates the grain displacement in the jointed specimens. It is noticed that for the individual joint length of $\eta = 140$ mm or 84 mm, the grains were mainly moving on the joint planes, while this trend became less apparent for shorter individual joints since new tension joints were formed around the pre-existing joints.

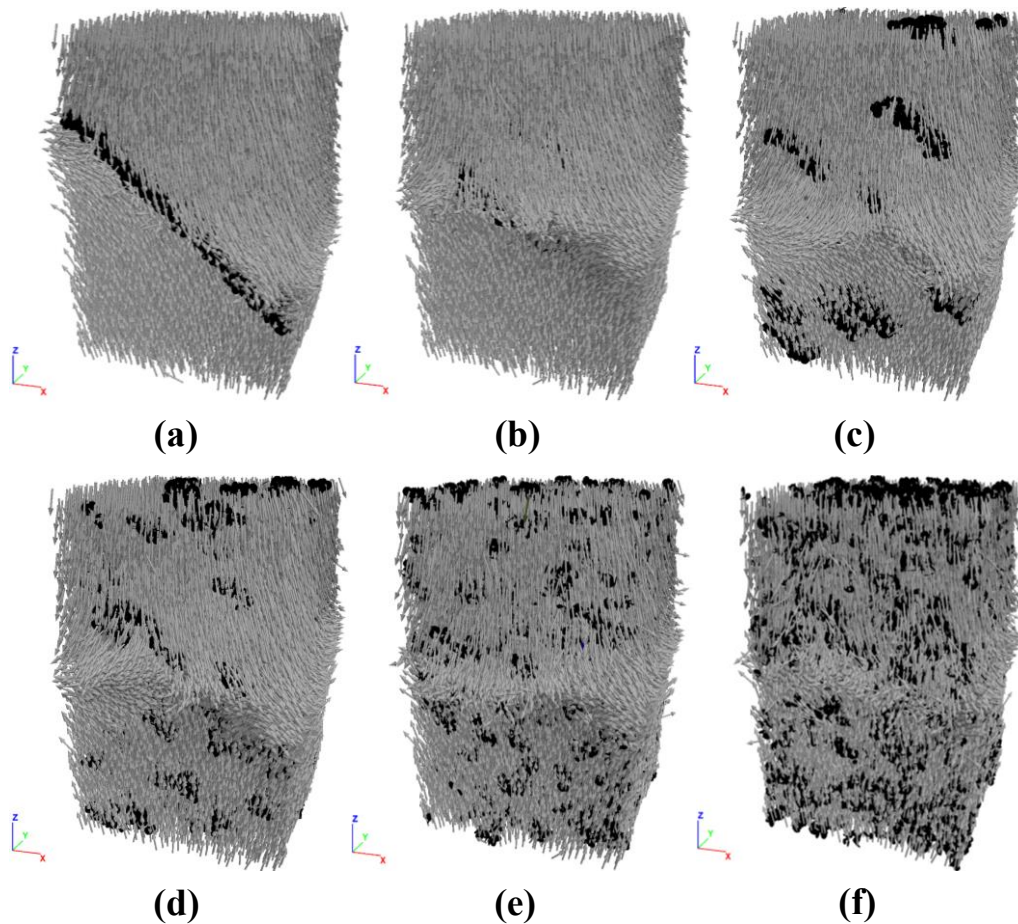


Figure 3.24. Particle displacement representation for jointed specimens at the axial strain of 15 % with normalised joint length (η/L) of (a) 1.4, (b) 0.84, (c) 0.28, (d) 0.112, (e) 0.056, and (f) 0.028 (grey: particle displacement and black: smooth-joint model contacts for joints)

3.5 Summary

Discrete element method (DEM) was used to investigate the effects of joint density on the mechanical properties of jointed rock mass. The contact properties were calibrated against the unconfined compressive test results available for an intact marble rock sample. Then, 18 samples with joint density values varying from 0 to $240 \text{ m}^2/\text{m}^3$ were simulated by introducing randomly distributed joints. The numerical results indicated that the joint density can influence the rock mass unconfined compressive strength and the Young's modulus of the rock mass significantly. In addition, by introducing more joints, the failure mechanism of the rock mass

can change from shear failure to tension failure. Furthermore, this method of replicating weak rocks have great potential of investigating further problems, such as analysing the axial compression load of pile foundation in weak rock, which can be used for predicting and studying the end bearing capacity and shaft resistance during the driving process.

Then, the effects of joint aperture and dip on the strength and deformability of weak rock specimens were investigated numerically using discrete element method. Two contact models have been adopted, namely the flat-joint model and smooth-joint contact model, to simulate the cementation effects of the rock mass and sliding effects of joints, respectively. For a given joint density, comparisons on the strength and deformability of rock specimens have been conducted through triaxial tests on 15 series of tests with joint apertures of 0, 1 and 4 mm, and joint dips of 0, 30, 45, 60 and 90 degrees. It can be summarised that:

1. The joint aperture could diminish the strength of the weak rock specimen; as the joint aperture increased, the strength of the jointed specimens reduced.
2. The extent in which joint aperture alters the strength and deformability of rock specimens depends on the dip of the joints.
3. It is noticed that with the joint dip parallel to the axial loading direction, the diminishing effects of joint aperture on the weak rock strength was minimal.
4. In contrast, the joint apertures influenced the strength and deformability of the rock specimen with inclined joints.

For a given joint density, the effects of the individual joint length on the strength and deformability of rock mass has been investigated using the discrete element method. The flat-joint model has been adopted and calibrated to replicate the micro-parameters of the intact weak rock, while the smooth-joint contact model has been used to simulate the joints. The stiffness and strength of jointed weak rock specimens were analysed through triaxial tests with same confining pressure as the one used for calibration. The individual joint length varied from

one long single joint to plenty of non-persistent short joints. For a given joint density of $\xi = 7 \text{ m}^2/\text{m}^3$, the shorter individual joints resulted in more reduction in strength and stiffness of weak rock. When the joint length to specimen width ratio $\eta/L > 0.28$, the effects of the individual joint length were insignificant. This study sheds light on the understanding of the mechanical behaviour of jointed weak rock with different individual joint lengths.

Chapter 4 - Assessment of the Internal Shaft Friction

4.1 General

This study focuses on the internal shaft friction of open-ended tubular piles induced by jointed weak rock plugs. To investigate the bearing mechanism of the plug, push-up load tests were carried out on the jointed mudstone inside a tubular pile. The discrete element method (DEM) was used in order to consider heterogeneity and to reproduce the discrete nature of the rock mass. A flat-joint model was used to reproduce the mechanical behaviour of mudstone and a smooth-joint contact model was used to replicate natural joints. The push-up load tests were carried out by utilising the calibrated properties of a weak mudstone. The effects of joint density and joint dip were examined in detail, and as expected, the push-up force of the rock plug was influenced by the joint properties because joint density and joint dip had to some extent, affected the plug resistance. The existing joints reduced the push-up force when the joints were steep, whereas the horizontal joints had a minimal effect on altering the inner shaft friction compared to the intact rock mass. The reduced friction along the pile was amplified with joint density, while the exponential increase of vertical stress from the top of the rock plug to the bottom revealed that the inner shaft resistance was mainly mobilised at the bottom portion of the rock plug. The findings of this study increase our understanding of joint dip and joint density affecting the internal shaft resistance of open-ended tubular piles; this knowledge can be used by practicing engineers while designing tubular piles in weak rock.

4.2 Background

Open-ended tubular piles are commonly used for offshore and bridge support foundations, which have the advantage of penetrating weak rock layer to reach virtual refusal on a hard unweathered stratum (Lin et al. 2014; Poon et al. 2017; Zhang 2017). There are many projects in Australia that tubular piles have been used, and some of them have penetrated into weak

rock. For example, the floodplain section of the bridge over Macleay River in New South Wales (NSW) was built on 750 mm and 825 mm tubular steel piled footings driven into alluvial sediment and weak rock (Zhang et al. 2013), meanwhile many other bridges on the Pacific Highway upgrade projects in NSW also adopted steel tubular piles. Those projects where tubular piles were driven into low strength siltstone and sandstone included an overflow bridge near Iluka and a twin bridge near Woodburn; the piles were 1,050 mm and 900 mm in diameter, respectively (Zhang 2017). The application and installation of steel tubular piles for one of the Pacific Highway upgrade project in east coast of Australia is illustrated in Figures 4.1 (a) and (b). Some bridge and offshore projects in Western Australia also utilised tubular piles. For instance in the Swan River Pedestrian Bridge, 74 tubular piles of 730 mm in diameter were used, while in the Barrow Island Load-Out Jetty, 654 tonnes tubular piles of 1,219 mm in diameter were applied (Engineering Heritage Western Australia 2014).

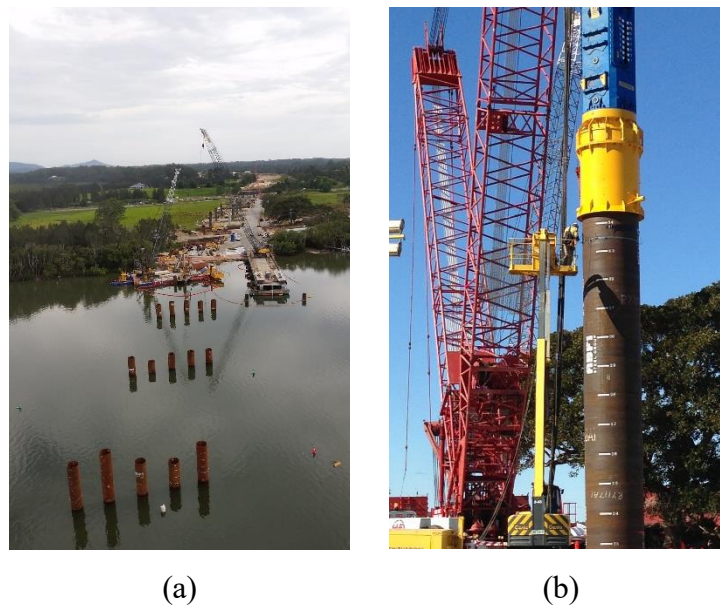


Figure 4.1. (a) Application of steel tubular piles for bridge foundation; and (b) installation technique for the tubular piles, for Pacific Highway Upgrade project in east coast of Australia

When open-ended tubular piles are first driven into soil and weak rock, the ground material enters the pile, but as the pile penetrates deeper it may fill the pile or the interior soil column may move down with the pile due to the internal shaft friction. The former is known as unplugged pile behaviour, while the latter is referred to the plugged pile response. If the interior column moves at the same rate as the pile, this condition is known as a fully plugged pile. However, the soil plug usually moves relative to the pile so that any increase in the height of the soil plug is just some fraction of the increase in depth to which the pile penetrates; this results in a partially plugged pile (Thongmuneet al. 2011; Ko and Jeong 2014). As Figure 4.2 shows, the bearing components of an open-ended tubular pile include the outer shaft resistance (Q_{outer}), the toe capacity of the annular pile base ($Q_{annular}$), and the soil plug capacity (Q_{plug}). The capacity of the soil plug is either the potential inner shaft capacity (Q_{inner}) or the bearing capacity of the soil beneath the plug base (Q_{bottom}), whichever is smaller (Matsumoto et al. 2007; Thongmuneet al. 2011; Kumara et al. 2016). Referring to Figure 4.2, the potential inner shaft capacity comes from the internal shear stress on the pile wall (τ_{in}) (Randolph et al. 1991; Lehane and Randolph 2002).

The factors affecting plugging behaviour are the relative density of the sand, the internal diameter of the pile, and the pile embedment, all of which are directly related to the capacity of the plug, as reported by many researchers (De Nicola and Randolph 1997; Yu and Yang 2011, 2012; Kumara et al. 2016). Even though design recommendations appreciate the impact of plug formation on the pile capacity, only the design method developed by Jardine et al. (2005) in both sand and clay includes the effects of lateral stresses on shaft friction (Tomlinson and Woodward 2008).

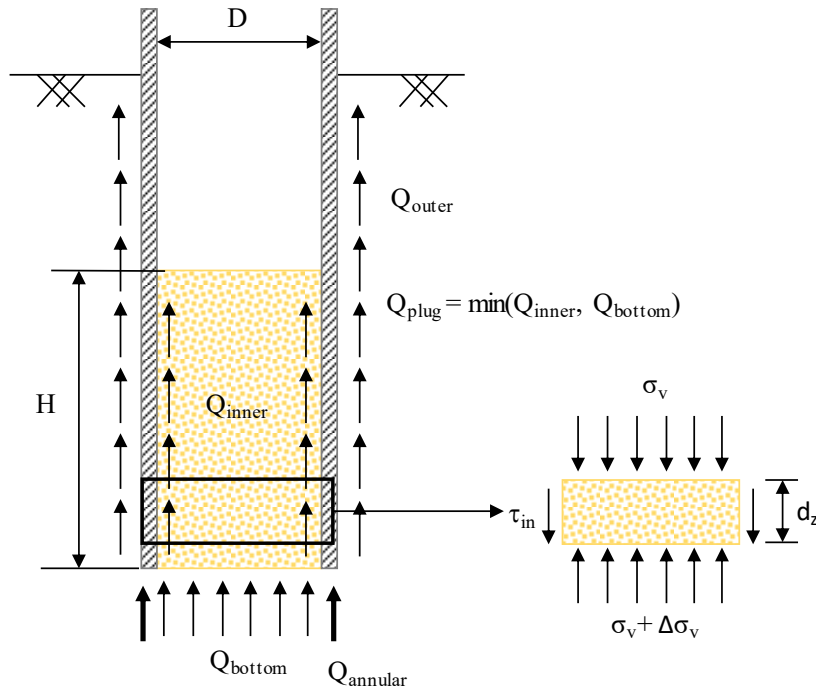


Figure 4.2. Components of bearing-capacity of an open-ended tubular pile

For cases that tubular piles were penetrated into weak rock, issues beyond the inner shaft resistance should also be considered. Zhang (2010) pointed out that when designing rock-socketed steel piles, the intact rock properties and the influence of discontinuities on the properties of the rock mass should be incorporated, even though this increases the complexity of predicting the rock plug resistance. Moreover, the penetration of tubular piles causes shattering and disruption of the in-situ rock fabric, which can potentially cause fracturing with increasing density of sub-vertical joint within the tubular pile, hence, inducing joints in addition to the pre-existing joints. Authors' experience on rock samples in New South Wales in Australia indicated that the more brittle medium to high strength Phyllite tends to crush more during the penetration of the tubular pile. This rock crushing mechanism was reflected in the unconfined compressive strength (UCS) tests in high strength rock, shown in Figures 4.3 (a) and (b), in which the high strength Phyllite sample experienced multiple axial failure. While the low strength Phyllite tended to exhibit expansive strain during failure due to the observed bulging, which was exemplified by the UCS test results for low strength rock, as shown in

Figures 4.3 (c) and (d). Meanwhile, as plotted in Figure 4.4, lower shaft resistance was obtained for higher strength rock. Indeed, the mobilised shaft frictions for various strengths of rock were back-figured from CAPWAP (Case pile wave analysis program) results obtained during the installation of a 2-m diameter steel tubular in Phyllite bedrock. For low to medium strength rock with the point load strength index ($I_{s(50)}$) of 0.2 to 0.3 MPa, the back-analysed shaft friction was higher than that of medium to high strength rock with the point load strength index of 1 MPa, as shown in Figure 4.4. This F_m might be explained by the crushing and fracturing behaviour of the rock fabric during the pile driving process, such that the rock fabric suffered a drop of confining stress surrounding the pile due to induced joints, which proves that joints properties could have a significant influence on the pile shaft resistance.

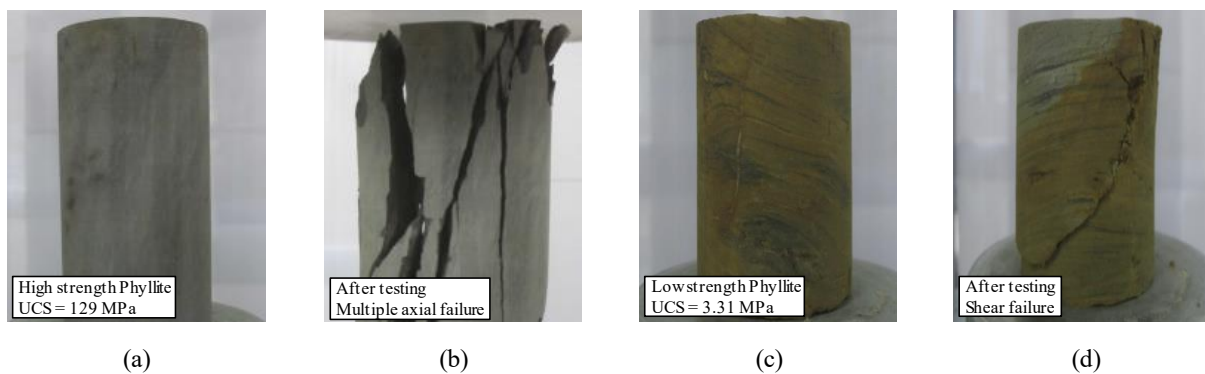


Figure 4.3. UCS test results for (a) high strength Phyllite before testing; (b) high strength Phyllite after testing; (c) low strength Phyllite before testing; and (d) low strength Phyllite after testing

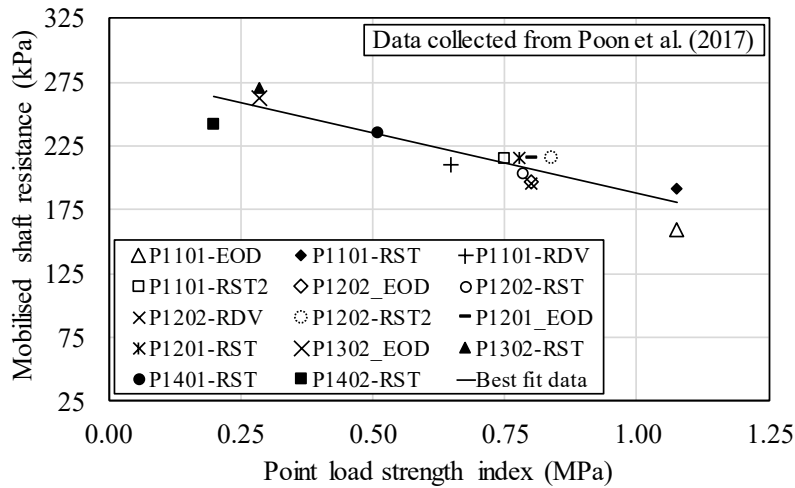


Figure 4.4. Back-calculated pile shaft resistances obtained from CAPWAP analysis for rocks with different point load strength indexes

While penetrating the open-ended tubular piles into hard soils or weak rocks, damage of the pile toe or failure in the performance might be encountered due to the difficult driving conditions, concentrated soil resistance, sloping surface of bedrock, shattering of jointed rock, and drilling out the soil plug (Long 1995; Hussein and Goble 2000; Mostafa 2011; Zhang et al. 2013; Randolph 2018). In practice, continued hard driving of tubular piles to refusal on rocks could result in splitting the rock at the toe of the pile, contributing to the reduction in the base resistance. The splitting may continue as the pile is driven down, thus requiring very deep penetration to regain the original resistance. Similarly where rock defects are steeply inclined with open transverse joints, the defect would propagate until the open joints are closed, or until the rock mass are crushed and locked together. During the construction of Moneypoint Jetty in south-west Ireland, a reduction in resistance was observed when the piles were re-driven (Long 1995). The piling operation had been held up for three months after three pile test failures, and then 142 piles were re-driven up to 3.1 m to reach the desired resistance. As reported by Long (1995), this could be due to penetrating piles into the heavily jointed mudstone, which shattered

the rock into small pieces, meanwhile, the reduction in resistance was mostly encountered in the zone with the mudstone of poor quality.

There are also cases that the open-ended tubular piles were hard to achieve the designed toe level when difficult driving conditions were encountered, while distortion at the pile toe was observed. In the medium strength or better quality rock, particularly with sloping rock surface, the risk of steel buckling or splitting increases. For instance, in the Macleay River and Floodplain Bridge project in NSW, two piles were suspected to be damaged and the possible cause could be driving onto the sloping rock surface (Zhang et al. 2013). As these two piles were extracted, the pile toe was found to be damaged and distorted heavily. The open-ended tubular piles in Rotterdam in Netherland also found to be damaged at the toe when installed into medium to dense sands at a raking angle around 11 degrees (Broos et al. 2017). The pile toe distortion could also be caused by removing soil plug inside the tubular pile. During the pile operation in Goodwyn Alpha Platform in north-west shelf of Australia, open-ended tubular piles were used as primary piles driven into the soil, and then the soil plug within the tubular pile was drilled out and the insert pile with a smaller diameter than the primary pile was placed through the tubular pile. However, during the removal of the soil plug within the tubular pile, 16 out of 20 piles had undergone progressive distortion, and these pile tips were deformed into a peanut shape. The distortion was encountered where a layer of cemented material was observed (Randolph 2018). In summary, the presence of stiff soil or rock layer, rock joints, and formation of plug inside the pile can influence the driveability and prediction on the pile resistance, inducing serious problems such as pile toe damage and distortion, leading to pile failure.

Therefore, as a first step in predicting the bearing capacity of open-ended tubular piles in weak rock, this study presents an investigation on the behaviour of a jointed rock plug. To achieve this purpose, the discrete element method (DEM) was used to simulate a push-up load test on

a jointed rock plug, because it can reproduce the discrete nature of rock with the cementation effect and also replicate the joints with desired joint properties. Flat-joint and smooth-joint contact models were used to replicate the behaviour of intact grains and sliding between the joints, respectively. The calibrated properties of a weak mudstone were used when carrying out push-up load tests on jointed mudstone, and the combined effect of joint density and dip on the inner shaft friction were studied in detail.

4.3 Discrete Element Simulations

In the discrete element method (DEM), rock is represented as an assembly of grains cemented by contacts, which are continuously updated during the deformation process to simulate the interaction between grains (Jing 2003; Bahaaddini et al. 2013). In this study, the DEM code PFC3D (particle flow code in three dimensions), was used to analyse the internal shaft resistance of weak rock with various joint dips and joint densities. In discrete element simulations, no pre-defined complex empirical constitutive relationships are needed, and natural rock masses with joints can be easily replicated by applying Newton's second law to the particles and force-displacement law for the contacts (Jing 2003; Potyondy and Cundall 2004). Moreover, choosing a particular crack propagation criteria is not required in DEM because crack initiation, propagation, and coalescence can be simulated explicitly by bond breakage (Zhang et al. 2011; Zhang and Stead 2014). Hence, the induced joints such as wing joints, which propagate at the tips of pre-existing joints due to the penetration of the tubular pile, can be captured.

4.3.1 Calibration of Discrete Element Model

The numerical simulations were initially calibrated and compared to the experimental data, reported for mudstone by Hayano et al. (1997). The test blocks were weak sedimentary mudstone obtained from the Sagamihara test site in Japan. The block sample was well

cemented mudstone with a dry unit density ranging from 1560 kg/m³ to 1680 kg/m³ and void ratios of 0.98 to 1.26. To replicate the properties of the mudstone, a density of 1600 kg/m³ and porosity of 0.5 was adopted in the numerical model. The simulated rock specimen was set to the same dimensions as the experimental test (i.e. 80 × 80 × 160 mm). The particles were subjected to a uniform size distribution with a minimum diameter (d_{min}) of 3 mm and a maximum to minimum diameter ratio (d_{min}/d_{max}) of 1.66; this is similar to previous simulations reported by some researchers (e.g., Potyondy and Cundall 2004; Schöpfer et al. 2009; Ding et al. 2014). The simulated rock specimen is shown in Figure 4.5 (a).

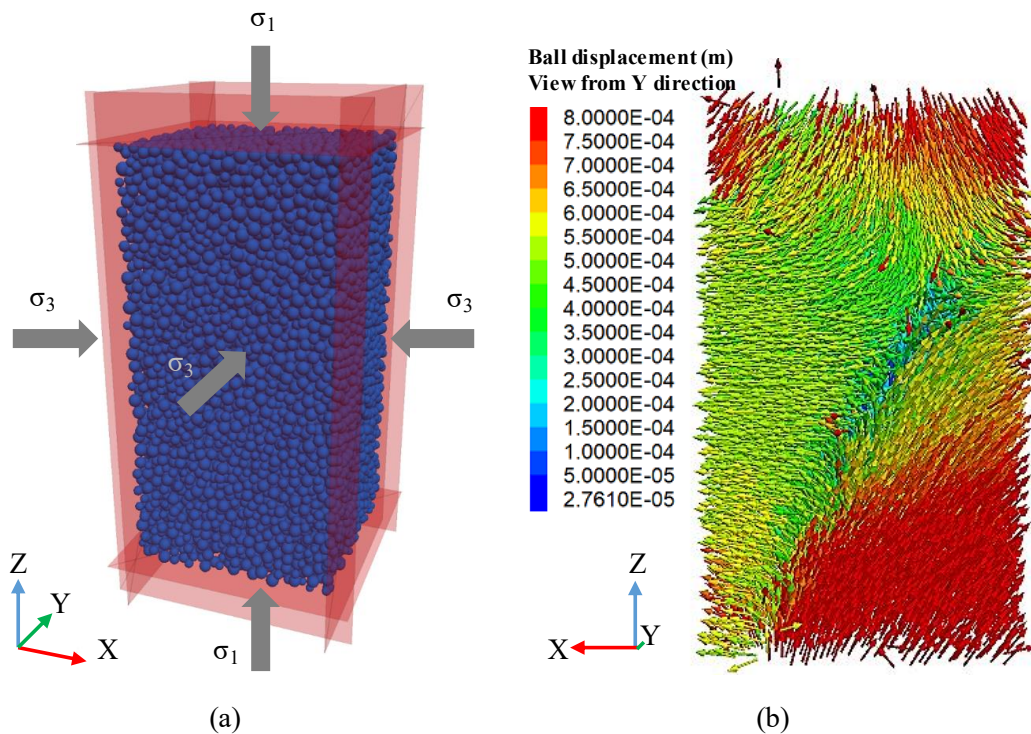


Figure 4.5. (a) Numerical model for intact mudstone under triaxial loading; and (b) displacement of individual grains of the specimen at an axial strain of 0.8%

The micro-parameters for the flat-joint model were calibrated by simulating a triaxial test with a confining pressure of 470 kPa. The sample was loaded by moving the top and bottom walls towards each other at a low velocity to keep the specimen under quasi-static equilibrium, while maintaining the confining pressure at the same level. The micro-parameters used to generate

the specimen are listed in Table 4.1. Three realisations with different random seeds were generated for the triaxial test. The comparison of the stress-strain behaviour of the numerical models and the experimental results, shown in Figure 4.6, reveals a good agreement. It is evident that the numerical simulation could capture the response of weak mudstone subjected to triaxial shear test, as reported in the experiment. As observed in Figure 4.8, the predicted post peak stresses are more than the measurements, mainly because confinement in the numerical model was simulated by the rigid walls, while the specimens in the experimental test were confined by the deformable membrane that allowed buckling. Figure 4.5 (b) presents the displacement of the individual grains at an axial strain of 0.8%. It is clear that the particles tended to separate and move in different directions and that led to the formation of a steep sliding surface.

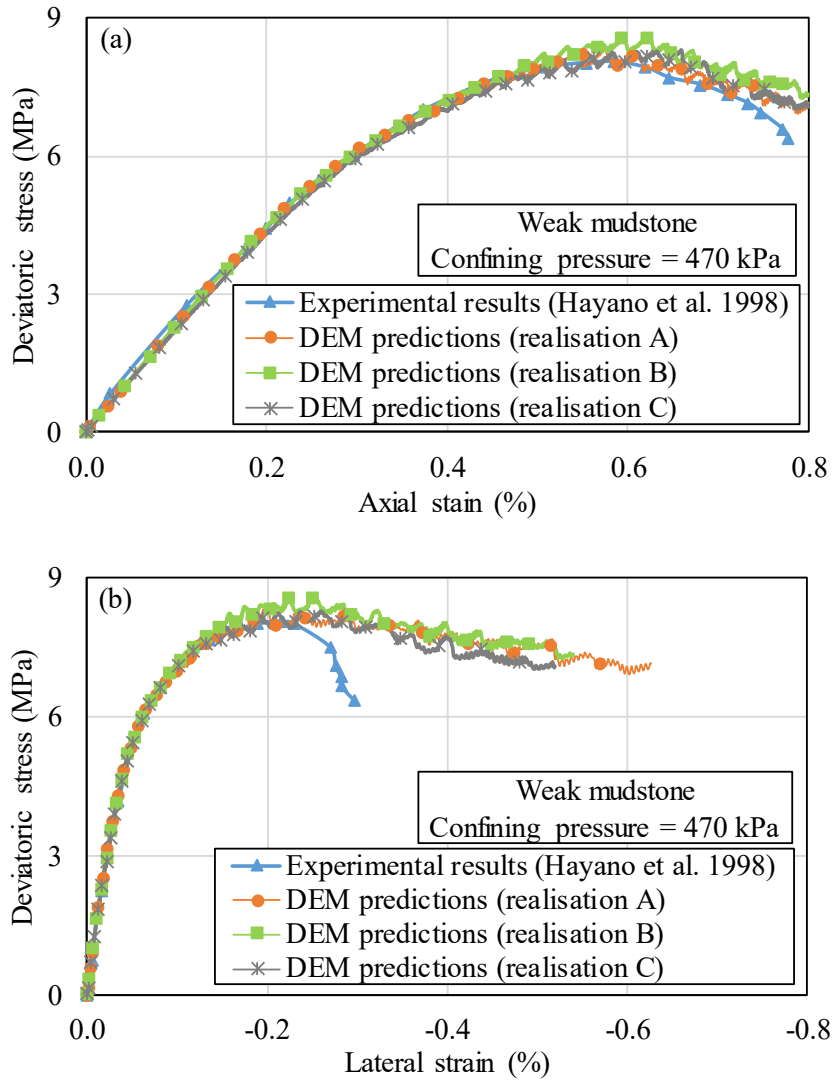


Figure 4.6. Stress-strain curves of triaxial tests from experimental and calibration exercises, (a) deviatoric stress against axial strain, and (b) deviatoric stress against lateral strain

Table 4.1. Calibrated parameters used in the discrete element modelling of weak mudstone in the triaxial test

Property	Value
Minimum particle diameter, d_{min}	3 mm
Maximum to minimum particle diameter ratio, d_{min}/d_{max}	1.66
Young's modulus for the particle to particle contact, E_c	5 GPa
Normal to shear stiffness ratio, k^*	2.5
Contact tensile strength, σ_c	15 MPa
Contact cohesion, c_c	5 MPa
Contact friction angle, ϕ_c	30°
Contact friction coefficient, μ_c	30°
Radius multiplier, λ	1

4.3.2 Push-up Load Tests in Tubular Pile on Jointed Mudstone

Numerical simulations of the relative motion between an open-ended tubular steel pile and jointed rock plugs have been carried out in this study. The pile is 300 mm in diameter, which fits the category of small open-ended tubular piles (Brown and Thompson III 2015). In the numerical model the pile was simulated as a rigid wall, so while deformation was not considered, a plate was placed at the toe in order to carry out a push-up load test. A rock plug was simulated inside the pile as an assembly of grains with a ratio of height to diameter (H_{plug}/D) of 3, which was also adopted by other researchers (e.g., Thongmune et al. 2011) to study the push-up load test. To simulate the effect of sliding along the surface of the pile,

the coefficient of friction between the pile and the rock plug was set at 0.5, which was equivalent to a friction angle of 26.6° and was based on the sliding friction for rocks reported by Gaffney (1976). The dilation angle between the simulated steel pile and rock plug was assumed to be zero. An overview of the numerical model adopted in this study is shown in Figure 4.7.

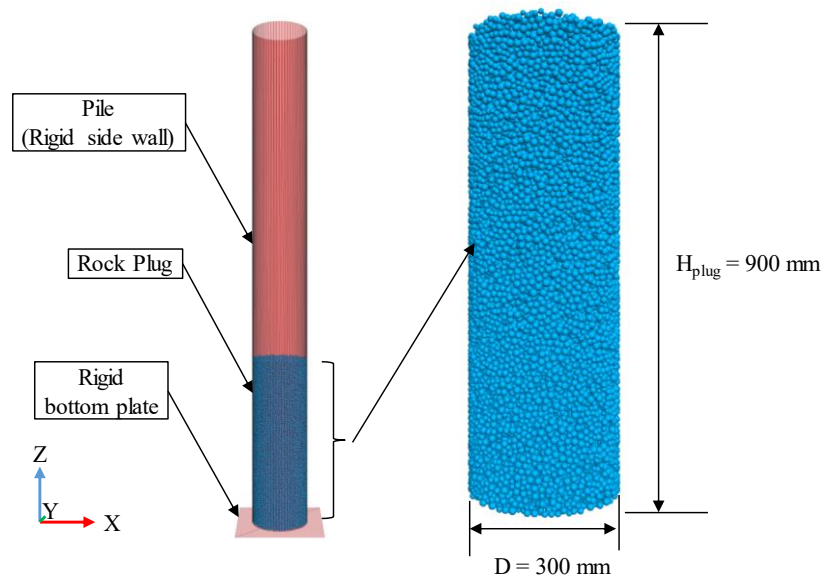


Figure 4.7. Analysis models of the push-up load test of model components and model dimensions

To compare the effect of the joints on the inner shaft resistance, an intact rock plug was formed inside the tubular pile and was set as a benchmark. The rock plug shown in Figure 4.7 contained 32,049 particles and achieved a porosity of 0.5 with a 1% variation from the top to the bottom of the rock mass. The particles were bonded using the calibrated contact properties listed in Table 4.1, and then the numerical model was brought to equilibrium under gravity loading. In DEM, the coordination number indicates how the particles are packed, and to represent the average number of contacts per particle. The coordination number from the top to the bottom of the sample varied between 8.0 and 8.3, indicating that it was a dense homogeneous assembly (Oda 1977; Wu and Xu 2016; Dong et al. 2018).

Like other researchers, the rock joints were simulated with the smooth-joint contact model (i.e., Bahaaddini et al. 2013; Bahrani and Kaiser 2016), and a reduced contact normal stiffness was used for this smooth-joint contact (k_{ns}), because the joints should obviously be weaker than the assembly of intact grains. The proposed joints were cohesionless with no dilation, to represent a smooth joint without filling materials.

The properties for the smooth-joint contact are summarised in Table 4.2. These parameters are similar to those used to model the synthetic rock mass (Ivars et al. 2008; Ivars et al. 2011). Joints 300 mm long were introduced into the rock plug so that the horizontal joints (i.e., joint dip, $\alpha = 0^\circ$) could cut through the entire rock plug. Push-up load tests were carried out on combination of joint dips (α) and controlled joint densities (ξ) with evenly distributed joint spacing. The studied joints dips were 0° , 30° , 45° , 60° , and 90° and the controlled joint densities were 1.1, 4.4 and $8.9 \text{ m}^2/\text{m}^3$. The former is known as the angle of the joint in a horizontal direction, while the latter is represented by the joint area over the volume of the rock mass. To compare different joint densities, the volume of the rock mass was kept the same for all the rock plugs, hence, the plug with higher joint density contained more joints. The representation of the jointed rock plugs with a joint dip of 0° is shown in Figure 4.8.

Table 4.2. Micro-parameters of smooth-joint contact for the joints adopted in this study

Property	Value
Normal stiffness (k_{ns})	40 GPa/m
Normal to shear stiffness ratio, k_{ns}/k_{ss}	4
Contact friction angle, ϕ_{cs}	35°
Radius multiplier, λ	1
Dilation angle, Ψ	0

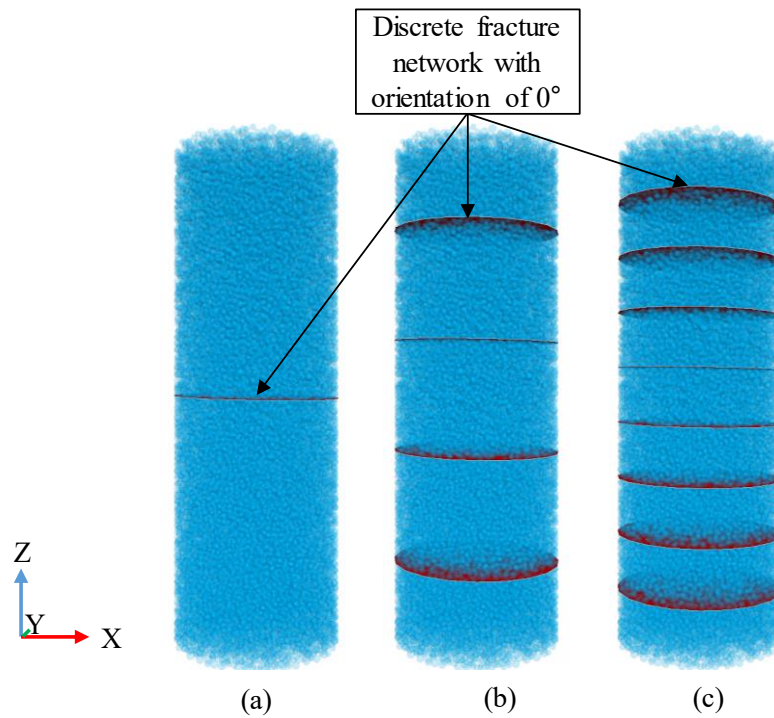


Figure 4.8. Representation of the jointed rock plugs with joint dip of 0° and joint density of (a) $1.1 \text{ m}^2/\text{m}^3$, (b) $4.4 \text{ m}^2/\text{m}^3$, and (c) $8.9 \text{ m}^2/\text{m}^3$

4.4 Effect of Loading Rate

A relative motion between the pile and the rock plug was generated by applying a constant upwards velocity to the bottom plate. As many researchers have reported (e.g., Zhang and Wong 2013; Xu et al. 2016), when the loading rate in a discrete element simulation is slow enough, it will not influence the results. As Hazzard et al. (2000) mentioned, the rocks simulated in DEM were free to crack and break apart under stresses, and stress waves were allowed to propagate outwards from each crack; with high loading rates, this propagation can have a significant effect on rock behaviour. Therefore, a slow loading rate is required to ensure that the force, displacement, velocity, and acceleration would not propagate from any particle further than its immediate neighbours during a single time step (Potyondy and Cundall 2004;

Ghazvinian et al. 2012). Apart from that, the strength of the specimens and joint toughness increase as the loading rate increases (Olsson 1991; Bažant et al. 1993; Zhang and Wong 2014). Researchers used loading rates ranging from 0.0075 m/s to 0.3 m/s when simulating tests such as the Brazilian test, uniaxial compressive test, and biaxial test (e.g., Hazzard et al. 2000; Cho et al. 2007; Park and Song 2009). Different load rates were tested in order to select a loading rate that would receive consistent numerical predictions and yet not depend on the loading rate. As Figure 4.9 shows, for all the loading velocities tested, the yielding points in push-up forces indicated that initially, the force increased rapidly in order to mobilise the friction force between the rock plug and the inner shaft of the pile; however, the static friction at the rock-wall interface has not been fully overcome and no part of the frictional force along the rock plug was mobilised. But once the friction at the bottom portion of the rock plug started to mobilise, the push-up force reached the yielding point, the arching effect and then the friction began to increase, while the upper portion of the rock plug was still mobilising the friction force. These phenomena also occurred in the experiments and DEM simulations of push-up load tests in sands (Thongmunee et al. 2011). Moreover, oscillation occurred after the push-up forces reached the yield point, and it became more noticeable as the loading rate increased. These oscillations in the push-up force are caused by the loading rate and the joints. Some researchers reported similar behaviour that a slower loading rate reduced the specimen's fluctuations in various tests (Cundall and Strack 1979; Ghazvinian et al. 2012; Zhang and Wong 2014). In DEM, the loading rate is directly related to the strain rate, so the higher the loading rate, the larger the strain rate (Cundall and Strack 1979; Zhang and Wong 2013), hence a higher value of change in strain results in greater oscillatory behaviour. However, the existence of initial irregularities in the numerical model and the real world, such as certain geometric patterns of discontinuities that may result in different outcomes, also leads to

fluctuation in behaviour (Itasca 2015). Similar oscillation was seen in direct shear tests on jointed rocks (Bandis 1980; Liu et al. 2017).

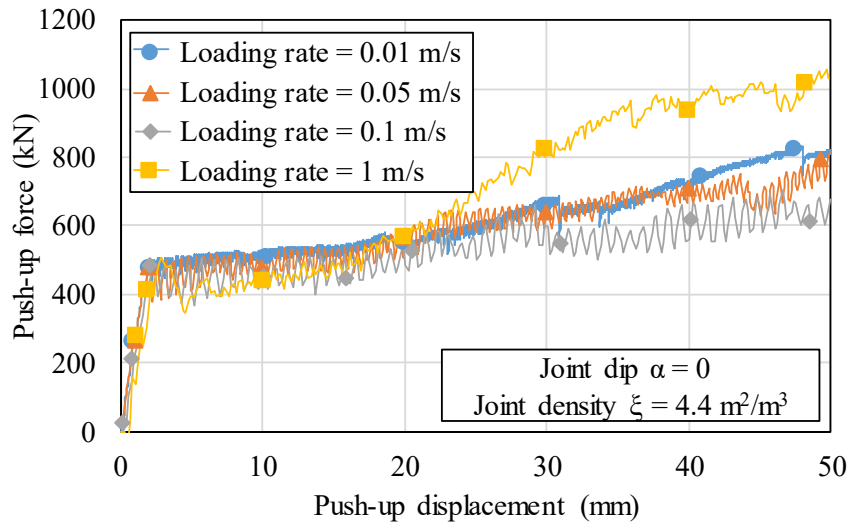


Figure 4.9. Comparison of loading rates on the push-up load tests

As shown in Figure 4.9, when the loading rate is slower than 0.05 m/s, it has a minor influence on the load-displacement curve. Thus, to ensure achieving proper accuracy and consistency, a push-up velocity of 0.05 m/s was adopted in this analysis; and accordingly, each analysis was carried out until the push-up displacement reached to 50 mm.

4.5 Effect of Joint Density

Push-up load tests for intact and jointed rock plug were carried out to determine the effect of joint density on plugging. Figure 4.10 (a) shows the push-up forces acting on the bottom plate while displacing the the rock plug with horizontal joint dip ($\alpha = 0^\circ$). Clearly, push-up forces increased rapidly with the push-up displacement at the initial stage and then gradually slowed down beyond the yielding point for intact and jointed rock plugs. Meanwhile, the unit shaft friction increased from the top to the bottom of the intact rock plug, referring to Figure 4.10 (b). The step increase in push-up forces at the initial stage, as shown in Figure 4.10 (a), was mainly due to mobilising the friction forces between the pile and the plug. This

was also noticed in Figure 4.10 (b), because when the push-up displacement $\Delta s = 0.5 \text{ mm}$ (i.e., before the push-up force reached the yielding point), the increase in unit shaft friction from the top to the bottom of the rock plug was linear. This linear increase in shaft resistance indicated that the bottom of the rock plug was still mobilising the frictional force along the pile, but then, when the rock plug was pushed up further (i.e., $\Delta s \geq 1.5 \text{ mm}$) at the same push-up displacement, the difference in the unit shaft friction at the bottom of the pile tended to be minimal, as shown in Figure 4.10 (b). This phenomenon demonstrated that the frictional force between the wall of the pile and the rock plug had been mobilised; arching then commenced, as presented in Figure 4.14 (a) and (b). The arching effect was due to the rock plug being more compressible than the pile material (i.e., steel), so the plug underwent greater deformation when the inner shaft friction resisted the push-up load; this led to an increase in horizontal stresses in the contact of rock and inner shaft that then resulted in higher frictional forces. This phenomenon was also observed by other researchers during field and laboratory tests of open-ended tubular piles (Jardine et al. 2006; Fattah and Al-Soudani 2016).

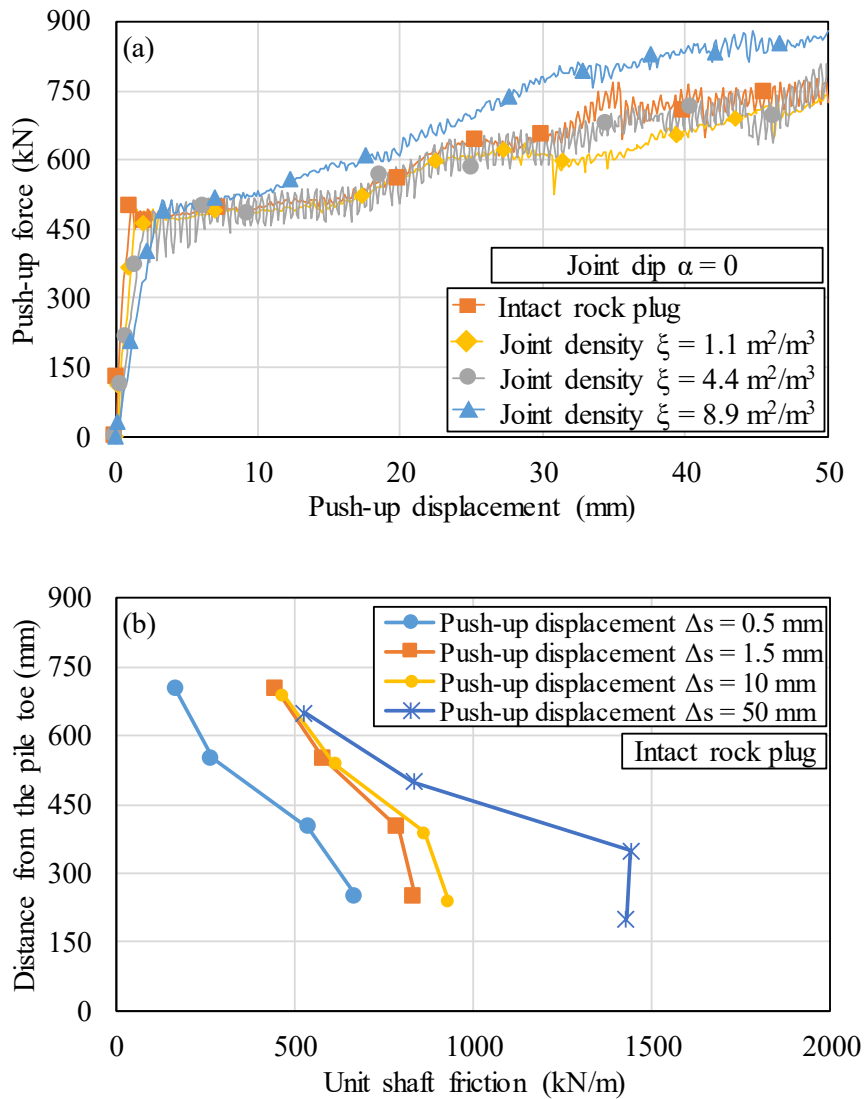


Figure 4.10. Behaviour of intact rock plug of (a) relationship between push-up displacement and force, and (b) vertical stress along the rock plug

As depicted in Figure 4.10 (a), when $\alpha = 0^\circ$, the presence of joints had a minimal effect on the push-up force, especially when the joint density was low (i.e. $\xi \leq 4.4 \text{ m}^2/\text{m}^3$). This is because when joints are perpendicular to the loading direction, the intact assembly would barely slip along the horizontal joint surfaces. As observed in Figure 4.10 (a), when $\xi = 8.9 \text{ m}^2/\text{m}^3$, the predicted push-up load was even higher than the corresponding value for the intact rock plug because part of the push-up force contributed to the joints coalescing. Figures 4.11 (a), (b), and (c) show the relationship between the push-up displacement and force of jointed rock plugs

with a joint density (ξ) of 1.1, 4.4, and 8.9 m^2/m^3 , respectively. Table 4.3 compares the push-up forces at the yielding point for different joint densities and dips; it is clear that an increase in joint density reduces the resistance of the rock plug, as shown in Figure 4.11 and Table 4.3. When $\xi = 1.1 m^2/m^3$, the effects of joint dip and density on the push-up force were insignificant, as illustrated in Figure 4.11 (a). In fact, a lower joint density indicates less discontinuity in the rock plug and has less effect on weakening the rock mass, whereas the location of the joint also influences the push-up force. There were joints at the centre of the plug when $\xi = 1.1 m^2/m^3$, while the frictional force tended to mobilise at the bottom part of the plug first, so the effects of joints were minimal. However, when the number and therefore the density of joints in the rock plug increased, the joint effects on the push-up force would be remarkable, particularly when $\alpha = 90^\circ$. As summarised in Table 4.3, when $\alpha = 90^\circ$ (i.e., vertical joints) is compared to the intact rock plug, the yielding push-up force for the jointed rock plug decreased by 23%, 61%, and 87%, with joint densities of 1.1, 4.4, and 8.9 m^2/m^3 , respectively. Indeed, the joints were rather smooth and without dilation so the sliding surface of the joint could barely resist the vertical forces; this led to a large reduction in the yielding push-up force. Moreover, joints with a joint dip of 90° obstructed the formation of arching because one of the conditions needed to trigger arching is an increase in horizontal stress inside the rock plug, while the vertical joints discontinue the stress path horizontally. Hence, the arching effect is rarely observed in jointed rock plugs with steeper joints and higher joint densities (i.e., $\alpha \geq 45^\circ$ and $\xi > 4.4 m^2/m^3$), as shown in Figure 4.14 (d), Figure 4.14 (e), and Figure 4.14 (f).

Table 4.3. Predicted push-up forces at the yielding point for jointed rock plugs

Joint dip α	Push-up force (kN)		
	Joint density $\xi = 1.1$ m^2/m^3	Joint density $\xi = 4.4$ m^2/m^3	Joint density $\xi = 8.9$ m^2/m^3
0°	490	482	510
30°	479	402	296
45°	450	278	160
60°	416	214	71
90°	380	193	64

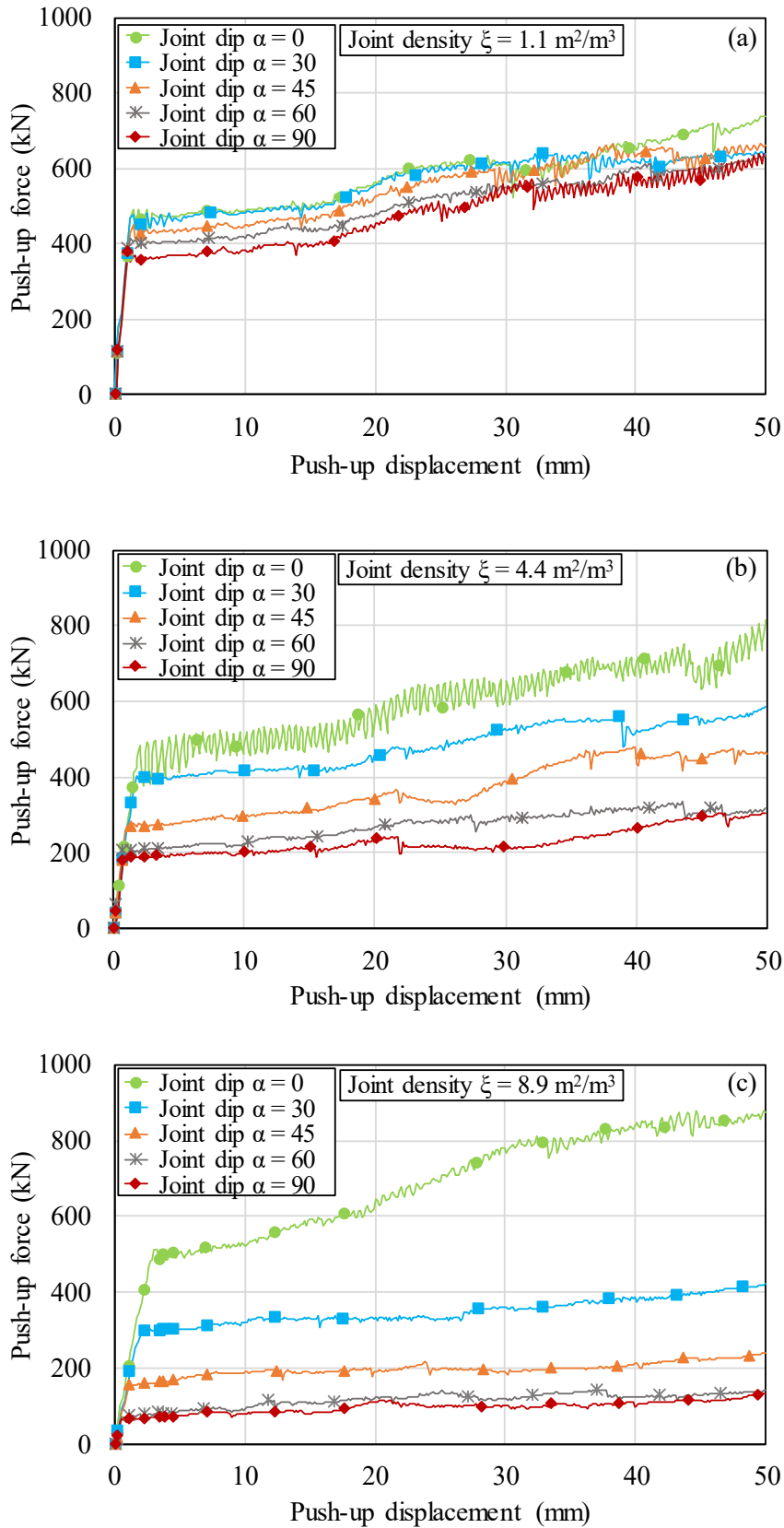


Figure 4.11. Relationship of the push-up displacement and force of jointed rock plugs with joint density of (a) $1.1 \text{ m}^2/\text{m}^3$, (b) $4.4 \text{ m}^2/\text{m}^3$, and (c) $8.9 \text{ m}^2/\text{m}^3$

4.6 Effects of Joint Dip

4.6.1 Effect of Joint Dip on the Triaxial Shear Test Results

To compare how joint dips affect the push-up force and mechanical behaviour of jointed rock plugs, triaxial tests on jointed rocks were simulated. The jointed rock specimens had the same dimension and confining condition as the intact specimen explained earlier in the calibration exercise. These simulated specimens had joint dips of 0° , 30° , 45° , 60° , and 90° with a controlled density (ξ) of $4.4 \text{ m}^2/\text{m}^3$ and also used the micro-parameters reported earlier in Table 4.2. Figures 4.12 (a) and (b) show a comparison between the stress-strain behaviour of the intact specimen and jointed specimens of triaxial tests where as expected, the rock mass became weaker due to the presence of joints. A joint dip of 90° resulted in the least reduction in the strength of the rock mass, whereas a joint oriented at 45° and 60° altered the mechanical behaviour more. These observations are consistent with the results reported by other researchers (e.g., Bahaaddini et al. 2013; Chiu et al. 2013; Huang et al. 2015). When $\alpha = 90^\circ$ (i.e., vertical joints), the joint was parallel to the axial loading direction and might not be aligned with the slip surfaces between grains, this would not facilitate the grains to slide on the joint surface. As shown in Figure 4.12, when $\alpha = 0^\circ$ (i.e., horizontal joints), the rock responded almost similar to the specimen with joint dip of 90° , where the former reached the peak stress at a larger axial strain, thus indicating ductile behaviour. Since joints remain closed under compression and transfer compression without yielding (no sliding or tension,) the joints that were perpendicular to the major principle stresses would alter the strength and stiffness of the rock mass to lesser extent. Referring to Figure 4.12, this trend was also observed for the joint orientated at $\alpha = 30^\circ$, whereas those joints with dips of 45° and 60° induced 30% and 23% reduction of the peak deviatoric stress of the rock mass, respectively (see Figure 4.12). Indeed, the inclined joints might be more aligned with the shear band zone or the sliding joints induced after peak stress, as shown in Figure 4.5 (b).

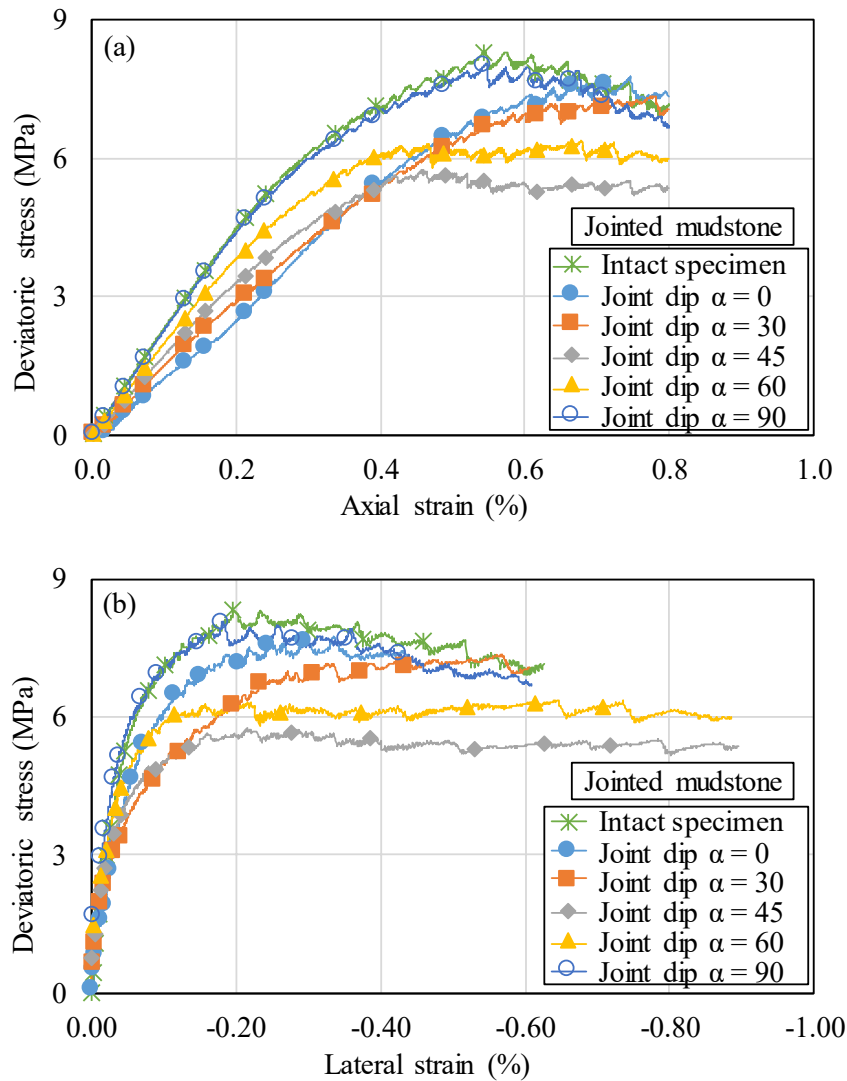


Figure 4.12. Stress-strain curves of triaxial test for intact and jointed specimens, (a) deviatoric stress against axial strain, and (b) deviatoric stress against lateral strain

4.6.2 Effect of Joint Dip on Push-up Load Test

Referring to Figure 4.10, when $\alpha = 0^\circ$, the predicted push-up forces for the jointed rock plug were similar to the intact rock plug regardless of joint density because as reported in Figure 4.10, the sample with horizontal joints indicated high resistance to compression in the triaxial test. As the comparison of results reported in Figures 4.11 and 4.13 shows, when the joints were inclined the push-up forces were related to the strength of the rock mass. Figure 4.13 (a) presents the axial stresses at the yielding point for different joint densities and dips measured

250 mm away from the pile toe, while Figure 4.13 (b) indicates the axial stresses at yielding point for the jointed mudstone obtained from the triaxial test. Clearly, steeper joints (i.e., $\alpha = 45^\circ$ and 60°) greatly reduced the yielding stresses in the push-up load tests and the triaxial test. Although Figure 4.10 indicates that the specimen with a joint dip of 90° was the strongest of the tested jointed rocks, the rock plugs generated their lowest resistance when the joints were parallel to the direction of the push-up load. Indeed, in addition to the joint properties, the frictional forces between the pile and rock plug and the arching effect within the rock grains can impact the plug capacity notably. The shaft resistance increased significantly due to the arching effect (see Figure 4.15), whereas due to the discontinuities of the stress-path generated by the joints, arching was barely observed in the rock mass with steep joints [referring to Figures 4.14 (e) and 4.15 (f)]. Therefore, without any evident increase in horizontal stresses and the formation of arching, the frictional force between the inside surface of the pile and the rock plug was lower when steep inclined joints were introduced, as shown in Figure 4.11.

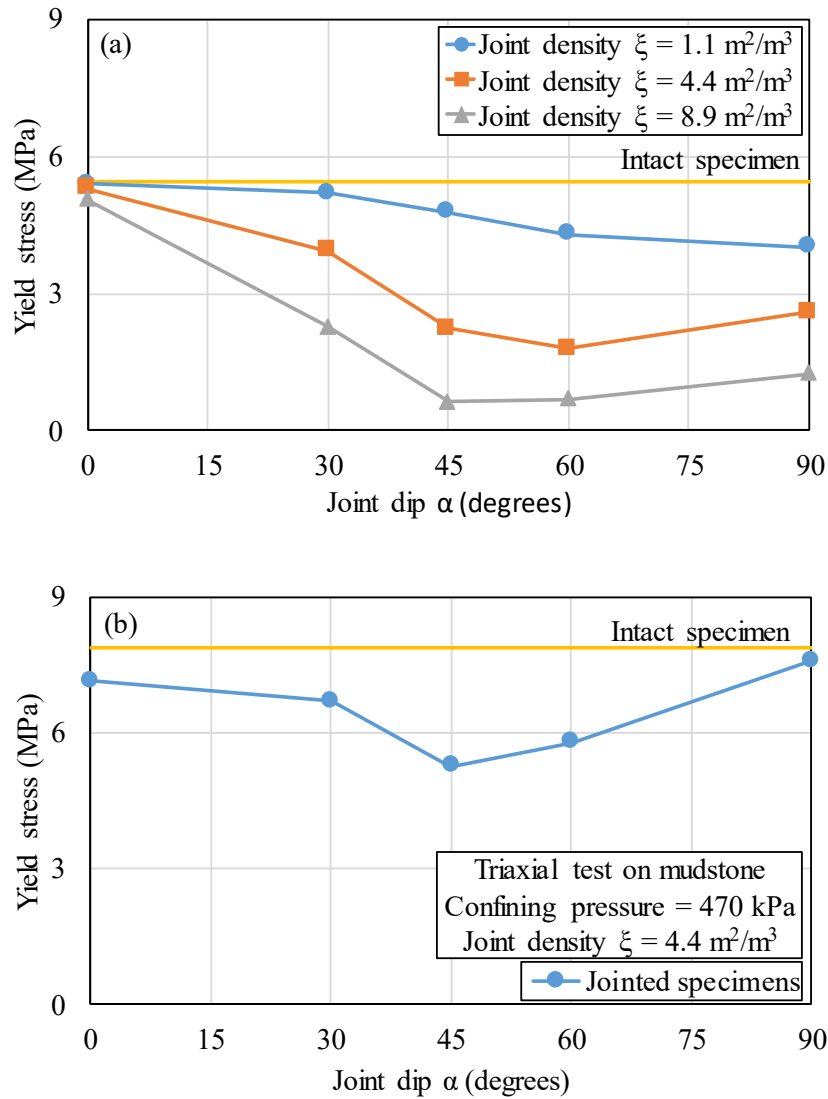


Figure 4.13. Yield axial stress of (a) rock plug in push-up load test, and (b) rock mass in triaxial test

Figure 4.14 depicts the displacement of individual rock grains when $\xi = 8.9 \text{ m}^2/\text{m}^3$ where convex deformations were clearly observed at the lower portions of the rock mass for the intact rock plug and jointed rock plug with gentle joints (i.e. $\alpha \leq 30^\circ$). As expected, the discontinuities introduced by the joints altered the movements of the grains. It is evident there was a large reduction in the push-up forces when $\alpha = 30^\circ$, particularly when more joints were present, as shown in Figures 4.11 (b) and (c). Indeed, as mentioned earlier, the discontinuities in the rock mass induced by the joints reduced the arching effect inside the plug, but when the

joint dip was greater than 30° , the grains tended to deform parallel to the sliding surface, when the displacement field passed through the joints, as illustrated in Figure 4.14 (c). In particular, Figures 4.14 (d) and (e) show that sliding on the joint became more obvious when the joints were orientated at steeper angles (i.e., $\alpha = 45^\circ$ or 60°).

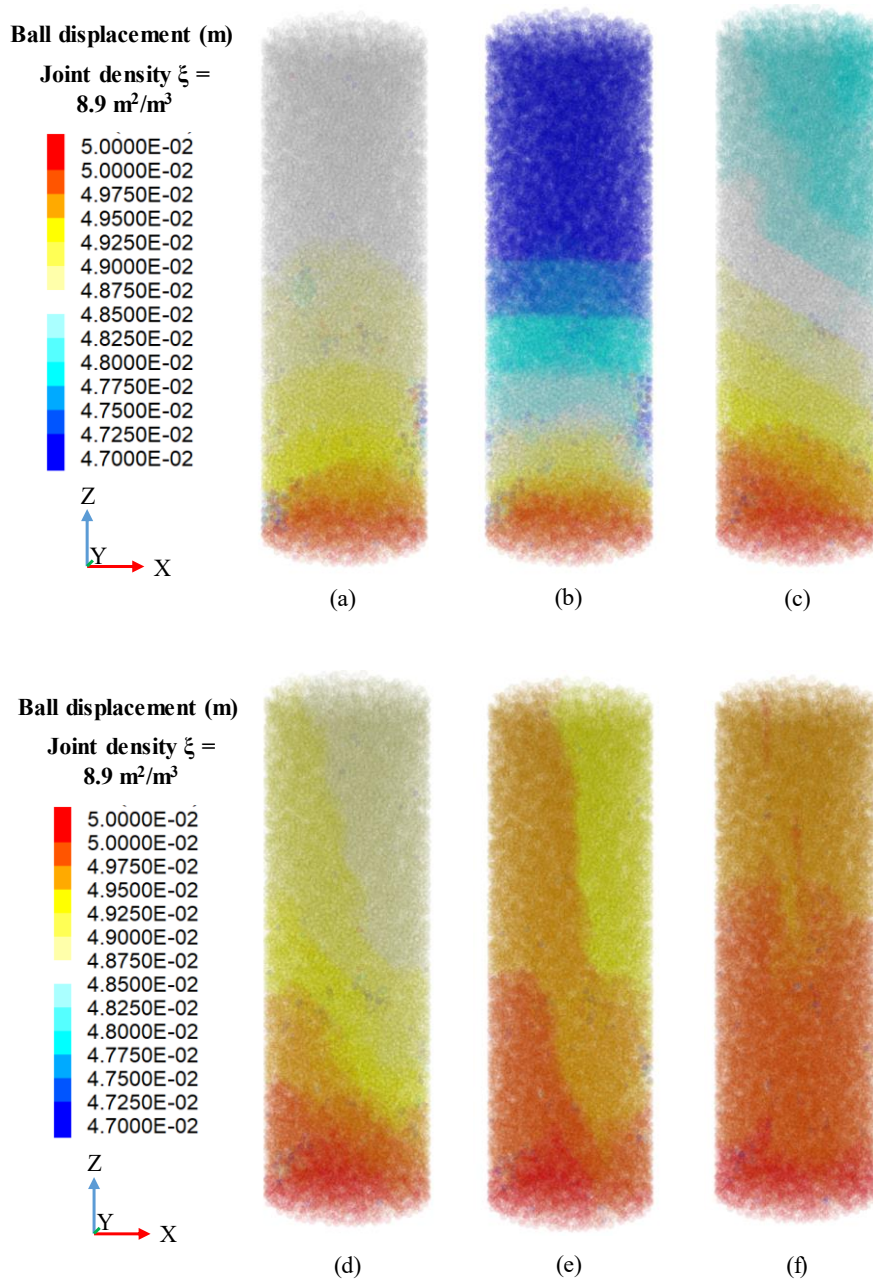
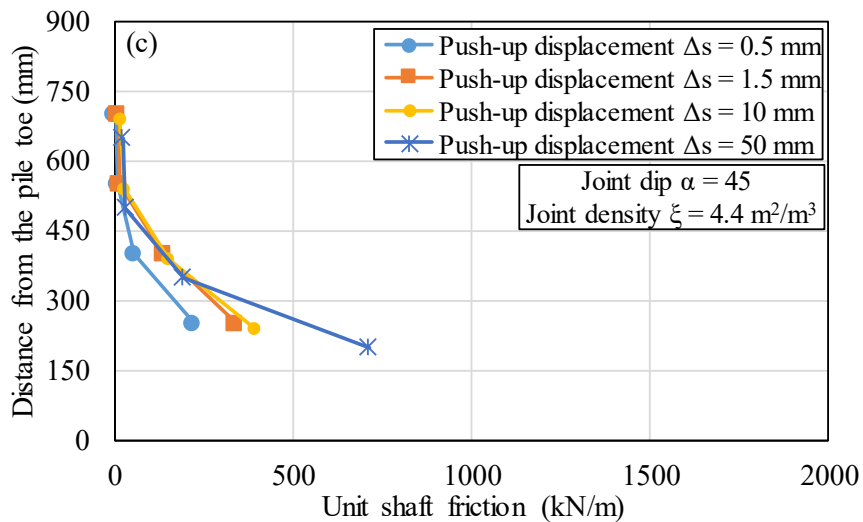
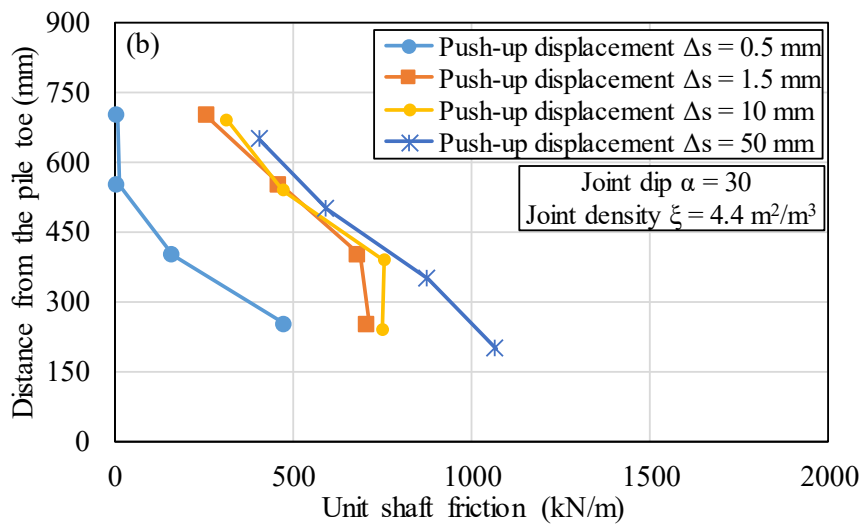
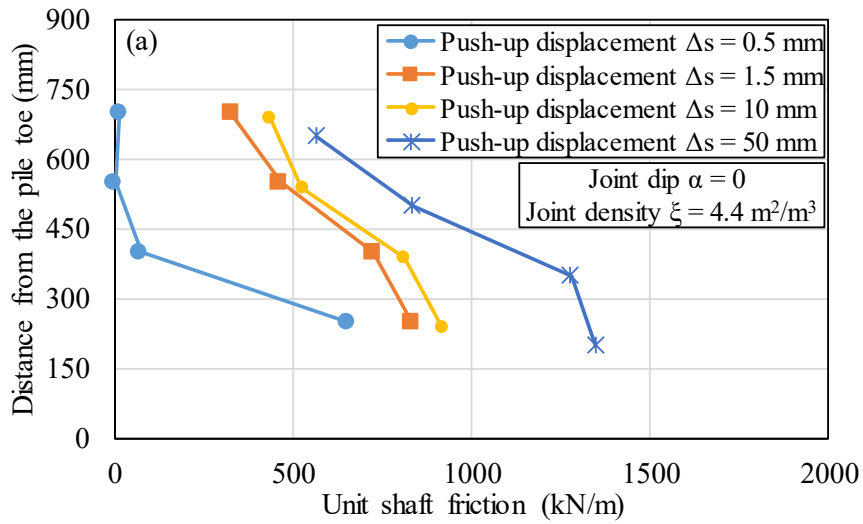


Figure 4.14. Displacement of individual grains of push-up load test for (a) intact rock plug, (b) joint dip of 0° , (c) joint dip of 30° , (d) joint dip of 45° , (e) joint dip of 60° , and (f) joint dip of 90°

Figure 4.15 shows the distribution of the unit shaft friction for rock plugs with a joint density of $4.4 \text{ m}^2/\text{m}^3$. The unit shaft resistance was calculated from the differences in vertical stresses ($\Delta\sigma_v$) along the rock plug and the height increment (d_z), as shown in Figure 4.2. As indicated in Figure 4.15, when the joint dips were gentle (i.e. $\alpha = 0^\circ$ or 30°), the increase in unit shaft friction from the top to the bottom of the rock plug was similar to the intact rock plug [referring to Figure 4.10 (b)]. When the rock plug moved relative to the pile wall, resistance to movement began at the bottom of the rock plug, so the unit skin friction increased rapidly at the bottom of the pile, as presented in Figures 4.15 (a) and (b). Then, as the rock plugs were pushed further, the frictional force tended to be mobilised at the bottom portion, the increase of unit shaft friction from top to bottom of the pile became slower and this increase also involved arching. However, when the joint dips were steeper (i.e., $\alpha = 45^\circ$ or 60°), the rock plugs behaved differently. Although the frictional forces tended to mobilise at the bottom portion of the rock plug, the discontinuities in the joints reduced the arching effect; the increases in unit shaft friction were not as evident as the rock plugs with gentle joint dips. When the joints were vertical (i.e., $\alpha = 90^\circ$), the unit shaft friction tended to be even from the top to the bottom of the pile wall. There were similar trends of the unit shaft friction along the plug when $\xi = 1.1 \text{ m}^2/\text{m}^3$ and $8.9 \text{ m}^2/\text{m}^3$.



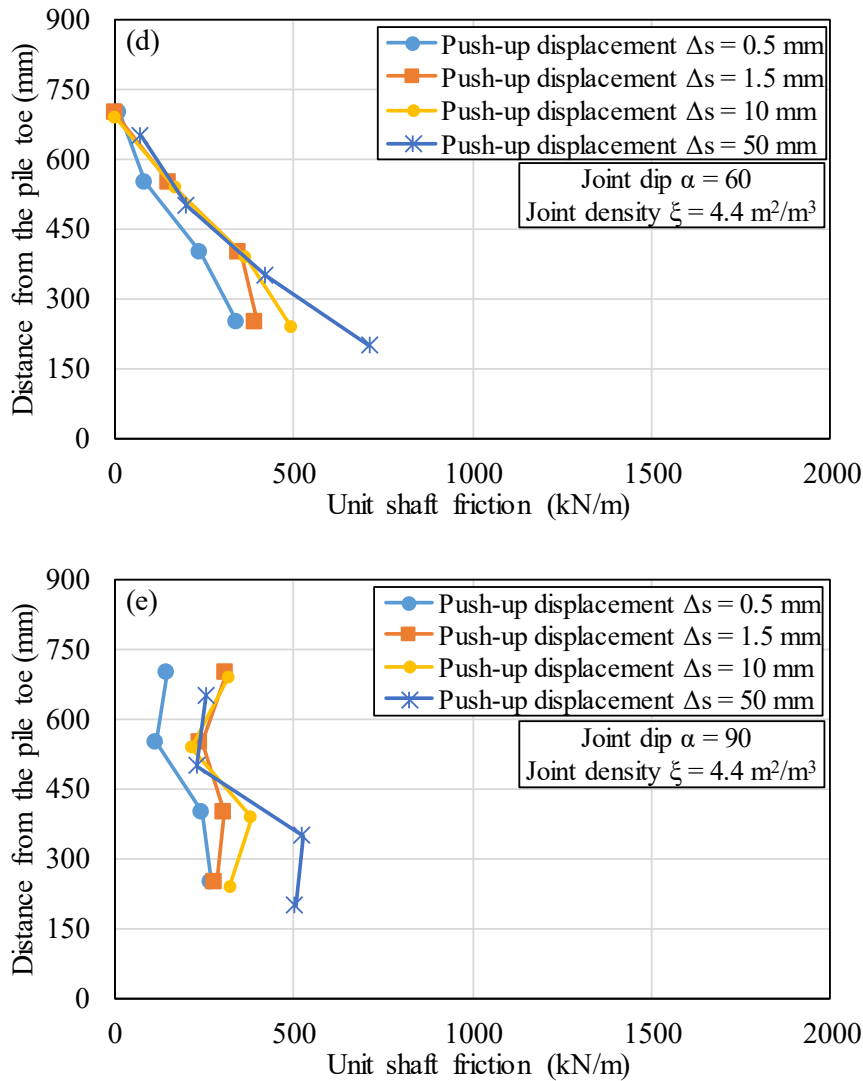


Figure 4.15. Distribution of unit shaft friction along the rock plugs with joint density of $4.4 \text{ m}^2/\text{m}^3$ and joint dip of (a) 0° , (b) 30° , (c) 45° , (d) 60° , and (e) 90°

4.7 Summary

Penetrating open-ended tubular piles into hard soil or weak rock could result in different problems, including inaccurate prediction of the resistance due to the shattering of jointed rock, difficult driving condition that could damage the pile toe, or pile distortion after drilling out the soil plug. To prevent such damage and failure in tubular piles, the understanding of the plugging behaviour of rock inside the pile is imperative. The present research study attempts to increase our understanding on the impact of joint dip and joint density on the plugging of

tubular piles in rocks; this knowledge can be used further to develop a design methodology to avoid undue conservatism of pile plugging assessment in the current practice. To investigate the plugging mechanism of weak rock in open-ended tubular piles, this study focused on assessing the effects of joint properties on the internal shaft friction. The push-up load tests on the jointed rock plugs were carried out on a weak mudstone adopting discrete element modelling. The flat-joint model was adopted for rock simulation such that the shear strength would follow the Coulomb criteria and the tensile strength is limited by the tension cut off. The smooth-joint contact model was used to model the behaviour of joints because the contacts that assigned to this model disregard the direction of the bond that forms inside the intact rock mass and follows the direction of the joint. The contact properties required in the discrete element simulation were obtained from the results of a calibration exercise from laboratory triaxial tests. A small 300mm diameter open-ended tubular pile was used to study the plug resistance that developed from jointed weak rock. The effects of joint dip and density on the push-up load tests were numerically studied and discussed.

The DEM predictions revealed that the joints perpendicular to the loading direction (i.e., $\alpha = 0^\circ$) had minimal effects on internal shaft resistance, but when they were parallel to the push-up loading direction (i.e., $\alpha = 90^\circ$), the joints had a large impact on the plugs and also reduced their capacity. For densely jointed rock (i.e., $\xi = 8.9 \text{ m}^2/\text{m}^3$), there was an 87% reduction in the push-up force at the yielding point. Although the triaxial tests on jointed rock masses indicated that the rock specimen with 90° joint dip did not provide the lowest strength, when it comes to plugging behaviour and shaft resistance, the behaviour of the jointed rock plug was not based solely on strength, other properties such as the arching effect, joint density, and joint dip must also be considered.

Yielding points were observed in the push-up forces when the rock plugs pushed up further, this indicated the state of mobilising the fictional force along the rock plug and pile shaft. It is

because before the push-up forces reached their yielding point, no part of the frictional force along the rock plug had been mobilised but once the bottom of the rock plugs reached a mobilised state, the push-up forces reached their yielding point and more portion of the frictional forces between the rock plug and the wall of the pile began to be mobilised. Arching also occurred as individual grains in the lower part of the rock plugs near the toe began to be displaced with different rates. The frictional forces predicted for those rock plugs that experienced arching were higher than the plugs with no arching; therefore joint dip altered the arching effect because the vertical joints destroyed the stress-path for increasing horizontal stress inside the plug, this is why the arching effect could barely be seen.

It is obvious that in addition to the strength of the rock mass, the frictional force between the pile and the rock plug and the arching that formed among rock grains, had a significant impact on the capacity of the rock plug inside tubular piles. It can be concluded that the joint properties can influence the inner shaft friction to a large extent. Hence, when predicting the capacity of tubular piles in weak rock, the strength of the rock mass, as well as joint properties such as the joint density and the joint dip need to be considered. Indeed, the influence of rock crushing and dilation of the rock joint on inner shaft friction can be significant; further studies on these areas can be conducted in future through studying the driving process of steel tubular piles in weak rocks with the consideration of the crushable rock and the effect of dilation of rock joint.

Chapter 5 - Investigation of the Axial Load Transfer Mechanism

5.1 General

In order to obtain a better understanding of the load transfer mechanism of open-ended tubular piles driven into weak rock, numerical analysis is conducted to study the internal and external shaft frictions, base resistance and the stress distribution pattern in the surrounding rock mass. Meanwhile, since pile shoes are often applied when driving to the rock layer, a common inner pile shoe attached to the open-ended tubular pile was analysed and compared with the pile without a shoe. In this study, the discrete element method (DEM), which can reproduce the discrete nature and replicate the mechanical behaviour of the rock mass, is adopted due to its ability to simulate large deformation problems such as pile penetration process. The flat-joint model that allows partial damage at the contact interface was employed to replicate the discrete nature of the rock mass. The rock mass was calibrated against a pyroclastic weak rock reported in the existing literature through triaxial tests, and then the calibrated rock mass was employed for the simulation of pile penetration. A 30° segment of the true-scale model was simulated using the DEM with a height of 3 m and a radius of 1.5 m, which was composed of about 557,000 particles. To accommodate a reasonable number of particles within the computational capacity, the particle refinement method was used in the modelling, in which the particles at the close vicinity to the pile had the same particle size as the triaxial test calibration exercise, and then upscaling factors were applied to the particles at the far field. Initial stresses were applied at the boundary of the testing chamber, while the side of the chamber was discretised into 6 sections with increasing horizontal stresses with depth to establish the at-rest condition. Numerical results for penetrating an open-ended tubular pile show that the internal shaft friction was less than the external shaft friction for both piles with and without a shoe. Plugging was observed for both piles with and without a driving shoe. This study sheds a light on the

load transfer mechanism of the open-ended tubular piles and the effect of shoes on the axial capacity of the pile.

5.2 Background

Nowadays, open-ended tubular piles are widely used to support superstructures that transfer high axial loads to the foundations. Compared to solid piles, open-ended tubular piles require less installation effort and induce less disturbance on the surrounding ground and structures. Due to the increasing demand in high rise buildings and heavy infrastructure such as long span bridges, open-ended tubular piles are often required to be embedded in the competent ground such as rock. The load bearing mechanism of an open-ended tubular pile stems from the internal shaft friction (Q_{inner}) or the plug resistance (Q_{plug}), the external shaft friction (Q_{outer}), and the base resistance (Q_b) (American Petroleum Institute 2002; Tomlinson and Woodward 2008). The bearing mechanisms of the open-ended tubular piles in sands and clays were investigated by many researchers (e.g., American Petroleum Institute 2002; Clausen et al. 2005; Jardine et al. 2005). Despite several well-established design recommendations for open-ended tubular piles in sand and clay deposits, some of the assumptions and effects still remain controversial and uncertain for practicing engineers. For example, different methods hold different views on the magnitude of internal and external shaft friction along the pile. In the NGI method (Clausen et al. 2005), the internal unit shaft friction is recommended to be three times larger than the external unit shaft friction along the pile in sands. The API method (American Petroleum Institute 2002) assumes the internal and external unit shaft frictions are equal. In the FHWA method (Hannigan et al. 1997), the internal unit shaft friction is half to one third of the external unit shaft friction.

In order to investigate the bearing mechanism of open-ended tubular piles, many researchers (e.g., Paik and Salgado 2003; Ko and Jeong 2014; Han et al. 2019) conducted field tests or

model tests in the laboratory using the twin-wall system to obtain the internal and external shaft frictions separately. The twin-wall system consists of two concentric piles with one being larger than the other in terms of diameter, while the two piles are welded either at the top or at the bottom. When the piles are welded at the top, the gap at the bottom is sealed with silicone. For example, Paik and Salgado (2003) conducted model tests of a twin-wall pile with an outer diameter of 42.7 mm in a calibration chamber with a diameter of 0.775 m. They measured the base load capacity (i.e., the sum of internal shaft load capacity and the annulus base load capacity) and outer shaft load capacity separately by attaching a number of strain gauges to the inner and outer piles. Through several tests with different horizontal and vertical stresses and relative densities for the sand, they observed that the ultimate external unit shaft resistance increased with relative density and horizontal stresses, while vertical stresses had insignificant effects. Later, Ko and Jeong (2014) adopted a twin-wall system with instrumented strain gauges on the outside and inside walls of the pile to obtain the internal and external shaft frictions separately in sandy soils. They examined three pile diameters ranging from around 500 mm to 900 mm by static and dynamic load tests. In the static load test, the internal shaft capacity took up around 10% of the ultimate bearing capacity for all three piles, then the external shaft provided 18% to 34% of the total capacity which depended on the pile diameter, and the annulus area contributed to 58% to 70% of the ultimate bearing capacity. It was found that the soil plugging in the lower portion of the pile had an influence on the internal shaft resistance. Moreover, Han et al. (2019) conducted the field tests of a twin-wall open-ended tubular pile and a closed-ended pile in sand and gravel to compare the internal shaft resistance (i.e., plug resistance), external shaft resistance, and annulus base resistance. They found that due to the shaft resistance degradation during the pile driving, the open-ended tubular pile resulted in a much lower unit shaft resistance than the closed-ended tubular pile. Meanwhile, by comparing the experimental data with the prediction from CPT-based design method including ICP

method (Jardine et al. 2005), UWA method (Lehane et al. 2005), and Purdue method (Lee et al. 2003), Han et al. (2019) pointed out that the gravel content affected the prediction of the shaft and base resistances. It was observed that when the gravel content exceeded 20%, these CPT-based design methods tended to over-predicted both the shaft resistance and base resistance of open-ended tubular piles. Similar to the test results reported by Ko and Jeong (2014), the static load tests performed by Han et al. (2019) showed that the internal shaft resistance contributed the least to the total resistance of the open-ended tubular pile, which was about 7%, while the external shaft resistance and annulus base resistance provided around 50% and 43% of the total resistance, respectively.

Some researchers investigated the shaft resistance and base resistance of piles in weak rocks (e.g., Matsumoto et al. 1995; Serrano and Olalla 2004; Abu-Hejleh et al. 2005; Huang et al. 2018). It is known that the strength of weak rocks falls in between the strength of soils and rocks, there are various classification systems for defining the boundaries between soils and weak rocks (i.e., lower boundary), and weak rocks and hard rocks (i.e., upper boundary). The commonly accepted lower boundary for the unconfined compressive strength of the intact rock is around 0.5 to 1 MPa, and the upper boundary is around 20 to 25 MPa (Bieniawski 1973; Klein 2001; Santi 2006; Kanji 2014; Zhai et al. 2017). To investigate the bearing mechanism of piles in weak rocks, Matsumoto et al. (1995) conducted static and dynamic pile testing on an open-ended steel tubular pile driven into a mudstone with an unconfined compressive strength of approximately 0.8 MPa. They observed that the pile did not reach the fully plugged condition during driving, while the soil plug displacement was almost equal to the pile head displacement during the static load test. However, their study was unable to investigate the internal and external shaft frictions separately. Later, Ng et al. (2001) compared the shaft resistance of bored piles socketed in various decomposed rocks including igneous, volcanic, and metasedimentary rocks. Through analysing the data from 79 tests in decomposed and

sedimentary rocks, Ng et al. (2001) concluded that the rate of mobilization of shaft resistance was generally scattered and there was no obvious relationship between the pile load – displacement curve and the socket length and pile diameter. Moreover, the model tests on piles socketed in the synthetic weak rock were conducted by Huang et al. (2018). In their study, the closed-ended piles were embedded in weak rock. They found that the shaft resistance increased with the depth, after reaching an ultimate value, then the shaft resistance reduced progressively. Review of existing literature shows that research studies on the axial load transfer mechanism of the open-ended tubular piles driven into weak rocks discussing both the internal and external shaft frictions separately, as well as the base resistance are scarce and indeed in demand.

On the other hand, pile shoes are often applied on the tip of the open-ended piles to prevent damage when driving the piles into the rock layer, to increase the base resistance or when there is a particular need to enhance the drivability. For example, the project of the free-standing Los Angeles Export Terminal wharf adopted the thick inner pile shoe to increase the annulus base area, hence, to enhance the pile toe as well as increase the capacity of the pile by increasing the base area (Bhushan 2004). In this project, the pile shoes with thicknesses of 50 mm and 100 mm were adopted for the pile with a wall thickness of 16 mm. Finlay et al. (2001) examined the inner and outer shaft friction and base resistance for piles with and without pile shoes in silt and sand by using a twin-wall system. They noted that the pile with shoe provided higher base resistance than the pile without a shoe. The pile with outer shoe provided the lowest external shaft friction, while the pile with inner shoe generated the lowest internal shaft friction. It is noted that the inner shaft friction was lower than outer shaft friction for all the tested piles. Finlay et al. (2001) found that the internal driving shoe could alter the horizontal stress distribution within the soil column and the plug length.

Another consideration in the open-ended tubular pile is the plugging mechanism. When the soil or rock enters the pile during the pile penetration and the increase in the height of the soil

or rock column would have the same rate as the increase in penetration depth, a fully coring mode is observed. However, under certain circumstances, the soil or rock column may move down as the pile penetrates deeper, in which the height of the soil or rock column may not increase (i.e., fully plugged mode) or increase at reduced rate (i.e., partially plugged mode) as the pile penetrates the ground (Ko and Jeong 2014; Guo and Yu 2016; Wang et al. 2020). Two parameters are commonly used to determine the degree of plugging, namely the incremental filling ratio (IFR) and the plug length ratio (PLR) (Brucy et al. 1991; Paik and Lee 1993). The IFR is calculated by the ratio of the incremental change of plug length (Δl) and the change in pile penetration depth (ΔH), as shown in Equation (5-1). Hence, for a pile in fully coring mode, the IFR is equal to 1, while for a fully plugged pile, the IFR is equal to 0. The PLR is the ratio of the soil plug length (l_i) and the penetration depth (H_i), as presented in Equation (5-2) (Paik and Lee 1993; Paik and Salgado 2003). Many researchers (e.g., Henke and Grabe 2008; Tomlinson and Woodward 2008; Guo and Yu 2016) believed that the degree of plugging could influence the internal shaft friction or the plug resistance, since the horizontal stresses inside the plug could increase during the formation of the plug.

$$IFR = \frac{\Delta l}{\Delta H} \times 100 \quad (5-1)$$

$$PLR = \frac{l_i}{H_i} \quad (5-2)$$

Although field or model tests can report the internal shaft friction, external shaft friction, and base resistance separately by using the twin-walled system, they are costly and the thickness of the instrumented pile is larger than the common thickness of the pile used in the field due to the feature of the twin-walled system required to separate internal and external shaft frictions. Thus, numerical simulations offer an alternative method of studying the micro-mechanics and macro-behaviour of pile penetration that can provide detailed information about the stress distribution and changes in the porosity of the geomaterial during the pile driving. Some

researchers (e.g., Li et al. 2019; Liu et al. 2019a; Liu et al. 2019b) conducted a numerical analysis for investigating the penetration process of open-ended tubular piles in sands. The two dimensional discrete element method (DEM) was adopted by Li et al. (2019) to investigate the installation processes and the soil plugging mechanism for the open-ended tubular piles. They simulated a pile with an inner diameter of 100 mm and a wall thickness of 10 mm penetrating into the sandy ground. From the change in the horizontal and vertical stresses of the soil column inside the pile, they concluded that the stresses varied exponentially with depth. Moreover, Liu et al. (2019a) also adopted 2D DEM analysis to study the behaviour of jacked open-ended piles with different diameters. They observed that the degree of plugging depended on the pile diameter. Meanwhile, via measuring displacements of each particle, it was found that soil flow along the inner surface of the pile was more significant than in the centre of the pile.

The discrete element method can simulate large deformation problems while replicating the rock mass with the bonded-particles that can control and investigate the interaction between individual grains (Potyondy and Cundall 2004). Therefore, the method has been adopted by many researchers to investigate the problems related to pile penetration or CPT test in granular materials (e.g., McDowell et al. 2012; Falagush et al. 2015; Chen et al. 2018; Li et al. 2019) and simulation of rock mass or cemented sand (e.g., Grenon et al. 2014; Bonilla-Sierra et al. 2015; de Bono et al. 2015; Scholtès and Donzé 2015). Research studies on open-ended tubular piles driven into weak rock are very scarce, and in this study, the DEM method was adopted to simulate this process. With the advantage of providing micro-mechanics and macro response in DEM, the response of the tubular piles in terms of inside and outside resistances, as well as base resistance of the pile is carefully studied. Indeed, the internal shaft friction, external shaft friction, and annulus base resistance of open-ended tubular piles were predicted from the simulations, while the stresses in the rock column inside the pile and in the surrounding rock

mass were analysed and could provide an insight into the bearing mechanism of the open-ended tubular piles in weak rocks.

5.3 Numerical Modelling

5.3.1 Fundamentals of the Contact Model

The particle flow code in three-dimension (PFC3D) was adopted in this study to conduct the DEM simulations for the pile penetration process in the weak rock. In the DEM, the rock grains are generally simulated via particles, and the forces and moments carried between particles are defined by contact models. In this study, the flat-joint (FJ) model was employed to control the interaction between particles. The FJ model is one of the bonded-particle models (BPM) and it is developed for simulating the mechanical behaviour of rock masses (Potyondy 2013). When two particles contact each other, there is a notional surface on each particle and an interface existed between each set of adjoining surfaces, as illustrated in Figure 5.1 (a). The interface was discretised into several elements that allowed partially breakage and each element could remain bonded or become unbonded. In the adopted 3D DEM simulation, the interface discretization was controlled by the number of elements in the radial (N_r) and circumferential (N_α) directions, as indicated in Figure 5.1 (b).

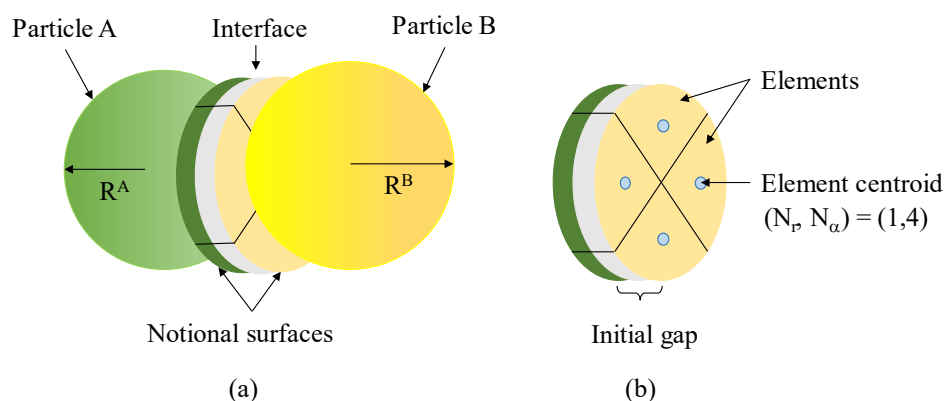


Figure 5.1. (a) flat-jointed particles with the contact interface; and (b) representatives of the elements discretised from the interface

Each element could carry a normal force, shear force and moment that obeyed the force-displacement constitutive law. The adopted particle interface elements were composed of a set of springs that had normal stiffness (k_n) and shear stiffness (k_s), as shown in Figure 5.2. The behaviour of a bonded element was linear elastic – perfectly plastic with Mohr–Coulomb shear failure limit with contact cohesion (c_c) and contact friction angle (ϕ_c), while an unbonded element followed linear elastic – perfectly plastic (frictional), with slip accommodated by imposing a frictional Coulomb limit with contact coefficient of friction (μ_c) as illustrated in Figure 5.2.

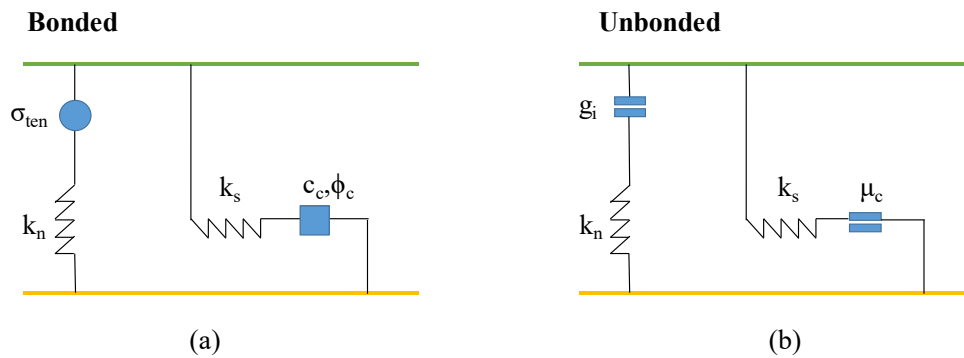


Figure 5.2. Rheological components of the flat-joint model for (a) bonded element, and (b) unbonded element

The force and moment carried by each element acted at the element centroid, as indicated in Figure 5.1 (b). The normal stress (σ^e) and shear stress (τ^e) on each element was calculated based on the normal force (F_n^e) and shear force (F_s^e) acting on the element and the area of the element (A^e), as presented in Equations (5-3) and (5-4). When the tensile stresses were applied and the interface gap was less than zero, the tensile stress at interface (σ_t) was calculated from the contact normal stiffness (k_n) and the interface gap (g), which followed the force-displacement constitutive law, as shown in Equation (5-5). It should be noted that the contact interface was discretised into several elements, the moments were implicitly embedded in the adopted FJ model (Ding and Zhang 2014; Wu and Xu 2016).

$$\sigma^e = \frac{F_n^e}{A^e} \quad (5-3)$$

$$\tau^e = \frac{F_s^e}{A^e} \quad (5-4)$$

$$\sigma_t = k_n g \quad (5-5)$$

Referring to Equation (5-5) and Itasca (2015), the contact normal stiffness was computed from the contact effective modulus (E_c), and the radius of the contacting particles (R^A , R^B), as presented in Equation (5-6). The adopted contact shear stiffness (k_s) depends on the normal-to-shear stiffness ratio (k^*) and the contact normal stiffness (k_n), as shown in Equation (5-7).

$$k_n = \frac{E_c}{R^A + R^B} \quad (5-6)$$

$$k_s = \frac{k_n}{k^*} \quad (5-7)$$

In the adopted contact model, the bond could break in tension or shear when the tensile or shear stresses on the element would exceed the tensile strength limit (σ_{ten}) or the shear strength limit (τ_{lim}), respectively, where the former is a pre-defined contact parameter, and the latter is computed by the contact cohesion (c_c), contact friction angle (ϕ_c), or contact coefficient of friction (μ_c), depending on the bond state of the element. It should be noted that for the unbonded element, the limit shear strength (τ_{lim}) was calculated from the relationship shown in Equation (5-8), which involves the contact coefficient of friction (μ_c) and the normal stress acting on the element (σ^e). For the bonded element, the limit shear strength was computed based on the contact cohesion (c_c), normal stress on the element (σ^e), and the frictional angle of the contact (ϕ_c), as captured in Equation (5-9).

$$\tau_{lim} = -\mu_c \sigma^e \quad (5-8)$$

$$\tau_{lim} = c_c - \sigma^e \tan \phi_c \quad (5-9)$$

5.3.2 Calibration of the Adopted Contact Model for Weak Rock

The weak rock sample adopted in the study is a pyroclastic weak rock reported by Cecconi and Viggiani (2001). The rock specimen was from the Colli Albani in Central Italy that had a dry density of around 1460 kg/m^3 and a porosity of 0.45. The mean diameter of the rock sample (D_{50}) was 2.5 mm and the unconfined compressive strength of the rock specimen was around 2 MPa, which falls into the strength range for weak rock (Bell 2000; Santi 2006). The triaxial tests were simulated numerically with a dimension of $100 \times 100 \times 200 \text{ mm}$, as shown in Figure 5.3 (a). To replicate the properties of the weak rock, a density that was approximately the same as in the experiments was adopted in the DEM simulations. The mean diameter (D_{50}) of the particles was enlarged to 5 mm to maintain the efficiency of the calculation, similar to the previous research studies (Lu and Frost 2010; de Bono and McDowell 2014). The maximum diameter to the minimum diameter (D_{max}/D_{min}) of 1.66 was employed, which is often adopted in the simulation of rock masses (e.g., Potyondy and Cundall 2004; Ding and Zhang 2014; Chen 2017). The particles were randomly distributed into the sample to achieve the porosity of 0.45 similar to the laboratory sample.

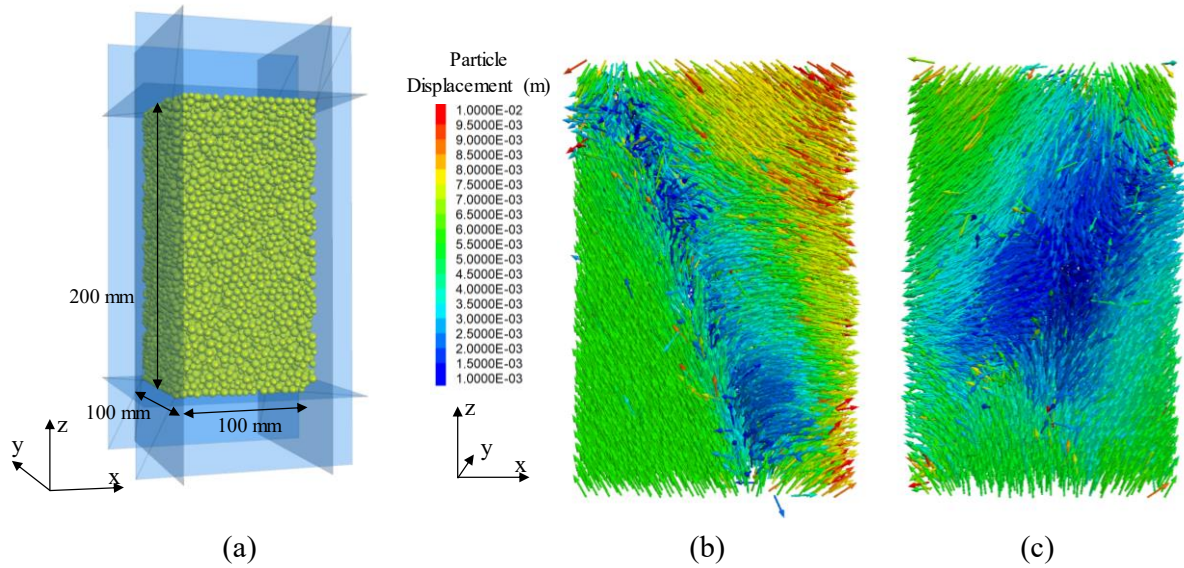


Figure 5.3. (a) Numerical triaxial test sample dimension; (b) particle displacement at the end of the triaxial test for confining pressure of 100 kPa; and (c) particle displacement at the end of the triaxial test for confining pressure of 350 kPa.

The micro-parameters required in the DEM model were calibrated through triaxial tests. The wall servo function was set to the sample boundary to bring the sample to the desired confining pressures, which were 100 kPa and 350 kPa as in the laboratory experiments. Then, the top and bottom walls were moved towards each other with a constant velocity simulating the loading process in the laboratory, while the side walls could maintain the confining pressure via wall servo function. The loading rate was slow enough to keep the quasi-static loading condition, as referring to Zhang et al. (2019). Through the trial and error process, the micro-parameters were back-calculated so that the mechanical behaviour of the numerical samples exhibited a reasonable match with the experimental results, as illustrated in Figure 5.4. The calibrated micro-parameters are summarised in Table 5.1. It is evident that the DEM simulation could capture the response of weak rock specimen subjected to a triaxial shearing with good agreement with experimental results. As observed in Figure 5.4 (b), the predicted volumetric strains slightly exceeded the experimental results, which could be potentially due to the fact

that the confinement in the numerical modelling was controlled by rigid walls instead of a deformable membrane utilised in the experiment. The particle displacement diagrams after the triaxial test for confining pressure of 100 kPa and 350 kPa are presented in Figures 5.3 (b) and (c), respectively. It is evident that the specimen tended to form a sliding surface under confining pressure of 100 kPa, while the specimen tended to split under a higher confining pressure of 350 kPa.

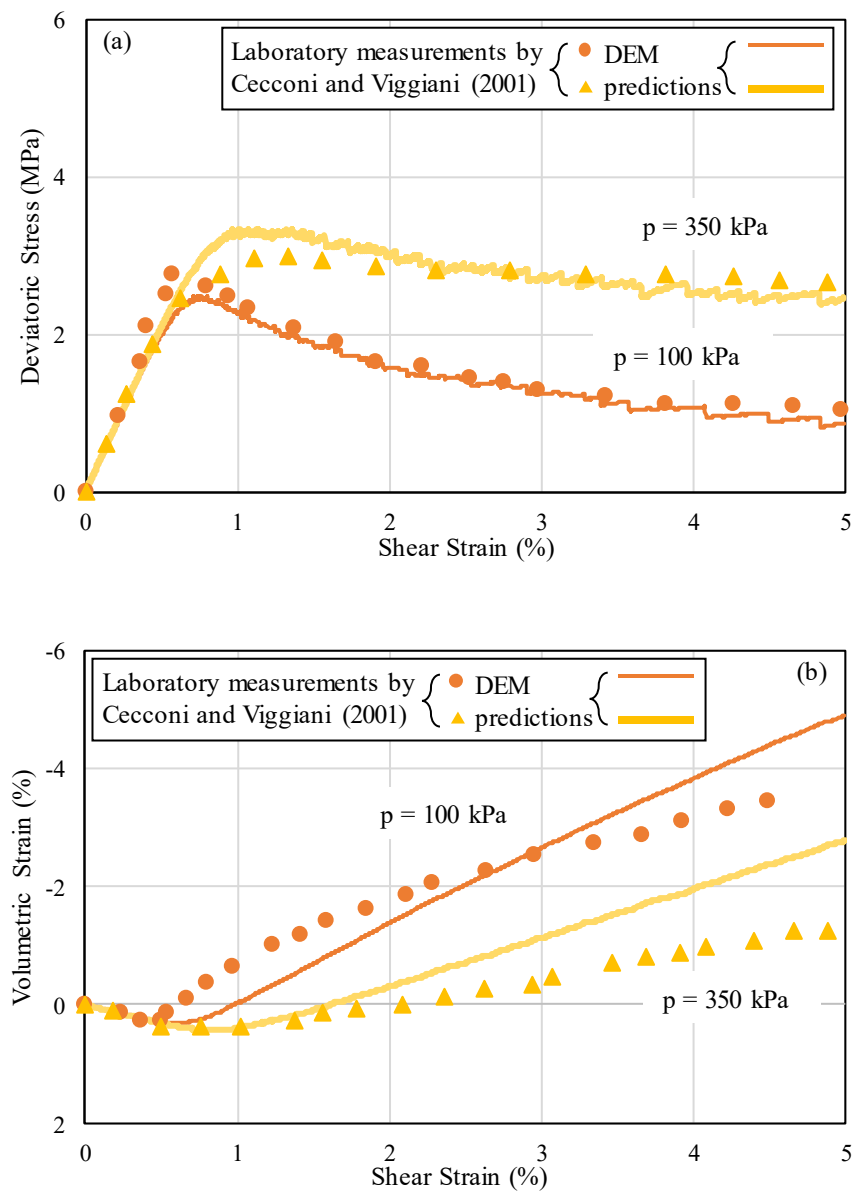


Figure 5.4. Calibration exercises comparing with the experimental results for the weak rock

Table 5.1. The calibrated micro-parameters adopted in the numerical model to simulate pyroclastic weak rock

Property	Value
The number of elements in the radial direction(N_r)	1
The number of elements in the circumferential directions (N_α)	4
The contact effective modulus (E^*)	0.8 GPa
The normal-to-shear stiffness ratio (k^*)	2
The tensile strength limit (σ_{ten})	1 MPa
The contact coefficient of friction (μ_c)	0.35
The contact cohesion (c_c)	2 MPa
The frictional angle of the contact (ϕ_c)	40°

5.3.3 Numerical Modelling of Pile Penetration

A numerical model with a 30° segment was built to conduct analysis on the open-ended tubular pile penetration as illustrated in Figure 5.5. Due to the asymmetry of the problem and the enormous calculation effort required in DEM analysis, many researchers were seeking the method to solve the problem effectively without diminishing the quality of the results. For example, the 30° segment testing chamber was adopted by several other researchers to simulate the penetration of the cone penetrometer (e.g., McDowell et al. 2012; Falagush et al. 2015). The model in this study had a diameter of 3 m and a height of 3 m, as shown in Figure 5.5 (a). The selected open-ended tubular pile had an outer diameter (D) of 0.2 m, representing a small

diameter tubular pile (Hannigan et al. 1997; Rajapakse 2008). As illustrated in Figure 5.5 (c), the thickness of the pile (t_{pile}) was 12 mm, which is commonly used in the open-ended tubular piles (Hannigan et al. 1997). In this study, the investigated final penetration depth (H) was 1 m. Hence, the ratio of model diameter to the pile diameter was $15D$, and the base of the model was located at least $10D$ below the pile tip after installation, which was similar to or larger than the values adopted by other researchers for penetration investigation (e.g., Kinloch and O'Sullivan 2007; Lobo-Guerrero and Vallejo 2007; Butlanska et al. 2013; Falagush et al. 2015).

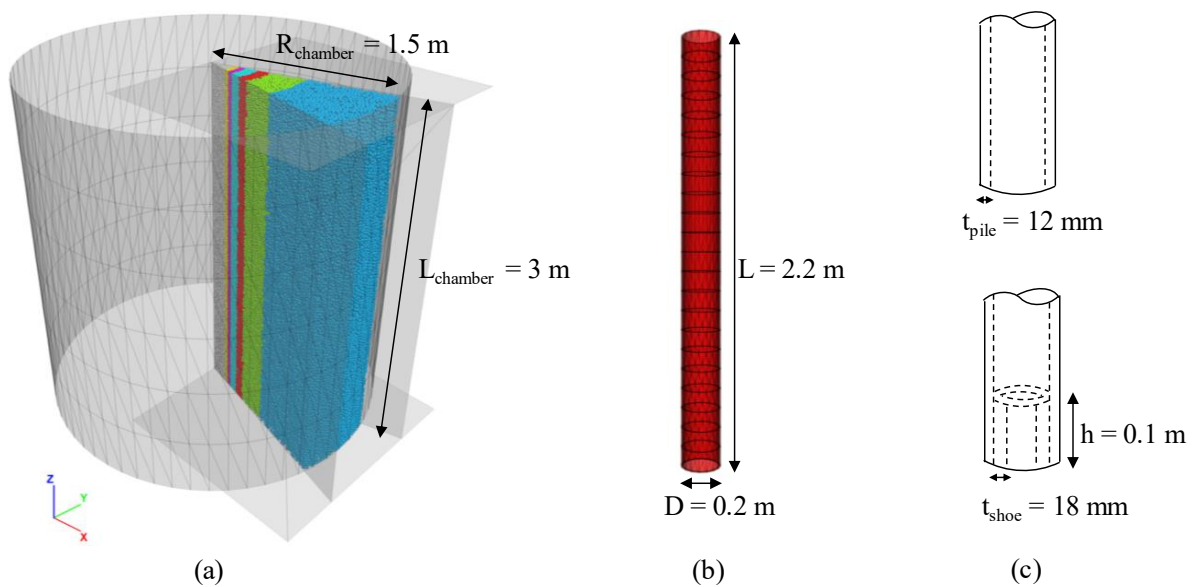


Figure 5.5. Geometry and dimension of the (a) the testing chamber; (b) the tested open-ended tubular pile; and (c) schematic diagram of the open-ended tubular pile with and without a shoe

Considering the size of the pile and the number of particles in contact with the pile toe, the particles at the area where the pile would break through the rock masses should be sufficiently small and realistic in size to ensure enough number of particles would interact with the pile toe. Obviously simulating the entire model with the fine particles would result in an excessive number of particles making the required computation infeasible. Therefore, the particle refinement method was adopted such that the particles at the areas of interest near the pile were

sufficiently small, and then the particle size gradually increased with radial distance from the pile. Following the recommendation by McDowell et al. (2012), the particle size increased with an upscale factor in a way that the small particles could not migrate into the voids of the large particles. The adopted upscale factors in this study are shown in Figure 5.6. It should be noted that a similar approach for upscaling was adopted in the literature by many other researchers (e.g., Camusso and Barla 2009; McDowell et al. 2012; Shi et al. 2019). To avoid the small particles migrating into the voids between large particles, the geometry of the numerical model was subdivided into seven regions. The region at or near the pile was filled with the fine particles having the same size and distribution as those adopted in the triaxial test used for calibration. Then, the next region was a transition area that had an upscale factor of 1.25, as indicated in Figure 5.6. The upscale factor kept increasing with the radial distance as shown in Figure 5.6. All model regions had the same porosity of about 0.45 and followed the same particle size distribution pattern (i.e., $\frac{D_{max}}{D_{min}} = 1.66$). The total number of particles generated in this 30° segment was approximately 557,000.

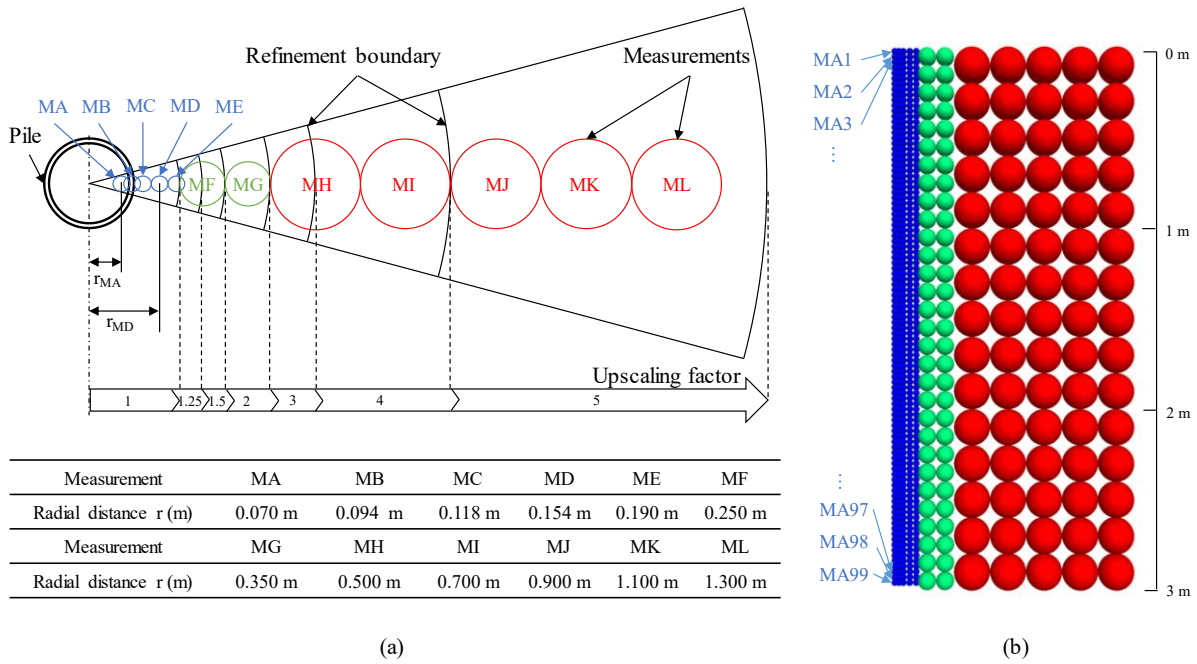


Figure 5.6. (a) Schematic illustration of the top view of the testing chamber with particle refinement upscale factors and radial distances; and (b) the side view of the measurements from top to bottom of the model

Subroutines were programmed for the measurement function in the adopted DEM analysis to record the porosity and stress distributions within the weak rock during pile penetration, as illustrated in Figure 5.6. Due to the geometry of the model and adopted region sizes, three different sizes of the measurement spheres were selected. Figure 5.6 (a) shows the schematic top view of the testing chamber, with measurement spheres named on the figure and the corresponding radial distances (r) from the centre of the pile. The measurement spheres were also extended downwards from the surface allowing data collection within the rock mass in the vertical direction, as shown in Figure 5.6 (b). For example, measurement spheres Series MA recorded the porosity and stresses inside the open-ended tubular pile near the pile wall during driving, whereas measurement spheres series MC recorded the information just outside the open-ended tubular pile near the wall during driving.

The initial condition applied to the model was a confining pressure of 100 kPa on the top and 145 kPa at the bottom. The side wall of the model was discretised into 6 sections with equal height with assigned lateral stresses corresponding to the vertical stresses considering the coefficient of lateral earth pressure at rest (K_0) as 1 to simulate a medium tectonic stress level as reported by other researchers (González de Vallejo and Hijazo 2008; Terente et al. 2017). After the model reached the equilibrium state under the gravity loading, the average porosity, radial stresses and vertical stresses measured from the measurement spheres were reported as plotted in Figure 5.7. After establishing the initial conditions, the model pile that had an outer diameter (D) of 200 mm and a wall thickness (t_{pile}) of 12 mm, as shown in Figures 5.5 (b) and (c), was introduced into the model and penetrated into the rock mass with a constant velocity until it reaches a depth of 1 m. To simulate the friction between the pile and the rock mass during the penetration, the friction angle between the rock and pile was set to 35° , which is a typical value for a rock - steel interface as suggested by Terente et al. (2017). The internal and external shaft frictions, and base resistance were recorded on the internal and external shafts, and annulus area of the pile toe, respectively. A workstation with Intel Xeon Gold 6146 CPU @ 3.2 GHz and a RAM of 96.0 GB was used for this simulation. The required time to establish the initial conditions was about 30 days. For the pile penetration processes of reaching 1 m depth, the simulation time was about 45 days for the pile without a shoe and about 48 days for the pile with a driving shoe.

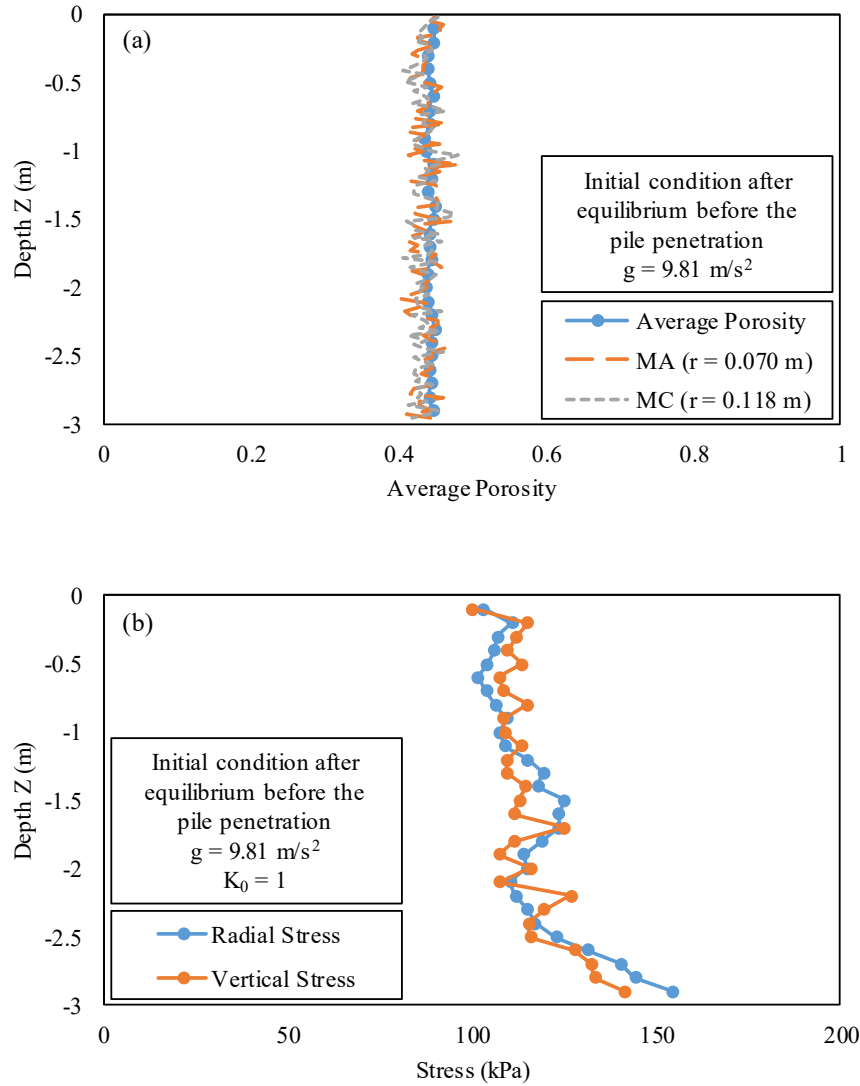


Figure 5.7. The initial condition of the large-scale model of (a) distribution of the porosity, and (b) vertical stress and radial stress

5.4 Results and Discussions

5.4.1 Predicted Resistances

The predicted internal and external shaft frictions, and base resistance during the penetration of the pile into the weak rock is shown in Figure 5.8. It is noteworthy to state that the base resistance was recorded from the annulus area of the pile toe (and not the entire cross section of the pile base). It is evident that the base resistance developed rapidly at the initial stages of driving, and then it was fully mobilised after a depth (Z) of 0.2 m (i.e., $Z = 1D$, i.e., depth

equal to the pile diameter). This observed response is similar to what is reported in the literature for the variations of the tip resistance in the cone penetrometer test (CPT) with the depth in a uniform ground condition (e.g., Schnaid 1990; Butlanska et al. 2013; Falagush et al. 2015). It should be noted that some researchers (e.g., Jardine et al. 2005; Han et al. 2019) had reported similar mechanisms for mobilisation of pile base resistance after significant penetration and CPT cone resistance.

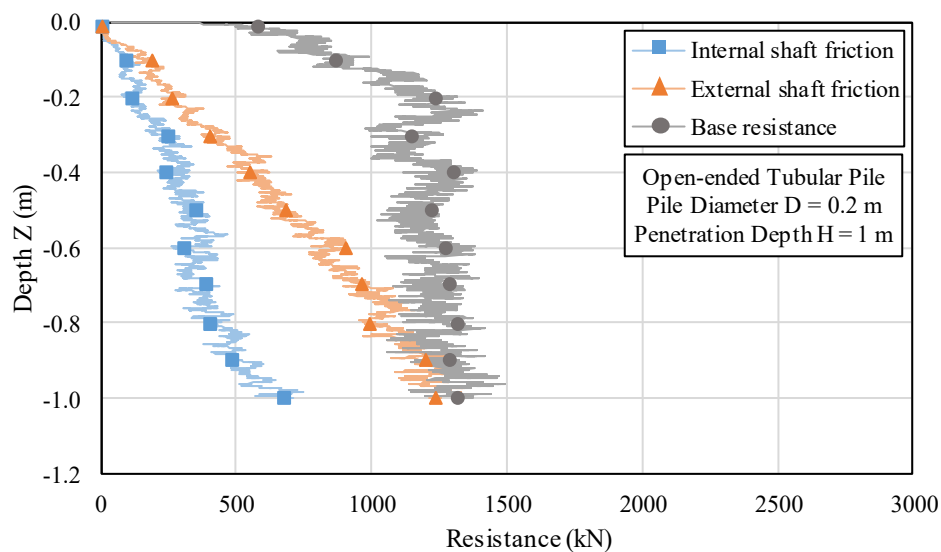


Figure 5.8. Pile resistance of open-ended tubular pile with depth

As expected, the increase of the total external shaft friction was approximately linear with depth into the rock mass as depicted in Figure 5.8, which is due to the fact that the external shaft area increased continuously and linearly during penetration. This trend matched well with the design method of shaft resistance of open-ended tubular pile in weak rocks reported by Terente et al. (2017), in which the shaft resistance should increase linearly with pile embedment depth. It is observed that the base resistance was mobilised at the early stage of the penetration process in the weak rock and was higher than the shaft friction, while after certain penetration depth, the shaft friction could overcome the base resistance generated at the annulus area.

Meanwhile, the internal shaft friction increased as the pile penetrated deeper but with a reduced rate. It is noted that the external shaft friction of the tested pile was larger than the internal shaft friction (refer to Figure 5.8). Indeed, the penetration of the pile altered the characteristics of the rock mass and referring to Long (1995), the integrity of the rock mass was changed as the pile broke through the rock mass and shattered the in situ rock fabric.

The contact states between particles are shown in Figure 5.9. It is observed that the vast majority of unbonded contacts were observed around the pile shaft, which was mainly induced by the penetration of the pile and breaking through the rock mass and unbonding the contacts. It is noteworthy to state that when a bond breaks in tension as well as shear, the contact becomes fully unbonded. When the pile penetrated deeper, as presented in Figure 5.9 (b) at the penetration depth (H) of 1 m, more contact bonds which were close to the centre of the pile broke both in tension and shear to result a higher number of fully unbonded contacts compared to the case in the penetration depth of 0.4 m (refer to Figure 5.9 (a)). Meanwhile, these fully unbonded contacts tended to be concentrated inside the pile as shown in Figure 5.9 (b). For the rock mass at the far field, many contacts remained bonded or only broke in tension or shear, and some of the contacts were unbonded. That indicated there was a higher chance that the rock mass inside the tubular pile might break into small blocks rather than the rock mass outside the pile.

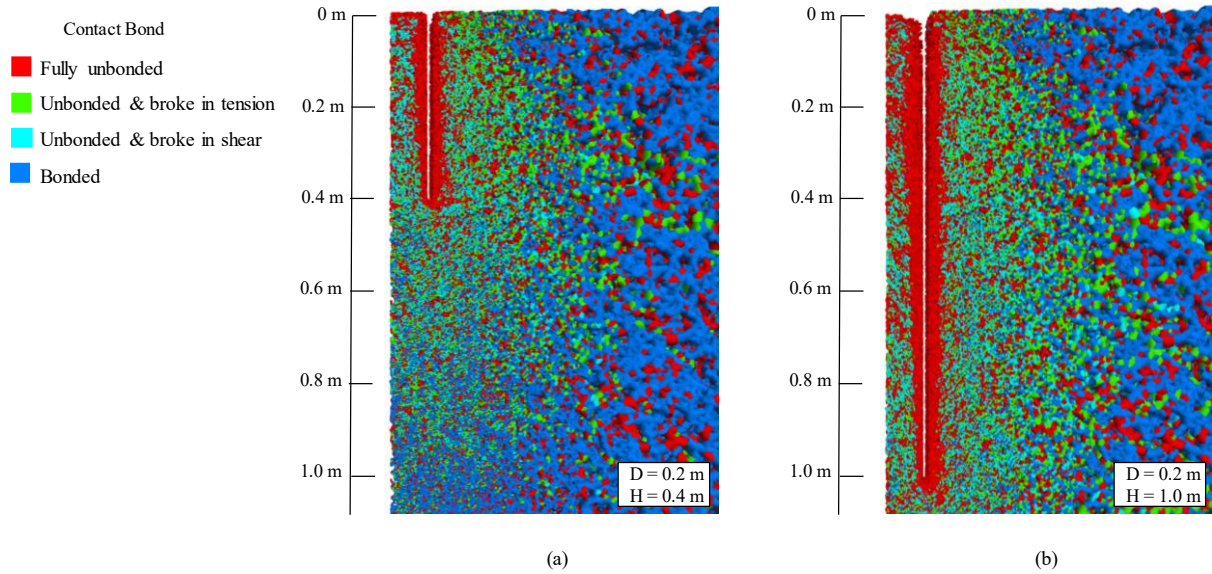


Figure 5.9. Contact network for the open-ended tubular pile without driving shoe at a penetration depth of (a) 0.4 m, and (b) 1.0 m

5.4.2 Unit Shaft Frictions

The unit internal and external shaft frictions at different depths are presented in Figures 5.10 (a) and (b), respectively. The penetration depth (H) was normalised to the outer diameter of the pile (D). As illustrated in Figure 5.10 (a), at the normalised penetration depth (H/D) of 1 (i.e., $H = D = 0.2$ m), the unit internal shaft friction (f_{s-i}) increased sharply at the bottom $0.5D$, which was also observed in other normalised penetration depths. Moreover, the final unit internal shaft friction at each penetration depth increased as the pile penetrated deeper. It can be noted that the internal shaft friction was mobilised mainly at the bottom $0.5D - 1D$ of the rock column inside the pile irrespective of the penetration depth. For the penetration depth (H) of 1 m, the internal shaft friction was concentrated at the bottom $0.1H - 0.2H$. Comparable findings were also reported by Ko and Jeong (2014) for the open-ended piles in sandy soil, and it was concluded that the inner shaft resistance was mostly mobilised at the bottom portion of the soil plug, which was approximately $0.15H - 0.2H$ of the penetration depth. Indeed arching happened in the rock column inside the pile, which was very evident at the bottom portion of

the rock plug. The increase in radial stresses due to the formation of the arch contributed to the mobilisation of the shaft friction inside the pile wall. It is observed that the radial stresses inside the rock column were higher than the radial stresses outside the pile near the pile toe at the depth of 1 m as shown in Figure 5.13 (c).

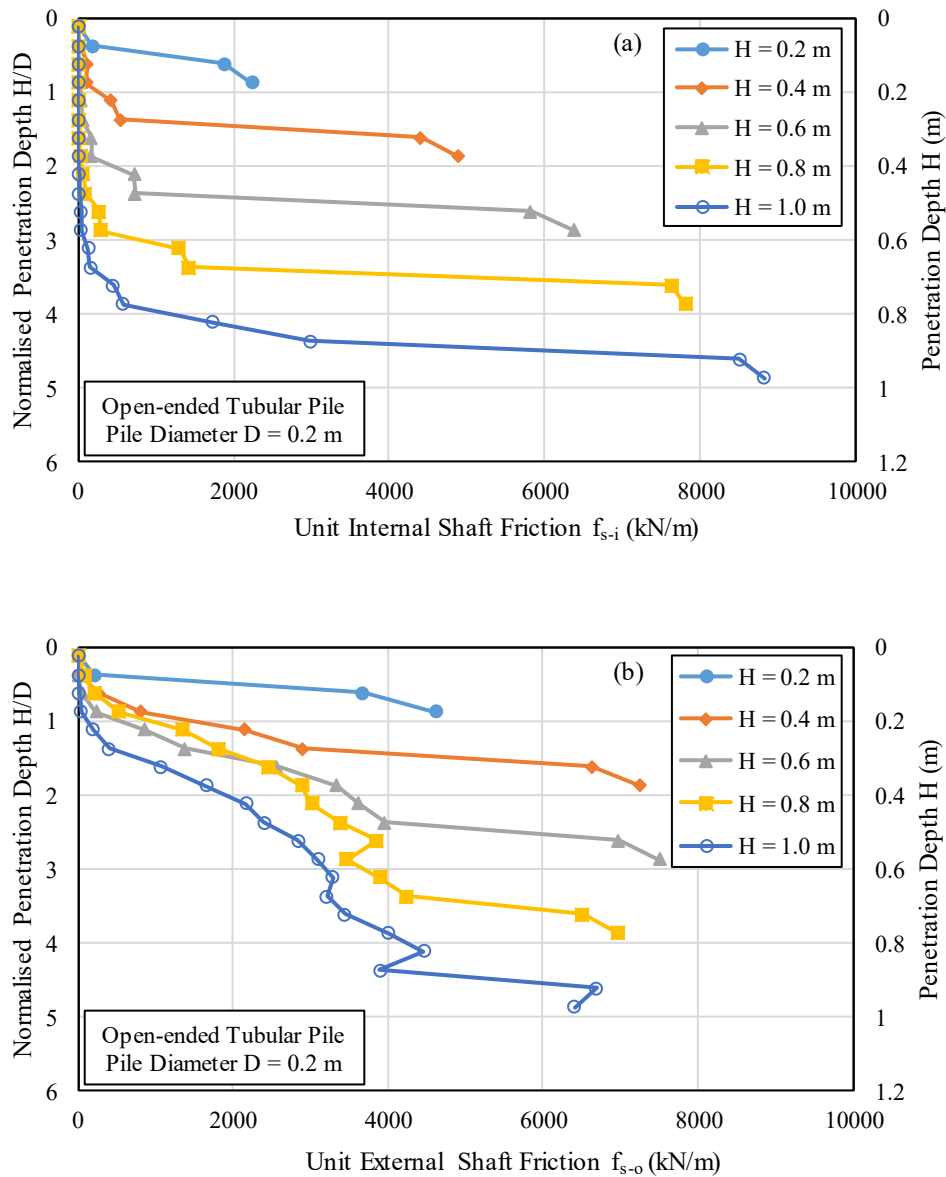


Figure 5.10. (a) Unit internal shaft friction of open-ended tubular pile at different penetration depths; and (b) Unit external shaft friction of open-ended tubular pile at different penetration depths

The distribution of the unit external shaft friction (f_{s-o}) with depth was significantly different from the unit internal shaft friction (f_{s-i}), as shown in Figure 5.10 (b). For the unit external shaft frictions at normalised penetration depth of 2 to 5, the increase in the unit external shaft friction was minimal at shallow depth (i.e., $H = 1D$), and then the increase was tended to be linear when the normalised penetration depth was between 2 and 5 (refer to Figure 5.10 (b)). Furthermore, beside the penetration depth of $1D$ (i.e., $H = 0.2$ m), the final unit external shaft friction tended to approach a similar value.

5.4.3 Particle Displacement Patterns

The individual particle displacement can be plotted in the DEM to establish the displacement field in the ground induced by the pile penetration. As shown in Figure 5.11, the rock mass in the close vicinity of the pile was influenced the most by the installation of the open-ended tubular pile. At the depth of 0.1 m (refer to Figure 5.11 (a)) where the pile cut through the ground, the particles in contact with the pile wall moved down due to friction between rock and pile, and ground deformation in excess of 20 mm was observed. As expected the ground displacement reduced significantly with the radial distance from the pile, with the far field displacement well below 1 mm, confirming the suitable model size. In addition, the rock inside the pile experienced rather minor deformations of less than 15 mm, as shown in Figure 5.11 (a). As the pile penetrated deeper (up to 1 m deep), referring to Figure 5.11 (b) and (c), all the rock particles inside the pile experienced more than 10 mm displacement and most of them went through a displacement greater than 20 mm, which indicated that partial plugging was observed and the rock mass inside the pile was impacted by the pile penetration. Indeed, as depicted in Figure 5.11 (c), the rock column inside the pile moved down during the penetration as the top surface of the rock column inside the pile was dropped. Meanwhile, it is noted that the top surface of the rock column inside the open-ended tubular pile was inclined, because the friction between the pile shaft and rock column dragged the rock grains down, while the rock

grains around the centre of the rock plug experienced shearing and did not move down at the same rate as the sliding observed on the pile shaft.

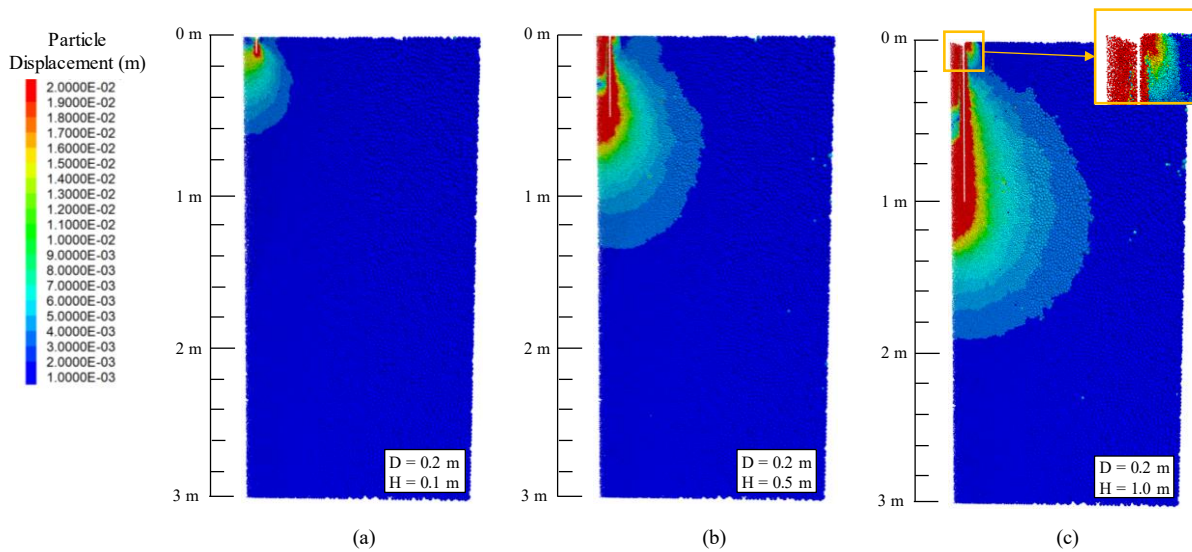


Figure 5.11. Individual particle displacement of the open-ended tubular pile without pile shoe at a pile penetration depth of (a) 0.1 m, (b) 0.5 m, and (c) 1.0 m

5.4.4 Porosity and Stress Distributions

Figure 5.12 (a) and (b) compare the initial porosity of the measurements in series MA ($r = 0.07$ m) and MC ($r = 0.118$ m) with the corresponding porosity after the pile penetration to the depth of 1 m in the weak rock; note measurement spheres MA and MC represent the rock column inside and outside the pile right next to the pile wall, respectively. It should be noted that due to some degree of plugging, the rock surface was dropped inside the pile with no particles present, which can also be observed in Figure 5.11 (c). As observed in Figure 5.12 (a), the porosity of the rock column inside the pile decreased with increasing depth and reached the lowest value near the pile toe, which is similar to the findings of the sand plug reported by Li et al. (2019). At the top section of the rock plug (i.e., $0.03 \text{ m} < Z < 0.8 \text{ m}$), the porosity was higher than the initial porosity due to the dilation of the rock mass. The dilation might be due to the blocks of broken rock moving relatively to each other (refer to Figure 5.9 (b)), which

was also mentioned by other researchers as the main reason for dilation in rock (e.g., Kaiser et al. 2000; Zhao et al. 2010). While at the bottom portion of the rock plug (i.e., $Z > 0.9$ m), where the porosity was lower than the initial porosity, the rock mass was compressed. Meanwhile, referring to the measurement spheres series MC ($r = 0.118$ m) outside the tubular pile as depicted in Figure 5.12 (b), it is evident that the rock mass dilated at the top portion (i.e. $Z < 0.3$ m), while the porosity at the middle portion (i.e. $0.5 \text{ m} < Z < 0.8 \text{ m}$) of rock slightly reduced followed by slight increase beneath the pile toe.

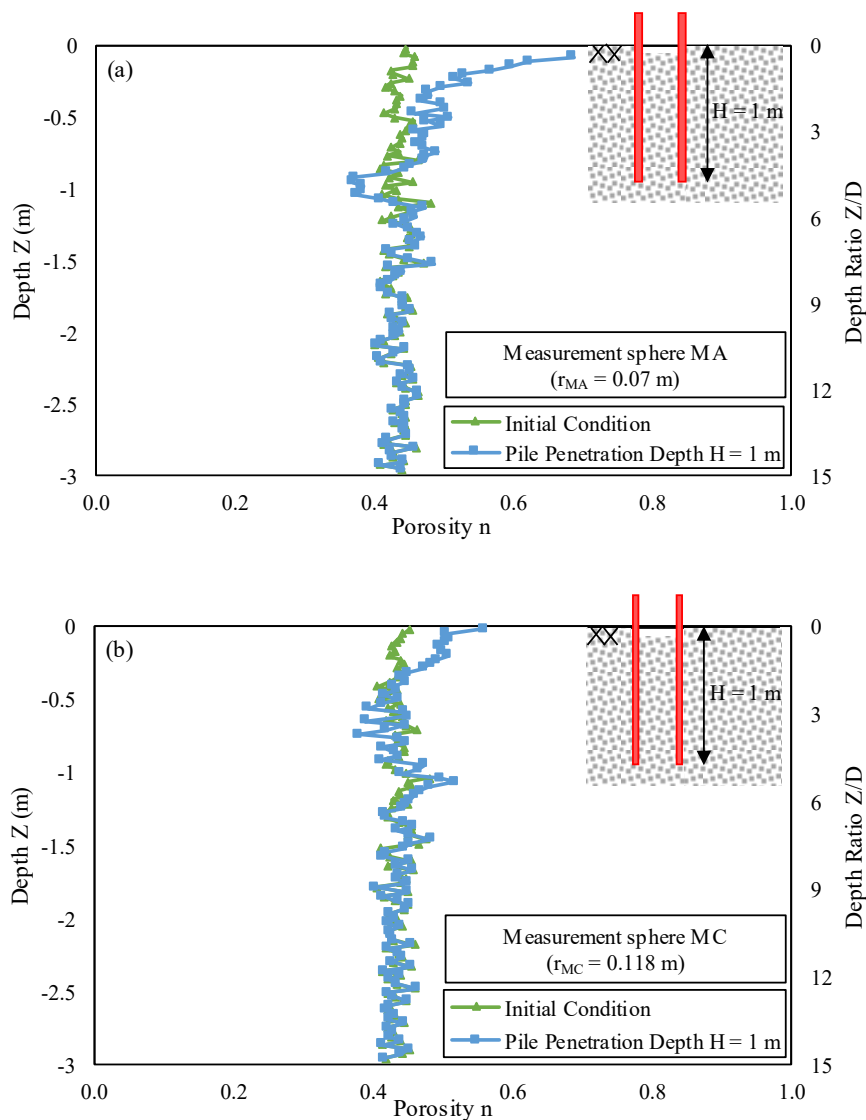


Figure 5.12. The porosity distribution pile before and after driving for the open-ended tubular pile (a) at the location inside the pile; and (b) at the location outside and adjacent to the pile

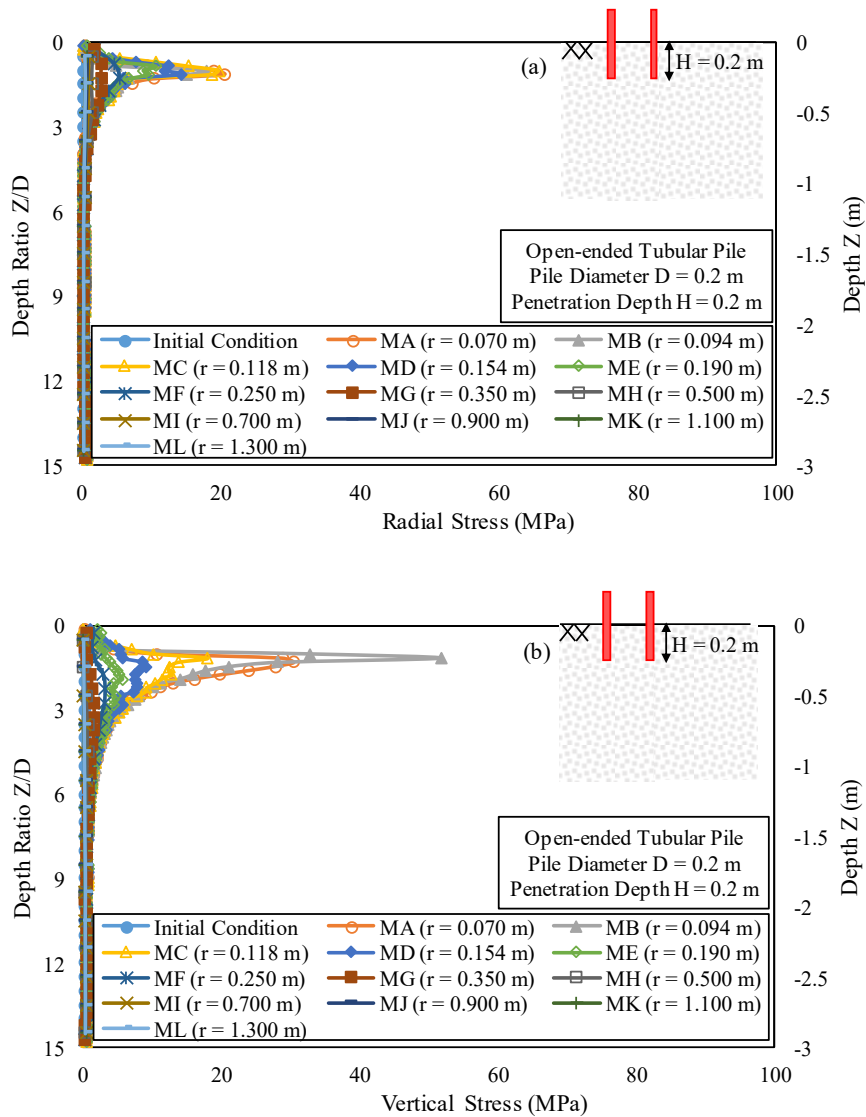
To further investigate the axial bearing mechanism of the open-ended tubular piles in weak rock, the radial and vertical stresses measured from the measurement spheres are presented in Figure 5.13. The stresses at the depth of 0.2 m are presented in Figures 5.13 (a) and (b). It is noted that both the radial and vertical stresses increased significantly at the tip of the pile, especially near the pile wall, represented by measurement spheres MA (inside the pile) and MC (right outside the pile). As expected, the impacts of installation on the stress field of surrounding soil reduced rapidly with the radial distance as presented in measurements spheres MD, ME and MF. Eventually, in the far field of the model, the stress field was approximately the same at the initial stress field, as the measurement sphere ML shows.

Indeed, the highest vertical stress was observed just beneath the pile toe, as refer to measurements sphere MB as evident in Figure 5.13 (b), which mobilised the base resistance of the open-ended tubular pile during driving. The vertical stress inside the rock column (i.e., measurement sphere MA) was higher than the stress in the rock mass just outside of the pile (i.e., measurement sphere MC). Moreover, the vertical and radial stresses in the measurement sphere MC had comparable values, while the vertical stresses were much higher than the radial stresses inside the pile and beneath the pile toe (i.e., measurement spheres MA and MC). This indicated that the shear strength of the rock mass inside and beneath the pile was higher than that of outside the pile.

Figures 5.13 (c) and (d) display the radial and vertical stresses from the measurements collected at the depth of $Z = 1$ m. Similarly, the highest radial and vertical stresses were observed at the level of the pile toe and higher radial and vertical stresses were observed as the depth increased from $Z = 0.2$ m (i.e., $Z/D = 1$) to $Z = 1$ m (i.e., $Z/D = 5$). It is noticed that the radial stresses in the measurement sphere MA (inside the pile) were much higher than the measurement spheres outside the pile, which revealed arching occurring in the rock column inside the pile. Indeed, the higher radial stresses inside the pile resulted in higher unit internal shaft friction as depicted

in Figure 5.10 (a), which are also in line with field results and numerical predictions reported by other researchers for tubular piles driven in soils (e.g., Jardine et al. 2006; Li et al. 2019).

The peak radial and vertical stresses at the depth of 0.2 m and 1 m are plotted in Figure 5.13 (e). Clearly, the peak stress reached the highest value at the close vicinity of the pile wall, and then the stresses reduced exponentially with the radial distance, which had similar response to the closed-ended piles in sands reported by Jardine et al. (2013) and Yang et al. (2014).



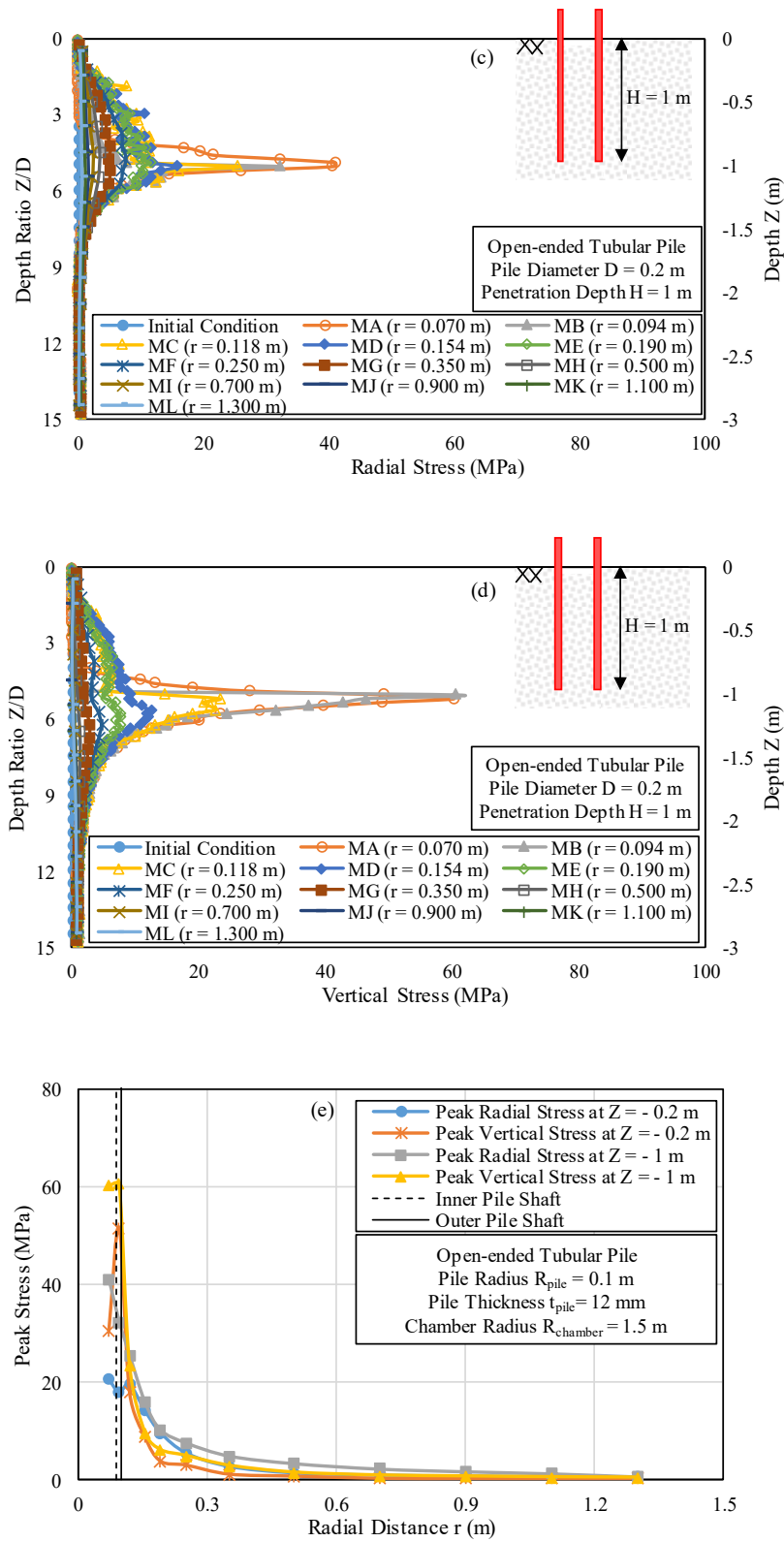


Figure 5.13. Stresses at different depth for open-ended pile: (a) radial stress at 0.2 m, (b) vertical stress at 0.2 m, (c) radial stress at 1 m, (d) radial stress at 1 m, and (e) peak stresses at 0.2 m and 1 m

5.5 Impacts of Pile Shoe

5.5.1 Predicted Resistances for Pile with Driving Shoe

Inner pile shoe is commonly applied to the open-ended tubular pile when driven into the rock, which can strengthen the pile toe and allow hard driving. Hence, the bearing mechanism of the open-ended tubular pile with an inner pile shoe was also examined in this study. A shoe with a height of 100 mm and a thickness of 18 mm was attached inside the pile wall, as illustrated in Figure 5.5 (c). Then the pile was loaded with the same velocity as the original pile without the shoe to a depth of 1 m in the same weak rock profile as shown in Figures 5.5 (a) and 5.7, so the results could be compared. Figure 5.14 shows the shaft and base resistances of the pile with the driving shoe.

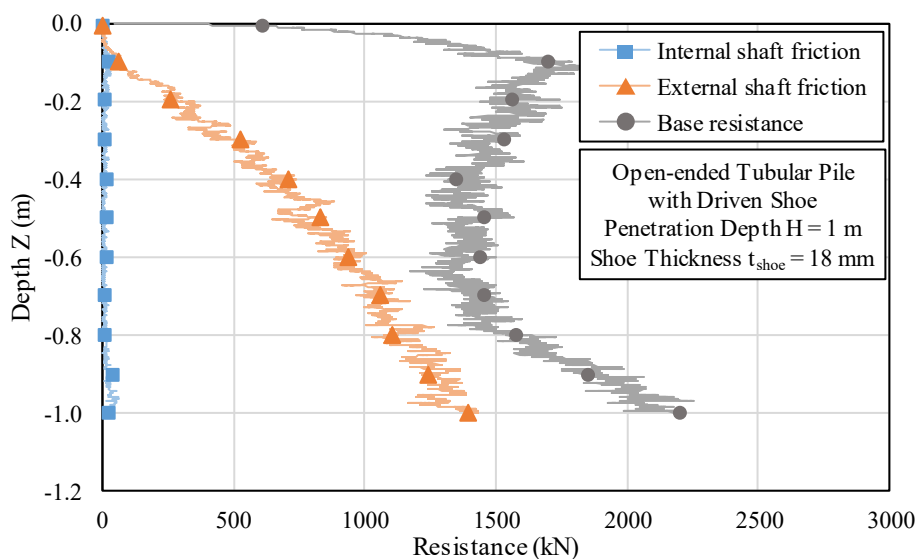


Figure 5.14. Pile resistance of open-ended tubular pile with an inner pile shoe

Similar to the pile without a shoe (refer to Figure 5.8), the external shaft resistance of the pile with inner pile shoe increased approximately linearly as the pile penetrated deeper, as shown in Figure 5.14. The external shaft resistance reached a value of around 1,390 kN at the final depth of 1 m, which is comparable with the corresponding value for the pile without a shoe (i.e., 1,256 kN). As expected, the base resistance for the pile with the shoe was higher than the

pile without a shoe, because the base resistance stemmed from the area of the annulus base, and the area of the pile with driving shoe was certainly more. It is noted that the annulus area of the pile was more than doubled (i.e., the ratio of the annulus area of the pile without a shoe to a pile with the shoe $\frac{A_p}{A_p+A_{shoe}} = 2.26$) by attaching the pile shoe, and the base resistance increased by 67%, from 2,201 kN to 1,313 kN. Similarly, for the field tests of open-ended tubular piles in soils reported by Bhushan (2004), the pile toe capacity increased by 86% when the annulus area was nearly tripled (i.e., $\frac{A_p}{A_p+A_{shoe}} = 2.89$) by attaching the driving shoe.

Comparing Figures 5.8 and 5.14, it is evident that the internal shaft friction of the open-ended tubular pile with the inner shoe was significantly lower than the corresponding pile without a shoe. Indeed the inner pile shoe alters the flow of the rock mass inside the pile when the weak rock enters the pile during penetration. As the pile advanced into the rock mass further and after the rock entered the pile and passed the pile shoe, the radial stress of the rock mass inside the pile dropped abruptly due to losing the confinement from the pile shoe. Hence, the pile internal shaft friction was reduced as a result of introducing the inner pile shoe. Field and experimental studies reported by De Nicola and Randolph (1997) and White et al. (2000) in soils also confirmed this reduction in the internal shaft friction. In terms of the total axial load capacity, the pile with driving shoe had a slightly higher capacity than the pile without a shoe. For the given thickness of the shoe in this study, the pile with inner pile shoe had a total capacity of 3,616 kN, while the corresponding pile without a shoe had a total capacity of 3,243 kN.

Moreover, the contact states between particles for the open-ended tubular pile with inner pile shoe at the penetration depths of 0.1m and 1 m are shown in Figures 5.15 (a) and (b), respectively. At the penetration depth (H) of 0.1 m, the contacts for the rock inside the pile were broken in shear or tension. It is noted that particle contacts for the rock inside the pile were mostly fully unbonded at the penetration depth (H) of 1 m. For these rock inside the pile

around the shoe, only few contacts did not reach the fully unbonded state, refer to Figure 5.15 (b). The above mentioned observation indicates that the rock mass was shattered after entering the pile and passing the pile shoe. However, the degree of shattering of the rock mass inside the pile may also relate to the pile diameter and shoe thickness, which needs further study.

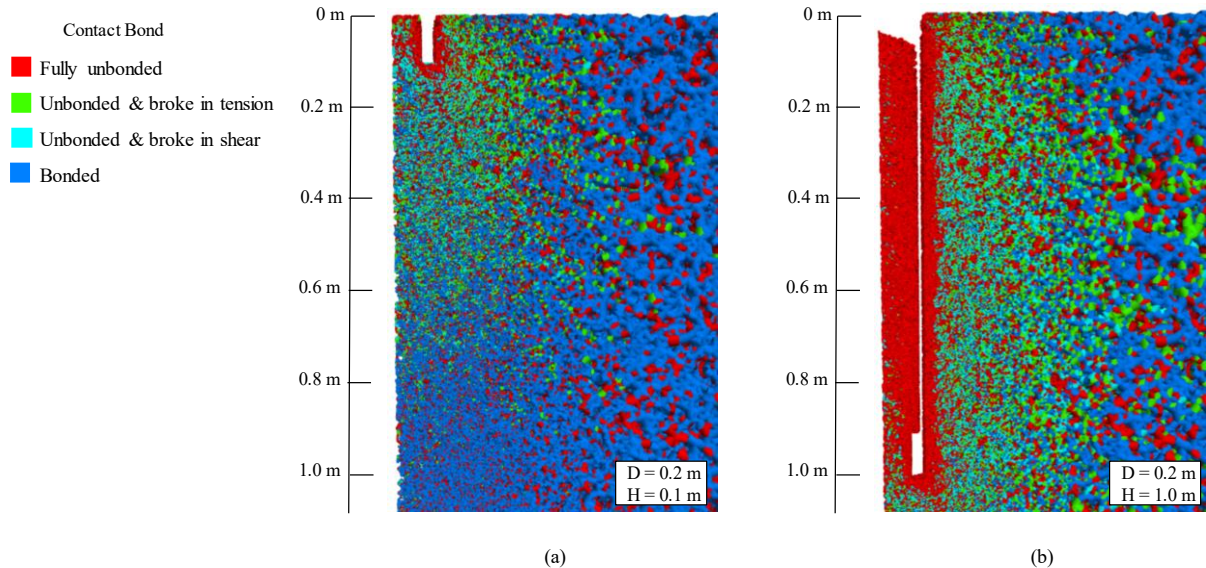


Figure 5.15. Contact network for the open-ended tubular pile with driving shoe at a penetration depth of (a) 0.1 m, and (b) 1.0 m

5.5.2 Effect of Pile Shoe on Unit Shaft Frictions

The unit internal and external shaft frictions for piles with and without shoes at the penetration depth of $5D$ (i.e., $H = 1$ m) are presented and compared in Figure 5.16. Indeed, a significant reduction in unit internal shaft frictions was observed by attaching the driving shoe inside the open-ended tubular pile, especially after the normalised penetration depth of $H/D = 3$ (i.e., $H = 0.6$ m). It is noted that the unit internal shaft friction of the pile with the shoe was concentrated at the bottom $0.5D$, where the shoe was located. Indeed, the shoe provided extra confinement to the rock inside the pile, and once the rock passed the pile shoe, the stress relief was evident, which resulted in decrease in the unit internal shaft friction. In comparison, for the pile without a shoe, the stress confinement also existed in the rock mass inside the pile due to the arching

effect, meanwhile, the radial stresses around the pile toe were significantly higher than the top portion of the rock column inside the pile, as evident in results of measurement sphere MA in Figure 5.13 (c). As shown in Figure 5.16, for the pile without a shoe, the unit internal shaft friction was concentrated at the bottom $1.5D$, where the most stress confinement was present. However, the unit internal shaft friction had similar value for both piles with and without shoe within the top section of the pile (i.e, $0 \text{ m} < H < 0.6 \text{ m}$), as shown in Figure 5.16. On the contrary, it is observed that the unit external shaft frictions were similar for the entire length of the piles with and without the shoe. Hence, it can state that the adopted inner pile shoe had minimal effect on the external shaft resistance.

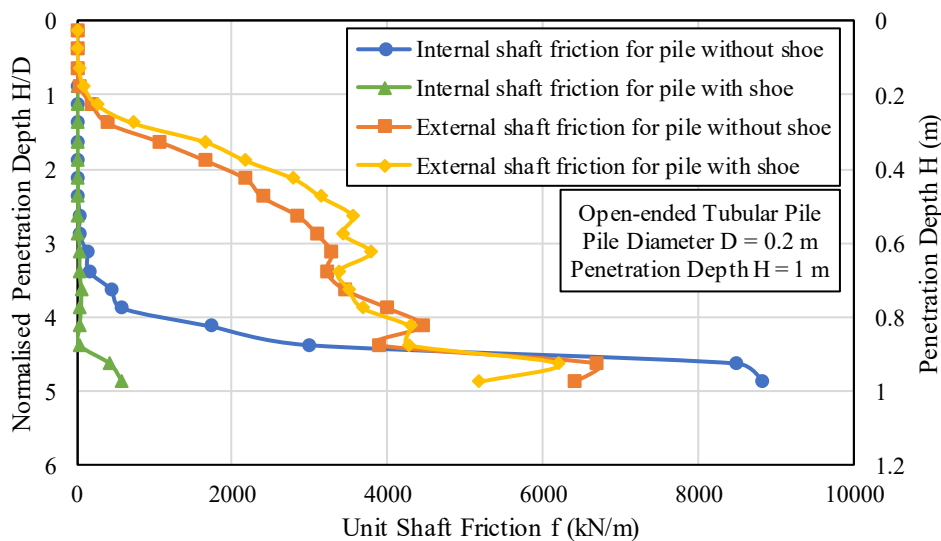


Figure 5.16. Comparison of the unit external and internal shaft friction for open-ended tubular piles with and without shoe

5.5.3 Porosity and Stress Distributions for Pile with Driving Shoe

Figure 5.17 presents the individual weak rock particle displacements when driving the pile with inner pile shoe. Clearly, due to the increase of the annulus base area by attaching the pile shoe, the influence zones at the penetration depths of 0.1 m and 0.5 m were larger than the open-ended tubular pile without a shoe (compare Figures 5.11 (a) and 5.17 (a), and Figures 5.11 (b)

and 5.17 (b)), especially in the vicinity of the pile toe. Indeed, the additional volume induced by the pile shoe resulted in a larger movement of the surrounding rock at the initial penetration, which became less significant after a certain depth of penetration (i.e., at the penetration depth of $H = 1$ m). It is evident that the rock column inside the pile was plugged at the penetration depth of 1 m as the top surface of the rock inside the pile dropped, as shown in Figure 5.17 (c).

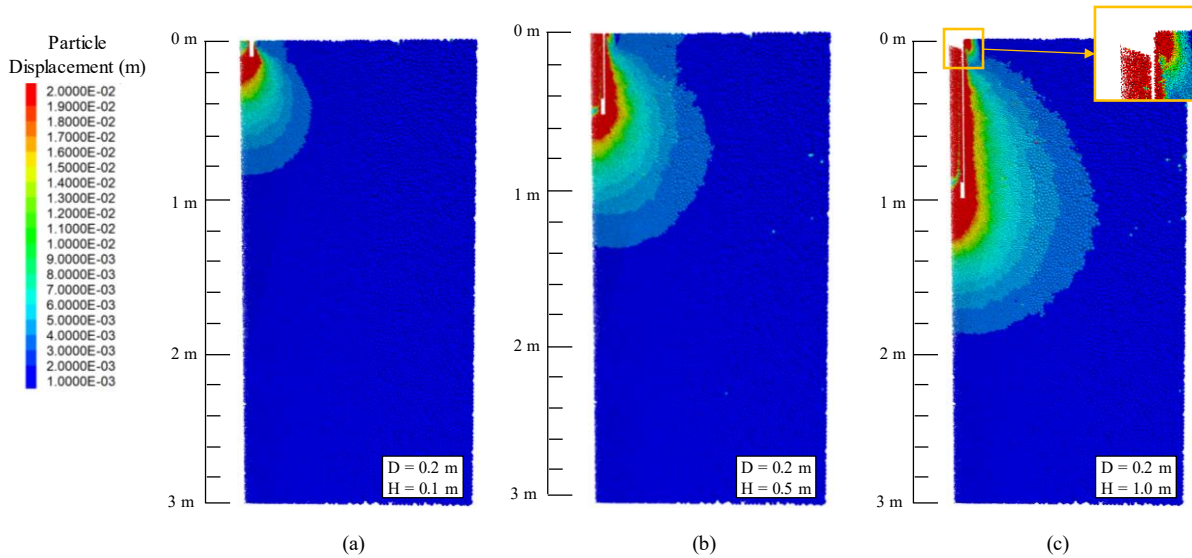


Figure 5.17. Individual particle displacement of the open-ended tubular pile with inner pile shoe at a penetration depth of (a) 0.1 m, (b) 0.5 m, and (c) 1.0 m

The changes in porosity of adopted weak rock during driving the open-ended tubular pile with the inner shoe are presented in Figures 5.18 (a) and (b). As shown in Figure 5.18 (a), since the rock surface dropped inside the pile due to plugging effects (refer to Figure 5.17 (c)) and the pile shoe located at the depth of 0.9 m to 1 m, no porosity could be recorded inside the rock column at the shallow depth (i.e., $Z < 0.05$ m) and around the pile shoe (i.e., $0.9 \text{ m} < Z < 1 \text{ m}$). It is noted that the porosity of the rock mass in the middle section of the rock column inside the pile increased due to the pile driving, which reveals that the rock had dilated. At the bottom portion of the rock column (e.g. Point A in Figure 5.18 (a)), the porosity reduced as the rock mass compressed. Referring to Figure 5.18 (b), for the region outside the pile in the vicinity of

the wall as reported in measurement sphere MC ($r = 0.118$ m), the porosity increased at the upper portion (e.g., Point A' in Figure 5.18 (b)), while the middle section near 0.5 m depth (e.g., Point B') was slightly compressed. An increase in porosity of the rock mass beneath the pile toe (e.g., Point C') was observed indicating weak rock the dilation as a result of relative movements between the blocks of broken rocks.

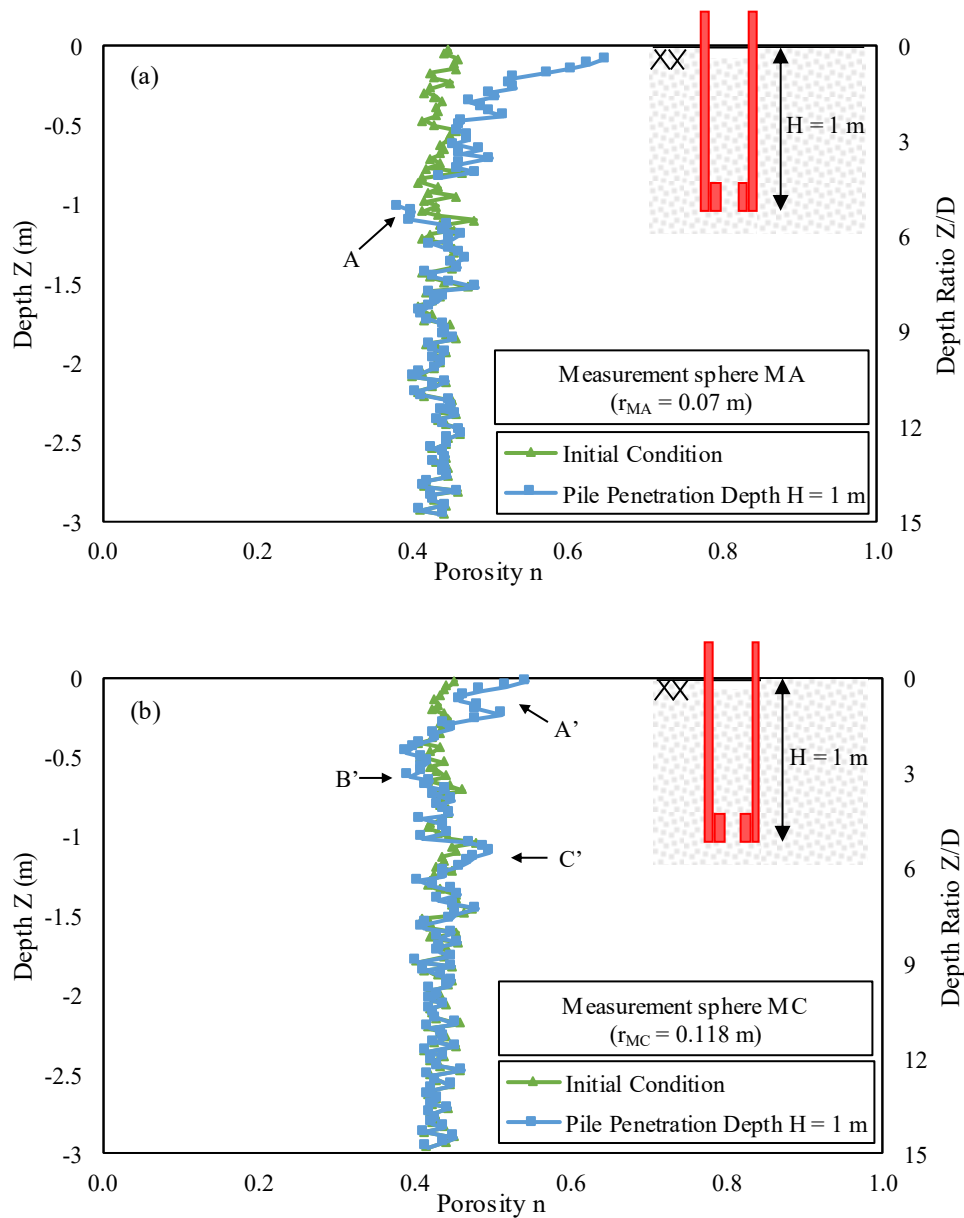


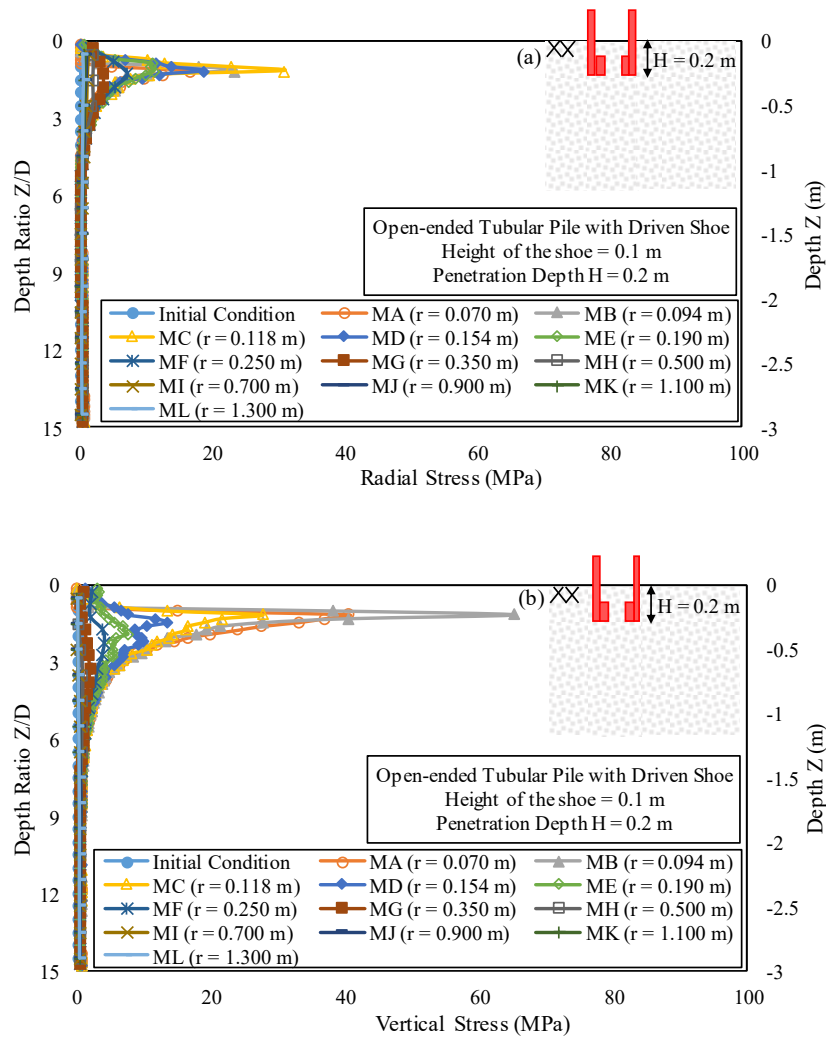
Figure 5.18. The porosity distribution pile before and after driving for the open-ended tubular pile with the inner shoe (a) at the location inside the pile; and (b) at the location outside and adjacent to the pile

The radial and vertical stresses for the pile with inner pile shoe at depths of 0.2 m and 1 m into the weak rock are presented in Figure 5.18. Comparing the results reported in Figure 5.13 (a) and Figure 5.19 (a), it can be noted that the highest radial stress for the pile with the shoe penetrated to the depth of $Z = 0.2$ m (i.e. $1D$) was higher than the corresponding radial stress for the pile without a shoe. Indeed, the addition of the shoe resulted in more weak rock displacement due to increases volume of the pile wall, hence, the stresses around the pile toe were amplified as shown in Figure 5.19 (a). Similarly, comparing Figure 5.13 (b) and Figure 5.19 (b), it is evident that the vertical stresses around the pile toe were increased due to the addition of the shoe.

As presented in Figure 5.19 (c), for the given depth of $Z = 1$ m (i.e. $5D$), the radial stresses inside the pile (i.e., measurement sphere MA) were significantly altered by introducing the driving shoe (refer to Figure 5.13 (c) for the results corresponding to pile with no driving shoe). For the pile with driving shoe, the radial stresses at the top portion of the weak rock inside the pile (i.e. $4.5D$) were equal to or less than the initial stress field. While at the bottom $0.5D$ near the toe, where the shoe located, the radial stresses were increased sharply. Indeed, the response of the rock above the pile shoe was altered considerably as a result of losing the stress confinement from the pile wall and the reduction in the radial stresses due to the introduced inner pile shoe.

Comparing Figures 5.13 (c) and Figure 5.19 (c), it can be noted that the radial stresses beneath the pile and outside in the vicinity of the wall (i.e., measurement spheres MB and MC) were similar to the corresponding values in the pile without a shoe. Thus it is evident that the inner pile shoe had insignificant effects on the radial stresses of the rock mass around the outer shaft, hence, no obvious effect of the introduced shoe was observed on the external shaft friction. In contrast, by comparing the results reported in Figure 5.13 (d) and Figure 5.19 (d), it becomes evident that the vertical stresses of the rock mass inside and beneath the pile toe for the pile

with the shoe were higher than the corresponding values in the pile without a shoe. As the opening of the tubular pile became smaller after attaching the pile shoe, it was harder for the rock mass to enter the pile. As expected, the impacts of the pile shoe on the stresses generated in the weak rock due to the pile driving was exponentially reduced with the radial distance from the pile, as depicted in Figure 5.19 (e).



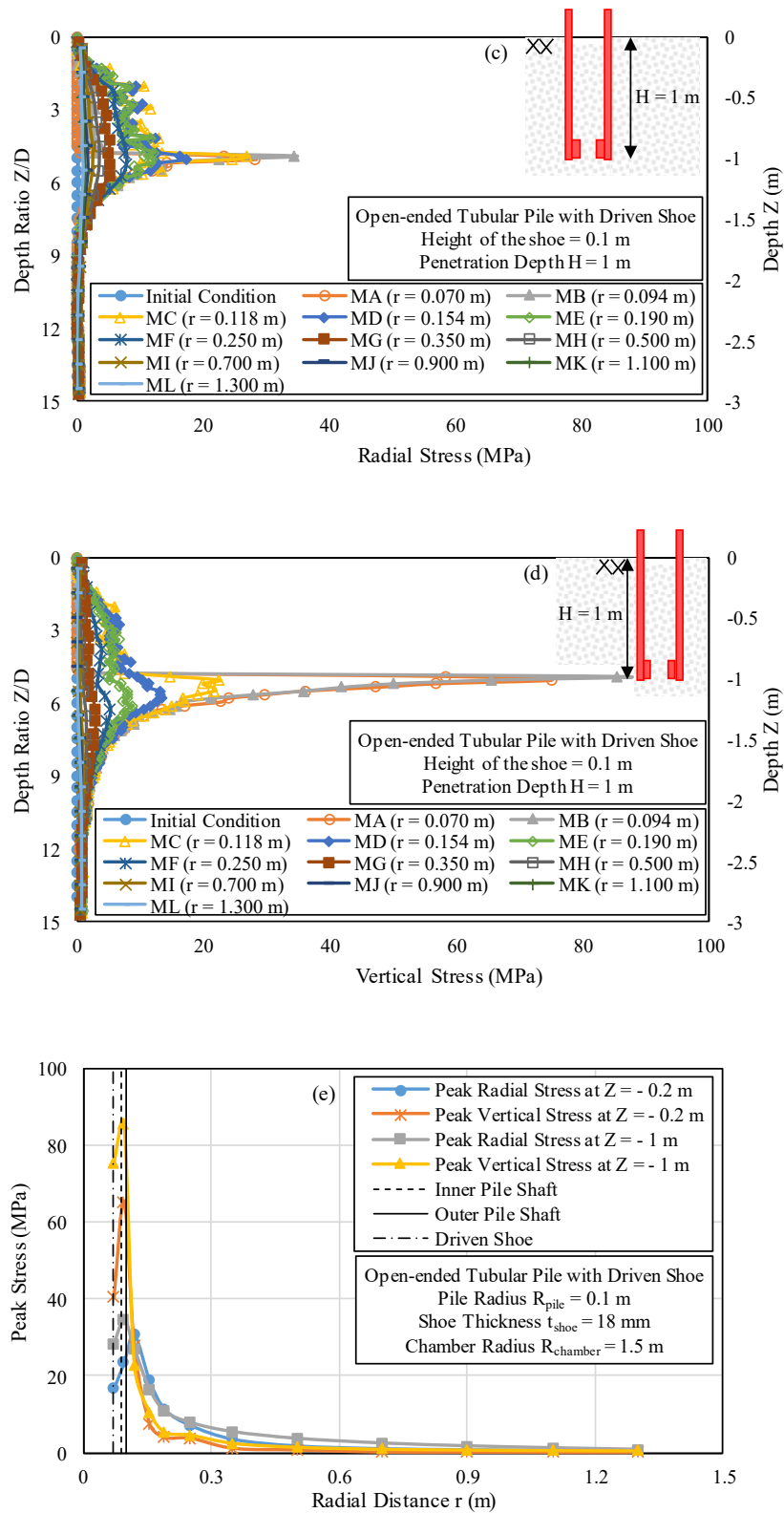


Figure 5.19. Stresses at different depth for open-ended pile with the inner shoe: (a) radial stress at 0.2 m, (b) vertical stress at 0.2 m, (c) radial stress at 1 m, (d) radial stress at 1 m, and (e) peak stresses at 0.2 m and 1 m

5.6 Degree of Plugging

As indicated in Figures 5.11 (c) and 5.17 (c), in both tested piles with and without shoe plugging was observed. To analyse the plugging behaviour, the incremental filling ratio (IFR) and the plug length ratio (PLR) of the pile without and with driving shoe were plotted in Figure 5.20. It is noticed that an increase in rock column height inside the pile started to be slower than the increase in penetration depth for penetration depth $H > 0.8$ m (i.e. $H > 4D$) for the pile without a shoe, while the corresponding penetration depth for the pile with inner pile shoe was $H > 0.7$ m (i.e. $H > 3.5D$). This indicates that the inner pile shoe allowed the pile partial plugging to occur at shallower penetration depth, even though the driving shoe decreased the internal shaft friction significantly. It is noted that the cross-sectional area of the opening was smaller for the pile with driving shoe than the pile without a shoe, which could result in plugging at lower depth since the degree of plugging is highly related to the inner diameter of the pile as reported by Lehane et al. (2005) and Ko et al. (2016).

It is noted that for a pile with IFR of 0, the pile is regarded as a fully plugged pile. When IFR = 100, the pile is in a fully coring mode. Both tested piles with and without shoes were considered to be partially plugged at the penetration depth of 1 m, because of the IFR of both piles were between 0 and 100. Moreover, as shown in Figure 5.20, the PLR decreased gradually with penetration depth for both piles and then reached 0.97 and 0.95 for the pile without a shoe and with driving shoe at the end of pile penetration, respectively.

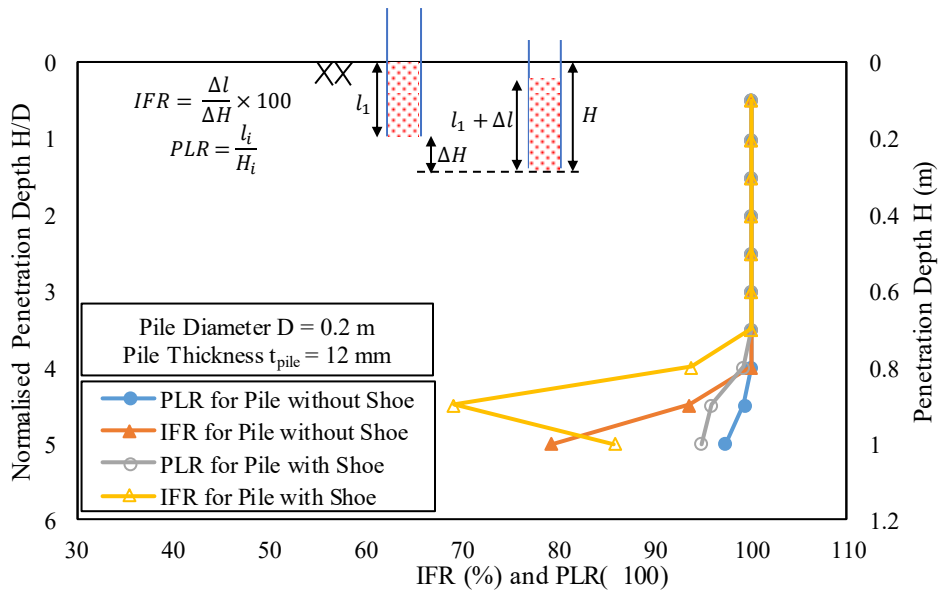


Figure 5.20. IFR and PLR values of open-ended tubular piles with and without driving shoe

Furthermore, as indicated in Figure 5.11 (c) and Figure 5.17 (c), it can be observed that the surface of the rock mass inside the pile was inclined toward the pile wall due to the friction between the pile wall and the weak rock. The inclination slope ($\tan \alpha$) of the top surface in relation to the plug length ratio (PLR) and incremental filling ratio (IFR) are presented in Figures 5.21 (a) and (b), respectively. It is evident that the inclination angle increased as PLR and IFR decreased. The correlations for the inclination angle against the PLR and IFR for the open-ended tubular pile in weak rock with and without shoe are presented in Figure 5.21. In this case, with a known inclination angle of the top surface of the rock plug, the degree of plugging might be predicted.

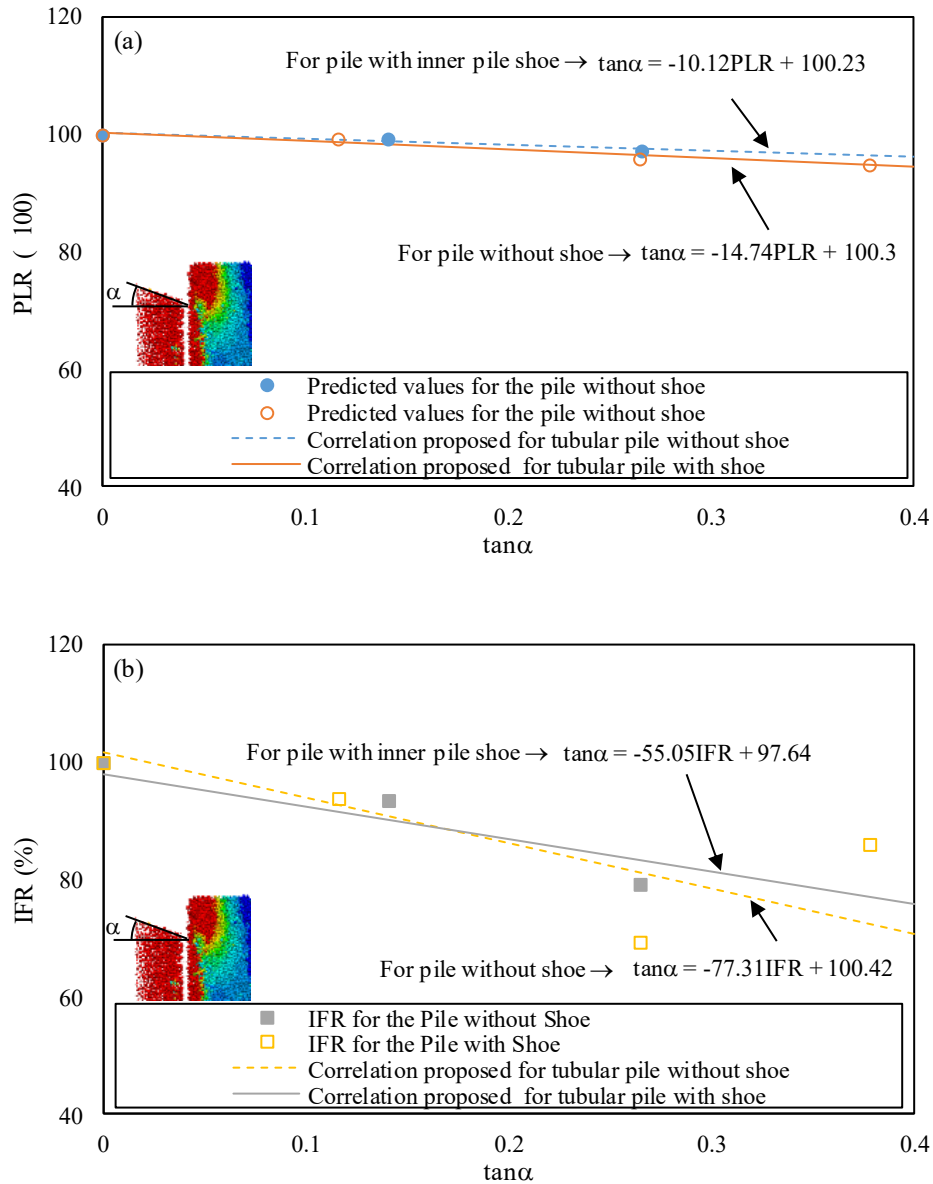


Figure 5.21. Inclination angle of the top surface of the rock plug in relation to (a) PLR, and (b) IFR

Figure 5.22 compares the obtained PLR and IFR in this study with the existing correlations between IFR and PLR reported by Jeong and Ko (2016) and Paik and Salgado (2003). Although the existing correlation were developed for the sandy soils, the obtained values in this study were in the same ballpark. Meanwhile, through the linear regression analysis, two specific correlations between IFR and PLR for the open-ended tubular pile without and with a shoe in weak rock were proposed in this study as shown in Equations (5-10) and (5-11), respectively.

$$IFR = 751.7PLR - 652.2 \quad (10)$$

$$IFR = 407.7PLR - 310.3 \quad (11)$$

It is evident that the IFR increased with PLR, which indicated that for a partially plugged pile, as the pile penetrated deeper, the degree of plugging was higher and the incremental change of the plug height (Δl) became slower. As shown in Figure 5.22, compared to the existing correlations for sand, the decrease in IFR tended to be more rapid with a decrease in PLR for open-ended tubular piles in weak rock assessed in this study. It can be predicted that once the partial plugging emerged for the piles in weak rock, the pile could reach a fully plugged mode at some stage corresponding to a higher value of PLR.

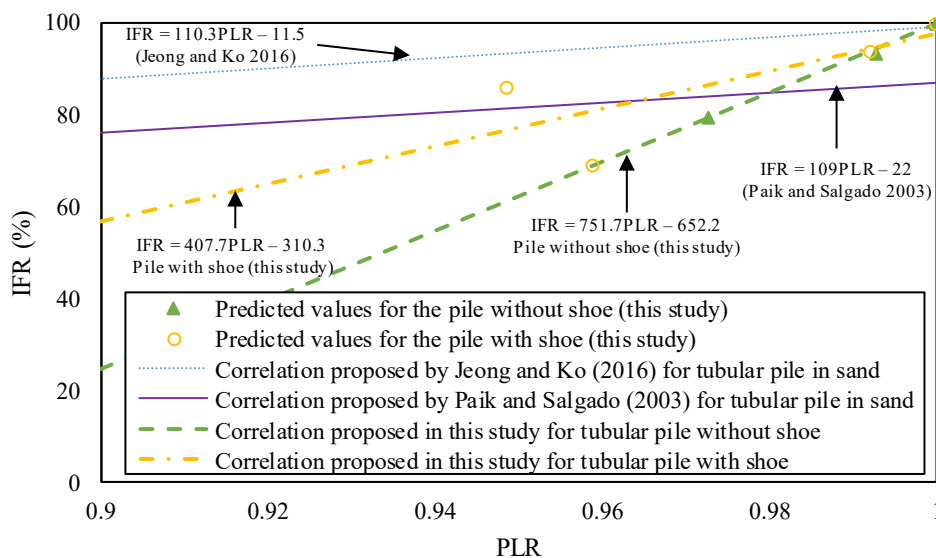


Figure 5.22. Relationship between the PLR and IFR and compared with other studies

It is clear that the tested piles in this study reached the partially plugged mode during the pile penetration. Although the driving shoe generated stress relief for the rock which entered the pile and passed the shoe, the cross-sectional area of the opening of the shoe was smaller and rock plug was formed for the tested pile with driving shoe. Meanwhile, predicting the penetration depth for a fully plugged mode can be useful in the pile design, as the pile can be regarded as a closed-ended pile as soon as the fully plugged mode is reached (American Petroleum

Institute 2002). With the proposed correlations between PLR and IFR for the open-ended tubular piles in weak rock, the penetration depth to form a fully plugged pile can be predicted when IFR reaches a value of 0.

5.7 Summary

In this study, open-ended tubular piles penetrating into the weak rock mass were simulated adopting the discrete element method (DEM). Triaxial test results on a pyroclastic weak rock was adopted for the calibration exercise. To replicate the mechanical behavior of the rock mass, the flat-joint model was employed, which is an advanced bonded-particle model for rock modelling. The micro-parameters were calibrated through simulating the triaxial tests with confining pressures of 100 kPa and 350 kPa. The DEM predictions agreed reasonably well with laboratory measurements for the adopted triaxial tests, in terms of stress-strain behavior and volume change. The calibrated weak rock characteristics were used in the pile penetration simulation. A DEM numerical model with a height of 3 m and a radius of 1.5 m was built to perform the pile penetration of an open-ended tubular pile with an outer diameter (D) of 0.2 m to a penetration depth of 1 m into the weak rock, which resulted in the ratio of model diameter to the pile diameter of $15D$, and the base of the model was located at least $10D$ below the pile tip after installation. A 30° segment was adopted considering the general axisymmetric arrangement of the system along with the particle refinement method, to ensure the number of particles in the DEM model, which was approximately 557,000 could be dealt with using the fast computing facilities available to the researcher team. The qualitative DEM predictions show that this technique can be used to investigate the axial load transfer mechanism of the open-ended tubular piles in weak rocks.

The bearing mechanisms including the internal shaft friction, external shaft friction, and base resistance were investigated in details. Meanwhile, the effect of the inner pile shoe was

assessed and discussed. As expected, both the internal and external shaft frictions increased as the pile penetrated deeper, while the base resistance was mobilised after a penetration depth of $1D$. It was noted that the predicted internal shaft friction was less than the external shaft friction, and the inner pile shoe resulted in a further reduction in the internal shaft friction while no obvious effect on the external shaft friction was observed. For the adopted pile shoe, even though the internal shaft friction reduced significantly by adding the shoe, the total capacity of the pile with driving shoe was slightly higher than that of the pile without a shoe.

In terms of the unit shaft frictions, the predicted unit external shaft friction was rather constant along the pile for both the piles with and without a shoe. Moreover, for the tubular pile with no driving shoe, the amplified unit internal shaft friction was observed at the bottom $1D$ near the pile toe. That indicated arching happening at the bottom portion of the rock column inside the pile. For the tubular pile with inner pile shoe, the unit shaft friction of the pile at the location above the pile shoe was minimal since when the rock entered the pile and passed the shoe, lost or experienced reduced stress confinement.

Meanwhile, the shattering of the rock mass due to the pile penetration was observed by inspecting the micro-mechanics of the DEM and the contact network. Most contact bonds in the rock plug were broken in tension, shear or both (i.e. fully unbonded). Indeed, for the pile with driving shoe, more contacts became fully unbonded for the rock inside the pile, especially for the rocks which passed the shoe.

Distributions of stresses and porosities of the weak rock during the pile penetration were presented and discussed in the study to shed light on the axial load bearing mechanism of tubular piles in weak rock. The porosity of the rock mass inside and outside the installed open-ended tubular pile was distinctly different. The bottom portion of the rock mass inside the pile compressed for both piles with and without driving shoe, while the porosity of the weak rock

outside and near the pile toe increased slightly. As expected, the radial and vertical stresses experienced the peak in the vicinity of the pile toe. The dramatic reduction in radial stresses inside the pile near the driving shoe indicated that the rock experienced stress relief as a result of the introduced driving shoe.

Clearly, partial plugging was observed for both piles with and without driving shoe. The plug length ratio (PLR) and incremental filling ratio (IFR) were reported to study the degree of plugging. The tested piles started to plug at a penetration depth of $3.5D$ to $4D$. Meanwhile, the inclination of the top surface of the rock plug was observed and reported as the inclination slope. It is noted that the inclination of the rock surface inside the plug increased as the PLR and IFR decreased. Correlations between the PLR and IFR were proposed for the piles with and without driving shoe. As expected, the value of IFR reduced as PLR decreased, once the partial plugging was observed; indeed the incremental change in the plug height tended to slow down as the plug impeded the entering of the rock into the pile. Moreover, these two proposed correlations were compared with the relationships proposed for open-ended tubular piles in sand. Clearly, for the same rate of decreasing PLR, the piles in weak rock could reach a fully plugged mode at a lower value of PLR in comparison to tubular piles in sand.

Chapter 6 - Conclusion

6.1 Summary

Recently, open-ended tubular piles have gained more popularity in a wide range of structures, such as road and railway bridges, deep mining, and high-rise buildings. Meanwhile, the penetration of such piles into weak rock layers is required due to the increasing demand of the infrastructures. However, having accurate predictions of the load-displacement relationship and bearing capacity of open-ended tubular piles in weak rocks are still challenging, due to the limited understanding of the interaction between the pile and weak rock and plugging mechanism influenced by the characteristics of the weak rocks. Moreover, the effect of the discontinuities are generally ignored when designing piles and the properties of the intact rock are usually used, while the joints can alter the strength of the rock mass that has already been considered in other geotechnical-structural designs, such as tunnelling. Therefore, the study on the axial load bearing mechanism of open-ended tubular piles with the consideration of joint properties and degree of plugging is essential. In this research, the discrete element method (DEM) was adopted to investigate the above mentioned problems microscopically and macroscopically.

An overview and the importance of investigating such problems were stated in Chapter 1, and the scope of this research was explained. The existing literature on the open-ended tubular piles and weak rocks were reviewed in Chapter 2 considering different aspects including the current design methods, the effect of the plug and pile shoe, characteristics of weak rocks, and methods for analysing the pile penetration problems.

As the first step of investigating the bearing mechanism of open-ended tubular piles in weak rocks, some of the characteristics of the weak rocks were studied. The findings were presented in Chapter 3 with the analysis and discussions of the effects of joint properties on rock masses

characteristics, which could assist with the further analysis of the influence of joint properties on the rock plug.

Considering the major influence of joints on the mechanical strength of rock mass, the impacts of joint density and joint dip on the internal shaft friction of open-ended tubular piles were presented in Chapter 4. The detailed analyses were conducted on small-diameter open-ended tubular piles with a diameter of 300 mm.

Then, a true scale discrete element model for pile penetration processes was presented in Chapter 5, adopting the particle refinement method to control the number of particles in the model to ensure the analysis was feasible within the available high performance computational facility (indeed the key disadvantage of the discrete element modelling is long computation time). The internal and external shaft friction, base resistance, degree of plugging, stress distribution were reported during the penetration of an open-ended tubular pile with an outer diameter of 200 mm in weak rock. Moreover, the effects of the inner pile shoe on the axial load bearing mechanism of the tubular pile in weak rock were presented and discussed.

6.2 Key Concluding Remarks

The key findings of this research can be summarised as follows:

1. The effects of joint density on the mechanical behaviour of jointed rock mass were investigated numerically using the discrete element method (DEM). The advanced bonded particle model, namely, the flat-joint model was used to simulate the intact rock mass and the contact properties were calibrated with the existing laboratory tests of an intact marble rock sample. Then, the joints were randomly distributed into the rock mass, which was replicated by discrete fracture network (DFN) and smooth-joint contact model. Through the analysis of the joint density ranged from 0 to 240 m²/m³, it is noted that the joint density affected both the unconfined compressive strength and

Young's modulus of the rock mass. It is observed that the rapid reduction in rock strength was found when the joint density was less than $60 \text{ m}^2/\text{m}^3$, and then the reduction became steady. With the increased in joint density, a high strength rock (i.e., the tested marble rock sample) could become a weak rock in terms of the unconfined compressive strength. Meanwhile, the failure mode of the rock mass changed from shear failure to tension failure due to the existence of rock joints.

2. Numerical simulations were conducted on weak rock samples with different joint aperture and dip. The flat-joint model and smooth-joint contact model were adopted to replicate the rock masses and sliding of the joints, respectively. For a given joint density, 15 series of triaxial tests were conducted with joint apertures of 0, 1, and 4 mm, representing a very tight, open, and moderately wide joints, respectively. The studied joint dips including 0, 30, 45, 60 and 90 degrees. Clearly, the joint aperture reduced the rock strength, and the amount of reduction was related to the joint dip. It is noted that the effect of joint apertures on the volume change was minimal for these joints in the joint dip of 90 degrees. Meanwhile, for these inclined joints, the joint aperture influenced both the strength and deformability of the rock sample. The most reduction in rock strength was found in the specimen that had the joint dip of 45 degree and joint aperture of 4 mm.
3. The influences of the individual joint length were studied through discrete element simulation. The rock specimen was calibrated against a weathered porphyrite to investigate the effects of the joint length on the mechanical behaviour of the weak rock. With a controlled joint density, the individual joint length ranging from a single long joint to plenty of non-persistent short joints were analysed. It was observed that the

shorter individual joints resulted in more reduction in strength and stiffness of weak rock for a given joint density. This finding revealed that plenty of non-persistent short joints had more effects on diminishing the rock strength than one long single joint that had the same joint density. For a long joint, the rock sample tended to slide on the joint, while for plenty of non-persistent short joints, loading the specimen could induce new wing joints that contacting the neighbouring joints to make the overall rock mass weak. The DEM predictions revealed that for a normalised joint length (i.e., the ratio of joint length to the specimen width) was greater than 0.28, the differences in the rock strength was minimal.

4. The effects of joint dip and joint density on the internal shaft friction were investigated numerically through the push-up load tests. A weak mudstone that reported in existing literature was adopted for the analysis. It is noted that the joints perpendicular to the loading direction had minimal effects on internal shaft resistance. However, the joints parallel to the loading direction had a large impact on the rock plugs and reduced the plug capacity, which was dissimilar to the effects in the triaxial test, where the joints parallel to the axial loading direction in the triaxial test did not provide the lowest strength. It is indicated that plugging behaviour and internal shaft friction was not solely based on rock strength. There was a significant reduction in the push-up load for densely jointed rock and the reduction was about 87% compared to the intact rock plug. Therefore, it can be noted that the joint properties affect the internal shaft friction significantly, hence, can affect the total bearing capacity of the open-ended tubular piles in weak rocks. Moreover, the plug mechanism was observed in the tests, such that the frictional force along the rock plug and pile shaft mobilised when the rock plugs pushed up further. Arching was observed at the lower part of the rock plugs, consequently, the

frictional forces predicted for those rock plugs that experienced arching were higher than the plugs with no arching. It is also noted that the joint dip altered the arching effect because the vertical joints destroyed the stress-path for increasing horizontal stress inside the plug.

5. A true-scale model was built using DEM to investigate the axial loading transfer mechanism of open-ended tubular piles in weak rock. The numerical model had a radius of 1.5 m and a height of 3 m for the penetration of an open-ended tubular pile with an outer diameter of 200 mm and a thickness of 12 mm to a penetration depth of 1 m. A pyroclastic weak rock with an UCS around 2 MPa, which was reported in the existing literature, was adopted for the calibration exercise of the rock mass. The numerical model for pile penetration was developed for a 30° segment with the application of the particle refinement method, which had the reasonable small particle sizes at the area of penetration and larger particle sizes at the area far away from the pile penetration. Through the analysis of penetration of a small diameter open-ended tubular pile into weak rock mass, it is observed that the base resistance mobilised after a penetration depth of 1D, and both the internal and external shaft frictions increased gradually as the pile penetrated deeper. Meanwhile, for the pile with an outer diameter of 200 mm, the internal shaft friction was less than the external shaft friction. Through the microscopic analysis of the contact network that was available in the proposed numerical model, it is noted that more fully unbonded contact were observed in the rock inside the pile, which indicated that the rock mass inside the pile was shattered and broken into piece, resulting in less internal shaft friction. The unit internal shaft friction was concentrated at the bottom 1D due to the arching effect, while the unit external shaft friction increased gradually with depth. Clearly, plugging was observed during the penetration

as the height of the rock column dropped. As expected, the radial and vertical stresses reached the highest value around the pile toe.

6. The effects of the pile shoe were studied numerically and compared with the pile without a shoe. The studied pile shoe had a thickness of 18 mm and a height of 100 mm, and attached to the open-ended tubular pile that had an outer diameter of 200 mm and a pile thickness of 12 mm. Clearly, the inner pile shoe altered the flow of the rock mass that entered the pile. The internal shaft friction reduced significantly after attaching the inner pile shoe, while no obvious impact was observed for the external shaft friction. The dramatic reduction in radial stress inside the pile around the pile shoe indicated that the shoe generated a stress relief. For the micro-response provided by the contact network, it is clear that for the rock inside the tubular pile, most of the contacts were fully unbonded for the rock which entered the pile and passed the shoe, hence, the shoe generated higher degree of shattering of the rock inside the pile. That could explain why the internal shaft friction was less compared to the pile without a shoe. It is noted that the base resistance was increased due to the additional annulus base area provided by the shoe. With the shoe added, the base resistance of the pile with shoe increased by 67% compared to the pile without a shoe. In terms of the total axial capacity, the tested pile with driving shoe showed slightly higher axial capacity than the pile without a shoe.
7. Partial plugging was observed for both tested piles with and without driving shoe. The incremental filling ratio (IFR) and the plug length ratio (PLR) were reported to analyse the degree of plugging. Clearly, the IFR increased with PLR since the rock plug impeded the rock mass entering into the pile. The obtained IFR and PLR were compared with the existing correlations for sandy soils, which were in the same ball park.

Meanwhile, two correlations were proposed between IFR and PLR for the open-ended tubular piles in weak rock corresponding to piles with and without driving shoe. Moreover, inclined rock surface was observed inside the pile for both tested piles once the pile experienced partial plugging. It is noted that the inclination angle increased as PLR and IFR decreased.

6.3 Recommendations for Future Studies

There are some areas requiring further investigations, and are recommended for future research studies as follows:

- Studying and analysing the different rock types and strength ranges with different rock quality designation (RQD), hence to propose comprehensive design recommendations on open-ended tubular piles in weak rocks with the consideration of discontinuities of the rock masses mapped in-situ and based on collected cores.
- Assessing the effects of induced joints during pile penetration as a result of rock shattering. As the pile penetration progresses through the rock, joints are generated within the rock mass and cause shattering of the rock fabric. Thus there are some induced joints as a result of pile installation impacting the plugging mechanism and axial load transfer mechanism of tubular piles. Indeed the generation of the new joints and degree of shattering need further studied considering the rock type, pile diameter, and pile thickness.
- Investigating the rock grain crushing during the pile penetration and the effects on the bearing axial bearing capacity. The sand particle crushing during the pile penetration is studied numerically by some researchers (e.g., Lobo-Guerrero and Vallejo 2005; Lobo-

Guerrero and Vallejo 2007), while rock grains may also be crushed during pile penetration that can be analysed through numerical simulation and laboratory tests.

- Examining the effects of pore water pressure on the axial load – displacement relationship for the open-ended tubular piles during and after driving adopting coupled DEM-CFD modelling. The pore water pressure may build up during the pile driving and then dissipate after driving, which can influence the driving resistance and the ultimate bearing capacity that needs to be studied further.
- Simulating large scale pile penetration using DEM can be very time consuming, which requires high computational effort. Hence, the large scale modelling in DEM may be difficult to conduct in the routine design.

Bibliography

- Abu-Hejleh, N.M., O'Neill, M.W., Hanneman, D. & Attwooll, W.J. 2005, Improvement of the geotechnical axial design methodology for Colorado's drilled shafts socketed in weak rocks, *Transportation research record*, vol. 1936, no. 1, pp. 100-107.
- American Petroleum Institute 2002, *RP2A-WSD, Recommended Practice for Planning, Designing and Constructing Fixed Offshore Platforms—Working Stress Design*, Washington.
- Australian Government 2016, *Infrastructure and Regional Development: Investing in Regional Growth—2016-17*, viewed 11 May 2018, <https://www.infrastructure.gov.au/department/statements/2016_2017/ministerial-statement/infrastructure-regional-development.aspx>.
- Bahaaddini, M., Sharrock, G. & Hebblewhite, B. 2013, Numerical investigation of the effect of joint geometrical parameters on the mechanical properties of a non-persistent jointed rock mass under uniaxial compression, *Computers and Geotechnics*, vol. 49, no. 1, pp. 206-225.
- Barton, N., Lien, R. & Lunde, J. 1974, Engineering classification of rock masses for the design of tunnel support, *Rock mechanics*, vol. 6, no. 4, pp. 189-236.
- Bell, F.G. 2000, *Engineering properties of soils and rocks*. Elsevier.
- Bertuzzi, R. & Pells, P.J. 2002, Geotechnical parameters of Sydney sandstone and shale, *Australian Geomechanics: Journal and News of the Australian Geomechanics Society*, vol. 37, no. 5, p. 41.
- Bhushan, K. 2004, Design & Installation of Large Diameter Pipe Piles for Laxt Wharf, *Current Practices and Future Trends in Deep Foundations*, pp. 370-89.
- Bieniawski, Z. 1973, Engineering classification of jointed rock masses, *Civil Engineer in South Africa*, vol. 15, no. 12.

- Bieniawski, Z.T. 1967, Mechanism of brittle fracture of rock: part I—theory of the fracture process, *International Journal of Rock Mechanics and Mining Sciences & Geomechanics Abstracts*, vol. 4, no. 4, pp. 395-406.
- Bieniawski, Z.T. 1989, *Engineering rock mass classifications: a complete manual for engineers and geologists in mining, civil, and petroleum engineering*, John Wiley & Sons.
- Bonilla-Sierra, V., Scholtes, L., Donzé, F. & Elmouttie, M. 2015, Rock slope stability analysis using photogrammetric data and DFN–DEM modelling, *Acta Geotechnica*, vol. 10, no. 4, pp. 497-511.
- Brucy, F., Meunier, J. & Nauroy, J. 1991, 'Behaviour of pile plug in sandy soils during and after driving', *Offshore Technology Conference*, Offshore Technology Conference. Houston.
- Bustamante, M. & Gianceselli, L. 1982, 'Pile bearing capacity prediction by means of static penetrometer CPT', *Proceedings of the 2-nd European Symposium on Penetration Testing*, pp. 493-500. Amsterdam.
- Butlanska, J., Arroyo, M. & Gens, A. 2009, 'Homogeneity and symmetry in DEM models of cone penetration', *AIP Conference Proceedings*, vol. 1145, pp. 425-8. American Institute of Physics.
- Butlanska, J., Arroyo, M., Gens, A. & O'Sullivan, C. 2013, Multi-scale analysis of cone penetration test (CPT) in a virtual calibration chamber, *Canadian Geotechnical Journal*, vol. 51, no. 1, pp. 51-66.
- Byrne, B. 1995, Driven pipe piles in dense sand, *Australian Geomechanics*, vol. 27, pp. 72-80.
- Camusso, M. & Barla, M. 2009, Microparameters calibration for loose and cemented soil when using particle methods, *International Journal of Geomechanics*, vol. 9, no. 5, pp. 217-229.
- Carter, T., Diederichs, M. & Carvalho, J. 2008, Application of modified Hoek-Brown transition relationships for assessing strength and post yield behaviour at both ends of the rock competence scale, *Journal of the Southern African Institute of Mining and Metallurgy*, vol. 108, no. 6, pp. 325-338.

- Carvalho, J., Carter, T. & Diederichs, M. 2007, 'An approach for prediction of strength and post yield behaviour for rock masses of low intact strength', *Rock Mechanics: Meeting Society's Challenges and Demands. Taylor & Francis*, pp. 277-85. Vancouver, Canada.
- Cecconi, M. & Viggiani, G.M. 2001, Structural features and mechanical behaviour of a pyroclastic weak rock, *International Journal for Numerical and Analytical Methods in Geomechanics*, vol. 25, no. 15, pp. 1525-1557.
- Chen, P.Y. 2017, Effects of microparameters on macroparameters of flat-jointed bonded-particle materials and suggestions on trial-and-error method, *Geotechnical and Geological Engineering*, vol. 35, no. 2, pp. 663-677.
- Chen, Y., Deng, A., Wang, A. & Sun, H. 2018, Performance of screw–shaft pile in sand: Model test and DEM simulation, *Computers and Geotechnics*, vol. 104, pp. 118-30.
- Chiu, C.C., Wang, T.T., Weng, M.C. & Huang, T.H. 2013, Modeling the anisotropic behaviour of jointed rock mass using a modified smooth-joint model, *International Journal of Rock Mechanics and Mining Sciences*, vol. 62, no. 1, pp. 14-22.
- Ciantia, M.O., Arroyo, M., Butlanska, J. & Gens, A. 2016, DEM modelling of cone penetration tests in a double-porosity crushable granular material, *Computers and Geotechnics*, vol. 73, pp. 109-127.
- CIRIA 1999, *Report 181 - piled foundations in weak rock*, London.
- Clausen, C., Aas, P. & Karlsrud, K. 2005, 'Bearing capacity of driven piles in sand, the NGI approach', *Proceedings of Proceedings of International Symposium. on Frontiers in Offshore Geotechnics, Perth*, pp. 574-80. Perth.
- Cundall, P.A. 1971, 'A computer model for simulating progressive, large-scale movement in blocky rock system', *Proceedings of the International Symposium on Rock Mechanics, 1971*.
- Cundall, P.A. & Strack, O.D. 1979, A discrete numerical model for granular assemblies, *Géotechnique*, vol. 29, no. 1, pp. 47-65.

- de Bono, J., McDowell, G. & Wanatowski, D. 2015, Investigating the micro mechanics of cemented sand using DEM, *International Journal for Numerical and Analytical Methods in Geomechanics*, vol. 39, no. 6, pp. 655-675.
- de Bono, J.P. & McDowell, G.R. 2014, DEM of triaxial tests on crushable sand, *Granular Matter*, vol. 16, no. 4, pp. 551-562.
- De Nicola, A. & Randolph, M. 1997, The plugging behaviour of driven and jacked piles in sand, *Géotechnique*, vol. 47, no. 4, pp. 841-856.
- Dershowitz, W. & Einstein, H. 1988, Characterizing rock joint geometry with joint system models, *Rock Mechanics and Rock Engineering*, vol. 21, no. 1, pp. 21-51.
- Dinc, O., Sonmez, H., Tunusluoglu, C. & Kasapoglu, K. 2011, A new general empirical approach for the prediction of rock mass strengths of soft to hard rock masses, *International Journal of Rock Mechanics and Mining Sciences*, vol. 48, no. 4, pp. 650-665.
- Ding, X. & Zhang, L. 2014, A new contact model to improve the simulated ratio of unconfined compressive strength to tensile strength in bonded particle models, *International Journal of Rock Mechanics and Mining Sciences*, vol. 69, no. 1, pp. 111-119.
- Ding, X., Zhang, L., Zhu, H. & Zhang, Q. 2014, Effect of model scale and particle size distribution on PFC3D simulation results, *Rock Mechanics and Rock Engineering*, vol. 47, no. 6, pp. 2139-2156.
- Dobereiner, L. & Freitas, M.D. 1986, Geotechnical properties of weak sandstones, *Géotechnique*, vol. 36, no. 1, pp. 79-94.
- Dong, J., Chen, F., Zhou, M. & Zhou, X. 2018, Numerical analysis of the boundary effect in model tests for single pile under lateral load, *Bulletin of Engineering Geology and the Environment*, pp. 1-12.
- Engineering Heritage Western Australia 2014, *Nomination of Stirling Bridge for an Engineering Heritage Australia Heritage Recognition Award*, Australia.

- Esposito, R.G., Velloso, R.Q., do Amaral Vargas Jr, E. & Danziger, B.R. 2018, Multi-scale sensitivity analysis of pile installation using DEM, *Computational Particle Mechanics*, vol. 5, no. 3, pp. 375-386.
- Falagush, O., McDowell, G. & Yu, H.S. 2015, Discrete element modeling of cone penetration tests incorporating particle shape and crushing, *International Journal of Geomechanics*, vol. 15, no. 6, p. 04015003.
- Fatahi, B., Basack, S., Ryan, P., Zhou, W.H. & Khabbaz, H. 2014, Performance of laterally loaded piles considering soil and interface parameters, *Geomechanics and Engineering*, vol. 7, no. 5, pp. 495-524.
- Fattah, M.Y. & Al-Soudani, W.H. 2016, Bearing capacity of open-ended pipe piles with restricted soil plug, *Ships and Offshore Structures*, vol. 11, no. 5, pp. 501-516.
- Fell, R., Hungr, O., Leroueil, S. & Riemer, W. 2000, 'Keynote lecture-geotechnical engineering of the stability of natural slopes, and cuts and fills in soil', *ISRM International Symposium*, International Society for Rock Mechanics.
- Finlay, T., White, D., Bolton, M. & Nagayama, T. 2001, 'Press-in piling: the installation of instrumented steel tubular piles with and without driving shoes', *5th International Conference on Deep Foundations Practice*, pp. 199-208.
- FinnRA 2000, *Steel pipe piles*, Finnish National Road Administration, Helsinki.
- Fleming, K., Weltman, A., Randolph, M. & Elson, K. 2008, *Piling engineering*, CRC press.
- Gavin, K. 1999, Experimental investigation of open and closed ended piles in sand, Trinity College Dublin.
- Gavin, K. & Lehane, B. 2003a, End bearing of small pipe piles in dense sand, *BGA International Conference on Foundations: Innovations, Observations, Design and Practice: Proceedings of the International Conference Organised by British Geotechnical Association and Held in Dundee, Scotland on 2-5th September 2003*, Thomas Telford, p. 321.

- Gavin, K.G. & Lehane, B.M. 2003b, The shaft capacity of pipe piles in sand, *Canadian Geotechnical Journal*, vol. 40, no. 1, pp. 36-45.
- Ghobadi, M.H. 1994, 'Engineering geologic factors influencing the stability of slopes in the Northern Illawarra region'. Ph.D. thesis, Department of Civil and Mining Engineering, University of Wollongong.
- Gokceoglu, C. & Aksoy, H. 2000, New approaches to the characterization of clay-bearing, densely jointed and weak rock masses, *Engineering Geology*, vol. 58, no. 1, pp. 1-23.
- González de Vallejo, L. & Hijazo, T. 2008, A new method of estimating the ratio between in situ rock stresses and tectonics based on empirical and probabilistic analyses, *Engineering geology*, vol. 101, no. 3-4, pp. 185-194.
- Goodman, R.E. & Ahlgren, C.S. 2000, Evaluating safety of concrete gravity dam on weak rock: Scott Dam, *Journal of Geotechnical and Geoenvironmental Engineering*, vol. 126, no. 5, pp. 429-442.
- Grabe, J. & Heins, E. 2017, Coupled deformation–seepage analysis of dynamic capacity tests on open-ended piles in saturated sand, *Acta geotechnica*, vol. 12, no. 1, pp. 211-223.
- Grenon, M., Bruneau, G. & Kalala, I.K. 2014, Quantifying the impact of small variations in fracture geometric characteristics on peak rock mass properties at a mining project using a coupled DFN–DEM approach, *Computers and Geotechnics*, vol. 58, pp. 47-55.
- Gudavalli, S., Safaqaq, O. & Seo, H. 2013, 'Effect of soil plugging on axial capacity of open-ended pipe piles in sands', *Proceedings of the 18th International Conference on Soil Mechanics and Geotechnical Engineering*, pp. 1487-90. Paris, France.
- Guo, Y. & Yu, X.B. 2016, Design and analyses of open-ended pipe piles in cohesionless soils, *Frontiers of Structural and Civil Engineering*, vol. 10, no. 1, pp. 22-29.
- Han, F., Ganju, E., Prezzi, M., Salgado, R. & Zaheer, M. 2019a, Axial resistance of open-ended pipe pile driven in gravelly sand, *Géotechnique*, vol. 70, no. 2, pp. 1-15.

- Han, F., Ganju, E., Salgado, R. & Prezzi, M. 2019b, Comparison of the load response of closed-ended and open-ended pipe piles driven in gravelly sand, *Acta Geotechnica*, vol. 14, no. 6, pp. 1785-1803.
- Hannigan, P.J., Goble, G.G., Thendean, G., Likins, G.E. & Rausche, F. 1997, *Design and construction of driven pile foundations-volume I*. National Highway Institute, US.
- Henke, S. & Bienen, B. 2013, Centrifuge tests investigating the influence of pile cross-section on pile driving resistance of open-ended piles, *International Journal of Physical Modelling in Geotechnics*, vol. 13, no. 2, pp. 50-62.
- Henke, S. & Grabe, J. 2008, Numerical investigation of soil plugging inside open-ended piles with respect to the installation method, *Acta Geotechnica*, vol. 3, no. 3, pp. 215-223.
- Henke, S. & Grabe, J. 2013, Field measurements regarding the influence of the installation method on soil plugging in tubular piles, *Acta Geotechnica*, vol. 8, no. 3, pp. 335-352.
- Hoek, E. 1983, Strength of jointed rock masses, *Géotechnique*, vol. 33, no. 3, pp. 187-223.
- Hoek, E., Carranza-Torres, C. & Corkum, B. 2002, 'Hoek-Brown failure criterion-2002 edition', *Proceedings of NARMS-Tac*, vol. 1, pp. 267-73.
- Hoek, E., Kaiser, P.K. & Bawden, W.F. 2000, *Support of underground excavations in hard rock*, CRC Press.
- Hoek, E., Marinos, P. & Benissi, M. 1998, Applicability of the Geological Strength Index (GSI) classification for very weak and sheared rock masses. The case of the Athens Schist Formation, *Bulletin of Engineering Geology and the Environment*, vol. 57, no. 2, pp. 151-160.
- Hoek, E., Marinos, P. & Marinos, V. 2005, Characterisation and engineering properties of tectonically undisturbed but lithologically varied sedimentary rock masses, *International Journal of Rock Mechanics and Mining Sciences*, vol. 42, no. 2, pp. 277-285.

- Huang, B., Zhang, Y., Lv, B., Yang, Z., Fu, X. & Zhang, B. 2018, Vertical bearing characteristics of rock-socketed pile in a synthetic soft rock, *European Journal of Environmental and Civil Engineering*, pp. 1-20.
- Huang, D., Wang, J. & Liu, S. 2015, A comprehensive study on the smooth joint model in DEM simulation of jointed rock masses, *Granular Matter*, vol. 17, no. 6, pp. 775-791.
- IAEG 1979, Report of the commission on engineering geological mapping, *Bull IAEG*, vol. 19, pp. 364-371.
- Igoe, D., Doherty, P. & Gavin, K. 2009, The development and testing of an instrumented open-ended model pile. *Geotechnical Testing Journal*, vol. 33, no. 1, pp. 72-82.
- Irvine, J., Terente, V., Lee, L. & Comrie, R. 2015, 'Driven pile design in weak rock', *Proc. Int. Symp. Frontiers in Offshore Geotechnics III, ISFOG 2015*, pp. 569-574.
- Ivars, D.M., Pierce, M.E., Darcel, C., Reyes-Montes, J., Potyondy, D.O., Young, R.P. & Cundall, P.A. 2011, The synthetic rock mass approach for jointed rock mass modelling, *International Journal of Rock Mechanics and Mining Sciences*, vol. 48, no. 2, pp. 219-244.
- Jardine, R., Chow, F., Overy, R. & Standing, J. 2005, *ICP design methods for driven piles in sands and clays*, Thomas Telford Publishing, London.
- Jardine, R., Standing, J. & Chow, F. 2006, Some observations of the effects of time on the capacity of piles driven in sand, *Géotechnique*, vol. 56, no. 4, pp. 227-244.
- Jardine, R., Zhu, B., Foray, P. & Yang, Z. 2013, Measurement of stresses around closed-ended displacement piles in sand, *Géotechnique*, vol. 63, no. 1, pp. 1-17.
- Jeong, S. & Ko, J. 2016, Inner skin friction of open-ended piles considering the degree of soil plugging, *Japanese Geotechnical Society Special Publication*, vol. 2, no. 37, pp. 1327-1332.
- Jeong, S., Ko, J., Won, J. & Lee, K. 2015, Bearing capacity analysis of open-ended piles considering the degree of soil plugging, *Soils and Foundations*, vol. 55, no. 5, pp. 1001-1014.

- Jiang, M., Yu, H.S. & Harris, D. 2006, Discrete element modelling of deep penetration in granular soils, *International Journal for Numerical and Analytical Methods in Geomechanics*, vol. 30, no. 4, pp. 335-361.
- Jing, L. 2003, A review of techniques, advances and outstanding issues in numerical modelling for rock mechanics and rock engineering, *International Journal of Rock Mechanics and Mining Sciences*, vol. 40, no. 3, pp. 283-353.
- Joseph, T., Houlsby, G., Burd, H. & Taylor, P. 2017, 'Finite Element Analysis of Soil Plug Behaviour within Open-ended Piles', paper presented to the *OSIG 2017 - Smarter Solutions for Future Offshore Developments*, London, UK.
- Kaiser, P., Diederichs, M., Martin, C., Sharp, J. & Steiner, W. 2000, 'Underground works in hard rock tunnelling and mining', *ISRM international symposium*, International Society for Rock Mechanics and Rock Engineering.
- Kanji, M.A. 2014, Critical issues in soft rocks, *Journal of Rock Mechanics and Geotechnical Engineering*, vol. 6, no. 3, pp. 186-195.
- Karlowskis, V. 2014, 'Soil Plugging of Open-Ended Piles During Impact Driving in Cohesion-less Soil'. Master Thesis, Department of Civil and Architectural Engineering, Royal Institute of Technology.
- Kinloch, H. & O'Sullivan, C. 2007, 'A micro-mechanical study of the influence of penetrometer geometry on failure mechanisms in granular soils', *Advances in Measurement and Modeling of Soil Behaviour*, pp. 1-11.
- Klein, S. 2001, 'An approach to the classification of weak rock for tunnel projects', *Proceedings of the Rapid Excavation and Tunneling Conference*, pp. 793-806.
- Ko, J. & Jeong, S. 2014, Plugging effect of open-ended piles in sandy soil, *Canadian Geotechnical Journal*, vol. 52, no. 5, pp. 535-547.

- Ko, J., Jeong, S. & Lee, J.K. 2016, Large deformation FE analysis of driven steel pipe piles with soil plugging, *Computers and Geotechnics*, vol. 71, no. 1, pp. 82-97.
- Kulhawy, F.H. & Goodman, R.E. 1980, 'Design of foundations on discontinuous rock', *International Conference on Structural Foundations on Rock, 1980, Sydney, Australia*, vol. 1.
- Kumara, J.J., Kikuchi, Y. & Kurashina, T. 2016, Effects of the lateral stress on the inner frictional resistance of pipe piles driven into sand, *International Journal of Geo-Engineering*, vol. 7, no. 1, pp. 1-14.
- Lambert, C. & Coll, C. 2014, Discrete modeling of rock joints with a smooth-joint contact model, *Journal of Rock Mechanics and Geotechnical Engineering*, vol. 6, no. 1, pp. 1-12.
- Le, T.M., Fatahi, B., Khabbaz, H. & Sun, W. 2017, Numerical optimization applying trust-region reflective least squares algorithm with constraints to optimize the non-linear creep parameters of soft soil, *Applied Mathematical Modelling*, vol. 41, pp. 236-56.
- Le, T.M., Fatahi, B. & Owen, D. 2016, Trust-region reflective optimisation to obtain soil visco-plastic properties, *Engineering Computations*, vol. 33, no. 2.
- Lee, J., Salgado, R. & Paik, K. 2003, Estimation of load capacity of pipe piles in sand based on cone penetration test results, *Journal of geotechnical and geoenvironmental engineering*, vol. 129, no. 5, pp. 391-403.
- Lehane, B., Schneider, J. & Xu, X. 2005, 'The UWA-05 method for prediction of axial capacity of driven piles in sand', *Frontiers in offshore geotechnics: ISFOG*, pp. 683-689.
- Leong, E. & Randolph, M. 1991, Finite element analyses of soil plug response, *International journal for numerical and analytical methods in Geomechanics*, vol. 15, no. 2, pp. 121-141.
- Li, L., Wu, W., El Naggar, M.H., Mei, G. & Liang, R. 2019, DEM analysis of the sand plug behaviour during the installation process of open-ended pile, *Computers and Geotechnics*, vol. 109, pp. 23-33.

- Lin, J. & Wu, W. 2012, Numerical study of miniature penetrometer in granular material by discrete element method, *Philosophical Magazine*, vol. 92, no. 28-30, pp. 3474-3482.
- Liu, J., Duan, N., Cui, L. & Zhu, N. 2019a, DEM investigation of installation responses of jacked open-ended piles, *Acta Geotechnica*, vol. 14, no. 6, pp. 1805-1819.
- Liu, J., Guo, Z. & Han, B. 2019b, Load Transfer of Offshore Open-Ended Pipe Piles Considering the Effect of Soil Plugging, *Journal of Marine Science and Engineering*, vol. 7, no. 9, p. 313.
- Liyanapathirana, D., Deeks, A. & Randolph, M. 1998, Numerical analysis of soil plug behaviour inside open - ended piles during driving, *International journal for numerical and analytical methods in geomechanics*, vol. 22, no. 4, pp. 303-322.
- Lobo-Guerrero, S. & Vallejo, L. 2005, DEM analysis of crushing around driven piles in granular materials, *Géotechnique*, vol. 55, no. 8, pp. 617-623.
- Lobo-Guerrero, S. & Vallejo, L.E. 2007, Influence of pile shape and pile interaction on the crushable behaviour of granular materials around driven piles: DEM analyses, *Granular Matter*, vol. 9, no. 3-4, p. 241-250.
- Long, M. 1995, 'The behaviour of driven tubular steel piles in the laminated mudstones of south-west ireland', *Proceedings of the Institution of Civil Engineers-Geotechnical Engineering*, vol. 113, no. 4, pp. 242-252.
- Lu, Y. & Frost, D. 2010, Three-dimensional DEM modeling of triaxial compression of sands, *Soil behaviour and geo-micromechanics*, pp. 220-226.
- Lüking, J. & Kempfert, H. 2013, Plugging Effect of Open-Ended Displacement Piles, *In Proceedings of the 18th International Conference on Soil Mechanics and Geotechnical Engineering*, pp. 2363-2366. Paris.
- Mabsout, M.E. & Tassoulas, J.L. 1994, A finite element model for the simulation of pile driving, *International Journal for numerical methods in Engineering*, vol. 37, no. 2, pp. 257-278.

- Marinos, P.V. 2010, 'New proposed GSI classification charts for weak or complex rock masses', *Proceedings of the 12th International Congress Patras*, vol. 43, no. 3, pp. 1248-1258.
- Matsumoto, T., Michi, Y. & Hirano, T. 1995, Performance of axially loaded steel pipe piles driven in soft rock, *Journal of geotechnical engineering*, vol. 121, no. 4, pp. 305-315.
- McDowell, G., Falagush, O. & Yu, H.-S. 2012, A particle refinement method for simulating DEM of cone penetration testing in granular materials, *Géotechnique Letters*, vol. 2, no. 3, pp. 141-147.
- Mohammadi, M. & Hossaini, M.F. 2017, Modification of rock mass rating system: Interbedding of strong and weak rock layers, *Journal of Rock Mechanics and Geotechnical Engineering*, vol. 9, no. 6, pp. 1165-1170.
- Mughieda, O. & Alzo'ubi, A.K. 2004, Fracture mechanisms of offset rock joints-A laboratory investigation, *Geotechnical and Geological engineering*, vol. 22, no. 4, pp. 545-562.
- Ng, C.W., Yau, T.L., Li, J.H. & Tang, W.H. 2001, Side resistance of large diameter bored piles socketed into decomposed rocks, *Journal of geotechnical and geoenvironmental engineering*, vol. 127, no. 8, pp. 642-657.
- Nguyen, L. & Fatahi, B. 2016, Behaviour of clay treated with cement & fibre while capturing cementation degradation and fibre failure—C3F Model, *International Journal of Plasticity*, vol. 81, no. 1, pp. 168-195.
- Nguyen, L., Fatahi, B. & Khabbaz, H. 2017, Development of a constitutive model to predict the behaviour of cement-treated clay during cementation degradation: C3 model, *International Journal of Geomechanics*, vol. 17, no. 7, p. 04017010.
- Nguyen, L.D., Fatahi, B. & Khabbaz, H. 2014, A constitutive model for cemented clays capturing cementation degradation, *International Journal of Plasticity*, vol. 56, pp. 1-18.
- Nickmann, M., Spaun, G. & Thuro, K. 2006, 'Engineering geological classification of weak rocks', *Proceedings of the 10th International IAEG Congress*, vol. 492, pp. 1-9.

- Paik, K. & Salgado, R. 2003, Determination of bearing capacity of open-ended piles in sand, *Journal of Geotechnical and Geoenvironmental Engineering*, vol. 129, no. 1, pp. 46-57.
- Paik, K., Salgado, R., Lee, J. & Kim, B. 2003, Behaviour of open-and closed-ended piles driven into sands, *Journal of Geotechnical and Geoenvironmental Engineering*, vol. 129, no. 4, pp. 296-306.
- Paik, K.H. & Lee, S.R. 1993, Behaviour of soil plugs in open - ended model piles driven into sands, *Marine Georesources & Geotechnology*, vol. 11, no. 4, pp. 353-373.
- Paluszny, A., Tang, X. & Zimmerman, R. 2012, 'A multi-modal approach to 3D Fracture and Fragmentation of Rock using Impulse-Based Dynamics and the Finite Element Method', *46th US Rock Mechanics/Geomechanics Symposium*, American Rock Mechanics Association.
- Pierce, M., Cundall, P., Potyondy, D. & Mas Ivars, D. 2007, 'A synthetic rock mass model for jointed rock', *Rock Mechanics: Meeting Society's Challenges and Demands, 1st Canada-US Rock Mechanics Symposium, Vancouver*, vol. 1, pp. 341-9.
- Potyondy, D. 2013, *PFC3D flat joint contact model version 1*, Itasca Consulting Group, Minneapolis.
- Potyondy, D. & Cundall, P. 2004, A bonded-particle model for rock, *International journal of rock mechanics and mining sciences*, vol. 41, no. 8, pp. 1329-1364.
- Prudencio, M. & Jan, M.V.S. 2007, Strength and failure modes of rock mass models with non-persistent joints, *International Journal of Rock Mechanics and Mining Sciences*, vol. 44, no. 6, pp. 890-902.
- Qiu, G., Henke, S. & Grabe, J. 2011, Application of a Coupled Eulerian–Lagrangian approach on geomechanical problems involving large deformations, *Computers and Geotechnics*, vol. 38, no. 1, pp. 30-39.
- Rajapakse, R.A. 2008, *Pile design and construction rules of thumb*, Butterworth-Heinemann.
- Randolph, M. 2018, Potential damage to steel pipe piles during installation, *IPA News Letter*, vol. 3, no. 1, pp. 3-10.

- Randolph, M., Leong, E. & Houlsby, G. 1991, One-dimensional analysis of soil plugs in pipe piles, *Géotechnique*, vol. 41, no. 4, pp. 587-598.
- Randolph, M., May, M., Leong, E., Hyden, A. & Murff, J. 1992, Soil plug response in open-ended pipe piles, *Journal of geotechnical engineering*, vol. 118, no. 5, pp. 743-759.
- Rowe, R. & Armitage, H. 1987, A design method for drilled piers in soft rock, *Canadian Geotechnical Journal*, vol. 24, no. 1, pp. 126-142.
- Santi, P.M. 2006, Field methods for characterizing weak rock for engineering, *Environmental & Engineering Geoscience*, vol. 12, no. 1, pp. 1-11.
- Schnaid, F. 1990, 'A study of the cone-pressuremeter test in sand'. Ph.D. Thesis, University of Oxford.
- Scholtès, L. & Donzé, F.V. 2015, A DEM analysis of step-path failure in jointed rock slopes, *Comptes Rendus Mécanique*, vol. 343, no. 2, pp. 155-165.
- Serrano, A. & Olalla, C. 2004, Shaft resistance of a pile embedded in rock, *International Journal of Rock Mechanics and Mining Sciences*, vol. 41, no. 1, pp. 21-35.
- Shi, D., Yang, Y., Deng, Y. & Xue, J. 2019, DEM modelling of screw pile penetration in loose granular assemblies considering the effect of drilling velocity ratio, *Granular Matter*, vol. 21, no. 3, p. 74.
- Singh, M., Rao, K. & Ramamurthy, T. 2002, Strength and deformational behaviour of a jointed rock mass, *Rock Mechanics and Rock Engineering*, vol. 35, no. 1, pp. 45-64.
- Sun, D.a., Feng, T. & Matsuoka, H. 2006, Stress-strain behaviour of weathered weak rock in middle-sized triaxial tests, *Canadian Geotechnical Journal*, vol. 43, no. 10, pp. 1096-1104.
- Sun, L., Grasselli, G., Liu, Q. & Tang, X. 2019, Coupled hydro-mechanical analysis for grout penetration in fractured rocks using the finite-discrete element method, *International Journal of Rock Mechanics and Mining Sciences*, vol. 124, p. 104138.

- Terente, V., Torres, I., Irvine, J. & Jaeck, C. 2017, 'Driven Pile Design Method for Weak Rock', *Offshore Site Investigation Geotechnics 8th International Conference Proceeding*, Society for Underwater Technology, vol. 652, pp. 652-657.
- Terzaghi, K. & Peck, R.B. 1967, *Soil Mechanics in Engineering Practice*, Wiley, New York.
- The Institution of Civil Engineers 1977, *Piles in Weak Rock*, Thomas Telford Ltd for the Institution of Civil Engineers, London.
- Thongmune, S., Matsumoto, T., Kobayashi, S.-i., Kitiyodom, P. & Kurosawa, K. 2011, Experimental and numerical studies on push-up load tests for sand plugs in a steel pipe pile, *Soils and Foundations*, vol. 51, no. 5, pp. 959-974.
- Tomlinson, M. & Woodward, J. 2008, *Pile design and construction practice*, 5th edn, CRC Press, London, UK.
- Tommasi, P., Verrucci, L. & Rotonda, T. 2014, Mechanical properties of a weak pyroclastic rock and their relationship with microstructure, *Canadian Geotechnical Journal*, vol. 52, no. 2, pp. 211-23.
- Tsoutrelis, C. & Exadaktylos, G. 1993, Effect of rock discontinuities on certain rock strength and fracture energy parameters under uniaxial compression, *Geotechnical and geological engineering*, vol. 11, no. 2, pp. 81-105.
- Vallejos, J.A., Salinas, J.M., Delonca, A. & Mas Ivars, D. 2016, Calibration and verification of two bonded-particle models for simulation of intact rock behaviour, *International Journal of Geomechanics*, vol. 17, no. 4, p. 06016030.
- Wang, C., Tannant, D. & Lilly, P. 2003, Numerical analysis of the stability of heavily jointed rock slopes using PFC2D, *International journal of rock mechanics and mining sciences (1997)*, vol. 40, no. 3, pp. 415-424.
- Wang, J. & Zhao, B. 2014, Discrete-continuum analysis of monotonic pile penetration in crushable sands, *Canadian Geotechnical Journal*, vol. 51, no. 10, pp. 1095-1110.

- Wang, T., Zhang, Y., Bao, X. & Wu, X. 2020, Mechanisms of soil plug formation of open-ended jacked pipe pile in clay, *Computers and Geotechnics*, vol. 118, p. 103334.
- Wasantha, P., Ranjith, P., Zhang, Q. & Xu, T. 2015, 'Do joint geometrical properties influence the fracturing behaviour of jointed rock? An investigation through joint orientation', *Geomechanics and Geophysics for Geo-Energy and Geo-Resources*, vol. 1, no. 1-2, pp. 3-14.
- White, D., Schneider, J. & Lehane, B. 2005, 'The influence of effective area ratio on shaft friction of displacement piles in sand', *Proceedings of the 1st International Symposium on Frontiers in Offshore Geotechnics, ISFOG 2005*, Taylor and Francis, pp. 741-8.
- White, D.J., Sidhu, H.K., Finlay, T.C., Bolton, M.D. & Nagayama, T. 2000, 'Press-in piling: the influence of plugging on driveability', *Proceedings of the 8th international conference of the Deep Foundations Institute, New York*.
- Williams, A.F., Johnston, I.W. & Donald, I.B. 1980, 'The design of socketed piles in weak rock', *Proceedings of International Conference on Structural Foundations on Rock*, Sydney, Australia, pp. 327-347.
- Wu, S. & Xu, X. 2016, A study of three intrinsic problems of the classic discrete element method using flat-joint model, *Rock Mechanics and Rock Engineering*, vol. 49, no. 5, pp. 1813-1830.
- Xu, X. 2007, 'Investigation of the end bearing performance of displacement piles in sand', Ph.D. Thesis, School of Civil and Resource Engineering, University of Western Australia.
- Xu, X., Schneider, J.A. & Lehane, B.M. 2008, Cone penetration test (CPT) methods for end-bearing assessment of open-and closed-ended driven piles in siliceous sand, *Canadian Geotechnical Journal*, vol. 45, no. 8, pp. 1130-1141.
- Yang, S., Jiang, Y., Xu, W. & Chen, X. 2008, Experimental investigation on strength and failure behaviour of pre-cracked marble under conventional triaxial compression, *International Journal of Solids and Structures*, vol. 45, no. 17, pp. 4796-4819.

- Yang, Y., Tang, X., Zheng, H., Liu, Q. & He, L. 2016, Three-dimensional fracture propagation with numerical manifold method, *Engineering Analysis with Boundary Elements*, vol. 72, pp. 65-77.
- Yu, F. & Yang, J. 2011, Improved evaluation of interface friction on steel pipe pile in sand, *Journal of Performance of Constructed Facilities*, vol. 26, no. 2, pp. 170-179.
- Yu, F. & Yang, J. 2012, Base capacity of open-ended steel pipe piles in sand, *Journal of Geotechnical and Geoenvironmental Engineering*, vol. 138, no. 9, pp. 1116-1128.
- Yang, Z.X., Jardine, R., Zhu, B. & Rimoy, S. 2014, Stresses developed around displacement piles penetration in sand, *Journal of Geotechnical and Geoenvironmental Engineering*, vol. 140, no. 3, p. 04013027.
- Zhai, H., Canbulat, I., Hebblewhite, B. & Zhang, C. 2017, Review of Current Empirical Approaches for Determination of the Weak Rock Mass Properties, *Procedia engineering*, vol. 191, pp. 908-917.
- Zhang, H. 2017, 'Case Histories of Large Diameter Driven Steel Tubular Piles on the East Coast of Australia', *Proceedings of the 1st International Conference on Geomechanics and Geoenvironmental Engineering (iCGMGE)*, Sydney, Australia.
- Zhang, H., Hewitt, P., Yip, G. & Lin, K. 2013, 'Aspects of driven piles on Macleay River and floodplain bridge', *Piling & Deep Foundations 2013*, Sydney, Australia.
- Zhang, X.-P. & Wong, L.N.Y. 2013, Loading rate effects on cracking behaviour of flaw-contained specimens under uniaxial compression, *International Journal of Fracture*, vol. 180, no. 1, pp. 93-110.
- Zhang, X.-P., Liu, Q., Wu, S. & Tang, X. 2015, Crack coalescence between two non-parallel flaws in rock-like material under uniaxial compression, *Engineering Geology*, vol. 199, pp. 74-90.
- Zhang, X., Fatahi, B., Khabbaz, H. & Poon, B. 2019, Assessment of the Internal Shaft Friction of Tubular Piles in Jointed Weak Rock Using the Discrete-Element Method, *Journal of Performance of Constructed Facilities*, vol. 33, no. 6, p. 04019067.

Zhao, X., Cai, M. & Cai, M. 2010, Considerations of rock dilation on modeling failure and deformation of hard rocks—a case study of the mine-by test tunnel in Canada, *Journal of Rock Mechanics and Geotechnical Engineering*, vol. 2, no. 4, pp. 338-349.

Zhou, M., Liu, H., Hossain, M.S., Hu, Y. & Zhang, T. 2016, Numerical simulation of plug formation during casing installation of cast-in-place concrete pipe (PCC) piles, *Canadian Geotechnical Journal*, vol. 53, no. 7, pp. 1093-1109.